Universidad de Alcalá

Programa de Doctorado en Tecnologías de la Información Geográfica

BURNED AREA MAPPING USING ACTIVE AND PASSIVE SENSORS OF MEDIUM SPATIAL RESOLUTION

Tesis Doctoral presentada por

MIGUEL ÁNGEL BELENGUER PLOMER

Directores:
Dr. Emilio Chuvieco Salinero
Dr. Mihai A. Tanase

Alcalá de Henares, 2020

«Los locos abren los caminos
que más tarde recorren los sabios.»

Carlo Dossi

Contents

Agradecimientos

Como no podría ser de otra manera, me gustaría empezar agradeciendo a Emilio y a Mihai, mis directores de tesis, la confianza depositada en mí desde que llegué a la Universidad de Alcalá en diciembre de 2016, hace casi tres años y medio. Pese a que ninguno de ellos había trabajado conmigo previamente, desde el primer día conté con una gran libertad a la hora de investigar y tomar mis propias decisiones, lo cual he valorado muchísimo durante todo este periodo. Pero al mismo tiempo, he podido contar con ellos cuando los he necesitado. Por ello, y por todo lo que me han enseñado durante mi etapa predoctoral, les estoy enormemente agradecido.

Corría el año 2018, y aunque ya llevaba casi dos años por Madrid, aún era capaz de quedarme horas esperando un autobús en la parada equivocada. Parecía que la gran ciudad no estaba hecha para mí. Fue entonces cuando apareció Gemma. No me hace falta utilizar ningún algoritmo de *machine learning* para predecir que sin ella, ni esta tesis ni yo mismo seriamos lo que somos. Ella ha sido el mayor punto de inflexión que ha habido en mi vida durante mis años de doctorado, como si de un nuevo km 0 se tratase. Siempre le estaré agradecido por su paciencia con los horarios de trabajo, cuanto menos peculiares, que he tenido algunas veces, por escuchar mis monólogos sobre el espectro electromagnético y más temas igual de interesantes o por darme un techo durante el corto, pero fantástico momento en el que fui *homeless*. En definitiva, gracias por estar, gracias por hacerme feliz.

Mis padres intuyeron que la felicidad de su hijo en la capital aumentaba conforme las visitas a Levante decrecían. Sabían que ambas variables eran inversamente proporcionales. Acertaron. Es a ellos, a mi madre y a mi padre, y al esfuerzo de ambos, a los que les tengo que agradecer que ahora esté redactando los agradecimientos de mi tesis doctoral. Sin ellos, sin su trabajo incansable, mi formación universitaria habría sido poco más que una ilusión. Gracias por apoyarme siempre, incluso cuando me incliné por estudiar Geografía, la cual no brilla por su alta tasa de empleabilidad. Intentaré que la próxima carrera tenga más salidas laborales.

Escribiendo sobre mis orígenes, se me hace imposible no pensar en mis amigos del pueblo. Los recuerdos de los buenos momentos que hemos pasado desde tiempos inmemoriales han sido esenciales, especialmente para mantener la salud mental durante los duros momentos del doctorado. Menos de los normales, más de los deseados. Aunque más visitas habrían sido de agradecer, gestos como que te acojan en Londres o que viajen casi hasta las antípodas para verte, por citar algunos, son actos que los tengo y tendré muy presentes. Gracias a todos, quién sabe si el destino nos acercará como en antaño. Esperemos que sí, todavía tenemos películas por rodar.

Al igual que el cine amateur, realizar un doctorado es algo muy vocacional, pues son muchas horas de trabajo que no tienen la remuneración que se merecen. Cuando además tu puesto de trabajo se encuentra en una sala sin ventanas ni luz natural, a veces cuesta mantener la motivación en hacer ciencia. Todo esto lo saben perfectamente mis compañeros de doctorado que realizan sus tesis en *el sótano*. Gracias por haberme motivado o ayudado cuando lo he necesitado. Vuestra compañía fue clave, especialmente cuando me encontraba solo, tan lejos de mi familia y amistades. También me gustaría agradecer el soporte y ayuda que se me ha prestado cuando me ha hecho falta por parte de los integrantes del departamento de Geología, Geografía y Medio Ambiente.

Una de las mejores partes de hacer la tesis, es la oportunidad de viajar que esta te ofrece. En 2018 tuve la ocasión de trabajar en Melbourne. Gracias a Cristina y a Mihai por darme la oportunidad de conocer esa parte del Mundo tan lejana, y haberse preocupado por mí durante mis aventuras en el hemisferio sur. Aunque mantener una diferencia horaria de ocho horas con España estaba bien, en 2019 decidí irme un poco más cerca, Italia sonaba bien. Mejor gastronomía que la australiana iba a ser fácil de encontrar. Pese a que mi italiano brilla por su ausencia, *grazie mille a Francesca per avermi dato l'opportunità di lavorare presso il RSLab di Trento e scoprire il Nord Italia*.

Finalmente, me gustaría también agradecer a todo aquel que de forma indirecta ha hecho posible que esta tesis sea una realidad. Especialmente a los profesores de la Universitat de València que me introdujeron en el mundo de las tecnologías de la información geográfica y de la investigación científica, en particular a Mª José, Joan Carles, Julia y Gustau. Asimismo, la constancia y disciplina que aprendí con la práctica del karate de la mano de mi *sensei*, Miquel, han sido fundamentales en el logro de todos los objetivos alcanzados hasta la fecha.

Por todo esto, y por todo lo que no he podido incluir, muchas gracias a todos,

Miguel A. Belenguer Plomer

Resumen

Esta tesis doctoral se centra en el desarrollo de nuevos algoritmos de cartografiado de áreas quemadas empleando sensores activos y pasivos de resolución espacial media. Así, la finalidad de la presente tesis es que los nuevos métodos desarrollados permitan reducir las incertidumbres actuales acerca de cuánta superficie es quemada anualmente en la Tierra. Actualmente, esta es estimada empleando imágenes ópticas de baja resolución espacial, que tienen limitaciones en zonas con una alta nubosidad, así como al cartografiar incendios pequeños, menores a 100 hectáreas. Dichas limitaciones se solventan en la presente tesis al incluir imágenes radar y al combinar estas con ópticas, todas ellas de resolución espacial media, tomadas desde los satélites de la Agencia Espacial Europea (ESA) Sentinel-1 y Sentinel-2. La tesis se estructura en ocho capítulos.

En el primer capítulo se hace referencia a la importancia del fuego, tanto a escala global como regional, resaltando la necesidad de poder disponer de productos de área quemada exactos para gestionar ecosistemas, monitorizar emisiones de gases de efecto invernadero (GEI) o modelar la vegetación. Desde sus inicios, la teledetección ha sido una fuente de información de gran valor para generar dichos productos, así, se explican los principios físicos que permiten cartografiar el área quemada empleando datos de teledetección. De forma complementaria, se incluye el estado del arte en cartografiado de áreas quemadas a través de imágenes ópticas, radar y la combinación de ambas. Finalmente se presenta la hipótesis, la motivación y los objetivos de la tesis.

En el segundo capítulo se aborda la generación de un algoritmo de cartografiado de área quemada basado en imágenes Sentinel-1 del coeficiente de retro-dispersión de banda C. Este aplica el detector Reed-Xiaoli (RXD) para distinguir cambios anómalos en el coeficiente de retro-dispersión, que se vinculan a incendios mediante el uso de anomalías térmicas adquiridas durante el período de detección por sensores térmicos. Cuando las anomalías térmicas no estuvieron disponibles, se utilizó un clasificador de aprendizaje automático (*random forests*) para detectar áreas quemadas. Los perímetros de área quemada derivados de imágenes ópticas (Landsat-8 y Sentinel-2) se utilizaron para validar los resultados del algoritmo en 21 millones de hectáreas distribuidas en 18 ubicaciones globalmente repartidas, que representan los principales biomas afectados por incendios. Se calculó un coeficiente de Dice (DC) medio sobre todas las ubicaciones estudiadas de 0.59±0.06 (± intervalo de confianza, 95%), mientras que los errores de omisión (OE) y comisión (CE) medios fueron de 0.43±0.08 y 0.37±0.06, respectivamente. Al comparar la exactitud lograda con la del producto global de área quemada más empleado, el MCD64A1, el algoritmo propuesto mejoró el DC en 0.13 mediante una reducción de los errores de omisión y comisión de 0.12 y 0.06, respectivamente. En el tercer capítulo se analiza la relación entre la exactitud del cartografiado y el tiempo de computación nece-

sario para el algoritmo basado en RXD, descrito en el capítulo dos, en diferentes tamaños de píxeles (20, 30, 40 y 50 m). El análisis se realizó en seis áreas de estudio distribuidas globalmente. Los resultados sugieren diferencias marginales en la exactitud al variar el tamaño de píxeles, detectándose mapas ligeramente más exactos al emplear espaciados mayores al de la resolución nominal de Sentinel-1 (20 m). No obstante, el tiempo de computación fue considerablemente mayor conforme el espaciado entre píxeles era más detallado. Así, las imágenes con un espaciado entre píxeles de 30 a 50 m proporcionan la relación tiempo-exactitud más idónea.

En el cuarto capítulo se analizan los factores que pueden influir en la exactitud del cartografiado del área quemada. El enfoque principal de análisis, fue el proceso de decorrelación temporal observado durante el desarrollo del algoritmo. La decorrelación temporal se refiere a que las diferencias temporales entre los valores del coeficiente de retro-dispersión previo y posterior al incendio pueden no ocurrir inmediatamente trascurrida la combustión de la vegetación. Diferentes variables ambientales que pueden influir en la retro-dispersión, incluida la severidad del incendio, la recuperación de la vegetación posterior al incendio, el contenido de agua del suelo y la vegetación, la pendiente y la orientación topográfica fueron analizadas. Se utilizó un clasificador de *random forests* para estimar la importancia de estas variables en el proceso de decorrelación temporal. El análisis mostró que más del 32% de los píxeles quemados ubicados en el área estudiada se vieron afectados por la decorrelación temporal, siendo la severidad del fuego, el contenido de agua de la vegetación y la humedad del suelo, sus principales impulsores. Sin embargo, cuando se detectaron áreas quemadas mucho después del incendio, el contenido de agua tanto del suelo como de la vegetación fue el principal causante de los cambios en el coeficiente de retro-dispersión.

En el quinto capítulo se aborda una comparativa entre algoritmos de cartografiado de áreas quemadas, dos basados en imágenes radar (Sentinel-1) y uno basado en ópticas (Sentinel-2). El análisis se llevó a cabo en diez áreas de estudio (10 millones de ha) en África. Los algoritmos se basaron en diversas estrategias de cartografiado y datos (reflectividad de superficie, coherencia interferométrica y coeficiente de retro-dispersión, siendo este último el presentado en el segundo capítulo). Para validar los mapas, se utilizaron perímetros de referencia derivados independientemente de imágenes ópticas (Landsat 8 y Sentinel-2). Al considerar todas las áreas de estudio, el algoritmo basado en datos ópticos proporcionó un aumento significativo de la exactitud en comparación con los basados en el radar, aunque este podría haber sido impulsado por el uso de los mismos datos ópticos al generar los perímetros de referencia que al cartografiar el área quemada. No obstante, el análisis sugirió que los algoritmos basados en imágenes ópticas proporcionan un incremento significativo en la exactitud sobre los algoritmos basados en radar. Sin embargo, en las regiones donde la nubosidad es más persistente, los algoritmos basados en radar ofrecen una valiosa fuente de datos, siendo los mapas basados en el coeficiente de retro-dispersión de mayor exactitud.

En el sexto capítulo se presenta un análisis exhaustivo sobre el uso de redes neuronales convolucionales (CNN) para la detección y cartografiado de áreas quemadas. Las CNN son un método de aprendizaje profundo (*Deep learning*) ampliamente aplicado en estudios recientes basados en teledetección. Las CNN se han utilizado en este capitulo para cartografiar áreas quemadas empleando imágenes radar (Sentinel-1), ópticas (Sentinel-2) y la combinación de ambas. Para ello, fueron consideradas diez áreas de estudio distribuidas

globalmente, de las cuales, cinco se emplearon para hallar la combinación óptima de los modelos ajustando la dimensión más apropiada para la extracción de atributos de clasificación de la imagen, la normalización de los datos y el número de capas ocultas incluidas en la red. Por otro lado, las cinco áreas restantes se emplearon para llevar a cabo una validación independiente de los modelos óptimos. Tanto la dimensión como la normalización de datos óptima fueron condicionadas por la clase de cobertura del suelo y el tipo de sensor (óptico o radar), mientras que el número de capas ocultas sólo condicionó el tiempo de computación sin mejorar la exactitud del cartografiado. Con la combinación de imágenes radar y ópticas se permitió cartografiar las áreas quemadas con una exactitud similar e incluso ligeramente superior a la observada en enfoques anteriores realizados en el programa Fire_cci basados tanto en Sentinel-1 (DC 0.57) como en Sentinel-2 (DC 0.7) y eliminar vacíos de información debido a la presencia de nubes que afecta a los mapas basados únicamente en sensores pasivos.

En el séptimo capítulo, dada la diferencia de exactitud entre los datos radar y ópticos al cartografiar áreas quemadas, proporcionando los segundos tipos de datos unos mapas más exactos. Se evaluaron diferentes índices temporales basados en el coeficiente de retro-dispersión, para así comprender su idoneidad al cartografiar áreas quemadas y poder mejorar los algoritmos de cartografiado basados en imágenes radar en trabajos futuros. El análisis se llevó a cabo utilizando el clasificador anteriormente citado, *random forests*, para estimar la importancia de cada índice al cartografiar áreas quemadas. Dependiendo del tipo de cobertura del suelo, la humedad y las condiciones topográficas, se observaron diferencias notables entre los índices temporales del coeficiente de retro-dispersión.

En el octavo y último capítulo, se incluyen las conclusiones finales derivadas de toda la investigación que se ha desarrollado en esta tesis doctoral. Se describen los principales hallazgos de la misma, así como las limitaciones encontradas. Asimismo, se incluyen las futuras líneas de investigación que pueden ayudar a mejorar el cartografiado global de áreas quemadas empleando, tanto imágenes radar como la combinación de estas con las ópticas.

Abstract

This doctoral thesis focuses on the development of new algorithms for burned area mapping using active and passive sensors of medium spatial resolution. Such algorithms shall allow reducing current uncertainties on areas affected by fire every year at global level. Currently, global burned area is estimated from low spatial resolution optical images, which have limitations in areas with high cloud cover, as well as when mapping small fires (i.e., less than 100 hectares). The developed algorithms reduce such limitations by using radar images and by combining radar and optical datasets acquired at medium spatial resolution by the European Space Agency (ESA) satellites Sentinel-1 and Sentinel-2. The thesis is structured in eight chapters.

The first chapter describes the importance of fire at global and regional level, and highlighting the need for accurate burned area products for a range of application including ecosystem management, GHGs emissions monitoring and vegetation modelling. Since its inception, remote sensing has been a highly valuable source of information for burned area detection and monitoring. Therefore, the physical principles on which burned area mapping is achieved through using remote sensing data are also explained and related to the state-of-the-art when mapping burned areas through optical images, radar images, and their combination. Finally, the hypothesis, motivation, and objectives of the thesis are presented.

In the second chapter, a burned area mapping algorithm based on C-band Sentinel-1 imagery is discussed. The algorithm applies the Reed-Xiaoli detector (RXD) to distinguish anomalous changes of the backscatter coefficient. Such changes are linked to fires events through spatially and temporally coincident thermal anomalies acquired by ancillary sensors. For periods with no thermal anomalies, a machine learning classifier, random forests, was used to detect the burned areas. Burned area perimeters derived from optical images (Landsat-8 and Sentinel-2) were used to validate the algorithm over 21 million hectares distributed worldwide in 18 locations that represent the main biomes affected by fires. The mean Dice coefficient (DC) was calculated over all the 18 locations revealed a burned area mapping accuracy of 0.59±0.06 (confidence interval, 95%), with the mean errors of omission (OE) and commission (CE) reaching 0.43±0.08 and 0.37±0.06, respectively. The results were compared with those provided by the most widely used global burned area product, the MCD64A1. The proposed algorithm improved, on average, the DC by 0.13 by reducing OE (0.12) and CE (0.06).

In the third chapter, and the relationship between mapping accuracy and computing time needed for the RXD-based algorithm, described in chapter two, was analysed for different pixel spacings (i.e., 20, 30, 40 and 50 m). The analysis was carried out in six

globally distributed study areas. The results suggest marginal differences in accuracy when varying the pixel spacing, with slightly more accurate maps being obtained using higher spacings when compared to the nominal of Sentinel-1 spatial resolution (20 m). However, the computing time was considerably higher at low pixel spacing with images between 30-50 m providing the optimum trade-off between accuracy and computing time.

In the fourth chapter, factors that may influence the burned area mapping accuracy were analysed. The main focus of the analysis was the temporal decorrelation process, observed during algorithm development. The temporal decorrelation refers to the temporal difference between the observed post-fire backscatter coefficient change in regard to the time of change which may occur long after the vegetation combustion. In this chapter, different environmental variables that may influence radar scattering were analysed including, fire severity, post-fire vegetation recovery, soil, and vegetation water content, slope and topographic aspect. A random forests classifier was used to estimate the importance of these variables for the temporal decorrelation process. The analysis showed that over than 32% of the burned pixels located in the studied area were affected by temporal decorrelation, with fire severity, vegetation water content and soil moisture being its main drivers. However, when burned areas were detected long after fire, soil and the vegetation water content of both were the most important drivers behind the observed changes of the backscatter coefficient.

The fifth chapter addresses the comparison between two burned area mapping algorithms based on radar images (Sentinel-1) and one based on optical (Sentinel-2). The analysis was carried out over ten study areas (10 million ha) in Africa. The algorithms were based on different mapping strategies and datasets (surface reflectivity, interferometric coherence and backscatter coefficient, the latter being presented in the second chapter). The maps were validated through reference perimeters derived independently from optical images (Landsat 8 and Sentinel-2). When considering all study areas, the optical data-based algorithm provided a significant increase in accuracy compared to radar-based ones. However, this may have been driven by the use of the same optical datasets when generating the reference fire perimeters (i.e., Sentinel-2). Nevertheless, the analysis suggested that optical image-based algorithms provide a significant increase in accuracy over radar-based algorithms. However, in regions with persistent cloud cover, the radar-based algorithms offered a valuable source of information, with radar-based detections being more accurate.

In the sixth chapter, a comprehensive analysis of the use of convolutional neural networks (CNN) for burned areas detection and mapping is presented. CNN is a Deep Learning method widely applied in recent remote sensing studies. CNN were used to develop a seamless burned area mapping algorithm that includes radar (Sentinel-1), optical (Sentinel-2) and radar-optical datasets. Ten globally distributed study areas were considered. Five areas were used to establish the optimum dimensionality for feature extraction (i.e., 1D or 2D, data normalisation and the number of hidden layers). The remaining five areas were used to carry out an independent validation of the optimal models. Both the dimension and the optimal data normalisation were conditioned by land cover class and the senor type (optical or radar). The number of hidden layers only influenced the computation time without any improvements in the mapping accuracy being observed. The combination of radar and optical images allowed mapping burned areas with similar, or slightly higher accuracies when compared to those achieved in previous approaches devel-

oped within the Fire_cci program and based on both Sentinel-1 (DC 0.57) or Sentinel-2 (DC 0.7) datasets. Furthermore, the combined radar-optic approach eliminated information gaps due to the presence of clouds which affect detections based on passive sensors alone.

In the seventh chapter, given the difference in accuracies between radar and optical data when mapping burned areas, various backscatter coefficient based temporal indices were evaluated to understand their suitability for burned areas mapping. The analysis was carried out to understand how radar-based burned area mapping algorithms may be improved in future work. The analysis is carried out using the random forests classifier, and the importance of each radar-based index is assessed when mapping burned areas. Depending on the land cover type, soil moisture, and topographic conditions, notable differences were observed between the temporal backscatter-based indices.

In the eighth and last chapter, the conclusions derived from all research carried out within this doctoral thesis are resumed. The main findings, as well as the limitations found, are described as well as future lines of research that may help improving global mapping of burned areas from radar datasets and the combination of radar and optical datasets.

Overview

Funding

Publications arising from this thesis

This doctoral thesis is presented as a compendium of articles except for the overall Introduction chapter and the general Conclusions chapter. All other chapters have been published in Journal Citation Reports (JCR), or Scopus indexed international journals or conference proceedings except for chapter six which is currently under review in the journal Remote Sensing of the Environment (Table 1).

Table 1: Publications arising from this doctoral thesis, Journal Citation Reports impact factor (IF), Scopus CiteScore (CS), and its correspondent thesis chapter.

Publication	IF	CS	Chapter
Belenguer-Plomer, M.A., Tanase, M.A., Fernandez-Carrillo, A. and Chuvieco, E. (2019). Burned area detection and mapping using Sentinel-1 backscatter coefficient and thermal anomalies. *Remote Sensing of Environment*, **233**, 111345.	8.218	8.89	2
Belenguer-Plomer, M.A., Chuvieco, E., and Tanase, M.A. (2020). Optimum Sentinel-1 pixel spacing for burned area mapping. *Accepted in IEEE Inter. Geos. and Rem. Sens. Symp. (IGARSS)*	——	0.59	3
Belenguer-Plomer, M.A., Chuvieco, E. and Tanase, M.A. (2019). Temporal decorrelation of C-band backscatter coefficient in Mediterranean burned areas. *Remote Sensing*, **11**(22), 2661.	4.118	4.89	4

Table continued on next page

Table 1 – continued from previous page

Publication	IF	CS	Chapter
Tanase, M.A., **Belenguer-Plomer, M.A.**, Roteta, E., Bastarrika, A., Wheeler, J., Fernández-Carrillo, Á., Tansey, K., Wiedemann, W., Navratil, P., Lohberger, S., Siegert, F., and Chuvieco, E. (2020). Burned area detection and mapping: Intercomparison of Sentinel-1 and Sentinel-2 based algorithms over Tropical Africa. *Remote Sensing*, **12**(2), 334.	4.118	4.89	5
Belenguer-Plomer, M.A., Tanase, M.A., Chuvieco, E. and Bovolo, F. (submitted on May 2020). A deep learning-based approach for burned area mapping using radar and optical data, *Remote Sensing of Environment*, in review.	8.218	8.89	6
Belenguer-Plomer, M.A., Chuvieco, E., and Tanase, M.A. (2019). Evaluation of backscatter coefficient temporal indices for burned area mapping, *Proc. SPIE 11154, Active and Passive Microwave Remote Sensing for Environmental Monitoring III, 111540D*	—-	0.5	7

Conferences

The achievements of this work have been presented at the following conferences and symposiums:

1. 2nd Symposium of Geographical Information Technologies PhD program, 20 November 2019, Alcalá de Henares (Spain).

2. 12th EARSeL Forest Fires SIG Workshop, 3-5 October 2019, Rome (Italy).

3. SPIE Remote Sensing, 9-12 September 2019, Strasbourg (France).

4. ESA Living Planet Symposium, 13-17 May 2019, Milan (Italy).

5. ForestSAT, 1-5 October 2018, Maryland (USA).

6. SPIE Remote Sensing, 10-13 September 2018, Berlin (Germany).

7. 1st Symposium of Geographical Information Technologies PhD program, 18 January 2018, Alcalá de Henares (Spain).

8. 2nd Workshop of Geography PhDs, 24 October 2017, Madrid (Spain).

9. 17th Congress of the Spanish Association of Remote Sensing, 3-7 October 2017, Murcia (Spain).

10. 11th EARSeL Forest Fires SIG Workshop, 25-27 September 2017, Chania (Greece).

Visits to international research centres

During the research period, the author of this doctoral thesis carried out two research internships at the:

1. Remote Sensing Laboratory, Fondazione Bruno Kessler (Trento, Italy).

    - Researcher in charge: Francesca Bovolo
    - Period: 15/04/2019 - 15/07/2019
    - Funding: FPU mobility grant (EST18/00497)

2. School of Ecosystems and Forest Sciences, The University of Melbourne (Australia).

    - Researcher in charge: Cristina Aponte
    - Period: 17/04/2018 - 16/07/2018
    - Funding: Mobility grant for researchers (UAH)

Awards

Both, *Temporal backscattering coefficient decorrelation in burned areas* and *Evaluation of backscatter coefficient temporal indices for burned area mapping* research papers won the Best Student Paper Award within the Active and Passive Microwave Remote Sensing for Environmental Monitoring session at SPIE Remote Sensing symposium in 2018 (Berlin) and 2019 (Strasbourg), respectively.

Chapter 1

Introduction

This chapter introduces the research topic, fires, and describes its effects from regional to global levels highlighting, at the same time, the need for accurate burned area mapping products for a range of application from ecosystem management, to GHGs emissions monitoring and vegetation modelling. The chapter focuses on remote sensing technologies as a tool for obtaining highly valuable information for burned area detection, mapping and monitoring. The physical principles underpinning burned area mapping from remote sensing data are briefly explained and related to the state-of-the-art satellite-based fire monitoring from optical and radar sensors as well as their joint use. The hypothesis, motivation, and objectives of this thesis are presented.

1.1   Fire impacts on the Earth system

Fire has been present since the Silurian period, around 420 million years ago (Scott & Glasspool, 2006), shaping terrestrial ecosystems as a natural selection agent (Pyne, 1982; Pausas & Paula, 2012). This presence resulted in species developing fire-adaptation strategies. For instance, in the Mediterranean climates, *Pinus halepensis* have serotinous cones that open after fire events to release the stored seeds (Goubitz et al., 2002; Lotan, 1976). In contrast, in dry and cold climates such as the Boreal, fire has a determinant ecological role by recycling organic matter and consequently, increasing soil nutrient concentration (DeBano et al., 1998; Harden et al., 2004).

Fire regimes, defined by frequency, size, intensity, seasonality, type and severity (Flannigan et al., 2000), have suffered oscillations mainly due to climate variations (Marlon et al., 2013). However, as humanity developed and began to manage territories, fire regimes changes were driven by social and economic needs (Chuvieco et al., 2019). Nowadays, main fire-affected areas are those where a marked dry season can be found such as African and Australian savannas, Mediterranean ecosystems, grasslands of Central Asia and boreal forests or America and Asia (Lizundia-Loiola et al., 2020; Chuvieco et al., 2016). However, there is uncertainty about the area which is burned each year globally, estimated at 4 to 4.5 million km^2 (Giglio et al., 2018; Lizundia-Loiola et al., 2020). Human activity is behind most of these fires. For instance, in Mediterranean environments, estimations relate up to 90% of fires to human activities (Vilar et al., 2016).

Human-induced processes have unbalanced the natural fire regimes. On the one hand, the population density increment and the expansion of the agricultural fields in savannas and grasslands have generated a global reduction of burned area over the past two decades (Arora & Melton, 2018; Andela et al., 2017). On the other hand, the occurrence of megafires (> 10000 ha) has increased, mainly as a result of a high occurrence of severe droughts (Stephens et al., 2014), a common consequence of climate change in many territories. A recent example is the unprecedented burned area in Australia during the summer of 2019-2020, where up to 21% of Temperate forested areas were burned, far from the historical average of 5% (Boer et al., 2020). These kinds of events have catastrophic consequences over society since may cause human fatalities, casualties and evacuations, especially when it occurs under heat waves and drought conditions, in which fire propagation is faster (Bowman et al., 2017; Tedim et al., 2020). Ecosystem services also suffer the fire effects through a loss of natural resources (e.g., wood), reducing tourism and recreation activities appealing, destroying properties as well as local agriculture production (Chuvieco et al., 2010; Diaz, 2012). Furthermore, fire impact on air quality may cause an increment of people mortality, particularly among those with previous respiratory pathologies (Reid et al., 2016; Kochi et al., 2016). Besides, such an unbalancing may incur regional to global environmental effects such as changes in soil fertility and water supply, loss of biodiversity, or the increment of atmospheric greenhouse gases (GHGs) as the vegetation sequestrated carbon is burned (Hansen et al., 2013; Van der Werf et al., 2010; Aponte et al., 2016; Bond et al., 2005; Lavorel et al., 2007; Pausas & Paula, 2012; Hoffmann et al., 2002). In consequence, global biochemical GHGs cycles, aerosols released into the atmosphere (Van Der Werf et al., 2017; Andreae & Merlet, 2001; Bowman et al., 2009) and the radiative energy balance (Jin & Roy, 2005; Bowman et al., 2009; Van Der Werf et al., 2017) may be modified. For instance, an increment of fire activity in Boreal latitudes has been evidenced

as the cause of changes in albedo and snow in Greenland (Evangeliou et al., 2019). While different temperature-response to fires has been found depending on the latitudes, having net cooling and warming effects in Boreal and Tropical areas, respectively (Liu et al., 2019). Fires may result in an Earth cooling due to a negative radiative forcing induced by the emitted aerosols into the atmosphere (Ward et al., 2012). In contrast, carbon emissions from fires may accelerate current global warming (Westerling et al., 2006), which in turn may progressively reinforce the role of fires on climate change (Flannigan et al., 2006; Langenfelds et al., 2002). Such opposite effects suggest a limited understanding of fire-induced impacts on the global climate (Liu et al., 2019; Krawchuk et al., 2009).

Given the relevance of fire effects on climate and environments, the Global Climate Observing System (GCOS) considers fire disturbance as an Essential Climatic Variable (ECV). According to Bojinski et al. (2014), "an ECV is a physical, biological, chemical or a group of connected variables capable of modifying the climate system". Through the Climate Change Initiative (CCI) programme of the European Space Agency (ESA), Earth observation datasets are being used to provide climate modellers with as products of many ECV's (Hollmann et al., 2013). Fire has been present in the CCI programme since its beginning in 2010 providing valuable knowledge as long-term time series of global burned area and new methods about burned area mapping (Chuvieco et al., 2018). The necessity of more accurate products of burned area capable of reducing current uncertainties when monitoring the fire-induced climate impacts was a main driving factor behind the project (Mouillot et al., 2014; Poulter et al., 2015).

1.2   Applications of burned area maps

There is an undeniable necessity of providing governments, users and scientists with burned area products. According to Mouillot et al. (2014), the main applications of such information include:

- Ecosystem management, since fire is considered a natural hazard, and consequently, the authorities of most of the countries make considerable efforts to extinguish it. Analysing the ignition, propagation and origin (i.e., climatic or human) of past fire events is needed to expand the fire-behaviour knowledge and build fire-propagation models. Such models need burned area products for development and calibration purposes (Filippi et al., 2014). Long time-series of burned area products are also valuable when analysing and defining fire regimes and their changes (Chang et al., 2008).

- Atmospheric fire-emissions, which are commonly estimated considering the burned area, fuel load, burning efficiency and emission factors using the approach proposed by Seiler & Crutzen (1980). Such an approach is the basis of the Global Fire Emissions Database (GFED) (Van der Werf et al., 2010), which has been widely used since its release when modelling the climate (Van Der Werf et al., 2017).

- Vegetation modelling, which takes into account the fluxes of energy, water and carbon between biosphere and atmosphere to estimate the patterns which vegetation will follow (Sitch et al., 2003; Mouillot et al., 2014). Given the dynamic characteristic of these models, fire size, shape and orientation are essential inputs and

are included through burned area products (Abatzoglou et al., 2018; Laurent et al., 2018).

1.3   Earth observation role in burned area mapping

Measurements provided from field campaigns have high value when studying environmental issues as fires. However, repeat field-based assessments over large areas is limited by high costs and scaling issues. Few are the countries in which it is possible to find reliable statistics about fires (Chuvieco et al., 2020). Besides, field measurements may also be limited by the reduced access of some fire scars, particularly in steep terrain or high latitudes (Chuvieco, 2020). Additional access limitations may arise due to wars, political instability, restricted mobility. For instance, while these lines are written, the world is under the pandemic effects of the COVID-19. In order to reduce virus spread, most countries have limited people mobility, including research field campaigns.

Fortunately, since its beginning in the 1970s with the Landsat programme, Earth observation from spaceborne sensors provide a reliable source of information for burned area mapping and fire monitoring (Chuvieco et al., 2019, 2020). Currently, several Earth observation satellites belonging to different agencies such as NASA (National Aeronautics and Space Administration), ESA (European Space Agency), JAXA (Japanese Aerospace Exploration Agency), CNES (Centre National D'Etudes Spatiales), INTA (Instituto Nacional de Técnica Aeroespacial), as well as private companies like Deimos, Planet or DigitalGlobe, are orbiting the Earth providing valuable information in the form of remotely sensed imagery. Furthermore, some agencies (e.g., NASA and ESA) provide the satellite data in near-real-time and under a free-data access policy.

The specific objective to achieve conditions the suitability of each Earth observation dataset. There are substantial differences among sensors aboard satellites which can be grouped into four resolutions:

- Radiometric, which defines the potential range in which the measurements (i.e., pixel values) are recorded. A clearer distinction between the captured elements is possible by increasing the radiometric resolution.

- Temporal, which depends on the revisit period of the satellite, i.e., the frequency in which a given sensor aboard a satellite can record data in a specific location.

- Spatial, which refers to the minimum separation between the recorded surface elements (pixels) on Earth's surface.

- Spectral, related to the separation and the number of electromagnetic spectrum bands in which the sensors acquired the datasets (Figure 1.1).

Generally, the higher the resolution considered, the higher the quality obtained. However, an increase in any resolution may limit one or more of the remaining resolution parameters of the sensor. Therefore, the most appropriate sensor, for a specific goal, is related to the application requirements. For instance, mapping burned area using 20 m spatial resolution imagery provides more accurate results than when using 500 m imagery.

However, the latter data required less computing and storage capacity, essential to consider when dealing with global approaches. Nevertheless, ever-improving processing hardware and new cloud-based processing services such as Google Earth Engine (GEE) or Amazon Web Services (AWS) facilitate massive processing amounts of data reducing such limitations. These improvements are essential to take advantage of the current medium spatial resolution sensors such as the C-band synthetic aperture radar (SAR) and the MultiSpectral Instrument (MSI) aboard on the ESA's Sentinel-1 and Sentinel-2 satellites respectively, used in this PhD thesis (see section 1.6 and section 1.7).

1.4 Principles of remote sensing-based fire monitoring

Earth observation from remote sensing uses the electromagnetic radiation recorded by sensors onboard satellites in different spectral regions (Figure 1.1). Such sensors provide valuable information about the Earth's surface as the electromagnetic radiation interacts differently with materials and environmental phenomena (e.g., fires) depending on the wavelength observed.
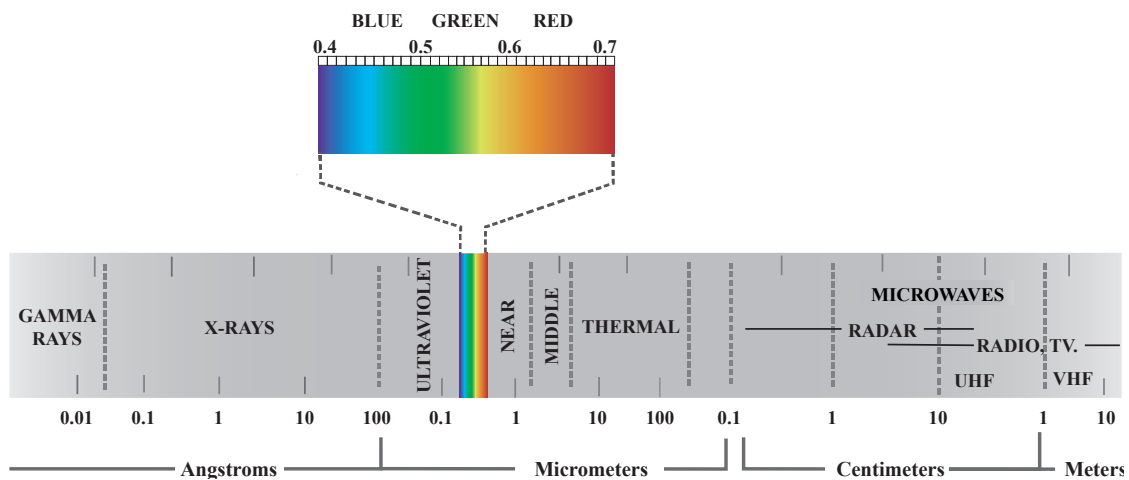
Figure 1.1: Electromagnetic spectrum (apadpted from Chuvieco (2020)).

Most Earth observation satellites have near-polar orbits around 700 km above the Earth surface. The radiation recorded by such sensors cross once the atmosphere when it is recorded the Earth's emitted energy, and twice when the energy is emitted outside the Earth, by the Sun or the sensor itself (i.e., active sensor). Since the presence of GHSs such as H_2O, CO_2, CH_4, and O_3 limits the atmospheric energy transmission, Earth observation is limited to spectral ranges where the absorption is low (Figure 1.2).

In the following sections, the main domains of the electromagnetic spectrum where Earth observation remote sensing operates (i.e., optical domain, middle and thermal infrared and microwaves) along with the physics principles on which burned area mapping is based, are explained for each spectrum domain considered in this PhD thesis.
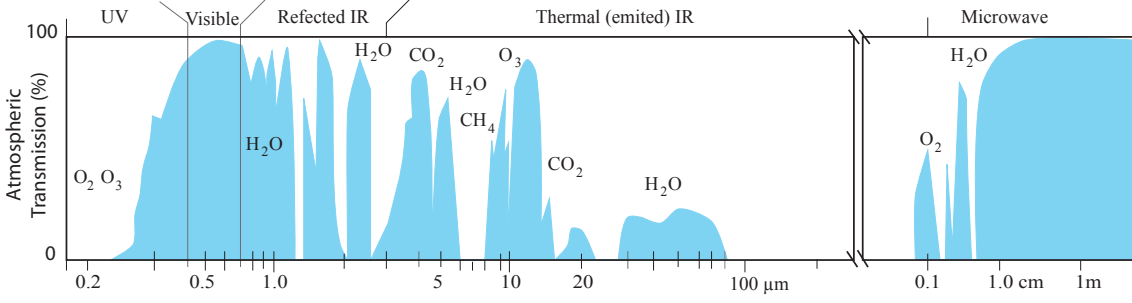
Figure 1.2: Atmospheric transmission and main gas absorption per wavelengths (adapted from NASA's Earth observatory).

1.4.1   Optical domain

Most remote sensing-based fire monitoring approaches have been based on the optical spectral domain which includes radiation from (i) the visible (i.e., blue: 0.4-0.5 μm, green: 0.5-0.6 μm and red: 0.6-0.7 μm), (ii) the near-infrared (NIR: 0.7-1.2 μm), and (iii) short-wave infrared (SWIR: 1.2-2.5 μm) regions of the electromagnetic spectrum (Figure 1.1). Sensors which record these wavelengths are passive, which means they measure the radiation emitted from external sources. In the optical domain, sensors record the radiation emitted by the Sun and reflected on Earth's surface towards sensors onboard satellites with the reflected energy being only a fraction of the incoming radiation (Equation 1.1).

$$L_i = L_r + L_a + L_t \tag{1.1}$$

where L_i is the incoming radiance (W m^{-2} sr^{-1}) while r, a and t refers to the reflected, absorbed and transmitted energy, respectively. In remote sensing such measurements are used in relative terms (Equation 1.2).

$$\frac{L_i}{L_i} = \frac{L_r}{L_i} + \frac{L_a}{L_i} + \frac{L_t}{L_i} \tag{1.2}$$

which frequently are represented as (Equation 1.3):

$$1 = \rho + \alpha + \tau \tag{1.3}$$

where ρ, α and τ refers to the reflected, absorbed and transmitted energy, which depends on the observed surface and wavelength (λ) as (Equation 1.4):

$$1 = \rho_\lambda + \alpha_\lambda + \tau \tag{1.4}$$

The optical region, and particularly NIR and SWIR wavelengths, are the most suitable for burned area mapping due to the sensitivity to fire-induced changes on vegetation, i.e., reduction of leaves chlorophyll content and vegetation water content which result in decreasing NIR values and increasing SWIR values (Pereira, 1999; García & Caselles, 1991; Stroppiana et al., 2003; Gao, 1996). In contrast, visible wavelengths were found less sensitive when mapping burned area (Pereira et al., 1997).

As the optical radiation passes through the atmosphere, it is being scattered and at-

tenuated before reaching the spaceborne sensors. Hence, the recorded radiance (L^s) is influenced by the Earth's atmosphere (Equation 1.5).

$$L^s = L^{su} + L^{pd} + L^{ps} \tag{1.5}$$

where su surface reflectance and unscattered by the atmosphere, pd atmospherically scattered and reflected to back to Earth (and vice versa), and ps reflectance uniquely scattered in the atmosphere.

A further factor affecting surface reflectance values in the optical domain is the topography, particularly in steep areas as the local incidence angle of solar radiation as well as the slope orientation modulates reflectance values. Indeed, burned area mapping accuracy from optical data has been improved when atmospheric and topographic corrections were considered (Said et al., 2015; Gitas & Devereux, 2006).

1.4.2 Middle and thermal infrared regions

The middle (MIR: 1.2-8 μm) and thermal (TIR: 8-14 μm) regions of the electromagnetic spectrum lay between the solar domain and the energy emitted by the Earth itself. From the MIR region onward the recorded signal is dependent on the temperature of the Earth surface, hence the name thermal, according to Planck's law, which refers to blackbodies (perfect radiators). However, the terrestrial Earth surface is formed by different materials (i.e., not blackbodies). Therefore, emissivity plays a crucial role in thermal remote sensing approaches and needs to be estimated (Valor & Caselles, 1996).

In burned area mapping, the MIR bands have shown potential due to sensitivity to the scattering effects of aerosols, whose presence is associated with biomass combustion. However, the mixture of Sun reflected radiation and Earth emitted radiation has limited the use of MIR bands (Libonati et al., 2010, 2015; Pereira, 1999). The TIR bands have also been used for recent mapping fires. However, several factors have restricted the use of thermal wavelengths for burned areas mapping including: (i) the cooling process of burned areas after fire extinction; and (ii) the coarse spatial resolution of the thermal sensors restricted the (Hawbaker et al., 2017, 2008). Despite such limitations, both TIR and MIR spectral regions are widely employed to generate valuable ancillary datasets, such as thermal anomalies (hotspots) that are associated with active fires, and thus frequently used in burned area mapping from a range of sensors (Schroeder et al., 2014; Giglio et al., 2003). In particular, the MIR region has been useful when detecting active fires due to the higher emittance of fires in such spectral-domain when compared to the non-fire background (Chuvieco, 2020). As for the optical wavelengths, the radiation emitted by Earth's surface is also affected by the atmosphere and particularly by GHGs gasses. However, such atmospheric modulation is weak at these wavelengths and thus have marginal effects on active fires monitoring (Barducci et al., 2002).

1.4.3 Microwaves

The microwave domain is formed by radiation with longer wavelengths, ranging from 1 mm to 1 m. The main advantage of microwave sensors in remote sensing is the independence of atmospheric conditions, including clouds. Earth emits energy in the microwave

wavelengths *per se*. Such energy is recorded by satellite sensors, known as passives microwave sensors, and widely used to estimate soil moisture or ocean salinity (Colliander et al., 2017; Saleh et al., 2004). However, such sensors are not suited for fire monitoring due to Earth's low emittance, which translates into very low spatial resolutions (tens of km). However, microwaves from active sensors, such as synthetic aperture radars (SAR) which emit and record the reflected radiation, have been used when mapping burned areas mainly due to microwaves independence of cloud cover and solar illumination (Bourgeau-Chavez et al., 2002; French et al., 1999).

SAR sensors can emit energy in the microwave domain. The energy is absorbed, transmitted, and reflected by the Earth surface. The amount of radiation which returns to the sensor is known as backscatter and has two components, phase and amplitude. The phase, which measures the difference of cycles between the emitted and returned waves from 0 to 2π. The phase is associated with the distance between the surface and sensor. The application of the phase information is based on combining two near-simultaneous measurements from slightly different observation geometries. The recorded phase differences are related to the three-dimensional position of the scattering elements and thus used to derive topographic and displacement information. A by-product of the phase combination is the interferometric coherence which provides information on the degree of correlation between the two radar images combined. Previous remote sensing-based approaches for fire monitoring have considered the interferometric coherence due to its ability to provide information on the biophysical properties of land classes (Liew et al., 1999; Tanase et al., 2010b). The coherence is given by the correlation of the two images in a range 0 (low) to 1 (high). The amplitude, which measures the energy scattered back to the sensor (Ps) from the incident (Pi) as shown in Equation 1.6 (Small, 2011).

$$\beta = P_s/P_i \tag{1.6}$$

The absence of defined target edges when monitoring Earth's surface involves computing the backscatter coefficient, which represents the backscatter (β) per reference area (Equation 1.7) (Emery & Camps, 2017).

$$\beta^0 = \beta/A_\beta \tag{1.7}$$

where A_β is the reference area without considering any Earth model (Raney et al., 1994). In contrast to β^0, there are σ^0 and γ^0 which both consider an ellipsoidal Earth model when estimating A. Nevertheless, σ^0 (Equation 1.8) does not take into account the topography effects assuming a flat Earth while the opposite is true for γ^0 (Equation 1.9).

$$\sigma^0 = \beta^0 \times \sin\theta_i \tag{1.8}$$

$$\gamma^0 = \beta^0 \times \tan\theta_i \tag{1.9}$$

where θ_i is the incidence angle (Figure 1.3).

As in most radar-based remote sensing approaches focused on fire monitoring, in this PhD thesis, the backscatter coefficient has been considered since it requires fewer computational resources than interferometric coherence. From the radar backscatter conventions, the γ^0 nought was chosen due to its benefits in steep and flat areas (Small et al., 2009).
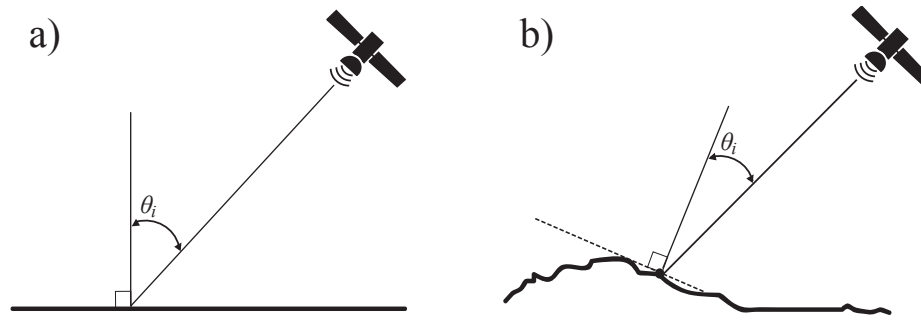
Figure 1.3: Incidence angles (θ_i) when assuming a flat Earth (a) and considering topography (b).

Fire events may result in variations of the backscatter coefficient variation as vegetation scattering elements (e.g., leaves, branches) are consumed by fire, thus reducing the scattering potential of vegetated areas (Van Zyl, 1993; Antikidis et al., 1998). Such variations may increase or decrease the backscatter coefficient values when compared to pre-fire records. SAR sensitivity to fire effects depends on several factors related to sensor characteristics, including:

- Frequency, which influences the waves-penetration capability into vegetated areas. Microwaves frequencies are grouped in bands. For SAR sensors aboard satellites the most common frequencies, from less to higher penetration potential, are X (2.5-3.75 cm; 12-8 GHz), C (3.75-7.5 cm; 8-4 GHz), S (7.5-15 cm; 4-2 GHz), and L (15-30 cm; 2-1 GHz).

- Polarisation, which determines the microwaves propagation orientation in the electromagnetic field. Co-polarised waves are transmitted and received in the same orientation, i.e., horizontal-horizontal (HH) or vertical-vertical (VV), while for cross-polarised waves, the energy return at the antenna is measured for the opposite orientation, i.e., vertical-horizontal (VH) or horizontal-vertical (HV). Cross-polarised waves are more suitable when monitoring vegetation changes as scattering from vegetation is mostly volumetric (Freeman & Durden, 1998; Yamaguchi et al., 2005; Van Zyl et al., 2011).

Other factors may affect the backscattered values, including:

- Soil moisture content, which modifies the dielectric constant and consequently the radar scattering

- Soil roughness, which may modify the waves reflection direction and consequently the backscatter coefficient. Generally, increases in soil roughness reduce specular reflection, thus increased the amount of energy returned to the sensor. In burned areas, the reduction of vegetated scattering elements increases scattering from the ground, thus enhancing then effects related to soil moisture and roughness when compared to fire-unaffected areas (Imperatore et al., 2017; Gimeno & San-Miguel-Ayanz, 2004; Ruecker & Siegert, 2000; Tanase et al., 2010a).

- Topography, which also influences the scattering process by modulating the energy returned to the sensor depending on the orientation and slope. Smaller local in-

cidence angles (LIA) tend to provide a better distinction of burned areas, particu-
larly for co-polarised waves (Gimeno & San-Miguel-Ayanz, 2004; Huang & Siegert,
2006; Tanase et al., 2010a). Moreover, over steep areas, the radar's slant-range ob-
servation geometry may generate additional effects including (a) foreshortening,
i.e., spatial compression between targets, (b) layover where the relief appears as in-
verted due to radar beams reflected from mountain peaks reaching the sensor faster
when compared to the mountain base, and (c) shadowed regions were, due to the
steep relief between, radar beams are not able to reach.

Hence, over burned areas, a vast range of backscatter behaviour may occur due to
the mentioned factors, which makes more difficult differentiating burned areas from fire-
unrelated changes when using radar datasets (Huang & Siegert, 2006). In addition, the
radar imagery is affected by the mutual interference of the coherent wavefronts, which
results in "salt and pepper" aspect (speckle) of the SAR images (Ryerson et al., 1998).
A common technique to reduce the presence of speckle is generating a multi-look image
where, through a convolution process, the values of each pixel are averaged, thus im-
proving image radiometric properties at the expense of the spatial resolution (Bruniquel
& Lopes, 1997). When using temporal-series, speckle reduction can also be achieved
through multi-temporal filtering, which allow preserving the original spatial resolution
(Quegan et al., 2000).

1.5 Remote sensing-based burned area products

Remote sensing for burned area mapping is an active research field where many new algo-
rithms and techniques are developed as a consequence of the general necessity for accurate
burned area products (see section 1.2) and as a consequence of the ever-increasing Earth
observation imagery available (Humber et al., 2018; Chuvieco et al., 2019). Since 1972,
when the first studies on burned area mapping from space sensors became available, over
4800 studies relating fire and remote sensing were released with an increasing and pro-
gressive trend being observed in the last years (Chuvieco et al., 2020). In the following
section, the most relevant satellite remote sensing for burned area mapping are reviewed.
The review is divided into three main sections according to the type of sensors used.

1.5.1 Optical

Optical imagery is from far the most common datasets used when mapping burned areas
both at global and regional scales. Globally, datasets derived from the NASA's Moder-
ate Resolution Imaging Spectrometer (MODIS) sensor onboard satellites Terra and Aqua
are the most used, in part due to their twenty years of uninterrupted service (Terra since
1999 and Aqua since 2002). Among MODIS based products, the MCD45 (Roy et al.,
2008), the MCD64 (Giglio et al., 2009, 2018) the Fire_cci v5.0 (Chuvieco et al., 2018)
and v5.1 (Lizundia-Loiola et al., 2020) are the most known. The first two products are
based on the 500 m spatial resolution bands with the latter two being based on the 250 m
bands. Despite its lower spatial resolution, the MCD64 is the global product most used
and the unique generated operatively currently (Chuvieco et al., 2020). Nevertheless, to
date, the Fire_cci v5.1 covers years 2001 to 2019, more than its previous version, the

Fire_cci v5.0 (2001 - 2017) and the MCD45 (2000 - 2017). The VEGETATION sensor onboard SPOT-4 and -5 (Satellite Pour Observation de la Terre), developed by the CNES, was also used for burned area mapping within global products such as the Global Burnt Area (GBA) 2000 (Tansey et al., 2004), the Globcarbon, which also included imagery ATSR (Plummer et al., 2006), the L3JRC (Tansey et al., 2008) and the Copernicus GIO_GL1_BA (Tansey et al., 2008). The latter product switched to PROBA V imagery in 2014 land.copernicus.eu/global/products/ba), and is the only one which is currently updated. In addition, recent efforts were made to generate long-time series (1982 to 2017) of burned area information using the advanced very high-resolution radiometer (AVHRR) sensor, despite its coarse spatial resolution of 5 km (Otón et al., 2019). As for the use of European sensors, the Globscar (Simon et al., 2004) and the Fire_cci v4.1 products were based on the European Remote Sensing Satellite - Advanced Along Track Scanning Radiometer (ERS2-ATSR2) and the Envisat MEdium Resolution Imaging Spectrometer (MERIS), respectively.

The main limiting factor of all the sensors considered on global approaches has been their coarse spatial resolution (>=250 m), which limits small size (< 100 ha) fires detection and mapping (Roteta et al., 2019; Randerson et al., 2012; Stroppiana et al., 2015). Regional products based on optical medium spatial resolution sensors are increasingly developed to cope with such limitations. For instance, in the US, the Landsat Burned Area Essential Climate Variable project mapped fire patches over four hectares from Landsat imagery from 1984 to now (Hawbaker et al., 2017) (https://www.mtbs.gov/). Similar projects focused on burned area mapping at national levels were carried out for Portugal (Oliveira et al., 2012) or Greece (Tompoulidou et al., 2016). At continental scales, burned area products from medium resolution satellite imagery are currently being developed. In this context, a new burned area product, based on Sentinel-2 imagery at 20 m pixel spacing, was recently released for Africa in the framework of the ESA's fire_cci project (FireCCISFD11) (Roteta et al., 2019).

Apart from products generated and released under operational frameworks, comprehensive research and activity are focused on developing new methods based on optical imagery of medium as well as coarse spatial resolution sensors to provide more accurate burned area maps. Such methods aim to combine datasets from different optical sensors (Roy et al., 2019), applying genetic programming (Cabral et al., 2018) and using machine learning algorithms such as random forests (Jakimow et al., 2018; Ramo & Chuvieco, 2017) and support vector machines (SVM) (Santos et al., 2019). More recently, the application of deep learning methods like convolutional neural networks (CNN) is becoming more frequent when mapping burned areas (Pinto et al., 2020, 2019; Knopp, 2019; Gargiulo et al., 2019) as a consequence of its massive implementation in others remote sensing-based applications in the recent years (Zhu et al., 2017). Despite these improvements, optical-based approaches are limited over areas frequently affected by clouds like the inter-tropical and boreal latitudes.

1.5.2 Radar

SAR images have been progressively used for mapping burned area as new sensors have become available due to their high-medium spatial resolution as well as potential to cope the main limitation of optical datasets, the null energy transmission through clouds within

the optical domain.

The SAR sensors onboard the European Remote Sensing (ERS) satellites ERS-1 and ERS-2 were used for burned areas mapping in boreal (Bourgeau-Chavez et al., 1997; Kasischke et al., 1994; Jenkins et al., 2014) and tropical ecosystems (Siegert & Hoffmann, 2000; Siegert & Ruecker, 2000; Ruecker & Siegert, 2000) with some studies also available for the Mediterranean ecosystems (Gimeno et al., 2004, 2002). The launch of RADARSAT and ALOS - PALSAR (Advanced Land Observation Satellite Phased Array type L-band Synthetic Aperture Radar) by the Canadian Space Agency and JAXA, respectively, increased the interest in burned areas mapping (Gimeno & San-Miguel-Ayanz, 2004; French et al., 1999; Polychronaki et al., 2013; Plank et al., 2019) from SAR sensors. However, these datasets had considerable shortcomings related to their low temporal resolution, co-polarised imagery, reduced incidence angles, data access restrictions, high temporal revisit times or not systematic acquisition plans.

Since 2014 with the launch of Sentinel-1 A (and B in 2015) such limitations were reduced. Sentinel-1 sensors have more precise orbital information and provide dual-polarised images (VV and VH) through more appropriate incidence angles for vegetation monitoring. In addition, the Sentinel-1 revisit period is down to three days when combining ascending and descending satellite passes from both satellites while access to data is provided free of cost. Taking advantage of such sensors, novel burned area mapping approaches have been developed at regional scales (Engelbrecht et al., 2017; Lohberger et al., 2018; Ban et al., 2020) with global the development of continental to global scale products being hindered by the different effect of fires on the backscattered energy with the ecosystem type (Huang & Siegert, 2006).

1.5.3   Optical and radar integration

Mapping burned areas from combined optical and radar datasets, although in its early stage, is rapidly emerging as a new research field in remote sensing. Few examples could be found in the literature before the launch of Sentinel-1 and Sentinel-2 sensors with older approaches being based on Landsat-5 TM and the C-band ENVISAT ASAR sensors (Stroppiana et al., 2015). Such studies were carried out over a few ecosystem types, i.e., the Mediterranean, where the radar contribution to the detection and mapping process is reduced as cloud-presence is low.

Once Sentinel-1 and Sentinel-2 datasets became available, more studies on SAR-optical data integration emerged. To date, such studies are still scarce. Moreover, their findings were inconsistent as some researchers suggest no gains from such approaches (Brown et al., 2018) while others concluded that SAR-optical integration might reduce limitations related to each sensor type (Verhegghen et al., 2016). In addition, the few studies carried out were developed and tested over reduced study areas which limit their findings and conclusions.

1.6 Hypothesis

Given (i) the high atmospheric transmission in the microwave region and the C-band SAR sensitivity to vegetation change, (ii) the suitability of the optical domain of the electromagnetic spectrum to fire monitoring, and (iii) the current context, in which the entire Earth is regularly imaged with both radar and optical sensors at medium spatial resolution and with a high frequency by the latest generation sensors onboard the ESA's satellite Sentinel-1 and Sentinel-2, this PhD thesis presents the following hypothesis:

The use of SAR data, as well as the SAR-optical integration, may improve the accuracy of mapping burned areas when compared to previous approaches based on most older SAR sensors or that of current global products based on low spatial resolution images (>250 m), especially in areas with frequent cloud cover.

1.7 Motivation and objectives

Despite efforts to provide accurate burned area maps from Earth observation datasets, the uncertainty of global burns is still high (Chuvieco et al., 2019). Medium spatial resolution optical-based datasets have already been demonstrated as an essential data-source to provide more accurate burned area maps (Roteta et al., 2019). However, atmospheric conditions limit their potential. Radar imagery may solve optical limitation, and radar-optical synergies may provide better results when compared to single sensor-based approaches. To date, few attempts have taken advantage of radar and radar-optical data integration. The current context, in which the European Copernicus programme is offering vast amounts of high-quality datasets imaged with both radar and optical remote sensing sensors (i.e., Sentinel-1 and Sentinel-2, respectively) brings an unprecedented opportunity to develop new algorithms for burned area mapping at medium spatial resolution and high temporal frequency.

These reasons have motivated this PhD thesis, whose aim was developing algorithms for burned areas mapping, applicable over all fire-prone biomes, based on radar time series as well as joint radar-optical datasets. In order to achieve this aim, the following specific objectives were pursued:

1. Algorithm theoretical framework development: analysis of C-band radar imagery strengths and limitations for burned areas mapping, including hybrid approaches based on radar and optical datasets.

2. Appraise the factors influencing mapping accuracy from radar images: environmental factors may alter the accuracy of burned area mapping products by modifying backscatter or optical reflectivity. Their effect needs to be assessed to reduce mapping uncertainties.

3. Radar and optical synergy analysis: explored the optimum combination strategy between optical and radar dataset when mapping burned. This combination can be before detection or later.

4. Validation: mapping algorithms need independent validation over a range of conditions related to ecosystem types and fire regime to analyse strengths and limitations related to the input datasets.

5. The relevance of the proposed algorithms: comparisons of the mapping accuracy with regard to existing operational products are essential to understand the significance of the work carried out.

1.8   References

Abatzoglou, J. T., Williams, A. P., Boschetti, L., Zubkova, M., & Kolden, C. A. (2018). Global patterns of interannual climate–fire relationships. *Global change biology*, *24*, 5164–5175.

Andela, N., Morton, D., Giglio, L., Chen, Y., Van Der Werf, G., Kasibhatla, P., De-Fries, R., Collatz, G., Hantson, S., Kloster, S. et al. (2017). A human-driven decline in global burned area. *Science*, *356*, 1356–1362.

Andreae, M. O., & Merlet, P. (2001). Emission of trace gases and aerosols from biomass burning. *Global Biogeochemical Cycles*, *15*, 955–966.

Antikidis, E., Arino, O., Arnaud, A., & Laur, H. (1998). ERS SAR Coherence & ATSR Hot Spots: a Synergy for Mapping Deforested Areas. The Special Case of the 1997 Fire Event in Indonesia. *European Space Agency-Publications-ESA SP*, *441*, 355–360.

Aponte, C., de Groot, W. J., & Wotton, B. M. (2016). Forest fires and climate change: causes, consequences and management options. *International Journal of Wildland Fire*, *25*, i–ii.

Arora, V. K., & Melton, J. R. (2018). Reduction in global area burned and wildfire emissions since 1930s enhances carbon uptake by land. *Nature communications*, *9*, 1–10.

Ban, Y., Zhang, P., Nascetti, A., Bevington, A. R., & Wulder, M. A. (2020). Near Real-Time Wildfire Progression Monitoring with Sentinel-1 SAR Time Series and Deep Learning. *Scientific Reports*, *10*, 1–15.

Barducci, A., Guzzi, D., Marcoionni, P., & Pippi, I. (2002). Infrared detection of active fires and burnt areas: theory and observations. *Infrared physics & technology*, *43*, 119–125.

Boer, M. M., de Dios, V. R., & Bradstock, R. A. (2020). Unprecedented burn area of Australian mega forest fires. *Nature Climate Change*, *10*, 171–172.

Bojinski, S., Verstraete, M., Peterson, T. C., Richter, C., Simmons, A., & Zemp, M. (2014). The concept of essential climate variables in support of climate research, applications, and policy. *Bulletin of the American Meteorological Society*, *95*, 1431–1443.

Bond, W. J., Woodward, F. I., & Midgley, G. F. (2005). The global distribution of ecosystems in a world without fire. *New Phytologist*, *165*, 525–538.

Bourgeau-Chavez, L., Harrell, P., Kasischke, E., & French, N. (1997). The detection and mapping of Alaskan wildfires using a spaceborne imaging radar system. *International Journal of Remote Sensing*, *18*, 355–373.

Bourgeau-Chavez, L., Kasischke, E., Brunzell, S., Mudd, J., & Tukman, M. (2002). Mapping fire scars in global boreal forests using imaging radar data. *International Journal of Remote Sensing*, *23*, 4211–4234.

Bowman, D. M., Balch, J. K., Artaxo, P., Bond, W. J., Carlson, J. M., Cochrane, M. A., D'Antonio, C. M., DeFries, R. S., Doyle, J. C., Harrison, S. P. et al. (2009). Fire in the Earth system. *Science*, *324*, 481–484.

Bowman, D. M., Williamson, G. J., Abatzoglou, J. T., Kolden, C. A., Cochrane, M. A., & Smith, A. M. (2017). Human exposure and sensitivity to globally extreme wildfire events. *Nature Ecology & Evolution*, *1*, 1–6.

Brown, A. R., Petropoulos, G. P., & Ferentinos, K. P. (2018). Appraisal of the Sentinel-1 & 2 use in a large-scale wildfire assessment: A case study from Portugal's fires of 2017. *Applied geography*, *100*, 78–89.

Bruniquel, J., & Lopes, A. (1997). Multi-variate optimal speckle reduction in SAR imagery. *International journal of remote sensing*, *18*, 603–627.

Cabral, A. I., Silva, S., Silva, P. C., Vanneschi, L., & Vasconcelos, M. J. (2018). Burned area estimations derived from Landsat ETM+ and OLI data: comparing genetic programming with maximum likelihood and classification and regression trees. *ISPRS Journal of Photogrammetry and Remote Sensing*, *142*, 94–105.

Chang, Y., He, H. S., Hu, Y., Bu, R., & Li, X. (2008). Historic and current fire regimes in the Great Xing'an Mountains, northeastern China: Implications for long-term forest management. *Forest Ecology and Management*, *254*, 445–453.

Chuvieco, E. (2020). *Fundamentals of satellite remote sensing: An environmental approach*. CRC press.

Chuvieco, E., Aguado, I., Salas, J., García, M., Yebra, M., & Oliva, P. (2020). Satellite Remote Sensing Contributions to Wildland Fire Science and Management, .

Chuvieco, E., Aguado, I., Yebra, M., Nieto, H., Salas, J., Martín, M. P., Vilar, L., Martínez, J., Martín, S., Ibarra, P. et al. (2010). Development of a framework for fire risk assessment using remote sensing and geographic information system technologies. *Ecological Modelling*, *221*, 46–58.

Chuvieco, E., Lizundia-Loiola, J., Pettinari, M. L., Ramo, R., Padilla, M., Mouillot, F., Laurent, P., Storm, T., Heil, A., & Plummer, S. (2018). Generation and analysis of a new global burned area product based on MODIS 250m reflectance bands and thermal anomalies. *Earth Syst. Sci. Data Discuss*, *512*, 1–24.

Chuvieco, E., Mouillot, F., van der Werf, G. R., San Miguel, J., Tanasse, M., Koutsias, N., García, M., Yebra, M., Padilla, M., Gitas, I. et al. (2019). Historical background and current developments for mapping burned area from satellite Earth observation. *Remote Sensing of Environment*, *225*, 45–64.

Chuvieco, E., Yue, C., Heil, A., Mouillot, F., Alonso-Canas, I., Padilla, M., Pereira, J. M., Oom, D., & Tansey, K. (2016). A new global burned area product for climate assessment of fire impacts. *Global Ecology and Biogeography*, *25*, 619–629.

Colliander, A., Jackson, T. J., Bindlish, R., Chan, S., Das, N., Kim, S., Cosh, M., Dunbar, R., Dang, L., Pashaian, L. et al. (2017). Validation of SMAP surface soil moisture products with core validation sites. *Remote Sensing of Environment*, *191*, 215–231.

DeBano, L. F., Neary, D. G., & Ffolliott, P. F. (1998). *Fire effects on ecosystems*. John Wiley & Sons.

Diaz, J. M. (2012). Economic impacts of wildfire. *Southern Fire Exchange*, *498*, 2012–7.

Emery, W., & Camps, A. (2017). *Introduction to satellite remote sensing: atmosphere, ocean, land and cryosphere applications*. Elsevier.

Engelbrecht, J., Theron, A., Vhengani, L., & Kemp, J. (2017). A simple normalized difference approach to burnt area mapping using multi-polarisation C-Band SAR. *Remote Sensing*, *9*, 764.

Evangeliou, N., Kylling, A., Eckhardt, S., Myroniuk, V., Stebel, K., Paugam, R., Zibtsev, S., & Stohl, A. (2019). Open fires in Greenland in summer 2017: transport, deposition and radiative effects of BC, OC and BrC emissions, .

Filippi, J.-B., Mallet, V., & Nader, B. (2014). Representation and evaluation of wildfire propagation simulations. *International Journal of Wildland Fire*, *23*, 46–57.

Flannigan, M. D., Amiro, B. D., Logan, K. A., Stocks, B., & Wotton, B. (2006). Forest fires and climate change in the 21 st century. *Mitigation and Adaptation Strategies for Global Change*, *11*, 847–859.

Flannigan, M. D., Stocks, B. J., & Wotton, B. M. (2000). Climate change and forest fires. *Science of the total environment*, *262*, 221–229.

Freeman, A., & Durden, S. L. (1998). A three-component scattering model for polarimetric SAR data. *IEEE Transactions on Geoscience and Remote Sensing*, *36*, 963–973.

French, N. H., Bourgeau-Chavez, L. L., Wang, Y., & Kasischke, E. S. (1999). Initial observations of Radarsat imagery at fire-disturbed sites in interior Alaska. *Remote Sensing of Environment*, *68*, 89–94.

Gao, B.-C. (1996). NDWI—A normalized difference water index for remote sensing of vegetation liquid water from space. *Remote sensing of environment*, *58*, 257–266.

García, M. L., & Caselles, V. (1991). Mapping burns and natural reforestation using Thematic Mapper data. *Geocarto International*, *6*, 31–37.

Gargiulo, M., Dell'Aglio, D. A. G., Iodice, A., Riccio, D., & Ruello, G. (2019). A CNN-Based Super-Resolution Technique for Active Fire Detection on Sentinel-2 Data. *arXiv preprint arXiv:1906.10413*, .

Giglio, L., Boschetti, L., Roy, D. P., Humber, M. L., & Justice, C. O. (2018). The Collection 6 MODIS burned area mapping algorithm and product. *Remote sensing of environment*, *217*, 72–85.

Giglio, L., Descloitres, J., Justice, C. O., & Kaufman, Y. J. (2003). An enhanced contextual fire detection algorithm for MODIS. *Remote Sensing of Environment*, *87*, 273–282.

Giglio, L., Loboda, T., Roy, D. P., Quayle, B., & Justice, C. O. (2009). An active-fire based burned area mapping algorithm for the MODIS sensor. *Remote Sensing of Environment*, *113*, 408–420.

Gimeno, M., San-Miguel, J., Barbosa, P., & Schmuck, G. (2002). Using ERS-SAR images for burnt area mapping in Mediterranean landscapes. *Forest Fire Research & Wildland Fire Safety. (Viegas T ed). Millpress, Rotterdam*, *90*.

Gimeno, M., & San-Miguel-Ayanz, J. (2004). Evaluation of RADARSAT-1 data for identification of burnt areas in Southern Europe. *Remote Sensing of Environment*, *92*, 370–375.

Gimeno, M., San-Miguel-Ayanz, J., & Schmuck, G. (2004). Identification of burnt areas in Mediterranean forest environments from ERS-2 SAR time series. *International Journal of Remote Sensing*, *25*, 4873–4888.

Gitas, I., & Devereux, B. (2006). The role of topographic correction in mapping recently burned Mediterranean forest areas from LANDSAT TM images. *International Journal of Remote Sensing*, *27*, 41–54.

Goubitz, S., Werger, M., & Ne'eman, G. (2002). Germination response to fire-related factors of seeds from non-serotinous and serotinous cones. *Plant Ecology*, *169*, 195–204.

Hansen, M. C., Potapov, P. V., Moore, R., Hancher, M., Turubanova, S., Tyukavina, A., Thau, D., Stehman, S., Goetz, S., Loveland, T. et al. (2013). High-resolution global maps of 21st-century forest cover change. *Science*, *342*, 850–853.

Harden, J., Neff, J., Sandberg, D., Turetsky, M. v., Ottmar, R., Gleixner, G., Fries, T., & Manies, K. (2004). Chemistry of burning the forest floor during the FROSTFIRE experimental burn, interior Alaska, 1999. *Global Biogeochemical Cycles*, *18*.

Hawbaker, T. J., Radeloff, V. C., Syphard, A. D., Zhu, Z., & Stewart, S. I. (2008). Detection rates of the MODIS active fire product in the United States. *Remote Sensing of Environment*, *112*, 2656–2664.

Hawbaker, T. J., Vanderhoof, M. K., Beal, Y.-J., Takacs, J. D., Schmidt, G. L., Falgout, J. T., Williams, B., Fairaux, N. M., Caldwell, M. K., Picotte, J. J. et al. (2017). Mapping burned areas using dense time-series of Landsat data. *Remote Sensing of Environment*, *198*, 504–522.

Hoffmann, W. A., Schroeder, W., & Jackson, R. B. (2002). Positive feedbacks of fire, climate, and vegetation and the conversion of tropical savanna. *Geophysical Research Letters*, *29*, 9–1.

Hollmann, R., Merchant, C. J., Saunders, R., Downy, C., Buchwitz, M., Cazenave, A., Chuvieco, E., Defourny, P., de Leeuw, G., Forsberg, R. et al. (2013). The ESA climate change initiative: Satellite data records for essential climate variables. *Bulletin of the American Meteorological Society*, *94*, 1541–1552.

Huang, S., & Siegert, F. (2006). Backscatter change on fire scars in Siberian boreal forests in ENVISAT ASAR wide-swath images. *IEEE Geoscience and Remote Sensing Letters*, *3*, 154–158.

Humber, M. L., Boschetti, L., Giglio, L., & Justice, C. O. (2018). Spatial and temporal intercomparison of four global burned area products. *International Journal of Digital Earth*, (pp. 1–25).

Imperatore, P., Azar, R., Calo, F., Stroppiana, D., Brivio, P. A., Lanari, R., & Pepe, A. (2017). Effect of the Vegetation Fire on Backscattering: An Investigation Based on Sentinel-1 Observations. *IEEE Journal of Selected Topics in Applied Earth Observations and Remote Sensing*, *10*, 4478–4492.

Jakimow, B., Griffiths, P., van der Linden, S., & Hostert, P. (2018). Mapping pasture management in the Brazilian Amazon from dense Landsat time series. *Remote sensing of environment*, *205*, 453–468.

Jenkins, L. K., Bourgeau-Chavez, L. L., French, N. H., Loboda, T. V., & Thelen, B. J. (2014). Development of methods for detection and monitoring of fire disturbance in the Alaskan tundra using a two-decade long record of synthetic aperture radar satellite images. *Remote Sensing*, *6*, 6347–6364.

Jin, Y., & Roy, D. P. (2005). Fire-induced albedo change and its radiative forcing at the surface in northern Australia. *Geophysical Research Letters*, *32*.

Kasischke, E. S., Bourgeau-Chavez, L. L., & French, N. H. (1994). Observations of variations in ERS-1 SAR image intensity associated with forest fires in Alaska. *IEEE Transactions on Geoscience and Remote Sensing*, *32*, 206–210.

Knopp, L. (2019). *Development of a burned area processor based on Sentinel-2 data using deep learning*. Ph.D. thesis Technische Universität München.

Kochi, I., Champ, P. A., Loomis, J. B., & Donovan, G. H. (2016). Valuing morbidity effects of wildfire smoke exposure from the 2007 Southern California wildfires. *Journal of Forest Economics*, *25*, 29–54.

Krawchuk, M. A., Moritz, M. A., Parisien, M.-A., Van Dorn, J., & Hayhoe, K. (2009). Global pyrogeography: the current and future distribution of wildfire. *PloS one*, *4*, e5102.

Langenfelds, R., Francey, R., Pak, B., Steele, L., Lloyd, J., Trudinger, C., & Allison, C. (2002). Interannual growth rate variations of atmospheric CO2 and its δ13C, H2, CH4, and CO between 1992 and 1999 linked to biomass burning. *Global Biogeochemical Cycles*, *16*, 21–1.

Laurent, P., Mouillot, F., Yue, C., Ciais, P., Moreno, M. V., & Nogueira, J. M. (2018). FRY, a global database of fire patch functional traits derived from space-borne burned area products. *Scientific data*, *5*, 180132.

Lavorel, S., Flannigan, M. D., Lambin, E. F., & Scholes, M. C. (2007). Vulnerability of land systems to fire: Interactions among humans, climate, the atmosphere, and ecosystems. *Mitigation and Adaptation Strategies for Global Change*, *12*, 33–53.

Libonati, R., DaCamara, C. C., Pereira, J. M. C., & Peres, L. F. (2010). Retrieving middle-infrared reflectance for burned area mapping in tropical environments using MODIS. *Remote Sensing of Environment*, *114*, 831–843.

Libonati, R., DaCamara, C. C., Setzer, A. W., Morelli, F., & Melchiori, A. E. (2015). An algorithm for burned area detection in the Brazilian Cerrado using 4 μm MODIS imagery. *Remote Sensing*, *7*, 15782–15803.

Liew, S., Kwoh, L., Padmanabhan, K., Lim, O., & Lim, H. (1999). Delineating land/forest fire burnt scars with ERS interferometric synthetic aperture radar. *Geophysical Research Letters*, *26*, 2409–2412.

Liu, Z., Ballantyne, A. P., & Cooper, L. A. (2019). Biophysical feedback of global forest fires on surface temperature. *Nature communications*, *10*, 1–9.

Lizundia-Loiola, J., Otón, G., Ramo, R., & Chuvieco, E. (2020). A spatio-temporal active-fire clustering approach for global burned area mapping at 250 m from MODIS data. *Remote Sensing of Environment*, *236*, 111493.

Lohberger, S., Stängel, M., Atwood, E. C., & Siegert, F. (2018). Spatial evaluation of Indonesia's 2015 fire-affected area and estimated carbon emissions using Sentinel-1. *Global change biology*, *24*, 644–654.

Lotan, J. E. (1976). Cone serotiny-fire relationships in lodgepole pine. *The Bark Beetles, Fuels, and Fire Bibliography*, (p. 8).

Marlon, J. R., Bartlein, P. J., Daniau, A.-L., Harrison, S. P., Maezumi, S. Y., Power, M. J., Tinner, W., & Vanniére, B. (2013). Global biomass burning: a synthesis and review of Holocene paleofire records and their controls. *Quaternary Science Reviews*, *65*, 5–25.

Mouillot, F., Schultz, M. G., Yue, C., Cadule, P., Tansey, K., Ciais, P., & Chuvieco, E. (2014). Ten years of global burned area products from spaceborne remote sensing—A review: Analysis of user needs and recommendations for future developments. *International Journal of Applied Earth Observation and Geoinformation*, *26*, 64–79.

Oliveira, S. L., Pereira, J. M., & Carreiras, J. M. (2012). Fire frequency analysis in Portugal (1975–2005), using Landsat-based burnt area maps. *International Journal of Wildland Fire*, *21*, 48–60.

Otón, G., Ramo, R., Lizundia-Loiola, J., & Chuvieco, E. (2019). Global Detection of Long-Term (1982–2017) Burned Area with AVHRR-LTDR Data. *Remote Sensing*, *11*, 2079.

Pausas, J. G., & Paula, S. (2012). Fuel shapes the fire–climate relationship: evidence from Mediterranean ecosystems. *Global Ecology and Biogeography*, *21*, 1074–1082.

Pereira, J., Chuvieco, E., Beaudoin, A., & Desbois, N. (1997). Remote sensing of burned areas: a review. *A review of remote sensing methods for the study of large wildland fires*, (pp. 127–184).

Pereira, J. M. (1999). A comparative evaluation of NOAA/AVHRR vegetation indexes for burned surface detection and mapping. *IEEE transactions on geoscience and remote sensing*, *37*, 217–226.

Pinto, M. M., Hurduc, A., DaCamara, C. C., Trigo, I. F., & Trigo, R. M. (2019). Burned Areas Segmentation with Convolutional Neural Networks. In *Geophysical Research Abstracts*. volume 21.

Pinto, M. M., Libonati, R., Trigo, R. M., Trigo, I. F., & DaCamara, C. C. (2020). A deep learning approach for mapping and dating burned areas using temporal sequences of satellite images. *ISPRS Journal of Photogrammetry and Remote Sensing*, *160*, 260–274.

Plank, S., Karg, S., & Martinis, S. (2019). Full-polarimetric burn scar mapping–the differences of active fire and post-fire situations. *International journal of remote sensing*, *40*, 253–268.

Plummer, S., Arino, O., Simon, M., & Steffen, W. (2006). Establishing a earth observation product service for the terrestrial carbon community: The GLOBCARBON initiative. *Mitigation and Adaptation Strategies for Global Change*, *11*, 97–111.

Polychronaki, A., Gitas, I. Z., Veraverbeke, S., & Debien, A. (2013). Evaluation of ALOS PALSAR imagery for burned area mapping in Greece using object-based classification. *Remote Sensing*, *5*, 5680–5701.

Poulter, B., Cadule, P., Cheiney, A., Ciais, P., Hodson, E., Peylin, P., Plummer, S., Spessa, A., Saatchi, S., Yue, C. et al. (2015). Sensitivity of global terrestrial carbon cycle dynamics to variability in satellite-observed burned area. *Global Biogeochemical Cycles*, *29*, 207–222.

Pyne, S. J. (1982). A cultural history of wildland and rural fire.

Quegan, S., Le Toan, T., Yu, J. J., Ribbes, F., & Floury, N. (2000). Multitemporal ERS SAR analysis applied to forest mapping. *IEEE Transactions on Geoscience and Remote Sensing*, *38*, 741–753.

Ramo, R., & Chuvieco, E. (2017). Developing a Random Forest Algorithm for MODIS Global Burned Area Classification. *Remote Sensing*, *9*, 1193.

Randerson, J., Chen, Y., Werf, G., Rogers, B., & Morton, D. (2012). Global burned area and biomass burning emissions from small fires. *Journal of Geophysical Research: Biogeosciences*, *117*.

Raney, R., Freeman, T., Hawkins, R., & Bamler, R. (1994). A plea for radar brightness. In *Proceedings of IGARSS'94-1994 IEEE International Geoscience and Remote Sensing Symposium* (pp. 1090–1092). IEEE volume 2.

Reid, C. E., Brauer, M., Johnston, F. H., Jerrett, M., Balmes, J. R., & Elliott, C. T. (2016). Critical review of health impacts of wildfire smoke exposure. *Environmental health perspectives*, *124*, 1334–1343.

Roteta, E., Bastarrika, A., Padilla, M., Storm, T., & Chuvieco, E. (2019). Development of a Sentinel-2 burned area algorithm: Generation of a small fire database for sub-Saharan Africa. *Remote Sensing of Environment*, *222*, 1–17.

Roy, D. P., Boschetti, L., Justice, C. O., & Ju, J. (2008). The collection 5 MODIS burned area product—Global evaluation by comparison with the MODIS active fire product. *Remote Sensing of Environment*, *112*, 3690–3707.

Roy, D. P., Huang, H., Boschetti, L., Giglio, L., Yan, L., Zhang, H. H., & Li, Z. (2019). Landsat-8 and Sentinel-2 burned area mapping-A combined sensor multi-temporal change detection approach. *Remote Sensing of Environment*, *231*, 111254.

Ruecker, G., & Siegert, F. (2000). Burn scar mapping and fire damage assessment using ERS-2 SAR images in East Kalimantan, Indonesia. *International Archives of Photogrammetry and Remote Sensing*, *33*, 1286–1293.

Ryerson, R. A., Henderson, F. M., & Lewis, A. J. (1998). *Manual of Remote Sensing, Principles and Applications of Imaging Radar* volume 2. Wiley.

Said, Y. A., Petropoulos, G. P., & Srivastava, P. K. (2015). Assessing the influence of atmospheric and topographic correction and inclusion of SWIR bands in burned scars detection from high-resolution EO imagery: a case study using ASTER. *Natural Hazards*, *78*, 1609–1628.

Saleh, K., Wigneron, J., Calvet, J., Lopez-Baeza, E., Ferrazzoli, P., Berger, M., Wursteisen, P., Simmonds, L., & Miller, J. (2004). The EuroSTARRS airborne campaign in support of the SMOS mission: First results over land surfaces. *International Journal of Remote Sensing*, *25*, 177–194.

Santos, F., Rodrigues, J., Libonati, R., Peres, L., Pereira, A., & Setzer, A. (2019). Burned area mapping in Brazil using NPP-VIIRS imagery and One Class Support Vector Machine. In *Geophysical Research Abstracts*. volume 21.

Schroeder, W., Oliva, P., Giglio, L., & Csiszar, I. A. (2014). The New VIIRS 375 m active fire detection data product: Algorithm description and initial assessment. *Remote Sensing of Environment*, *143*, 85–96.

Scott, A. C., & Glasspool, I. J. (2006). The diversification of Paleozoic fire systems and fluctuations in atmospheric oxygen concentration. *Proceedings of the National Academy of Sciences*, *103*, 10861–10865.

Seiler, W., & Crutzen, P. J. (1980). Estimates of gross and net fluxes of carbon between the biosphere and the atmosphere from biomass burning. *Climatic change*, *2*, 207–247.

Siegert, F., & Hoffmann, A. A. (2000). The 1998 forest fires in East Kalimantan (Indonesia): A quantitative evaluation using high resolution, multitemporal ERS-2 SAR images and NOAA-AVHRR hotspot data. *Remote Sensing of Environment*, *72*, 64–77.

Siegert, F., & Ruecker, G. (2000). Use of multitemporal ERS-2 SAR images for identification of burned scars in south-east Asian tropical rainforest. *International Journal of Remote Sensing*, *21*, 831–837.

Simon, M., Plummer, S., Fierens, F., Hoelzemann, J. J., & Arino, O. (2004). Burnt area detection at global scale using ATSR-2: The GLOBSCAR products and their qualification. *Journal of Geophysical Research: Atmospheres*, *109*.

Sitch, S., Smith, B., Prentice, I. C., Arneth, A., Bondeau, A., Cramer, W., Kaplan, J. O., Levis, S., Lucht, W., Sykes, M. T. et al. (2003). Evaluation of ecosystem dynamics, plant geography and terrestrial carbon cycling in the LPJ dynamic global vegetation model. *Global change biology*, *9*, 161–185.

Small, D. (2011). Flattening gamma: Radiometric terrain correction for SAR imagery. *IEEE Transactions on Geoscience and Remote Sensing*, *49*, 3081–3093.

Small, D., Miranda, N., & Meier, E. (2009). A revised radiometric normalisation standard for SAR. In *2009 IEEE International Geoscience and Remote Sensing Symposium* (pp. IV–566). IEEE volume 4.

Stephens, S. L., Burrows, N., Buyantuyev, A., Gray, R. W., Keane, R. E., Kubian, R., Liu, S., Seijo, F., Shu, L., Tolhurst, K. G. et al. (2014). Temperate and boreal forest mega-fires: characteristics and challenges. *Frontiers in Ecology and the Environment*, *12*, 115–122.

Stroppiana, D., Azar, R., Calò, F., Pepe, A., Imperatore, P., Boschetti, M., Silva, J., Brivio, P. A., & Lanari, R. (2015). Integration of optical and SAR data for burned area mapping in Mediterranean Regions. *Remote Sensing*, *7*, 1320–1345.

Stroppiana, D., Grégoire, J.-M., & Pereira, J. M. (2003). The use of SPOT VEGETA-TION data in a classification tree approach for burnt area mapping in Australian savanna. *International journal of remote sensing*, *24*, 2131–2151.

Tanase, M. A., Santoro, M., de La Riva, J., Fernando, P., Le Toan, T. et al. (2010a). Sensitivity of X-, C-, and L-band SAR backscatter to burn severity in Mediterranean pine forests. *IEEE Transactions on Geoscience and Remote Sensing*, *48*, 3663–3675.

Tanase, M. A., Santoro, M., Wegmüller, U., de la Riva, J., & Pérez-Cabello, F. (2010b). Properties of X-, C-and L-band repeat-pass interferometric SAR coherence in Mediter-ranean pine forests affected by fires. *Remote Sensing of Environment*, *114*, 2182–2194.

Tansey, K., Grégoire, J.-M., Defourny, P., Leigh, R., Pekel, J.-F., van Bogaert, E., & Bartholomé, E. (2008). A new, global, multi-annual (2000–2007) burnt area product at 1 km resolution. *Geophysical Research Letters*, *35*.

Tansey, K., Grégoire, J.-M., Stroppiana, D., Sousa, A., Silva, J., Pereira, J., Boschetti, L., Maggi, M., Brivio, P. A., Fraser, R. et al. (2004). Vegetation burning in the year 2000: Global burned area estimates from SPOT VEGETATION data. *Journal of Geophysical Research: Atmospheres*, *109*.

Tedim, F., Leone, V., Coughlan, M., Bouillon, C., Xanthopoulos, G., Royé, D., Cor-reia, F. J., & Ferreira, C. (2020). Extreme wildfire events: The definition. In *Extreme Wildfire Events and Disasters* (pp. 3–29). Elsevier.

Tompoulidou, M., Stefanidou, A., Grigoriadis, D., Dragozi, E., Stavrakoudis, D., & Gitas, I. Z. (2016). The Greek National Observatory of Forest Fires (NOFFi). In *Fourth International Conference on Remote Sensing and Geoinformation of the Environment (RSCy2016)* (p. 96880N). International Society for Optics and Photonics volume 9688.

Valor, E., & Caselles, V. (1996). Mapping land surface emissivity from NDVI: Application to European, African, and South American areas. *Remote sensing of Environment*, *57*, 167–184.

Van Der Werf, G. R., Randerson, J. T., Giglio, L., Van Leeuwen, T. T., Chen, Y., Rogers, B. M., Mu, M., Van Marle, M. J., Morton, D. C., Collatz, G. J. et al. (2017). Global fire emissions estimates during 1997-2016. *Earth System Science Data*, *9*, 697–720.

Van Zyl, J. J. (1993). The effect of topography on radar scattering from vegetated areas. *IEEE Transactions on Geoscience and Remote Sensing*, *31*, 153–160.

Van Zyl, J. J., Arii, M., & Kim, Y. (2011). Model-based decomposition of polarimetric SAR covariance matrices constrained for nonnegative eigenvalues. *IEEE Transactions on Geoscience and Remote Sensing*, *49*, 3452–3459.

Verhegghen, A., Eva, H., Ceccherini, G., Achard, F., Gond, V., Gourlet-Fleury, S., & Cerutti, P. O. (2016). The potential of Sentinel satellites for burnt area mapping and monitoring in the Congo Basin forests. *Remote Sensing*, *8*, 986.

Vilar, L., Camia, A., San-Miguel-Ayanz, J., & Martín, M. P. (2016). Modeling temporal changes in human-caused wildfires in Mediterranean Europe based on land use-land cover interfaces. *Forest Ecology and Management*, *378*, 68–78.

Ward, D., Kloster, S., Mahowald, N., Rogers, B., Randerson, J., & Hess, P. (2012). The changing radiative forcing of fires: global model estimates for past, present and future. *Atmospheric Chemistry and Physics*, *12*, 10857–10886.

Van der Werf, G. R., Randerson, J. T., Giglio, L., Collatz, G., Mu, M., Kasibhatla, P. S., Morton, D. C., DeFries, R., Jin, Y. v., & van Leeuwen, T. T. (2010). Global fire emissions and the contribution of deforestation, savanna, forest, agricultural, and peat fires (1997–2009). *Atmospheric Chemistry and Physics*, *10*, 11707–11735.

Westerling, A. L., Hidalgo, H. G., Cayan, D. R., & Swetnam, T. W. (2006). Warming and earlier spring increase western US forest wildfire activity. *science*, *313*, 940–943.

Yamaguchi, Y., Moriyama, T., Ishido, M., & Yamada, H. (2005). Four-component scattering model for polarimetric SAR image decomposition. *IEEE Transactions on Geoscience and Remote Sensing*, *43*, 1699–1706.

Zhu, X. X., Tuia, D., Mou, L., Xia, G.-S., Zhang, L., Xu, F., & Fraundorfer, F. (2017). Deep learning in remote sensing: A comprehensive review and list of resources. *IEEE Geoscience and Remote Sensing Magazine*, *5*, 8–36.

Chapter 2

Burned area detection using backscatter coefficient

This chapter describes a proposed burned area mapping algorithm based on change detection of Sentinel-1 C-band backscatter coefficient. The algorithm applies the Reed-Xiaoli detector (RXD) to distinguish anomalous changes of the backscatter coefficient. Such changes are linked to fire events derived from thermal anomalies (hotspots) available as ancillary data from the Moderate Resolution Imaging Spectroradiometer (MODIS) and the Visible Infrared Imaging Radiometer Suite (VIIRS) sensors. The algorithm automatically adapts to the local radar scattering conditions, and it is robust to variations of the input datasets. Land cover maps are used to account for changing backscatter behaviour as the RXD-based algorithm is land cover class dependent. A machine learning classifier (random forests) is used to detect burned areas where hotspot data are not available.

Burned area perimeters derived from optical images (Landsat-8 and Sentinel-2) are used to validate the algorithm with the validation dataset covering over 21 million hectares distributed between 18 locations representing the main biomes affected by fires, from boreal forests to tropical and sub-tropical forests and savannas.

Algorithm validation results suggest improved mapping accuracy when compared to the MODIS based MCD64A1 Version 6 global products with a mean Dice coefficient (DC) of 0.59±0.06 (± confidence interval, 95%), mean omission (OE) of 0.43±0.08 and mean commission errors (CE) of 0.37±0.06. The improvements over the MCD64A1 product are promising as the DC increased on average by 0.13 by reducing the OE and CE by 0.12 and 0.06, respectively.

2.1   Introduction

Fire is one of the natural agents that most alter terrestrial ecosystems and has a key eco-
logical role in large part of the Earth's surface. Fires may have local to global effects as
they reduce soil fertility, change water supply, increase biodiversity loss and negatively
influence carbon sequestration (Hoffmann et al., 2002; Van der Werf et al., 2010; Hansen
et al., 2013; Bond et al., 2005; Aponte et al., 2016; Pausas & Paula, 2012; Lavorel et al.,
2007). Fires may also alter global biochemical cycles by modifying the emitted green-
house gases (GHGs) and aerosols presence in the atmosphere (Van Der Werf et al., 2017;
Andreae & Merlet, 2001; Bowman et al., 2009). Annual global estimates of carbon emis-
sions from forest fires are quite variable. Van der Werf et al. (2010) place them between
1.6 and 2.8 PgC per year, which is equivalent to 20 to 30% of the global carbon emissions
generated by burning fossil fuels (Kloster et al., 2012; Flannigan et al., 2009). However,
other authors estimate fire-related emissions at 2 to 4 PgC per year, the equivalent of up
to 50% of fossil fuel emissions (Bowman et al., 2009). Regardless of the actual value,
changes in global burned area (BA) remains an important source of interannual variability
of atmospheric carbon concentration. Direct relationships between global warming and
the frequency of fires at the global level imply a positive feedback process with sufficient
potential to be a key factor in climate change (Flannigan et al., 2009; Hoffmann et al.,
2002; Knorr et al., 2016). Although the current understanding of all these interactions is
limited (Krawchuk et al., 2009), increased carbon concentration in the atmosphere may
reinforce the effect of climate on fire frequency and intensity (Langenfelds et al., 2002;
Flannigan et al., 2006). Such increases are spatially variable. Furthermore, some areas
may not experience changes with respect to current fire regimes, while others may even
experience reduced fire occurrence (Flannigan et al., 2009; Kloster et al., 2012; Andela
et al., 2017).

Given the relationship between the fire regime and climate, the Global Climate Ob-
serving System (GCOS) considers fire as an Essential Climatic Variable (ECV). An ECV
is a physical, chemical, biological or a group of linked variables that contributes in a crit-
ical way to the characterisation of the climate system, being key to study and predict its
evolution (Bojinski et al., 2014). The origin of ECVs dates back to the 1990s, when gaps
in climate knowledge and the reduction of observation networks in many countries led
GCOS to develop the ECV concept to simplify the study of climate through systematic
observations of a limited set of variables with great climatic importance using satellite
remote sensing data (Hollmann et al., 2013; Bradley et al., 2012). In 2010, the European
Space Agency (ESA) started the Climate Change Initiative (CCI) programme as the main
contribution of the Agency to the GCOS agenda. The CCI programme aims to obtain
information on different ECVs using remote sensing data to help improving climate mod-
elling (Plummer et al., 2017; Hollmann et al., 2013). Fire Disturbance is one of the ECV
included in the first phase of the CCI programme initiated in 2010. The goals of this project
were to produce long-term and consistent time series of global BA information (Chuvieco
et al., 2016). The interest of global BA products for climate modelling has been reviewed
by several authors (Mouillot et al., 2014; Poulter et al., 2015). Moreover, many global
BA products have been released over the last years (Humber et al., 2018). Three such
products were based on data from the NASA's Moderate Resolution Imaging Spectrom-
eter (MODIS) sensor, the MCD45 (Roy et al., 2008), the MCD64 (Giglio et al., 2009,
2018) and the MODIS Fire_CCI v5.0 (Chuvieco et al., 2018). Images acquired by the

VEGETATION sensor onboard the SPOT-4 (Satellite Pour Observation de la Terre) satellite have also been used to generate global BA products, namely the Global Burnt Area (GBA) 2000 (Tansey et al., 2004), Globcarbon (Plummer et al., 2006), L3JRC (Tansey et al., 2008) and the Copernicus Global Land Service Burnt Area (based on Proba-V since 2014: land.copernicus.eu/global/products/ba). Furthermore, the European Remote Sensing Satellite - Advanced Along Track Scanning Radiometer (ERS2-ATSR2) was used to generate the Globscar product (Simon et al., 2004) while the MEdium Resolution Imaging Spectrometer (MERIS) data were used to generate the Fire_CCI v4.1 product (Alonso-Canas & Chuvieco, 2015; Chuvieco et al., 2016). All these products were obtained using passive remote sensing datasets (optical and thermal wavelengths) which have significant limitations in areas with persistent cloud cover. Another limitation comes from the relatively coarse (>250 m) spatial resolutions of these sensors, which makes the detection of small fires difficult (Stroppiana et al., 2015a; Randerson et al., 2012).

Several factors limit burned area mapping from remote sensing data. These factors are related to both the sensor characteristics and the observed scene. The type of sensor (passive or active) and the region of the electromagnetic spectrum in which the images are acquired are decisive in the success of the burned area detection. Among the scene characteristics influencing detection accuracy, the size and shape of fire patches, land cover type, fire unrelated changes (e.g., phenology, floods, harvest, insects) and the presence of clouds (optical and thermal part of the spectrum) are the most relevant. Since sensor and scene related factors interact, the degree to which each of the mentioned factors affects BA detection success varies (Eva & Lambin, 1998; Boschetti et al., 2004; Belenguer-Plomer et al., 2018a; Padilla et al., 2015). The spatial and temporal resolution of the sensor has a significant impact on BA mapping accuracy, determining the minimum size of the fires that can be detected (Boschetti et al., 2004) and the time interval between fire and detection (Eva & Lambin, 1998). However, previous studies suggest that temporal resolution is less important than the spatial resolution when it comes to the accuracy of the BA detection (Boschetti et al., 2010).

In a survey based on a questionnaire of 47 researchers who used BA products and an extended literature review, Mouillot et al. (2014) suggested that BA products should have commission errors (CE) in the range of 4% (ideal) to 17 % (maximum) while omission errors (OE) above 19% were deemed less useful for the climate modelling efforts. A first global comparison analysis found that NASA's MCD64 was the most accurate BA product (Padilla et al., 2015), but was far from achieving these goals with CE and OE reaching 42% and respectively 68%. These errors were in part due to the low spatial resolution, which results in small fires being overlooked (Randerson et al., 2012). A recent study has demonstrated that the contribution of small fires may be in fact even greater, as comparing Sentinel-2 and MODIS products for Africa showed an underestimation of almost 45% of BA (Roteta et al., 2019). Therefore, the development of new BA detection algorithms is a relevant research topic in the current context where climate change is a key issue. To achieve this improvement, the use of images from new satellites, such as those of the Copernicus missions of ESA, is necessary. Furthermore, alternative mapping options (e.g., radar-based) are needed over areas where optical images are limited by persistent cloud cover (e.g., tropical areas).

During the last decade, synthetic aperture radar (SAR) data have been increasingly used for BA mapping as data from multiple sensors became available. Such studies have

taken advantage of radar independence of cloud cover and solar illumination, their increased spatial resolution and the availability of multiple polarisations and incidence angles (Bourgeau-Chavez et al., 2002; French et al., 1999). The European Remote Sensing (ERS) SAR satellites (ERS-1 and ERS-2) were widely used in boreal (Bourgeau-Chavez et al., 1997; Kasischke et al., 1994), tropical (Siegert & Hoffmann, 2000; Siegert & Ruecker, 2000; Ruecker & Siegert, 2000) and Mediterranean (Gimeno et al., 2004, 2002) ecosystems to detect and map BA. More recently, RADARSAT (Gimeno & San-Miguel-Ayanz, 2004; French et al., 1999) and ALOS - PALSAR (Advanced Land Observation Satellite Phased Array type L-band Synthetic Aperture Radar) (Polychronaki et al., 2013) were employed for the same purpose. However, past SAR missions only provided data with low temporal resolution, which hindered the development of efficient radar-based BA detection and mapping algorithms over large areas. In addition, the utility of past sensors was limited by the available polarisations (mostly single co-polarised sensors), steep viewing geometries (far from ideal when monitoring changes in vegetation) and data access restrictions.

With the launch of ESA's Sentinel-1 satellite constellation (A and B platforms, operational since October 2014 and December of 2015, respectively) such limitations have been largely reduced. The Sentinel-1 constellation could theoretically provide images every three days by combining datasets acquired during ascending and descending trajectories. The independence from cloud cover and solar illumination added to improvements in sensors characteristics (e.g., dual polarisation, increased spatial resolution and incidence angle, precise orbital information), provides untapped opportunities for BA detection. A few studies have already explored the potentials of Sentinel-1 SAR images for BA detection, but these studies are focused on specific regions (Engelbrecht et al., 2017; Lohberger et al., 2018). To date, few studies tried integrating active and passive datasets for BA detection. Such a study detected BA independently from Sentinel-1 and Sentinel-2 datasets on a relatively small area in the Congo basin suggesting that a combined sensor approach compensates for the strengths and limitations of each individual sensor (Verhegghen et al., 2016). However, SAR based BA detection has limitations, as discussed in more detail in subsection 2.3.2. Lastly, fusion approaches combining optical and radar data have been considered for BA detection. In Stroppiana et al. (2015b,a) Landsat-5 TM and C-band ENVISAT ASAR data were integrated into a fuzzy algorithm aimed at burned area detection in a Mediterranean environment.

This chapter presents a novel radar-based BA mapping algorithm based on temporal series of C-band backscatter coefficient, that self-adapts to local scattering conditions and it is able to detect small fires (down to 1 ha) in a fairly automatic way. The specific objectives of this study were to (i) present the proposed algorithm and explain its functionalities, (ii) validate the BA detections over major biomes, (iii) compare the detection accuracy with that of existing products based on passive datasets, and (iv) analyse the factors influencing the algorithm accuracy.

2.2   Study area and dataset

The algorithm was developed using data from four sites, three located in the Amazon basin and one located in the Iberian Peninsula. Subsequently, the algorithm was validated over

18 sites around the world (Figure 2.1). The validation areas were located within biomes where fire events frequently occur, from boreal forests to tropical and sub-tropical forests, savannas and grasslands.
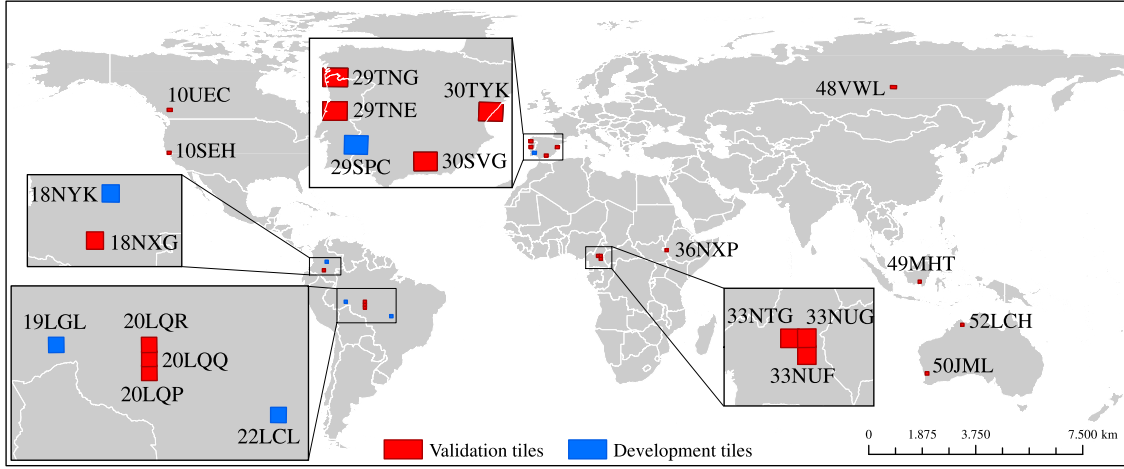
Figure 2.1: Location of the Military Grid Reference System tiles used for algorithm development and validation.

The algorithm relies on temporal series of Ground Range Detected (GRD) dual-polarised (vertical-vertical VV, and vertical-horizontal VH polarisations) SAR images acquired by the Sentinel-1 A/B satellites in interferometric wide (IW) swath mode. The GRD data were processed on a tile base structure using as grid the 100×100 km Military Grid Reference System (MGRS). For each tile, Sentinel-1 images from ascending and descending passes (when available) and from all intersecting relative orbits were used. Land cover (LC) classification and hotspots derived from thermal anomalies were used as ancillary data.

The land cover classification was produced in the framework of the ESA's Land Cover CCI project. This project delivers time series of consistent global LC maps at 300 m spacing on an annual basis from 1992 to 2015. The most recent map (i.e., 2015) was used. CCI land cover maps were generated using a combination of sensors, including MERIS and Proba-V time series of surface reflectance (Kirches et al., 2014). Since the SAR images were processed at a significantly higher pixel spacing (40 m, see subsection 2.3.1) than the LC map, the later was resized using a nearest-neighbour interpolation to coincide with the SAR spacing. In addition, the Land Cover Classification System (LCC) (Di Gregorio, 2005) was simplified by joining similar cover types into six groups: shrublands, grasslands, forests, crops, non-burnable, and others. One should notice that BA detection takes place over 100×100 km tiles. Therefore, for any given tile, the simplified LCC classification groups very similar classes.

Hotspots were available from NASA's Fire Information for Resource Management System (FIRMS). The hotspots were recorded by two sensors, the VIIRS (Visible Infrared Imaging Radiometer Suite) sensor at 375 m spatial resolution (Schroeder et al., 2014) and the MODIS sensor at 1 km spatial resolution (Giglio et al., 2003). The VIIRS and MODIS database was last accessed in January 2018.

To derive the validation fire perimeters (see subsection 2.3.4), Landsat-8 optical images were retrieved from the United States Geological Survey repository (USGS) as atmospherically corrected surface reflectance products (Vermote et al., 2016). The validation period was adjusted for each tile considering the fire season length and the availability of Landsat images with a cloud cover under 30%. Sentinel-2 Level-1C images retrieved from the Copernicus Open Access Hub were considered to reduce temporal gaps in the validation dataset and thus large discrepancies between the validation period and the Sentinel-1 detection period.

The effect of soil moisture, an important factor affecting radar backscatter, on BA detection accuracy was analysed using the global Soil Moisture Active Passive (SMAP) product. Specifically, the Enhanced Level 3 Passive Soil Moisture Product based on L-Band Radiometer (9 km pixel spacing and three days revisit period) was used. The reliability of this product was demonstrated by a correlation coefficient above 0.8 between the estimated soil moisture and *in situ* measurements (Chan et al., 2018; Chen et al., 2018). From this product, the descending pass images (6 AM Equator crossing), more accurate than ascending, according to Chan et al. (2018), were used so that all measurements represented the same acquisition time (Chan, 2016). As for the LC map, the product was resized to 40 m using the nearest-neighbour interpolation.

2.3   Methods

2.3.1   SAR data pre-processing

The Sentinel-1 data were processed using open-source libraries available in the Orfeo ToolBox (OTB), an image processing software developed by the National Centre for Space Studies (CNES), France (Inglada & Christophe, 2009). The OTB-based processing chain uses Ground Range Detected (GRD) Sentinel-1 images with the SAR data being tiled to 100 km using the MGRS system. The chain is highly scalable and autonomous once few parameters are set, and includes the data download from Sentinel-1 repositories. The SAR data processing may be grouped in several steps including, pre-processing, geocoding and temporal filtering (Figure 2.2).
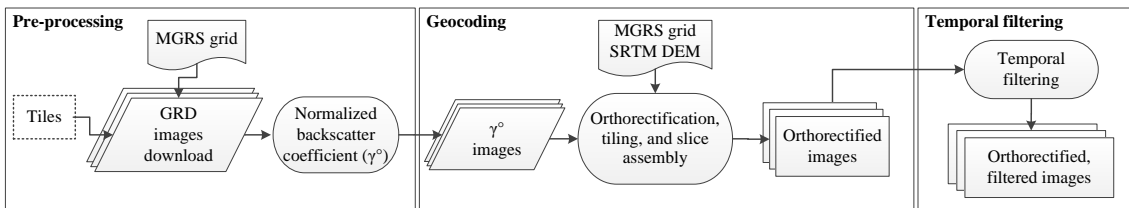
Figure 2.2: SAR data processing with the Orfeo Toolbox.

The pre-processing step includes data download of the specified MGRS tiles and radiometric normalisation to gamma nought (γ^0) using the gamma nought lookup table provided in the product metadata. Only SAR images acquired in the interferometric wide swath mode, the Sentinel-1 default acquisition mode over land, were used. The calibrated images were orthorectified to ground geometry using elevation information from the Shut-

tle Radar Topography Mission (SRTM) one arc-second DEM and the bicubic interpolator. The orthorectified images were clipped to the processing tile, and the data acquired from the same orbital path but provided within different slices were mosaicked (i.e., slice assembly). It should be noted that the BA algorithm uses temporal backscatter differences of the same relative orbit; hence, terrain-flattening (Small, 2011; Frey et al., 2013) was not necessary as the DEM-derived normalisation (illumination) area for a given pixel is constant in time thus not affecting the pre- to post-fire backscatter coefficient variations (Tanase et al., 2010c, 2015, 2018). The last step was a multi-temporal filtering of the products for each satellite pass (Quegan et al., 2000). The GRD data were processed to the nominal Sentinel-1 resolution (20 m) through the OTB based chain.

The BA detection algorithm deployment over large areas is conditioned by its performance (speed) and accuracy. Both parameters are influenced by the pixel spacing to which products are processed as omission and commission errors are highly depended on speckle while the processing speed increases with decreasing pixel size. Analysing the effect of pixel spacing on image radiometric properties, processing time and BA detection accuracy was essential for selecting the optimum pixel spacing for deployment. Tanase & Belenguer-Plomer (2018) carried out an analysis for four pixel spacing (i.e., 20, 30, 40 and 50 m) over two test tiles. A 40 m spacing provided the optimum trade-off between speckle reduction, storage and computing requirements and the accuracy of the detected BA. Therefore, the temporally filtered images were aggregated to 40 m.

Radio Frequency Interference (RFI) may contaminate SAR data. Since RFI are principally observed over highly populated urban areas (Li et al., 2004; Njoku et al., 2005; Lacava et al., 2013) and considering that burned areas are usually located away from large cities, such effects were not observed and consequently were not considered.

2.3.2 Backscatter behaviour in burned areas

To better understand the proposed algorithm, its development, and the decision-making process that shaped it, this subsection describes the behaviour of C-band backscatter coefficient after fire events.

Fire on vegetated areas results in variations of the backscatter coefficient, which may increase or decrease depending on the polarisation, the remaining vegetation and the environmental conditions (i.e., rainfall) during SAR data acquisition. Fire consumption reduces the number of vegetation scattering elements, potentially reducing the backscatter coefficient (Van Zyl, 1993; Antikidis et al., 1998). However, biomass consumption may increase scattering from the ground due to reduced signal attenuation (less vegetation) and the increased effect of soil surface properties, such as moisture and roughness (Tanase et al., 2010b). Hence, microwaves backscatter behaviour in areas affected by fires may be more heavily influenced by soil moisture properties when compared to unburned areas, particularly when rainfall occurs after the fire (Imperatore et al., 2017; Gimeno & San-Miguel-Ayanz, 2004; Ruecker & Siegert, 2000). Rain and melting snow are the main causes of increased soil moisture (Huang & Siegert, 2006), influencing the radar signal and consequently reducing C-band sensitivity to fire-induced changes (Tanase et al., 2010b). SAR-based BA mapping may be further hindered by spatial changes in soil moisture due to unrelated fire factors (e.g., temperature, insolation, wind, slope and ori-

entation, soil roughness) which are difficult to embed into detection algorithms. The local incidence angle (LIA) is yet another factor influencing C-band sensitivity to fire-induced changes, with smaller LIA values providing increased burned to non-burned differentiation for co-polarised waves (Gimeno & San-Miguel-Ayanz, 2004; Huang & Siegert, 2006; Tanase et al., 2010b). Finally, wave polarisation is also a fundamental variable, with cross-polarised waves being more sensitive to changes in vegetation (volumetric scattering) and less to surface properties (e.g., soil moisture and roughness) when compared to the co-polarised waves (Freeman & Durden, 1998; Yamaguchi et al., 2005; Van Zyl et al., 2011). Such contrasting effects may generate a wide range of possible backscatter variations over burned areas that depend on the interplay between the SAR sensor characteristics (e.g., wavelength, polarisation, incidence angle) and environmental conditions at SAR acquisition (e.g., fire impact, soil surface properties, meteorological conditions).

The impact of fire on the backscattering coefficient was actually found to cause ambiguous effects. A strong backscatter decrease was found for burned tropical forests at C-band VV polarisation under dry weather conditions due to the decreased volume scattering and increased heat flux, which led to a dryer ground (Ruecker & Siegert, 2000; Lohberger et al., 2018). After rainfall, discrimination from the unburned surrounding forests was difficult as the backscatter coefficient over BA increased (Siegert & Ruecker, 2000). In the temperate region and the Mediterranean basin, lower backscatter values were found in fire-affected areas for cross-polarised C-band when compared to adjacent unburned forest (Rignot et al., 1999; Imperatore et al., 2017). In boreal forests, higher backscatter values, when compared to the adjacent unburned areas, were observed at C-band VV polarisation when soil moisture was high, whereas lower backscatter was observed for sites with better drainage (Bourgeau-Chavez et al., 2002; Huang & Siegert, 2006; Kasischke et al., 1994). In Australian woodlands and open forests, the post-fire backscatter increased for co-polarised waves and decreased for cross-polarised waves (Menges et al., 2004) while for African open forests the backscatter decreased for both co- and cross-polarised C-band channels, although only the co-polarised channel was deemed useful for BA detection (Verhegghen et al., 2016). Changes in the post-fire backscatter levels appear to be strongly related to changes in soil moisture, with data acquired after rainfall being less suitable for classification or biophysical parameters retrieval. However, some fire-related studies reported increased differentiation potential for BA after rainfall in the Mediterranean basin (Gimeno & San-Miguel-Ayanz, 2004).

2.3.3   Burned area detection and mapping algorithm

The main requirements of the BA detection algorithm were (i) the use of cloud insensitive satellite data (i.e., SAR), (ii) sensitivity to local burn conditions, and (iii) a high degree of automation. The algorithm was designed to make use of existing datasets for training purposes by using sets of susceptible burned and unburned pixels for locally dominant land cover types. The algorithm has six stages with its simplified structure being provided in Figure 2.3. The following paragraphs explain in detail each stage.

2.3.3.1   Stage 1: Anomaly change detection

An anomalous change implies variations outside the typical behaviour expected for a given area and time. Burned areas were considered anomalies since fires are inconsistent spatial
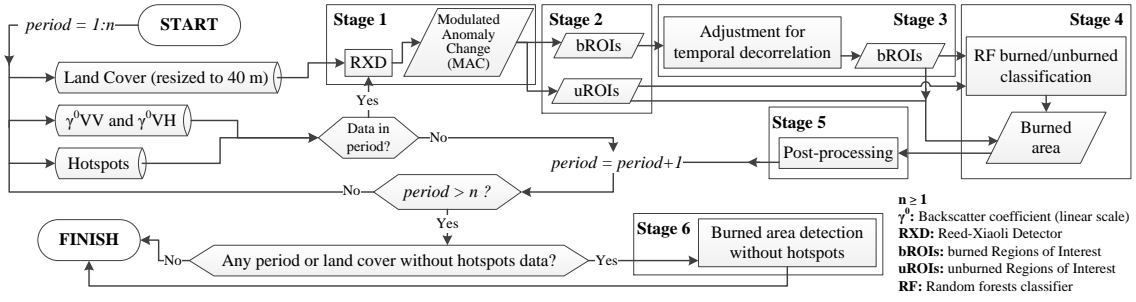
Figure 2.3: Flowchart of the SAR based algorithm for burned area detection.

and temporal events. The Reed-Xiaoli detector (RXD), proposed by Reed & Yu (1990), extracts signatures that are distinct from the surroundings without the need for *a priori* information. Anomalies have two characteristics that make them outliers: (i) spectral signatures different from the surrounding pixels; and (ii) low occurrence probability (Stein et al., 2002; Banerjee et al., 2006; Kwon & Nasrabadi, 2005). Hence, RXD allows distinguishing anomalous changes, such as burned areas, from pervasive changes (e.g., seasonal effects) that occur periodically and extend over large swathes of the image (Theiler & Perkins, 2006). The RXD uses the covariance matrix to calculate the Mahalanobis distance from a given pixel to the mean of the surrounding (background) pixels (Dabbiru et al., 2012). Thus, for any given pixel, the anomalous change (AC) score is computed by the RXD (Equation 2.1).

$$AC(x) = (\mathbf{x}\prime - \boldsymbol{\mu})^{\top} \mathbf{C}^{-1} (\mathbf{x}\prime - \boldsymbol{\mu}) \tag{2.1}$$

where x is any given pixel, $\mathbf{x}\prime$ is a vector formed by the image bands values of the pixel x, $\boldsymbol{\mu}$ is a vector composed by the mean value of the background pixels (e.g., stable areas) in each image band and $\mathbf{C}$ is the covariance matrix of the image bands (computed from the background pixels). The background value may be computed as the mean sample of a subset image where only pixels of the same land cover class of x are included to differentiate anomalous changes from pervasive, since seasonal effects and soil moisture variations may affect the backscatter coefficient in a divergent way as a function of land cover class. When *a priori* information is available, the background value may be computed from areas where anomalies are not expected. For BA detection, *a priori* information was provided by MODIS and VIIRS active fire databases. MODIS and VIIRS hotspots corresponding to the current detection period (CDP) were used to mask areas likely affected by fires while the remaining pixels were used to calculate the background values. The BA masks were derived by taking a buffer of 0.75 km around each hotspot. This buffer was considered the influence area of each individual hotspot (IAhs), and it roughly corresponds to the pixel size for VIIRS and MODIS thermal channels while also considering location uncertainty.

The RXD was applied to a set of temporal ratios of the backscatter coefficient (Equation 2.2 and 2.3). Such temporal indices were previously used for estimating the impact of different disturbance agents (e.g., fire, insects, wind) on vegetation (Tanase et al., 2015, 2018). The selected temporal radar indices mainly use the VH backscatter, which is more responsive to volumetric scattering from vegetation and less affected by changes in surface properties (e.g., soil moisture, surface roughness) when compared to the co-polarised (VV polarisation) channel (Freeman & Durden, 1998; Yamaguchi et al., 2005; Van Zyl et al.,

2011).

$$RI_1 = \gamma^0 VH_{t-1}/\gamma^0 VH_{t+1} \tag{2.2}$$

$$RI_2 = \left(\gamma^0 VH_{t-1}/\gamma^0 VV_{t-1}\right)/\left(\gamma^0 VH_{t+1}/\gamma^0 VV_{t+1}\right) \tag{2.3}$$

where γ^0 is the backscatter coefficient (linear scale) of VV or VH polarisations, and $t-1$ and $t+1$ are respectively pre- and post-fire detection dates that define the CDP.

To reduce commission errors related to signal variation due to changes associated to post-fire events (e.g., vegetation regrowth), the AC values for CDP were modulated by the AC values recorded for the previous detection period (PDP) (Equation 2.4). Practically, AC scores of the PDP were subtracted from the AC of the CDP. The result was a Modulated Anomalous Changes (MAC) score used in all subsequent algorithm stages.

$$\mathrm{MAC}\,(x) = \mathrm{AC}\,(x)_{[t-1..t+1]} - \mathrm{AC}\,(x)_{[t-2..t-1]} \tag{2.4}$$

2.3.3.2   Stage 2: Burned and unburned regions of interest

In this stage, burned and unburned Regions of Interest (ROIs) were automatically extracted using the MAC scores and ancillary information from hotspots and land cover data. Since information on hotspots was acquired daily from two independent sensors (VIIRS and MODIS) most burned pixels in the selected study areas (94.3%) were in fire patches with at least one hotspot within 0.75 km, the selected buffer considered as hotspot area of influence (IAhs) even for the tropical regions, where cloud cover is frequent. The presence of hotspots greatly facilitated the attribution of the detected MAC values to burned areas. This allowed distinguishing BA from other changes, such as logging, crop harvesting, flooding, or vegetation disturbance due to insects or diseases. When hotspots were not available, due to the cloud cover or small fire size, a different attribution method was used as explained in Stage 4. Burned ROIs (bROIs) were extracted in two steps: seeding and growing. This is an approach previously used for BA mapping algorithms (Bastarrika et al., 2011; Alonso-Canas & Chuvieco, 2015; Roteta et al., 2019). To obtain the seeds, spatially connected IAhs pixels were first grouped in uniquely identified objects: $q_1 : n$, where n is the number of the unique objects. A pixel x inside an object q, was considered burned seed (bSeed) if Equation 2.5 was met.

$$
\begin{aligned}
x = \mathrm{bSeed}\,(q) \to\ &(\mathrm{MAC}\,(x) \geq \min\,(s,v) > 0) \vee \\
&(\mathrm{MAC}\,(x) \geq \max\,(s,v) > 0 \wedge \min\,(s,v) < 0)
\end{aligned}
\tag{2.5}
$$

where $s = \mu\left(\mathrm{MAC}_{q'}\right)$, being μ the mean and q' a region around q bounded by $dist_q$ and $dist_q + \sqrt{dist_q}$, with $dist_q$ being the maximum span of object q. Thus, q' delineates likely unburned areas in the vicinity of q; and $v = \mu\left(\mathrm{MAC}_{\mathcal{N}_G}\right)$, with $\mathcal{N}_G$ being the neighbour pixels of G, where G is a pool of pixels inside q with MAC values below $\mu(\mathrm{MAC}_q)$. Essentially, for a pixel to be considered seed it had to fulfil two conditions, one related to vicinity to a hotspot (within IAhs) and the second related to the magnitude of backscatter change (MAC score).

The bSeed pixels were extracted considering the major land cover type for each q

object. Therefore, pixels in q' region were stratified by land cover type with only pixels of the same land cover type as predominant of q being used for computations. In addition, the selected q' pixels needed to be outside the IAhs of any other hotspot. Figure 2.4 shows graphically the concepts of q, q' and $dist_q$. Once bSeed pixels for q were extracted, an open morphological operator (3×3 window) was used to eliminate isolated bSeed pixels. With increasing window size, BA omission errors increased while commission errors decreased. To determine the optimum size, an error analysis was carried out using different window sizes (3×3, 5×5 and 7×7) over the four algorithm development tiles (analysis not shown). The 3×3 window was selected since it least affected the detection of small size fires while still managing to reduce commission errors. The same window size was used in previous works to reduce speckle effects (Menges et al., 2004).
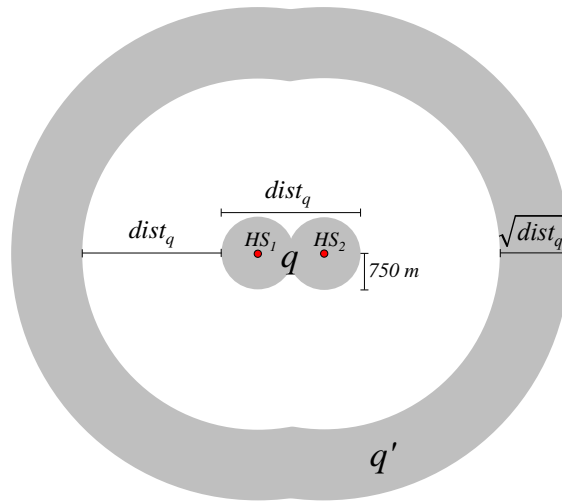
Figure 2.4: Graphical representation of concepts needed to extract bROIs, being HS - hotspot.

Given an object q and its predominant land cover class k, the growing phase started by masking out all the pixels of the image which MAC values were below the mean MAC value of all image pixels of land cover class k. The remaining pixels were used to compute a new mean of the MAC values, which was used as the minimum threshold to label Likely Burned Pixels (LBP) of q (Equation 2.6).

$$x = \text{LBP}(q) \rightarrow \text{MAC}(x) > \mu(\text{MAC} > \mu(\text{MAC}_k)) \tag{2.6}$$

Connected LBP(q) pixels were grouped and subsequently overlapped with the extracted bSeed pixels of q. LBP(q) groups overlapping bSeed pixels of q were assigned to the bROIs and constituted the first component of the detected burned areas. The second component was detected using no parametric classification (i.e., random forests) as explained in Stage 4.

The unburned ROIs (uROIs) were derived iteratively by land cover type. The histogram of bROIs pixels identified in the previous step was used to calculate the MAC values for the 25 and 75 percentiles (P_{25} and P_{75}, respectively). These values constituted thresholds used to classify the MAC image in burned and unburned. Pixels with MAC values below P_{25} or above P_{75} were considered possible unburned seeds since (i) MAC values below P_{25} indicate small changes, likely unrelated to fires (e.g., vegetation growth,

changes in vegetation water content), and (ii) MAC values above P_{75} are usually associated with significant changes, such as logging, crop harvesting, or floods. One should note that high severity fires may also result in MAC values above P_{75}. However, such areas are regularly associated with hotspots and therefore were not labelled as uROIs. An open morphological operator 3×3 window) was applied to the classified binary image to remove noise. The effect of the open morphological operator was an increased number of unburned pixels. Pixels from the not burnable LC map classes (i.e., bare soils, water, snow and ice, urban areas) were labelled as uROIs, while pixels overlapping IAhs or bROIs were filtered out. Additionally, for the cropland cover class, groups of pixels over 56 ha (0.75×0.75 km, being 0.75 km the double of VIIRS spatial resolution), not overlapping hotspots were included as uROIs to account for fire-unrelated changes, such as crop harvesting or changes in surface properties (roughness) due to agricultural works (e.g., ploughing).

2.3.3.3   Stage 3: Adjustment for temporal decorrelation

During algorithm development, a temporal decorrelation between fire events (i.e., hotspots date) and backscatter coefficient change was observed (Belenguer-Plomer et al., 2018b). Such decorrelation events may be the result of delayed backscatter decrease after fire due to multiple factors including (i) pre-fire conditions, e.g., drier than usual weather may result in low values for the pre-fire backscatter coefficient, (ii) post-fire weather, e.g., precipitations may temporally increase the backscatter coefficient, and (iii) vegetation-dependent backscatter response to fire events. For example, over forests, VH backscatter decrease may be delayed as there are still sufficient scattering elements (tree trunks and branches) present after fire. As time passes, trunks and branches dry up, which results in decreased backscatter from vegetation.

To account for temporal decorrelation, the BA was detected iteratively for each period. Delayed changes in backscatter were accounted for computing the bROIs detected in periods formed by the current pre-fire image ($t-1$) and images acquired during following 90 days past the CDP (i.e., $t+2$, $t+3$). This temporal threshold was based on empirical observations (Belenguer-Plomer et al., 2018b). Such bROIs were labelled as burned in the CDP ($t-1$ to $t+1$) when overlapping hotspots from the CDP. Additionally, these bROIs must not overlap hotspot recorded past the CDP.

2.3.3.4   Stage 4: Random forests burned / unburned classification

Only a fraction of the anomalous pixels were labelled as burned based on information from hotspots due to the rather restrictive criteria (i.e., MAC score) used in Stage 2 and 3. Pixels not meeting the imposed criteria also needed labelling. To avoid subjectivity, such pixels were labelled using a non-parametric classifier (i.e., random forests) trained with data extracted from bROIs and uROIs by each land cover classes and CDP. The random forests (RF) classifier was used as it is robust to data noise (Gislason et al., 2006; Rodriguez-Galiano et al., 2012; Du et al., 2015; Waske & Braun, 2009) and less sensitive, when compared to other machine learning techniques, to the quality of training samples and overfitting (Belgiu & Drăguţ, 2016). Moreover, RF was already used to classify SAR data (Waske & Braun, 2009) and solve similar fire mapping problems (Collins et al., 2018; Fernandez-Carrillo et al., 2018; Ramo & Chuvieco, 2017; Meddens et al., 2016).

RF is an ensemble classifier that consists of a group of decision trees $\{h(\mathbf{x}\prime, \Theta_z),$ $= 1,...\}$, where $\mathbf{x}\prime$ is the input vector of any given pixel (x), and Θ_z are an independently bootstrap sampled vectors with replacement in each decision tree (z). Each tree provides a unique class for x, being the class of x assigned as the most popular voted class (Breiman, 2001). In this study, *TreeBagger* from MATLAB ® software package was used to construct the RF classifiers.

RF classifiers are customisable through different parameters, such as (i) number of trees, (ii) number of training samples, (iii) proportion of training samples by class, and (iv) number of independent variables employed in each tree. The number of trees is a key adjustment in RF classification since for more trees the generalisation error converges and models are not over-fit (Breiman, 2001; Pal, 2005; Rodriguez-Galiano et al., 2012). On the other hand, using more trees demands more computational resources. An empirical analysis (not shown) concluded that 250 trees provided the best trade-off between speed and accuracy for BA classification in this study. Since the number of pixels in bROIs and uROIs is high, computational costs may be reduced by using just a fraction for training purposes. This fraction was determined, by land cover classes, as 1% of all bROIs and uROIs pixels divided by the number of trees (250). Unbalanced training samples may result in infra-classification of the minority classes. According to Chen et al. (2004), several approaches may be used to address such problems: (i) reducing the overall learning cost, with high costs being assigned to the miss-classification of the minority classes (Pazzani et al., 1994); (ii) under-sampling the majority and over-sampling the minority classes; or (iii) a combination of both techniques (Chawla et al., 2002). The latter approach was used in this study. Depending on the misclassification cost, the *TreeBagger* function generated in-bag samples by oversampling the burned class and under sampling the unburned class. The proportion of training data were empirically adjusted to 40% and 60% for burned and unburned classes, respectively.

The number of variables considered for trees growing in each split was computed as the square root of the total number of variables (Gislason et al., 2006), as it reduces the correlation of trees and thus improves global accuracy (Rodriguez-Galiano et al., 2012; Gislason et al., 2006). In addition to the SAR based metrics used for RXD (Equation 2.2 and 2.3), up to 30 SAR metrics were used for RF classification. These metrics were computed as in Equation 2.7 to 2.12. The non-parametric classification was carried out considering the land cover type with specific models being built for each land cover class. The BA detected by RF was added to bROIs detected in Stage 2 and 3, and formed the total BA for the CDP.

$$\mu\left(\gamma^0 XY_{[t',t-1]}\right) - \gamma^0 XY_{t+i} \tag{2.7}$$

$$\mu\left(\gamma^0 XY_{[t',t-1]}\right) / \gamma^0 XY_{t+i} \tag{2.8}$$

$$\gamma^0 XY_{t-1} - \gamma^0 XY_{t+i} \tag{2.9}$$

$$\gamma^0 XY_{t-1} / \gamma^0 XY_{t+i} \tag{2.10}$$

$$\left(\gamma^0 VH_{t-1}/\gamma^0 VV_{t-1}\right) / \left(\gamma^0 VH_{t+i}/\gamma^0 VV_{t+i}\right) \tag{2.11}$$

$$\mu\left(\gamma^0 VH_{[t',t-1]}/\gamma^0 VV_{[t',t-1]}\right) / \left(\gamma^0 VH_{t+i}/\gamma^0 VV_{t+i}\right) \tag{2.12}$$

where $\gamma^0 XY$ is the backscatter intensity (linear scale) of VV and VH polarisations, t' is $t-1$ minus the double of days distance between $t-1$ and $t+1$, and i is 1 or 2, being 30

the maximum number of indices computed.

2.3.3.5   Stage 5: Post-processing

Post-processing was needed to account for temporal decorrelation and improve detection results over problematic land covers such as cropping areas. To adjust for temporal decorrelation, the BA detected by the non-parametric classifier for the CDP was compared to the IAhs of previous detection periods, up to 90 days before the pre-fire image $(t-1)$ (Belenguer-Plomer et al., 2018b). If burned areas detected in the current CDP (i.e., objects formed by contiguous pixels) overlapped previous IAhs (objects) by more than 75% (set from empirical observations), they were masked out and considered previous burns. Three additional post-processing steps were then carried out to improve the results further: (i) on cropping lands, groups of burned pixels (objects) with areas above 56 ha (see Stage 2) that did not overlap IAhs (i.e., no local hotspot) were removed. The rationale was that lack of hotspots over a large changing cropping area is an indication of harvesting rather than fire; (ii) burned objects below one hectare were removed to reduce noise in BA detections due to residual speckle; and (iii) a modal filter with a convolution kernel of 3×3 pixels was applied to smooth the salt and pepper effects typical for SAR based classifications.

Post-processing also deals with joining the BA detected in the different relative orbits intersecting a specific tile. The BA was detected separately for each relative orbit, to avoid misinterpreting backscatter changes due to changing azimuth angles or illumination geometry as fire-related changes. To reduce topographic related effects such as layover, foreshortening and shadowing, burned areas detected in different relative orbits (i.e., from ascending and descending passes) were joined to obtain the final BA maps.

2.3.3.6   Stage 6: Burned area detection without hotspots

As clouds may prevent the propagation of radiation from active fires to the thermal sensors onboard satellites, the algorithm was built with a backup mechanism to cope with the absence of hotspots for a specific land cover type and detection period. However, for the algorithm to work, hotspots need to be available for each land cover class at some point during the analysed fire season.

The algorithm first detected the BA for all land cover types during detection periods for which hotspots were available. For detection periods without hotspots, the data were temporally stored for later processing. During detection, the algorithm saved a database containing the P_{25} and P_{75} of MAC values for bROIs (Stage 2) and the trained RF models (Stage 4) for each land cover class. This database is hereafter referred to as the Classifier Model and Criteria (CMC). Once detections for land cover classes and detection periods with hotspots ended, the CMC database was used to classify the temporally stored data (i.e., land cover types without hotspots during detection periods) if two conditions were met: (i) the CDP was within the fire season. The length of the fire season was computed using the daily hotspots frequency as the interval between the dates corresponding to the P_5 and P_{95}; and (ii) the difference between the CDP and the date for the nearest CMC was less than one month, thus avoiding possible confusions due to changes in vegetation phenology. When CMC entries from different detection periods met the conditions, the

one closest to the CDP was used. The MAC image for the CDP was segmented into possibly burned and unburned based on the CMC P_{25} and P_{75}, with the possible burned pixels being subsequently classified using the stored RF models by land cover class. When CMC entries were spaced equally in time when compared to the CDP (i.e., one entry is from a previous period and one from a posterior period), each entry was used separately and only the commonly detected BA was kept. The post-processing operations from Stage 5 were carried out on the detected BA from this stage.

An additional operation was carried out to reduce possible commission errors during this stage. The operation was carried out over BA detected on different relative orbits. Note that detections were always carried out using time-series of images from the same relative orbit. If several relative orbits intersected a given tile, the algorithm worked through the data from each relative orbit separately. BA products composites were subsequently formed using detections from different relative orbits and the same detection period. For each detection period, BA pixels detected in different relative orbits were grouped in objects. If all pixels of an object were classified as unburned in one orbit, the object was removed from the detected BA for the CDP. Since dual-pass (ascending and descending) acquisition were not available for all tiles and spatially overlapping relative orbits only partially covered any given tile, this additional operation reduced commission errors where BA detections intersected.

2.3.4   Reference images and validation metrics

The reference burned perimeters extraction for validation purposes was based on a well-established framework (Padilla et al., 2014, 2015, 2017). The reference data were obtained from Landsat-8 images using an RF classifier and training polygons selected by an independent operator. The validation perimeters were generated from 120 multi-temporal pairs of images with a maximum separation of 32 days. The temporal separation of the pairs was short to ensure that fire scars were clearly visible in the post-fire image. Before running the classification, clouds were removed using the pixel quality band of the Landsat product, and each pair of images was clipped to the extent of its corresponding MGRS tile. Training areas were selected using a false colour composite (RGB: SWIR, NIR, R) that allowed for clear discrimination of burned areas. Three training classes were considered: burned, unburned, and no data.

The variables selected as input for the RF classifier were (i) Landsat-8 bands 5 and 7, (ii) the Normalised Burn Ratio (NBR), and (iii) the temporal difference between the pre- and post-fire NBR values (dNBR). The NBR (Equation 2.13) is defined as the normalised difference between the reflectance of NIR and SWIR wavelengths (García & Caselles, 1991; Key & Benson, 2004).

$$\text{NBR} = (\text{Band 5 - Band 7}) / (\text{Band 5 + Band 7}) \qquad (2.13)$$

where Band 5 is the surface reflectance in the near infrared (NIR) wavelength (0.85 - 0.88 ţm) and Band 7 is the surface reflectance in the shortwave infrared (SWIR) wavelength (2.11 - 2.29 ţm).

After the RF classification, fire perimeters were visually revised to correct possible errors. New training fields were iteratively added, and the RF was re-run until the

classification result was deemed accurate. Reference BA perimeters were resized using a nearest-neighbour interpolation to the selected pixel spacing of the Sentinel-1 product (40 m). Temporal gaps between the Landsat-8 reference period and the Sentinel-1 detection period were filled in through photo-interpretation of Sentinel-2 images.

The Sentinel-1 BA detections were validated using confusion matrices (Table 2.1). Three accuracy metrics were computed for the burned area class using the confusion matrices, the omission error (Equation 2.14), the commission error (Equation 2.15) and the Dice coefficient (Equation 2.16) (Padilla et al., 2015).

Table 2.1: Confusion matrix example.

| Detection | Refererence data | | |
	Burned	Unburned	Row total
Burned	P_{11}	P_{12}	P_{1+}
Unburned	P_{21}	P_{22}	P_{2+}
Col. total	P_{+1}	P_{+2}	N

$$OE = P_{21}/P_{+1} \tag{2.14}$$
$$CE = P_{12}/P_{1+} \tag{2.15}$$
$$DC = 2P_{11}/(P_{1+} + P_{+1}) \tag{2.16}$$

2.4   Results

2.4.1   Algorithm accuracy

The OE and CE over the validation tiles varied, with the highest errors (0.54 to 0.81) being observed over Australian grasslands and the lowest (0.19 to 0.2) over the Mediterranean forests and shrublands (Table 2.2). The highest BA detection accuracy (DC 0.82) was observed over the tile 22LQP located in the Amazon basin (Figure 2.5). By land cover type, the algorithm produces more accurate results over forested areas (DC 0.64), followed by shrublands (DC 0.56). The lowest detection accuracy was observed over grasslands (DC 0.28) (Figure 2.6). Note that error metrics by land cover type were computed by pooling pixels with the same land cover type from all tiles.

2.4.2   Comparison with existing global products

The accuracy metrics of the Sentinel-1 BA detections obtained from the presented algorithm were compared to those derived from the current most widely used BA global product, the MCD64A1 Version 6 (Giglio et al., 2018). The magnitude of the error metrics may be influenced by the temporal match between the images used to generate the reference perimeters and those used to generate the BA products. To account for detection errors caused by slightly different validation and detection periods, the MCD64A1 product was temporally subset to match the Sentinel-1 detection periods.

Table 2.2: Error metrics for Sentinel-1 burned area detections for each MGRS tile analysed.

MGRS	Ref. period	Det. period	P	Dd	nIM	LC	C	DC	OE	CE
10SEH	04/10/2017 05/11/2017	28/09/2017 03/11/2017	B	12	16	G	NA	0.61	0.34	0.43
10UEC	05/07/2017 22/08/2017	08/07/2017 25/08/2017	B	12	32	F	NA	0.76	0.31	0.16
18NXG	30/10/2016 02/03/2017	03/11/2016 03/03/2017	A	24	6	F	SA	0.64	0.35	0.36
20LQP	20/07/2016 22/09/2016	03/07/2016 25/09/2016	D	84	4	F	SA	0.82	0.14	0.22
20LQQ	04/07/2016 22/09/2016	03/07/2016 25/09/2016	D	36	5	F	SA	0.55	0.42	0.48
20LQR	04/07/2016 25/09/2016	03/07/2016 25/09/2016	D	36	8	F	SA	0.64	0.26	0.43
29TNE	05/10/2017 06/11/2017	04/10/2017 04/11/2017	B	6	24	S	Eu	0.7	0.38	0.2
29TNG	05/10/2017 06/11/2017	04/10/2017 05/11/2017	B	6	24	S	Eu	0.67	0.36	0.3
30SVG	30/06/2015 16/07/2015	26/06/2015 20/07/2015	B	12	9	S	Eu	0.65	0.19	0.46
30TYK	12/06/2017 30/07/2017	10/06/2017 28/07/2017	B	12	26	S	Eu	0.69	0.31	0.3
33NTG	28/11/2015 16/02/2016	21/11/2015 13/02/2016	A	12	14	F	Af	0.63	0.47	0.21
33NUF	07/12/2015 23/12/2015	28/11/2015 22/12/2015	A	12	3	F	Af	0.52	0.52	0.43
33NUG	21/11/2015 24/01/2016	16/11/2015 27/01/2016	A	12	8	F	Af	0.52	0.52	0.44
36NXP	30/12/2016 15/01/2017	01/01/2017 26/01/2017	D	6	6	S	Af	0.46	0.62	0.41
48VWL	12/06/2017 21/06/2017	11/06/2017 23/06/2017	D	12	3	F	As	0.58	0.57	0.15
49MHT	02/07/2015 04/09/2015	26/06/2015 06/09/2015	D	24	5	O	As	0.67	0.35	0.32
50JML	07/03/2017 10/05/2017	04/03/2017 15/05/2017	D	12	13	G	Au	0.21	0.81	0.76
52LCH	05/04/2017 21/04/2017	26/03/2017 24/04/2017	D	12	7	S	Au	0.31	0.78	0.51

Reference period - period for which the reference burn perimeters were derived; Detection period - first and last Sentinel-1 images of the data series; P - satellite pass (A-ascending, D-descending, and B-both); Dd - day difference between images (mode); nIM - number of SAR images within the detection period; LC - predominant land cover (G-grassland, S-shrub, F-forest, and O-others); C - continent for each tile (NA-North America, SA-South America, Eu-Europe, Af-Africa, As-Asia, and Au-Australia); DC - Dice coefficient; OE - omission error; and CE - commission error.
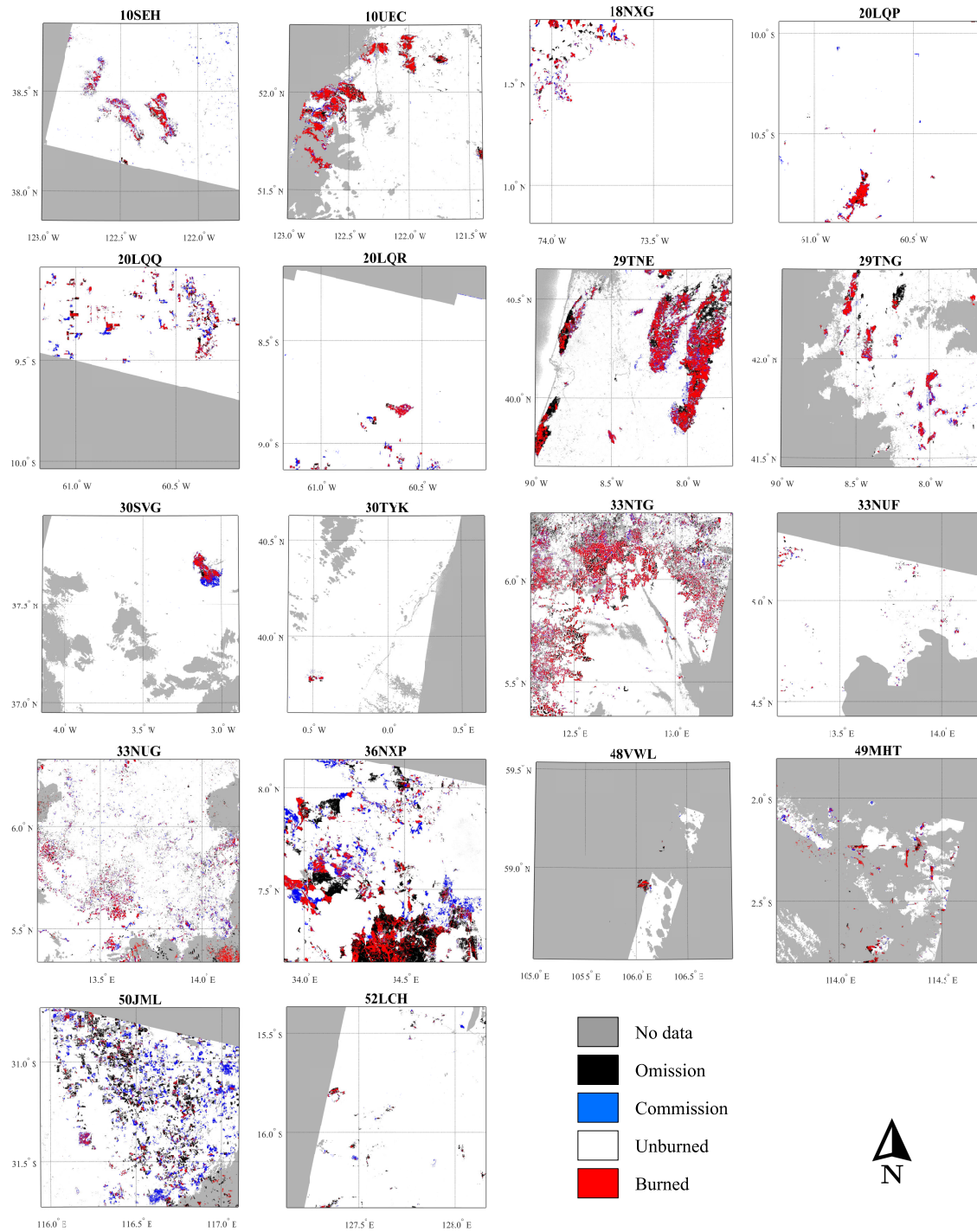
Figure 2.5: Maps of burned area detected using Sentinel-1 data per MGRS tiles. Errors of omission and commission are also shown.
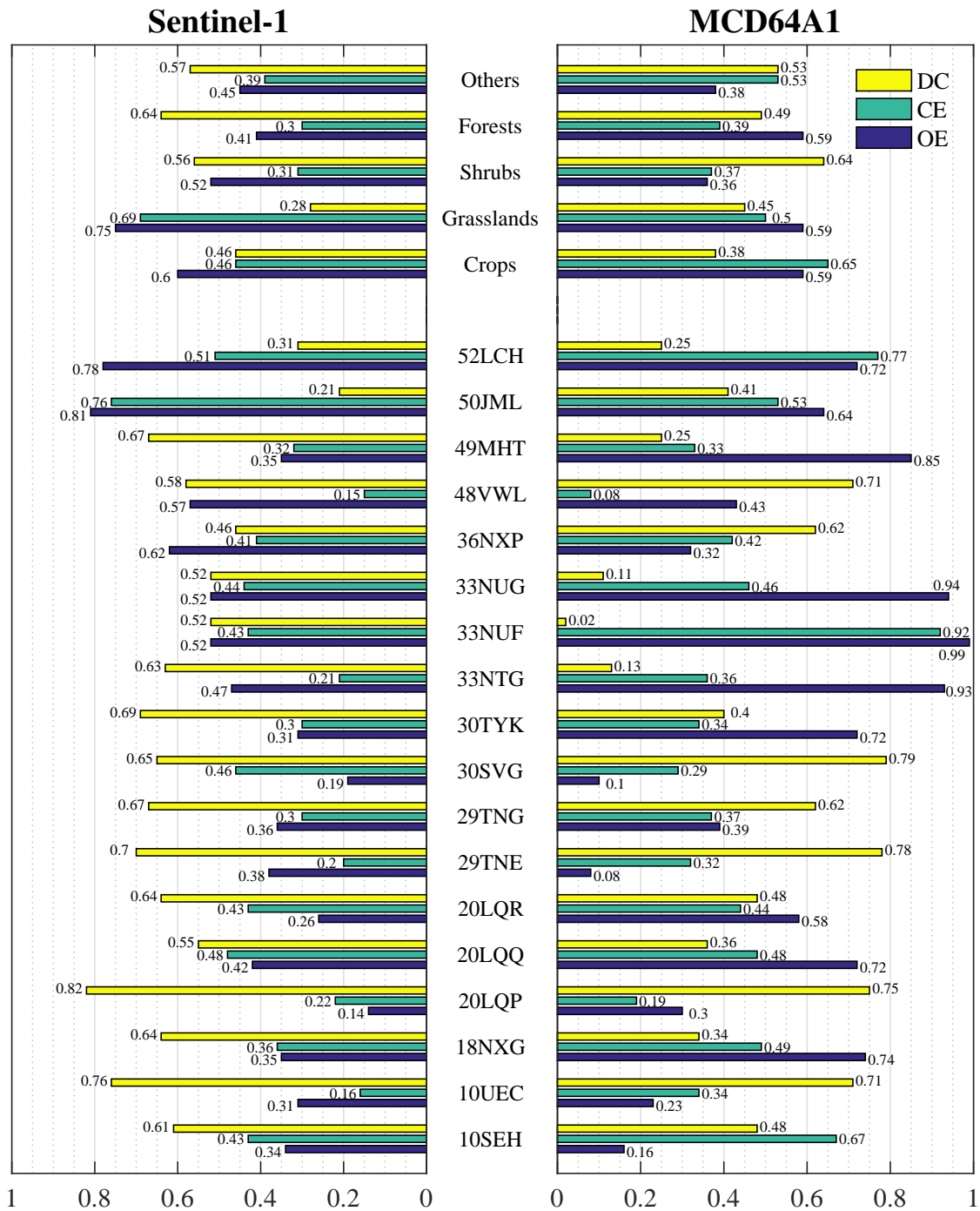
Figure 2.6: Assessment metrics of Sentinel-1 and MCD64A1 Version 6 burned area detections per MGRS tiles and land cover classes. The metrics by land cover were computed using confusion matrices formed by pixels of the same land cover class from all tiles. DC - Dice coefficient, OE - omission error and CE - commission error.

The accuracy metrics were analysed by tile as well as by land cover classes. The tile-based analysis showed particularly poor results for the MCD64A1 product over the tiles 18NXG, 20LQQ, 20LQR, 30TYK, 33NTG, 33NUF and 33NUG (Figure 2.6). For the remaining tiles, the accuracy of the two BA detection algorithms was closely matched, with some tiles being more accurately estimated by the Sentinel-1 algorithm while others by the MCD64A1. By land cover class, the MCD64A1 achieved higher accuracies over grasslands while the Sentinel-1 detections were considerably more accurate over forests. For the remaining land cover classes, both products showed similar accuracies over burned areas. Overall, the BA was more accurately detected using the SAR based algorithm. On average Sentinel-1 detections improved the DC of the MCD64A1 product from 0.46 ± 0.11 to 0.59 ± 0.06 ($\pm$ confidence interval, 95%) and reduced the OE from 0.55 ± 0.14 to 0.43 ± 0.08 and CE from 0.43 ± 0.08 to 0.37 ± 0.06 (Figure 2.7).
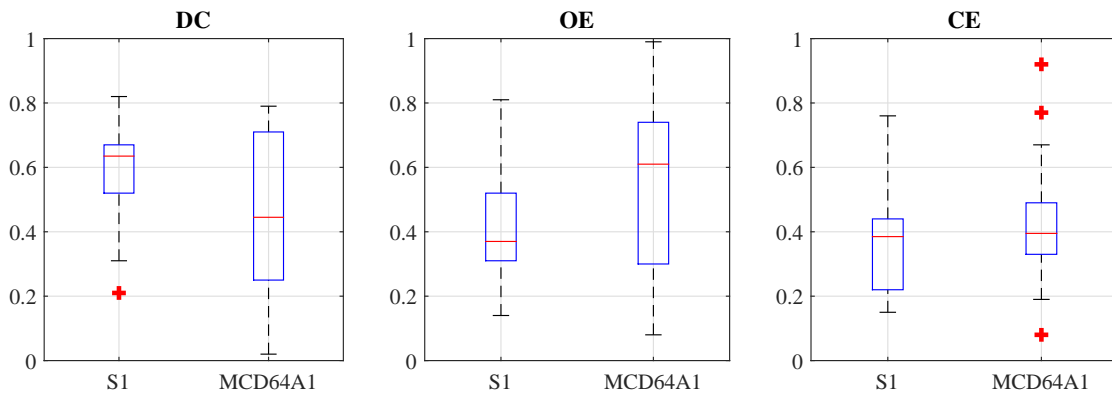

Figure 2.7: Dispersion of Dice coefficient (DC), omission and commission errors (OE and CE) of burned area detected for all tiles for Sentinel-1 (S1) and MCD64A1 Version 6. The red line indicates median value, and top and bottom box edges indicate the 75th and 25th percentiles, respectively, while red dots indicate outliers.

2.4.3 Factors influencing the algorithm accuracy

The MAC values (Equation 2.4), and the temporal variation (pre- minus post-fire date) of backscatter coefficient and soil moisture were analysed by land cover class for each Sentinel-1 temporal pair after the BA classification. Four categories were studied: burned, unburned, commission and omission errors. Data from all tiles were pooled (Figure 2.8). The analysis confirmed that, over burned and commission error pixels, VH backscatter mean variation was higher (1.72 ± 0.002 dB) when compared to the VV polarisation (0.34 ± 0.0023 dB) for all land cover classes. As expected, MAC values were on average considerably higher over burned pixels and commission errors (13.5 ± 0.15) when compared to unburned and omission errors pixels (0.17 ± 0.03), following the trends observed for VH backscatter coefficient mean variation. Soil moisture variations from the SMAP product were very similar between burned and unburned pixels with no particular trend being apparent. For crops and shrubs soil moisture variations were slightly higher over burned areas while for the other land cover classes, the opposite was true (Figure 2.8).

Since the algorithm uses hotspots derived from thermal sensors to map BA, the accuracies metrics (by land cover class) of the pixels located within and outside the IAhs
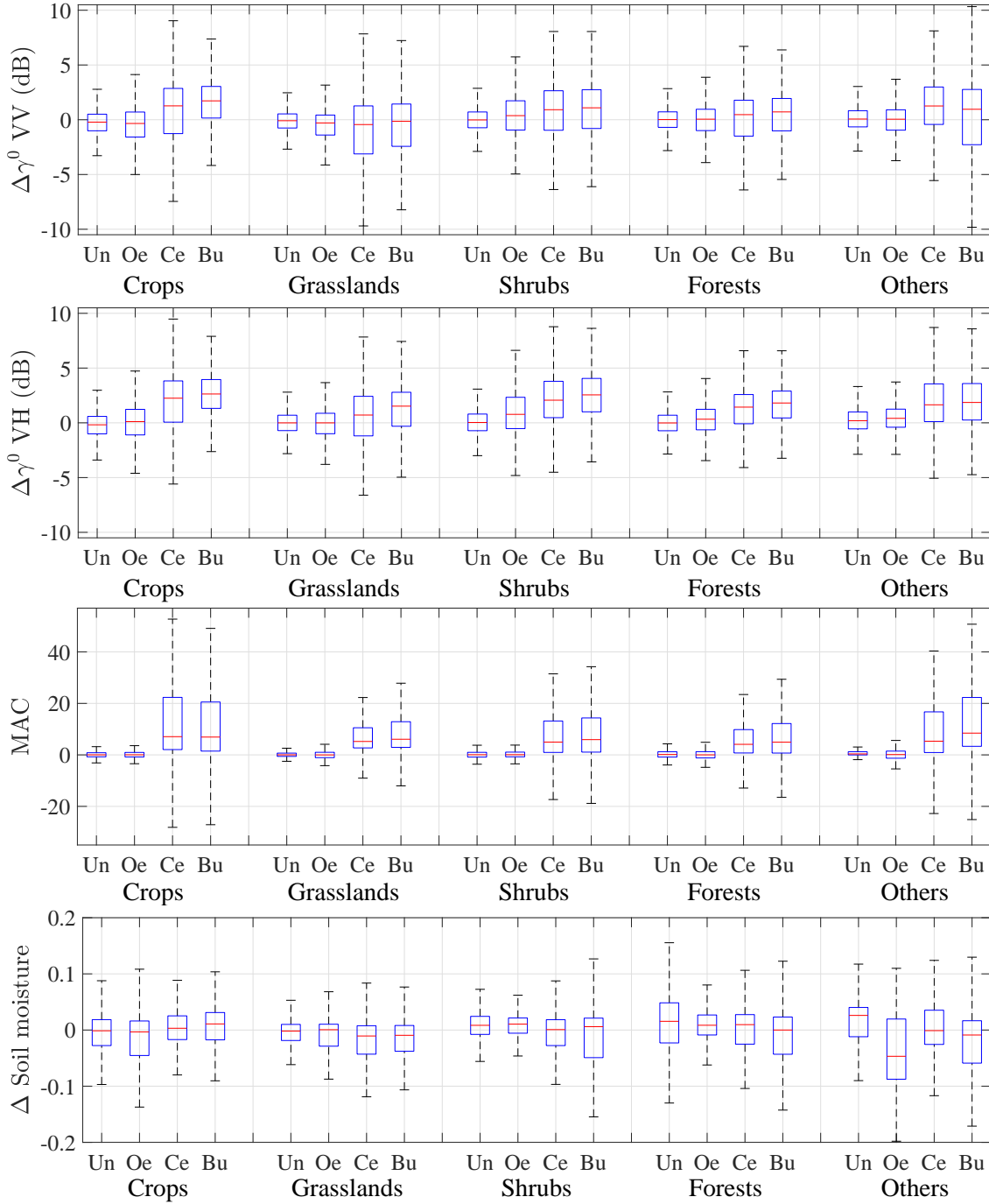
Figure 2.8: Temporal variations ($\Delta = data_{pre} - data_{post}$) of the backscatter coefficient (dB) and soil moisture (from SMAP) between pre- and post-dates for BA detection periods. MAC values from RXD are also presented. Values are displayed by land cover classes for four categories of pixels: unburned (Un), burned (Bu) and commission (Ce) and omission errors (Oe). Red line indicates median value. Top and bottom box edges indicate the 75th and respectively the 25th percentiles. Outliers not shown to improved graphs discernibility.

were also compared (Table 2.3). The highest BA accuracy (DC) and lowest omission and commission errors were observed for the pixels located within the IAhs over all land cover classes as expected. Likewise, VH and VV pre- to post-fire backscatter coefficient temporal differences were also compared for both cases. Similar trends, as observed in Figure 2.8, where burned and commission error pixels had a significant higher variation when compared to unburned and omission errors pixels were found over both polarisations independently of the location with respect to the IAhs.

Table 2.3: Assessment metrics for Sentinel-1 BA detections and pre- to post-fire backscatter variations assessed as a function of proximity with respect to the hotspots influence area (IAhs).

		Crops	**Grasslands**	**Shrubs**	**Forests**	**Others**
Inside IAhs	DC	0.55	0.34	0.63	0.71	0.61
	CE	0.38	0.64	0.27	0.27	0.36
	OE	0.5	0.68	0.45	0.32	0.43
	Δ VH (bp)	2.52±0.02	1.06±0.01	2.24±0.005	1.48±0.003	2.33±0.03
	Δ VH (cp)	1.27±0.03	0.64±0.01	1.54±0.01	0.91±0.01	1.26±0.03
	Δ VH (op)	0.15±0.01	-0.33±0.01	0.98±0.003	0.31±0.002	0.43±0.01
	Δ VV (bp)	1.42±0.02	-0.73±0.02	0.66±0.01	0.26±0.003	0.84±0.04
	Δ VV (cp)	0.03±0.03	-0.91±0.01	0.21±0.01	-0.13±0.01	0.42±0.04
	Δ VV (op)	-0.29±0.01	-0.78±0.01	0.61±0.004	0.06±0.002	-0.1±0.01
Outside IAhs	DC	0.11	0.17	0.39	0.27	0.45
	CE	0.84	0.79	0.44	0.56	0.54
	OE	0.92	0.86	0.7	0.81	0.57
	Δ VH (bp)	2.6±0.09	1.2±0.03	3.63±0.01	2.25±0.01	0.9±0.05
	Δ VH (cp)	3.31±0.04	0.33±0.02	3.39±0.01	2.18±0.02	3.33±0.08
	Δ VH (op)	-0.01±0.02	0.08±0.01	0.81±0.01	0.22±0.004	0.52±0.02
	Δ VV (bp)	0.46±0.11	-0.53±0.03	1.73±0.01	0.27±0.02	-1.44±0.07
	Δ VV (cp)	2±0.05	-1.34±0.02	2.03±0.01	1.21±0.02	2.78±0.09
	Δ VV (op)	-0.73±0.02	-0.55±0.01	0.12±0.01	-0.39±0.01	-0.03±0.02

Δ - pre- to post-fire temporal differences of VV and VH backscatter data by pixels classes of: burned (bp) and commission (cp) and omission (oe) errors.

For six of the validation sites, images from ascending and descending Sentinel-1 passes were available. Therefore, a more detailed analysis was carried out to understand the difference in BA accuracy between ascending and descending passes (Figure 2.9). Overall, BA omission errors were minimum when both passes were used while BA commission errors increased. However, DC values showed that BA detection generally improved when data from both passes were available.

The effect of topography and the environmental conditions (soil moisture) were analysed for each acquisition pass over the six tiles. The LIA was often used to analyse the effect of topography on the backscatter coefficient in areas affected by fires (Tanase et al., 2009, 2010a; Kalogirou et al., 2014; Gimeno & San-Miguel-Ayanz, 2004; Kurum, 2015). However, the wide swath of the Sentinel-1 IW mode results in a variation of the incidence angle of about 17° from near (29°) to far (46°) range. Since LIA is a function of incidence angle and local slope (U), DC scores were analysed (by satellite pass) as a function of both
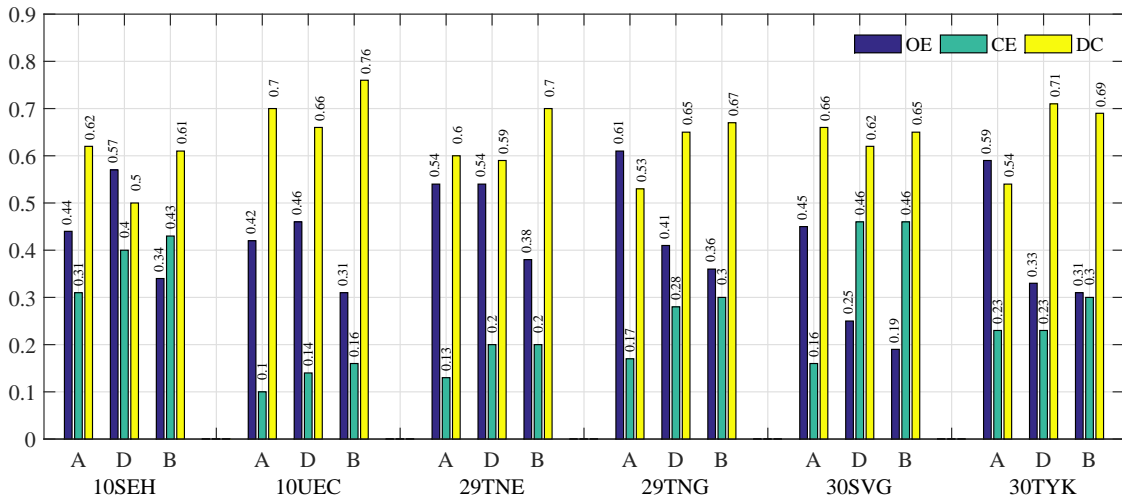
Figure 2.9: Assessment metrics of Sentinel-1 burned area detections per ascending (A), descending (D) and both satellite passes (B). DC - Dice coefficient, OE - omission error and CE - commission error.

angles after grouping in five degrees classes (Tanase et al., 2010a). Similar trends were observed for both passes (Figure 2.10) with better accuracies being observed for low LIAs and Us groups ($<40°$).

Nevertheless, analysing BA accuracy by LIA and U angles has limitations as LIA groups may include areas of different slopes while U groups may include slopes oriented towards and away from the sensor with completely different scattering properties. Therefore, the sloped areas ($U \geq 5°$) were further analysed by their orientation (V) with respect to the satellite viewing geometry (Figure 2.10). Notice that positive V values are observed for slopes oriented towards the sensor while negative values are observed for slopes oriented away from the sensor. The BA accuracy improved over pixels oriented toward the sensor with omission error being lower for such pixels while commission errors slightly higher. Notice that a paired t-test showed no significant difference (p-value > 0.05) between the percentage of pixels (by ten degrees V groups) from ascending and descending satellite passes.

Since Sentinel-1 ascending and descending images were acquired at different dates, variations in soil moisture (from the global SMAP product) between the pre- and post-dates delineating the CDPs were analysed to ascertain the influence of this important environmental parameter on BA detection errors. Over five of the six tiles, the difference in soil moisture between ascending and descending passes were reduced. However, for tile 30SVG soil moisture increased considerably over some areas for descending pass acquisitions which translated in much larger commission errors (0.46) when compared to those observed for the ascending pass (0.16), where soil moisture was stable (Figure 2.11). The increased commission errors were the result of a large and compact area located south of the fire perimeter that was misclassified as burned (Figure 2.12). The temporal variations of the backscatter coefficient between ascending and descending passes (tile 30SVG) were correlated with the accuracy metrics. An important variation of the backscatter coefficient during the descending pass was observed over the misclassified burned area (CE) for both VV (2.8±0.029) and VH (1.0±0.027) polarisations (Figure 2.12).
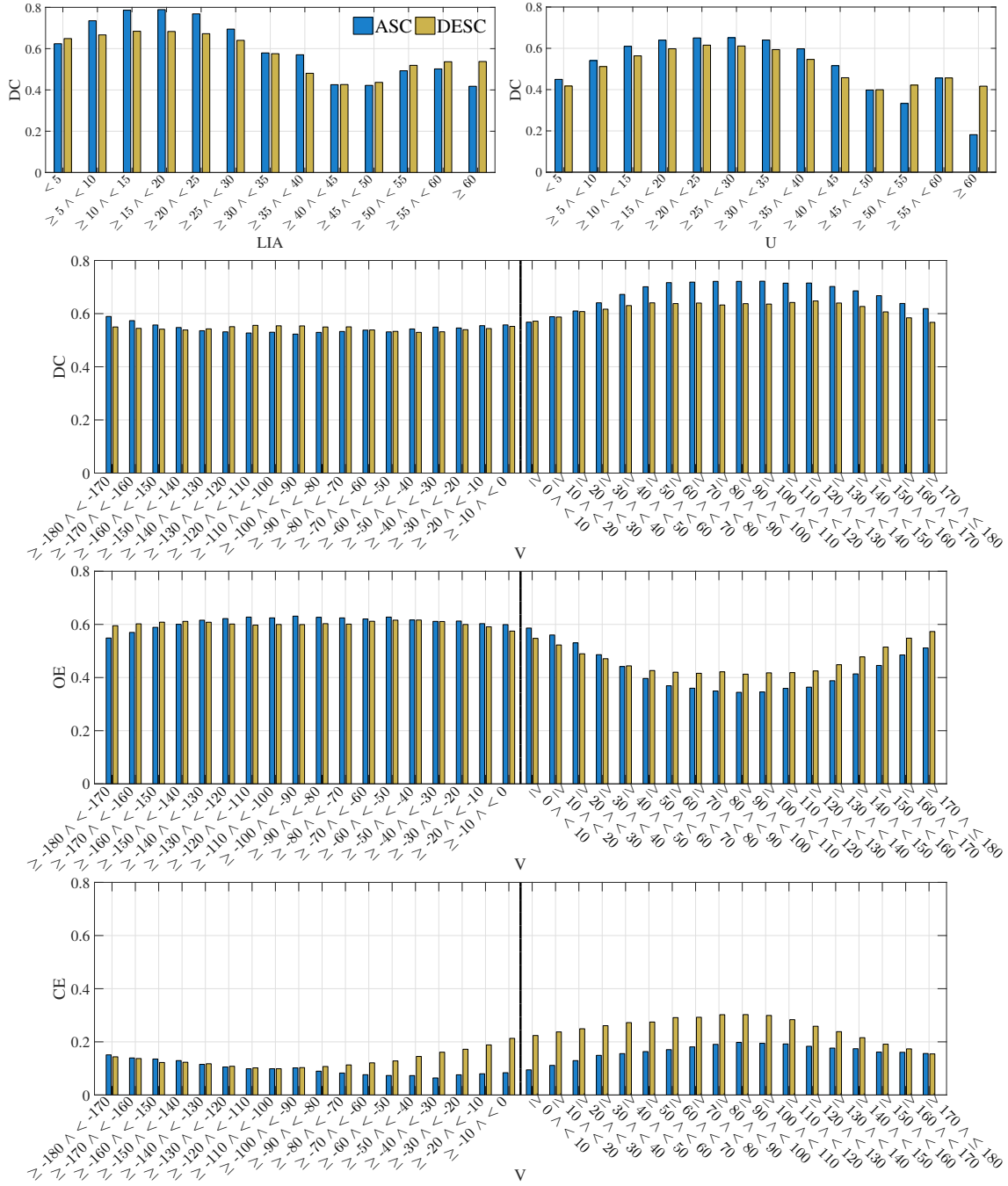
Figure 2.10: Dice coefficient (DC) by local incidence angle (LIA) and local slope (U) groups. For sloped areas (U≥5°) the DC, commission (CE) and omission errors (OE) are shown as a function of slope orientation (V) with respect to the Sentinel-1 viewing geometry. Negative V values show slopes oriented away from the sensor while positive V values show slopes oriented toward the sensor. The BA metrics are shown for six tiles where both ascending (ASC) and descending (DESC) passes were available (i.e., 10SEH, 10UEC, 29TNE, 29TNG, 30SVG and 30TYK).
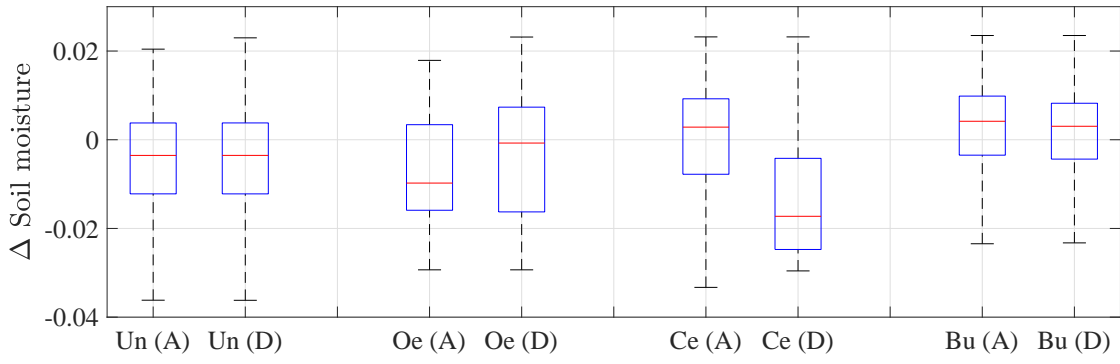
Figure 2.11: Temporal variations of soil moisture (SM) from Soil Moisture Active Passive (SMAP) mission for pre- and post-fire dates ($\Delta_{SM} = SM_{pre} - SM_{post}$), in tile 30SVG. Ascending (A) and descending (D) passes are analyzed separately. Pixels are grouped by classes of unburned (Un) and burned (Bu). Pixels from areas affected by commission (Ce) and omission errors (Oe) are also shown. The red line indicates median value, and top and bottom box edges indicate the 75th and respectively the 25th percentiles. Outliers are not shown to improve graph discernibility.
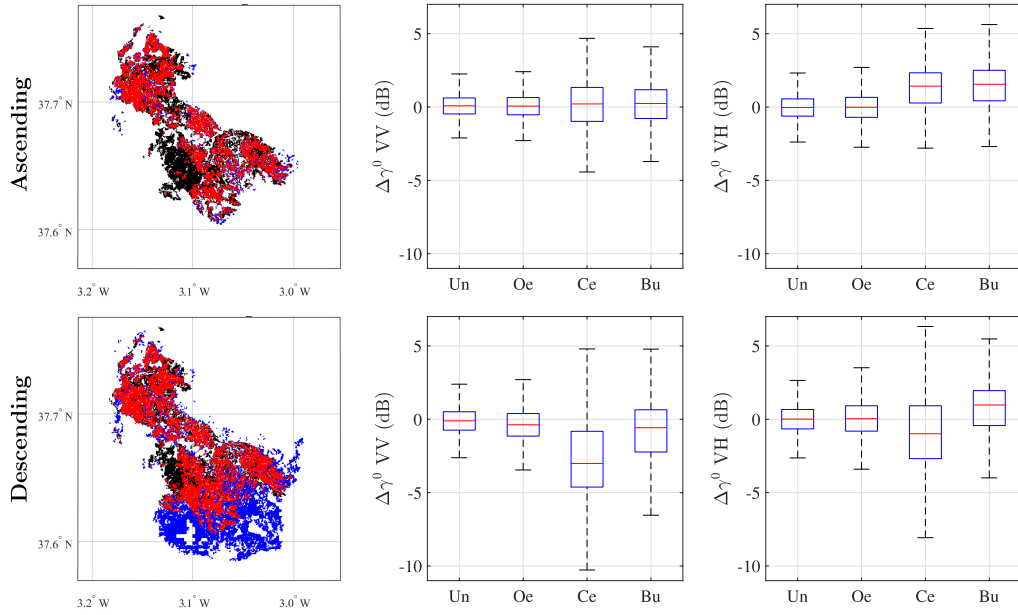
Figure 2.12: Burned area from ascending (top row) and descending (bottom row) passes in tile 30SVG: red - burned (Bu), white - unburned (Un), black - omission errors (Oe) and blue - commission errors (Ce). VV and VH backscatter coefficient variations ($\Delta\gamma^0 = pre_{fire} - post_{fire}$) is also shown for each pass.

2.5   Discussion

2.5.1   Algorithm development

The Reed-Xiaoli anomaly detector (Reed & Yu, 1990), not widely used with SAR images except for levee slide detection (Dabbiru et al., 2012, 2016, 2018), seemed to work coherently when detecting burned areas as errors of omission appeared when low backscatter

changes were observed over burned areas while the commission error appeared due to fire unrelated backscatter variations over unburned areas. These trends were reflected by the MAC values for OE and CE classes which were close to those observed for unburned and respectively burned areas suggesting a correct estimation of the covariance matrices by taking advantage of the *a priori* information from stable areas (i.e., likely unburned pixels). Comparing backscatter variability over burned and unburned classes, one may notice notably smaller MAC values over the later, which also suggests a properly functioning of the anomaly detector according to the input data. To test the correct delineation of stable areas (i.e., background), a t-test was used to analyse the statistical difference between the inverted covariance matrices (used by RXD) obtained using hotspots and those obtained using the BA validation perimeters from optical data (section 3.4). The analysis showed no statistical difference (p-values > 0.05) between the two methods demonstrating that hotspots may be reliably used to identify likely burned and unburned pixels as a preliminary source of burned area.

The use of ancillary information from thermal anomalies (hotspots) allowed for attributing anomalous changes of SAR backscatter data as BA though a locally derived knowledge extraction. Hence, burned pixels were extracted without the need for relying on fixed thresholds on the SAR signal, which may depend not only on the land cover type but also on backscatter variations due to spatially variable influencing factors (e.g., soil and vegetation moisture) that are difficult to model. Temporal decorrelation between hotspots (i.e., fire date) and the date at which radar backscatter changes were detected (Belenguer-Plomer et al., 2018b) was observed over most tiles. One should notice that temporal decorrelation is not specific to burned area nor the C-band frequency as similar effects were observed for L-band HV polarisation over areas affected by deforestation (Watanabe et al., 2018). Therefore, temporal studies using SAR-based change detection techniques must devise methods to reduce or account for such effects (see the proposed approach in the Stage 3).

The use of a non-parametric classifier was essential to cope with the temporal lack of hotspots due to persistent cloud cover or small fire size (i.e., not detected by thermal sensors). Parametrising random forests classifier (RF) for BA classification may prove complex as almost an infinite combinations of parameter settings are possible. Ramo & Chuvieco (2017) proposed using 600 trees and a stratified training, where 10% of training data were burned pixels and the rest not burned, for the classification of MODIS images in burned and unburned classes. Such a setting was tested during algorithm development, but the results were not as accurate as expected. Therefore, the RF set-up was customised based on empirical observations. The substantial differences in RF parametrisation settings were mainly caused by the algorithm design since it is building specific RF models for each land cover type and detection period. Hence, it does not have to cope with widely varying land cover and burn conditions as the work of Ramo & Chuvieco (2017), which used one uniquely trained model worldwide.

2.5.2   Comparison with global products

Over most validation areas, the accuracy of the proposed algorithm was higher when compared to the MCD64A1 Version 6 product (Giglio et al., 2018). The mean DC value over all studied locations was 0.13 higher for the Sentinel-1 BA detections (i.e., 28% higher).

The DC values of Sentinel-1 detections per tiles were statistically higher than those of MCD64A1 (paired t-test p-value of 0.024). In addition, the variability of Sentinel-1 BA detection accuracy was considerably lower when compared to the MCD64A1 product. The mean values for OE and CE over all tiles were also lower for the Sentinel-1 detections.

The analysis showed that for 13 tiles (72% of the studied areas), the Sentinel-1 BA detections had higher DC scores than the MCD64A1 product. For one tile, 33NUF, the difference in accuracy (DC) of the two products is 0.5. The very low accuracy (DC 0.02) observed over this tile for the MCD64A1 product is difficult to explain with the data at hand; hence the tile was considered an outlier. For five tiles (i.e., 18NXG, 30TYK, 33NTG, 33NUG, and 49MHT) the improvement of the Sentinel-1 product was substantial with DC increasing on average by 144% when compared to the MCD64A1 product. The large difference in DC scores was mainly caused by the high OE (0.72 to 0.94) in the MCD64A1 product. Detection of small burned areas (< 120 ha) is problematic using MODIS data due to the coarse sensor resolution (Giglio et al., 2009). To evaluate if reduced spatial resolution of MODIS was the reason behind MCD64A1 product poor performance, the percentage of BA from fire scars below 120 ha was computed based on the reference datasets. In tiles 33NUG, 33NTG, and 49MHT fires below 120 ha constituted 85%, 53% and respectively 48% of the total BA suggesting that the lower performance may be related to the coarser MODIS spatial resolution. Therefore, these results suggest that improvements in BA detection accuracy may be possible not only in areas with frequent cloud cover. However, for tiles 18NXG and 30TYK small fires (< 120 ha) constituted only 34% and respectively 25% of the total BA indicating that fire size may not be the only factor influencing detection accuracy when using coarse-resolution sensors.

For five tiles (i.e., 29TNE, 30SVG, 36NXP, 48VWL and 50JML) the MCD64A1 product showed higher DC scores when compared to the Sentinel-1 based detections. The mean difference between the four first tiles was only 0.13. However, for tile 50JML, this difference was higher, with the MCD64A1 product being markedly more accurate (DC 0.41 vs 0.21). It seems such large differences were related to the conditions encountered over the Australian grasslands, where backscatter variations recorded from pre- to post-fire periods were low, hindering the detection algorithm. By land cover class, the results indicate that a radar-based BA mapping algorithm may provide BA products with better or similar accuracies when compared to available global products, except for grasslands. The most significant difference in accuracy was observed over grasslands, where the MCD64A1 was more accurate than the Sentinel-1 based BA (DC 0.45 vs 0.28). Conversely, over forests, Sentinel-1 derived BA was more accurate (DC 0.64 vs 0.49).

2.5.3 Factors influencing BA accuracy

Temporal variation of pre- and post-fire VH and VV backscatter coefficient over pixels affected by CE and OE were similar to those observed over burned and respectively unburned pixels. Following, the main factors affecting burned area classification were discussed.

2.5.3.1 Environmental conditions

CE may only be related to factors that modify the scattering proprieties in a similar manner to fires (e.g., soil moisture variations) when backscatter changes are concentrated in

a reduced part of the image (anomalous changes), since the RXD may identify such variations as spatial anomalies and consequently the algorithm may misclassify them as BA. For instance, unrelated fire backscatter variations which did not affect the entire image occurred over tile 30SVG, where the highest difference between commission errors for ascending (0.16) and descending (0.46) passes was observed. For this tile, soil moisture variations over CE pixels varied notably between ascending and descending passes. For the descending pass, post-fire soil moisture was on average 0.014 ± 1.18e-04 m^3/m^3 higher when compared to pre-fire soil moisture, while for the ascending pass the increment was marginal (6.2e-04 m^3/m^3). Consequently, over pixels affected by CE, an average increase of 2.8 ± 0.029 dB for VV polarisation and 1.0 ± 0.027 dB for the VH polarisation was recorded from pre- to post-fire date for the descending acquisitions. The differentiated increase by polarisation confirmed the larger influence of the soil surface properties on the VV polarisation when compared to the VH polarisation as noted previously by other authors (Freeman & Durden, 1998; Yamaguchi et al., 2005; Van Zyl et al., 2011). The backscatter coefficient change generated by variations in soil moisture was incorrectly mapped as burned since (i) the algorithm does not account for the sign of the backscatter change, and (ii) the image part affected by rainfall was located close to hotspots (areas bordering the fire perimeter). This suggests that algorithm improvements may further mitigate commission errors related to soil moisture variations by considering the backscatter change direction. Notice that, tile 30SVG was an exception as, at this location, a major part (67.6%) of the CE were concentrated in a large enough area (3420 ha) to extract useful information from the coarse pixel spacing SMAP product. The influence of soil moisture on BA accuracy was inconclusive for the rest of the tiles, most probably due to the coarse pixel spacing of the SMAP product (9 km). The use of higher spatial resolution soil moisture products such as the Copernicus Surface Soil Moisture (SSM), a Sentinel-1 based product with 1 km of pixel spacing (Bauer-Marschallinger et al., 2018), shall be investigated once they become available at global level. Further, as global products of harvest, defoliation, floods or logging at enough detailed pixel spacing, when compared to Sentinel-1 spatial resolution, are not available and precipitation products based on extrapolation of data from rain gauges have a much coarser pixel spacing (0.5°) and own errors (Hu et al., 2018), it was not possible to identify all the commission errors sources and filter them out.

2.5.3.2 Fire impact

Conversely, pixels affected by OE may have been the result of the effects of different variables which attenuated the vegetation combustion effects on the C-band backscatter coefficient. Fire severity, the degree of organic matter loss due to fire combustion (Keeley, 2009), constrains the temporal backscatter variation between pre- and post-fire (Tanase et al., 2010b, 2014). The dNBR mean values over the pixels affected by omission errors (0.068 ± 6.65e-05) was 22.73% lower when compared to the dNBR values observed for correctly detected burned pixels (0.088 ± 7.5e-05). Notice that the dNBR index is widely used to detect BA and estimate fire severity over a range of biomes (Escuin et al., 2008; Loboda et al., 2007; Van Wagtendonk et al., 2004; Tanase et al., 2011) and that high fire severity implies a more significant reduction of vegetated scattering elements due to combustion.

2.5.3.3 Topography

Topography also affected the BA accuracy, with a tendency of increased burned areas omission being observed for the pixels oriented away from the sensor most likely due to the existence of shadowed regions (Tanase et al., 2010a, 2009). Conversely, for the pixels oriented towards the sensor, the commission errors increased since soil proprieties had a higher influence on radar scattering. Since the OE due to topographic effects were higher when compared to the CE, BA accuracy was improved by joining detections from different relative orbits when available (see subsubsection 2.5.3.5).

2.5.3.4 Land cover type

The variables mentioned above affect the scattering processes over burned and unburned areas differently depending on the land cover class observed and translated into variable map accuracies. Lower BA accuracies were found over grasslands as the scattering elements characteristic for this vegetation type interact to a lesser extent with the C-band waves when compared to the scattering elements encountered in shrubs and forests (stems, branches). However, the most important factor affecting the algorithm sensitivity to fire in grasslands seemed to be related to fire timing. In areas characterised by long intervals (months) between grass curing and fire events the algorithm encountered difficulties as the cured (i.e., dry) grass has low scattering properties being mostly transparent to the radar waves (Menges et al., 2004). Therefore, grass consumption by fire results in small or nil VV and VH backscatter changes from vegetation consumption which hinders BA detection. This observation seemed supported by the lower temporal variation of the backscatter coefficient over burned when compared unburned grasslands. Conversely, forest and shrubs, besides containing scattering elements more susceptible to interact to C-band radar waves, are not affected by curing to the same extent (i.e., some water needs to be retained to ensure plant survival). Thus, vegetation consumption by fire results in a noticeable scattering decrease which is detected by the algorithm, although sometimes a temporal gap between fire and detection was observed (temporal decorrelation) as discussed in Belenguer-Plomer et al. (2018b).

2.5.3.5 Ancillary information and SAR data availability

The use of hotspots was essential, given that only two backscatter channels were available (VV and VH polarisations). Without hotspots, differentiation of burned areas from other land changes (e.g., floods, logging, harvest, vegetation disturbance due to pests, drought) that modulate the backscatter coefficient in a similar fashion was difficult as also noted by Huang & Siegert (2006). Lower BA detection accuracies were found in pixels located far (outside IAhs) when compared to pixels located in close proximity (within 750 m) of hotpots events. According to the reference data, only a 15.3% of burned pixels were not located within IAhs, allowing for BA detection rates comparable or better than those of currently available global products.

Joining detections from different relative orbits (from ascending and descending passes) increased the detected burned area. Inherently, the availability of several orbits covering the same area resulted in reduced OE, which is particularly true when different viewing geometries were used over areas with steep topography. Conversely, the CE

increased as wrongly detected areas are also joined in post-processing (Stage 5 of the algorithm). Despite the increased CEs, the use of both Sentinel-1 passes generally improved the BA accuracy. It should be noted that consistent dual pass (ascending and descending) acquisitions are currently available only over Europe and North America. The analysis suggested that differences in BA accuracy between ascending and descending passes were mainly caused by the interaction between the viewing geometry and the local topography as explained in subsection 2.4.3, with the highest accuracies being achieved over areas oriented towards the sensor. Using images acquired in a single pass may result in increased omission errors, particularly in regions with accentuated topography. These results confirm previous findings that highlight the effect of topography on burned area detection and fire impact estimation (Gimeno & San-Miguel-Ayanz, 2004; Huang & Siegert, 2006; Tanase et al., 2010b). Further investigations of topographic effects reduction are needed as, under the current observation scenario, for most of the Earth surface Sentinel-1 data are consistently acquired in only one pass (i.e., ascending or descending).

The accuracy of the Sentinel-1 product was also assessed as a function of the number of SAR images available during the detection period as well as the number of days between consecutive acquisitions. The BA was detected regardless of the image number or their temporal distance, thus coping with the variable acquisition strategy (temporal frequency) of the Sentinel-1 mission over different regions. The main temporal factor which limited the algorithm accuracy was the post-fire vegetation regrowth cycle. Where image acquisitions were more frequent, when compared to vegetation regrowth cycles, the algorithm detected the changes in backscatter coefficient generated by fires and labelled them as BA. However, the relationship between BA detection accuracy (DC) and the number of images used and their acquisition frequency (day difference of consecutive images) per tiles was weak (0.32 and respectively 0.38 Pearson's correlation coefficient) since additional factors affected the algorithm accuracy (i.e., topography and fire unrelated changes). Thus, it was concluded that current Sentinel-1 temporal frequencies might be sufficient for global retrieval. Nevertheless, the relatively small number of test samples may have obscured some effects. In addition, the relationship between Sentinel-1 acquisition frequency and the detection accuracy may vary with the land cover type (different post-fire regrowth cycle).

2.5.4   Comparison with previous Sentinel-1 based approaches

Previous studies based on Sentinel-1 data for BA detection were carried out only at local to regional scales. However, C-band backscatter from fire-affected areas varies with the local conditions. Therefore, locally trained algorithms are difficult to transfer to other regions. Engelbrecht et al. (2017) used empirical thresholds to detect BA in South Africa, achieving OE and CE of 0.29 and 0.48, respectively. Depending on the area, the proposed algorithm may achieve similar or better accuracies. Lohberger et al. (2018) used an object-based image analysis approach to detect BA in Indonesia. However, since only information on the overall accuracy was provided, comparisons were difficult. Finally, Verhegghen et al. (2016) tested the most suitable thresholds when separating burned from unburned pixels in the Congo Basin, but did not provide accuracy metrics of their detected BA. Nevertheless, since such studies relied on algorithms heavily optimised over local to regional scales, comparisons with the proposed algorithm are of little relevance.

2.6   Conclusions

This chapter introduced an automated and cloud cover insensitive algorithm for BA detection using Sentinel-1 dual-polarised backscatter images. Hotspots from active fires and land cover data were used as ancillary information when attributing anomalous backscatter changes to burned and unburned classes. The algorithm was validated at 18 locations (100×100 km tiles) covering over 21 million hectares worldwide. Algorithm accuracy was assessed using reference burn perimeters derived from optical sensors (Landsat-8 and Sentinel-2). The agreement between the Sentinel-1 algorithm and the reference perimeters was compared with that of the most widely used global BA product, the MCD64A1 Version 6. Over all tiles, the mean OE and CE for BA were 0.43 and 0.37, respectively. The mean DC was 0.59. When compared with the MCD64A1, the proposed algorithm improved burned area detection (DC) by 28% (from 0.46 to 0.59) over the analysed tiles. Such improvements in accuracy were mainly related to reduced OE, a useful trait demonstrating that Sentinel-1 data may be a key source of information when optical data-based products have information gaps due to persistent cloud cover.

According to our analysis, strong topography conditioned the BA accuracy with slopes oriented away from the sensor being subject to higher errors. Such effects were reduced by combining detections from different relative orbits. Likewise, it was observed that reduced fire severity translated into increased omission errors. On the other hand, commission errors seemed to correlate with fire unrelated changes affecting the scattering processes. Furthermore, scattering from burned areas was directly influenced by vegetation type with higher accuracies being observed over forested areas (DC 0.64) and lower over grasslands (DC 0.28) which were attributed to the difficulty in tracking changes of cured vegetation using the C-band data. The main advantages of the proposed algorithm were related to: (i) self-adapting to local scattering conditions without the need for *a priori* information of the observed area or the use of fixed thresholds; and (ii) ability to detect BA during periods with no thermal anomalies. On the other hand, the main limitations were related to: (i) misclassification of fire unrelated changes; (ii) positive relationship between accuracy and hotspots availability; and (iii) accuracy dependence on variables affecting radar scattering processes (e.g., ecosystem type, topography). To reduce such limitations, further improvements shall be investigated.

Acknowledgements

2.7   References

Alonso-Canas, I., & Chuvieco, E. (2015).   Global burned area mapping from ENVISAT-MERIS and MODIS active fire data. *Remote Sensing of Environment*, *163*, 140–152.

Andela, N., Morton, D., Giglio, L., Chen, Y., Van Der Werf, G., Kasibhatla, P., De-Fries, R., Collatz, G., Hantson, S., Kloster, S. et al. (2017). A human-driven decline in global burned area. *Science*, *356*, 1356–1362.

Andreae, M. O., & Merlet, P. (2001).   Emission of trace gases and aerosols from biomass burning. *Global Biogeochemical Cycles*, *15*, 955–966.

Antikidis, E., Arino, O., Arnaud, A., & Laur, H. (1998). ERS SAR Coherence & ATSR Hot Spots: a Synergy for Mapping Deforested Areas. The Special Case of the 1997 Fire Event in Indonesia. *European Space Agency-Publications-ESA SP*, *441*, 355–360.

Aponte, C., de Groot, W. J., & Wotton, B. M. (2016). Forest fires and climate change: causes, consequences and management options. *International Journal of Wildland Fire*, *25*, i–ii.

Banerjee, A., Burlina, P., & Diehl, C. (2006). A support vector method for anomaly detection in hyperspectral imagery. *IEEE Transactions on Geoscience and Remote Sensing*, *44*, 2282–2291.

Bastarrika, A., Chuvieco, E., & Martín, M. P. (2011). Mapping burned areas from Landsat TM/ETM+ data with a two-phase algorithm: Balancing omission and commission errors. *Remote Sensing of Environment*, *115*, 1003–1012.

Bauer-Marschallinger, B., Freeman, V., Cao, S., Paulik, C., Schaufler, S., Stachl, T., Modanesi, S., Massari, C., Ciabatta, L., Brocca, L. et al. (2018).   Toward global soil moisture monitoring with Sentinel-1: Harnessing assets and overcoming obstacles. *IEEE Transactions on Geoscience and Remote Sensing*, *57*, 520–539.

Belenguer-Plomer, M. A., Tanase, M. A., Fernandez-Carrillo, A., & Chuvieco, E. (2018a). Insights into burned areas detection from Sentinel-1 data and locally adaptive algorithms. In *Active and Passive Microwave Remote Sensing for Environmental Monitoring II* (p. 107880G). International Society for Optics and Photonics volume 10788.

Belenguer-Plomer, M. A., Tanase, M. A., Fernandez-Carrillo, A., & Chuvieco, E. (2018b). Temporal backscattering coefficient decorrelation in burned areas. In *Active and Passive Microwave Remote Sensing for Environmental Monitoring II* (p. 107880T). International Society for Optics and Photonics volume 10788.

Belgiu, M., & Drăguţ, L. (2016). Random forest in remote sensing: A review of applications and future directions. *ISPRS Journal of Photogrammetry and Remote Sensing*, *114*, 24–31.

Bojinski, S., Verstraete, M., Peterson, T. C., Richter, C., Simmons, A., & Zemp, M. (2014). The concept of essential climate variables in support of climate research, applications, and policy. *Bulletin of the American Meteorological Society*, *95*, 1431–1443.

Bond, W. J., Woodward, F. I., & Midgley, G. F. (2005). The global distribution of ecosystems in a world without fire. *New Phytologist*, *165*, 525–538.

Boschetti, L., Flasse, S. P., & Brivio, P. A. (2004). Analysis of the conflict between omission and commission in low spatial resolution dichotomic thematic products: The Pareto Boundary. *Remote Sensing of Environment*, *91*, 280–292.

Boschetti, L., Roy, D. P., Justice, C. O., & Giglio, L. (2010). Global assessment of the temporal reporting accuracy and precision of the MODIS burned area product. *International Journal of Wildland Fire*, *19*, 705–709.

Bourgeau-Chavez, L., Harrell, P., Kasischke, E., & French, N. (1997). The detection and mapping of Alaskan wildfires using a spaceborne imaging radar system. *International Journal of Remote Sensing*, *18*, 355–373.

Bourgeau-Chavez, L., Kasischke, E., Brunzell, S., Mudd, J., & Tukman, M. (2002). Mapping fire scars in global boreal forests using imaging radar data. *International Journal of Remote Sensing*, *23*, 4211–4234.

Bowman, D. M., Balch, J. K., Artaxo, P., Bond, W. J., Carlson, J. M., Cochrane, M. A., D'Antonio, C. M., DeFries, R. S., Doyle, J. C., Harrison, S. P. et al. (2009). Fire in the Earth system. *Science*, *324*, 481–484.

Bradley, A. V., Tansey, K., & Chuvieco, E. (2012). The ESA climate change initiative: Merging burned area estimates for the Fire Essential Climate Variable. In *Geoscience and Remote Sensing Symposium (IGARSS), 2012 IEEE International* (pp. 7153–7156). IEEE.

Breiman, L. (2001). Random forests. *Machine learning*, *45*, 5–32.

Chan, S. (2016). In *Enhanced Level 3 Passive Soil Moisture Product Specification Document*. Jet Propulsion Lab., California Inst. Technol.: Pasadena, CA, USA.

Chan, S., Bindlish, R., O'Neill, P., Jackson, T., Njoku, E., Dunbar, S., Chaubell, J., Piepmeier, J., Yueh, S., Entekhabi, D. et al. (2018). Development and assessment of the SMAP enhanced passive soil moisture product. *Remote sensing of environment*, *204*, 931–941.

Chawla, N. V., Bowyer, K. W., Hall, L. O., & Kegelmeyer, W. P. (2002). SMOTE: Synthetic Minority Over-sampling Technique. *Journal of Artificial Intelligence Research*, *16*, 321–357.

Chen, C., Liaw, A., & Breiman, L. (2004). Using random forest to learn imbalanced data. *University of California, Berkeley*, *110*.

Chen, Q., Zeng, J., Cui, C., Li, Z., Chen, K.-S., Bai, X., & Xu, J. (2018). Soil moisture retrieval from smap: A validation and error analysis study using ground-based observations over the little washita watershed. *IEEE Transactions on Geoscience and Remote Sensing*, *56*, 1394–1408.

Chuvieco, E., Lizundia-Loiola, J., Pettinari, M. L., Ramo, R., Padilla, M., Mouillot, F., Laurent, P., Storm, T., Heil, A., & Plummer, S. (2018). Generation and analysis of a new global burned area product based on MODIS 250m reflectance bands and thermal anomalies. *Earth Syst. Sci. Data Discuss*, *512*, 1–24.

Chuvieco, E., Yue, C., Heil, A., Mouillot, F., Alonso-Canas, I., Padilla, M., Pereira, J. M., Oom, D., & Tansey, K. (2016). A new global burned area product for climate assessment of fire impacts. *Global Ecology and Biogeography*, *25*, 619–629.

Collins, L., Griffioen, P., Newell, G., & Mellor, A. (2018). The utility of random forests for wildfire severity mapping. *Remote Sensing of Environment*, *216*, 374–384.

Dabbiru, L., Aanstoos, J. V., Ball, J. E., & Younan, N. H. (2018). Machine Learning Framework for Mapping of Mississippi River Levees and Damage Assessment Using Terrasar-X Data. In *IGARSS 2018-2018 IEEE International Geoscience and Remote Sensing Symposium* (pp. 5855–5858). IEEE.

Dabbiru, L., Aanstoos, J. V., Mahrooghy, M., Li, W., Shanker, A., & Younan, N. H. (2012). Levee anomaly detection using polarimetric synthetic aperture radar data. In *Geoscience and Remote Sensing Symposium (IGARSS), 2012 IEEE International* (pp. 5113–5116). IEEE.

Dabbiru, L., Aanstoos, J. V., & Younan, N. H. (2016). Earthen levee slide detection via automated analysis of synthetic aperture radar imagery. *Landslides*, *13*, 643–652.

Di Gregorio, A. (2005). *Land Cover Classification System: Classification Concepts and User manual*. United Nations Food and Agriculture Organization.

Du, P., Samat, A., Waske, B., Liu, S., & Li, Z. (2015). Random forest and rotation forest for fully polarized SAR image classification using polarimetric and spatial features. *ISPRS Journal of Photogrammetry and Remote Sensing*, *105*, 38–53.

Engelbrecht, J., Theron, A., Vhengani, L., & Kemp, J. (2017). A simple normalized difference approach to burnt area mapping using multi-polarisation C-Band SAR. *Remote Sensing*, *9*, 764.

Escuin, S., Navarro, R., & Fernandez, P. (2008). Fire severity assessment by using NBR (Normalized Burn Ratio) and NDVI (Normalized Difference Vegetation Index) derived from LANDSAT TM/ETM images. *International Journal of Remote Sensing*, *29*, 1053–1073.

Eva, H., & Lambin, E. F. (1998). Remote sensing of biomass burning in tropical regions: sampling issues and multisensor approach. *Remote Sensing of Environment*, *64*, 292–315.

Fernandez-Carrillo, A., Belenguer-Plomer, M., Chuvieco, E., & Tanase, M. (2018). Effects of sample size on burned areas accuracy estimates in the Amazon Basin. In *Earth Resources and Environmental Remote Sensing/GIS Applications IX* (p. 107901S). International Society for Optics and Photonics volume 10790.

Flannigan, M. D., Amiro, B. D., Logan, K. A., Stocks, B., & Wotton, B. (2006). Forest fires and climate change in the 21 st century. *Mitigation and Adaptation Strategies for Global Change*, *11*, 847–859.

Flannigan, M. D., Krawchuk, M. A., de Groot, W. J., Wotton, B. M., & Gowman, L. M. (2009). Implications of changing climate for global wildland fire. *International Journal of Wildland Fire*, *18*, 483–507.

Freeman, A., & Durden, S. L. (1998). A three-component scattering model for polarimetric SAR data. *IEEE Transactions on Geoscience and Remote Sensing*, *36*, 963–973.

French, N. H., Bourgeau-Chavez, L. L., Wang, Y., & Kasischke, E. S. (1999). Initial observations of Radarsat imagery at fire-disturbed sites in interior Alaska. *Remote Sensing of Environment*, *68*, 89–94.

Frey, O., Santoro, M., Werner, C. L., & Wegmuller, U. (2013). DEM-based SAR pixel-area estimation for enhanced geocoding refinement and radiometric normalization. *IEEE Geoscience and Remote Sensing Letters*, *10*, 48–52.

García, M. L., & Caselles, V. (1991). Mapping burns and natural reforestation using Thematic Mapper data. *Geocarto International*, *6*, 31–37.

Giglio, L., Boschetti, L., Roy, D. P., Humber, M. L., & Justice, C. O. (2018). The Collection 6 MODIS burned area mapping algorithm and product. *Remote sensing of environment*, *217*, 72–85.

Giglio, L., Descloitres, J., Justice, C. O., & Kaufman, Y. J. (2003). An enhanced contextual fire detection algorithm for MODIS. *Remote Sensing of Environment*, *87*, 273–282.

Giglio, L., Loboda, T., Roy, D. P., Quayle, B., & Justice, C. O. (2009). An active-fire based burned area mapping algorithm for the MODIS sensor. *Remote Sensing of Environment*, *113*, 408–420.

Gimeno, M., San-Miguel, J., Barbosa, P., & Schmuck, G. (2002). Using ERS-SAR images for burnt area mapping in Mediterranean landscapes. *Forest Fire Research & Wildland Fire Safety. (Viegas T ed). Millpress, Rotterdam*, *90*.

Gimeno, M., & San-Miguel-Ayanz, J. (2004). Evaluation of RADARSAT-1 data for identification of burnt areas in Southern Europe. *Remote Sensing of Environment*, *92*, 370–375.

Gimeno, M., San-Miguel-Ayanz, J., & Schmuck, G. (2004). Identification of burnt areas in Mediterranean forest environments from ERS-2 SAR time series. *International Journal of Remote Sensing*, *25*, 4873–4888.

Gislason, P. O., Benediktsson, J. A., & Sveinsson, J. R. (2006). Random forests for land cover classification. *Pattern Recognition Letters*, *27*, 294–300.

Hansen, M. C., Potapov, P. V., Moore, R., Hancher, M., Turubanova, S., Tyukavina, A., Thau, D., Stehman, S., Goetz, S., Loveland, T. et al. (2013). High-resolution global maps of 21st-century forest cover change. *Science*, *342*, 850–853.

Hoffmann, W. A., Schroeder, W., & Jackson, R. B. (2002). Positive feedbacks of fire, climate, and vegetation and the conversion of tropical savanna. *Geophysical Research Letters*, *29*, 9–1.

Hollmann, R., Merchant, C. J., Saunders, R., Downy, C., Buchwitz, M., Cazenave, A., Chuvieco, E., Defourny, P., de Leeuw, G., Forsberg, R. et al. (2013). The ESA climate change initiative: Satellite data records for essential climate variables. *Bulletin of the American Meteorological Society*, *94*, 1541–1552.

Hu, Z., Zhou, Q., Chen, X., Li, J., Li, Q., Chen, D., Liu, W., & Yin, G. (2018). Evaluation of three global gridded precipitation data sets in central Asia based on rain gauge observations. *International Journal of Climatology*, *38*, 3475–3493.

Huang, S., & Siegert, F. (2006). Backscatter change on fire scars in Siberian boreal forests in ENVISAT ASAR wide-swath images. *IEEE Geoscience and Remote Sensing Letters*, *3*, 154–158.

Humber, M. L., Boschetti, L., Giglio, L., & Justice, C. O. (2018). Spatial and temporal intercomparison of four global burned area products. *International Journal of Digital Earth*, (pp. 1–25).

Imperatore, P., Azar, R., Calo, F., Stroppiana, D., Brivio, P. A., Lanari, R., & Pepe, A. (2017). Effect of the Vegetation Fire on Backscattering: An Investigation Based on Sentinel-1 Observations. *IEEE Journal of Selected Topics in Applied Earth Observations and Remote Sensing*, *10*, 4478–4492.

Inglada, J., & Christophe, E. (2009). The Orfeo Toolbox remote sensing image processing software. In *Geoscience and Remote Sensing Symposium, 2009 IEEE International, IGARSS 2009* (pp. IV–733). IEEE volume 4.

Kalogirou, V., Ferrazzoli, P., Della Vecchia, A., & Foumelis, M. (2014). On the SAR backscatter of burned forests: A model-based study in C-band, over burned pine canopies. *IEEE Transactions on Geoscience and Remote Sensing*, *52*, 6205–6215.

Kasischke, E. S., Bourgeau-Chavez, L. L., & French, N. H. (1994). Observations of variations in ERS-1 SAR image intensity associated with forest fires in Alaska. *IEEE Transactions on Geoscience and Remote Sensing*, *32*, 206–210.

Keeley, J. E. (2009). Fire intensity, fire severity and burn severity: a brief review and suggested usage. *International Journal of Wildland Fire*, *18*, 116–126.

Key, C., & Benson, N. (2004). Ground measure of severity, the Composite Burn Index; and Remote sensing of severity, the Normalized Burn Ratio. In G. T. R. RMRS-GTR-164 (Ed.), *FIREMON: Fire Effects Monitoring and Inventory System* chapter Landscape assessment (LA): Sampling and analysis methods. (pp. 1–51). Ogden: USDA Forest Service, Rocky Mountain Research Station.

Kirches, G., Brockmann, C., Boettcher, M., Peters, M., Bontemps, S., Lamarche, C., Schlerf, M., Santoro, M., & Defourny, P. (2014). Land cover cci-product user guide-version 2. In *ESA Public Document CCI-LC-PUG*. ESA Climate Change Initiative–Land Cover_cci.

Kloster, S., Mahowald, N., Randerson, J., & Lawrence, P. (2012). The impacts of climate, land use, and demography on fires during the 21st century simulated by CLM-CN. *Biogeosciences*, *9*, 509–525.

Knorr, W., Jiang, L., & Arneth, A. (2016). Climate, CO 2 and human population impacts on global wildfire emissions. *Biogeosciences*, *13*, 267–282.

Krawchuk, M. A., Moritz, M. A., Parisien, M.-A., Van Dorn, J., & Hayhoe, K. (2009). Global pyrogeography: the current and future distribution of wildfire. *PloS one*, *4*, e5102.

Kurum, M. (2015). C-band SAR backscatter evaluation of 2008 Gallipoli forest fire. *IEEE Geoscience and Remote Sensing Letters*, *12*, 1091–1095.

Kwon, H., & Nasrabadi, N. M. (2005). Kernel RX-algorithm: A nonlinear anomaly detector for hyperspectral imagery. *IEEE Transactions on Geoscience and Remote Sensing*, *43*, 388–397.

Lacava, T., Coviello, I., Faruolo, M., Mazzeo, G., Pergola, N., & Tramutoli, V. (2013). A multitemporal investigation of AMSR-E C-band radio-frequency interference. *IEEE Transactions on Geoscience and Remote Sensing*, *51*, 2007–2015.

Langenfelds, R., Francey, R., Pak, B., Steele, L., Lloyd, J., Trudinger, C., & Allison, C. (2002). Interannual growth rate variations of atmospheric CO2 and its δ13C, H2, CH4, and CO between 1992 and 1999 linked to biomass burning. *Global Biogeochemical Cycles*, *16*, 21–1.

Lavorel, S., Flannigan, M. D., Lambin, E. F., & Scholes, M. C. (2007). Vulnerability of land systems to fire: Interactions among humans, climate, the atmosphere, and ecosystems. *Mitigation and Adaptation Strategies for Global Change*, *12*, 33–53.

Li, L., Njoku, E. G., Im, E., Chang, P. S., & Germain, K. S. (2004). A preliminary survey of radio-frequency interference over the US in Aqua AMSR-E data. *IEEE Transactions on Geoscience and Remote Sensing*, *42*, 380–390.

Loboda, T., O'neal, K., & Csiszar, I. (2007). Regionally adaptable dNBR-based algorithm for burned area mapping from MODIS data. *Remote Sensing of Environment*, *109*, 429–442.

Lohberger, S., Stängel, M., Atwood, E. C., & Siegert, F. (2018). Spatial evaluation of Indonesia's 2015 fire-affected area and estimated carbon emissions using Sentinel-1. *Global change biology*, *24*, 644–654.

Meddens, A. J., Kolden, C. A., & Lutz, J. A. (2016). Detecting unburned areas within wildfire perimeters using Landsat and ancillary data across the northwestern United States. *Remote Sensing of Environment*, *186*, 275–285.

Menges, C., Bartolo, R., Bell, D., & Hill, G. E. (2004). The effect of savanna fires on SAR backscatter in northern Australia. *International Journal of Remote Sensing*, *25*, 4857–4871.

Mouillot, F., Schultz, M. G., Yue, C., Cadule, P., Tansey, K., Ciais, P., & Chuvieco, E. (2014). Ten years of global burned area products from spaceborne remote sensing—A review: Analysis of user needs and recommendations for future developments. *International Journal of Applied Earth Observation and Geoinformation*, *26*, 64–79.

Njoku, E. G., Ashcroft, P., Chan, T. K., & Li, L. (2005). Global survey and statistics of radio-frequency interference in AMSR-E land observations. *IEEE Transactions on Geoscience and Remote Sensing*, *43*, 938–947.

Padilla, M., Olofsson, P., Stehman, S. V., Tansey, K., & Chuvieco, E. (2017). Stratification and sample allocation for reference burned area data. *Remote Sensing of Environment*, *203*, 240–255.

Padilla, M., Stehman, S. V., & Chuvieco, E. (2014). Validation of the 2008 MODIS-MCD45 global burned area product using stratified random sampling. *Remote Sensing of Environment*, *144*, 187–196.

Padilla, M., Stehman, S. V., Ramo, R., Corti, D., Hantson, S., Oliva, P., Alonso-Canas, I., Bradley, A. V., Tansey, K., Mota, B. et al. (2015). Comparing the accuracies of remote sensing global burned area products using stratified random sampling and estimation. *Remote Sensing of Environment*, *160*, 114–121.

Pal, M. (2005). Random forest classifier for remote sensing classification. *International Journal of Remote Sensing*, *26*, 217–222.

Pausas, J. G., & Paula, S. (2012). Fuel shapes the fire–climate relationship: evidence from Mediterranean ecosystems. *Global Ecology and Biogeography*, *21*, 1074–1082.

Pazzani, M., Merz, C., Murphy, P., Ali, K., Hume, T., & Brunk, C. (1994). Reducing misclassification costs. In *Machine Learning Proceedings 1994* (pp. 217–225).

Plummer, S., Arino, O., Simon, M., & Steffen, W. (2006). Establishing a earth observation product service for the terrestrial carbon community: The GLOBCARBON initiative. *Mitigation and Adaptation Strategies for Global Change*, *11*, 97–111.

Plummer, S., Lecomte, P., & Doherty, M. (2017). The ESA Climate Change Initiative (CCI): A European contribution to the generation of the Global Climate Observing System. *Remote Sensing of Environment*, *203*, 2–8.

Polychronaki, A., Gitas, I. Z., Veraverbeke, S., & Debien, A. (2013). Evaluation of ALOS PALSAR imagery for burned area mapping in Greece using object-based classification. *Remote Sensing*, *5*, 5680–5701.

Poulter, B., Cadule, P., Cheiney, A., Ciais, P., Hodson, E., Peylin, P., Plummer, S., Spessa, A., Saatchi, S., Yue, C. et al. (2015). Sensitivity of global terrestrial carbon cycle dynamics to variability in satellite-observed burned area. *Global Biogeochemical Cycles*, *29*, 207–222.

Quegan, S., Le Toan, T., Yu, J. J., Ribbes, F., & Floury, N. (2000). Multitemporal ERS SAR analysis applied to forest mapping. *IEEE Transactions on Geoscience and Remote Sensing*, *38*, 741–753.

Ramo, R., & Chuvieco, E. (2017). Developing a Random Forest Algorithm for MODIS Global Burned Area Classification. *Remote Sensing*, *9*, 1193.

Randerson, J., Chen, Y., Werf, G., Rogers, B., & Morton, D. (2012). Global burned area and biomass burning emissions from small fires. *Journal of Geophysical Research: Biogeosciences*, *117*.

Reed, I. S., & Yu, X. (1990). Adaptive multiple-band CFAR detection of an optical pattern with unknown spectral distribution. *Acoustics, Speech and Signal Processing, IEEE Transactions on*, *38*, 1760–1770.

Rignot, E., Despain, D., & Holecz, F. (1999). The 1988 Yellowstone fires observed by imaging radars. In *Proceedings of the Joint Fire Sciences Conference and Workshop*. volume 1.

Rodriguez-Galiano, V. F., Ghimire, B., Rogan, J., Chica-Olmo, M., & Rigol-Sanchez, J. P. (2012). An assessment of the effectiveness of a random forest classifier for land-cover classification. *ISPRS Journal of Photogrammetry and Remote Sensing*, *67*, 93–104.

Roteta, E., Bastarrika, A., Padilla, M., Storm, T., & Chuvieco, E. (2019). Development of a Sentinel-2 burned area algorithm: Generation of a small fire database for sub-Saharan Africa. *Remote Sensing of Environment*, *222*, 1–17.

Roy, D. P., Boschetti, L., Justice, C. O., & Ju, J. (2008). The collection 5 MODIS burned area product—Global evaluation by comparison with the MODIS active fire product. *Remote Sensing of Environment*, *112*, 3690–3707.

Ruecker, G., & Siegert, F. (2000). Burn scar mapping and fire damage assessment using ERS-2 SAR images in East Kalimantan, Indonesia. *International Archives of Photogrammetry and Remote Sensing*, *33*, 1286–1293.

Schroeder, W., Oliva, P., Giglio, L., & Csiszar, I. A. (2014). The New VIIRS 375 m active fire detection data product: Algorithm description and initial assessment. *Remote Sensing of Environment*, *143*, 85–96.

Siegert, F., & Hoffmann, A. A. (2000). The 1998 forest fires in East Kalimantan (Indonesia): A quantitative evaluation using high resolution, multitemporal ERS-2 SAR images and NOAA-AVHRR hotspot data. *Remote Sensing of Environment*, *72*, 64–77.

Siegert, F., & Ruecker, G. (2000). Use of multitemporal ERS-2 SAR images for identification of burned scars in south-east Asian tropical rainforest. *International Journal of Remote Sensing*, *21*, 831–837.

Simon, M., Plummer, S., Fierens, F., Hoelzemann, J. J., & Arino, O. (2004). Burnt area detection at global scale using ATSR-2: The GLOBSCAR products and their qualification. *Journal of Geophysical Research: Atmospheres*, *109*.

Small, D. (2011). Flattening gamma: Radiometric terrain correction for SAR imagery. *IEEE Transactions on Geoscience and Remote Sensing*, *49*, 3081–3093.

Stein, D. W., Beaven, S. G., Hoff, L. E., Winter, E. M., Schaum, A. P., & Stocker, A. D. (2002). Anomaly detection from hyperspectral imagery. *IEEE Signal Processing Magazine*, *19*, 58–69.

Stroppiana, D., Azar, R., Calò, F., Pepe, A., Imperatore, P., Boschetti, M., Silva, J., Brivio, P. A., & Lanari, R. (2015a). Integration of optical and SAR data for burned area mapping in Mediterranean Regions. *Remote Sensing*, *7*, 1320–1345.

Stroppiana, D., Azar, R., Calò, F., Pepe, A., Imperatore, P., Boschetti, M., Silva, J. M., Brivio, P. A., & Lanari, R. (2015b). Remote sensing of burned area: A fuzzy-based framework for joint processing of optical and microwave data. In *Geoscience and Remote Sensing Symposium (IGARSS), 2015 IEEE International* (pp. 1409–1412). IEEE.

Tanase, M., Kennedy, R., & Aponte, C. (2015). Radar Burn Ratio for fire severity estimation at canopy level: An example for temperate forests. *Remote Sensing of Environment*, *170*, 14–31.

Tanase, M., de la Riva, J., & Pérez-Cabello, F. (2011). Estimating burn severity at the regional level using optically based indices. *Canadian Journal of Forest Research*, *41*, 863–872.

Tanase, M., Santoro, M., de la Riva, J., & Pérez-Cabello, F. (2009). Backscatter properties of multitemporal TerraSAR-X data and the effects of influencing factors on burn severity evaluation, in a Mediterranean pine forest. In *Geoscience and Remote Sensing Symposium, 2009 IEEE International, IGARSS 2009* (pp. III–593). IEEE volume 3.

Tanase, M. A., Aponte, C., Mermoz, S., Bouvet, A., Le Toan, T., & Heurich, M. (2018). Detection of windthrows and insect outbreaks by L-band SAR: A case study in the Bavarian Forest National Park. *Remote Sensing of Environment*, *209*, 700–711.

Tanase, M. A., & Belenguer-Plomer, M. A. (2018). 03. D3 Intermediate validation results: SAR pre-processing and burned area detection, version 1.0. In *ESA CCI ECV Fire Disturbance*. ESA Climate Change Initiative–Fire_cci.

Tanase, M. A., Perez-Cabello, F., de La Riva, J., & Santoro, M. (2010a). TerraSAR-X data for burn severity evaluation in Mediterranean forests on sloped terrain. *IEEE Transactions on Geoscience and Remote Sensing*, *48*, 917–929.

Tanase, M. A., Santoro, M., Aponte, C., & de la Riva, J. (2014). Polarimetric properties of burned forest areas at C-and L-band. *IEEE Journal of Selected Topics in Applied Earth Observations and Remote Sensing*, *7*, 267–276.

Tanase, M. A., Santoro, M., de La Riva, J., Fernando, P., Le Toan, T. et al. (2010b). Sensitivity of X-, C-, and L-band SAR backscatter to burn severity in Mediterranean pine forests. *IEEE Transactions on Geoscience and Remote Sensing*, *48*, 3663–3675.

Tanase, M. A., Santoro, M., Wegmüller, U., de la Riva, J., & Pérez-Cabello, F. (2010c). Properties of X-, C-and L-band repeat-pass interferometric SAR coherence in Mediterranean pine forests affected by fires. *Remote Sensing of Environment*, *114*, 2182–2194.

Tansey, K., Grégoire, J.-M., Defourny, P., Leigh, R., Pekel, J.-F., van Bogaert, E., & Bartholomé, E. (2008). A new, global, multi-annual (2000–2007) burnt area product at 1 km resolution. *Geophysical Research Letters*, *35*.

Tansey, K., Grégoire, J.-M., Stroppiana, D., Sousa, A., Silva, J., Pereira, J., Boschetti, L., Maggi, M., Brivio, P. A., Fraser, R. et al. (2004). Vegetation burning in the year 2000: Global burned area estimates from SPOT VEGETATION data. *Journal of Geophysical Research: Atmospheres*, *109*.

Theiler, J., & Perkins, S. (2006). Proposed framework for anomalous change detection. In *ICML Workshop on Machine Learning Algorithms for Surveillance and Event Detection* (pp. 7–14).

Van Der Werf, G. R., Randerson, J. T., Giglio, L., Van Leeuwen, T. T., Chen, Y., Rogers, B. M., Mu, M., Van Marle, M. J., Morton, D. C., Collatz, G. J. et al. (2017). Global fire emissions estimates during 1997-2016. *Earth System Science Data*, *9*, 697–720.

Van Wagtendonk, J. W., Root, R. R., & Key, C. H. (2004). Comparison of AVIRIS and Landsat ETM+ detection capabilities for burn severity. *Remote Sensing of Environment*, *92*, 397–408.

Van Zyl, J. J. (1993). The effect of topography on radar scattering from vegetated areas. *IEEE Transactions on Geoscience and Remote Sensing*, *31*, 153–160.

Van Zyl, J. J., Arii, M., & Kim, Y. (2011). Model-based decomposition of polarimetric SAR covariance matrices constrained for nonnegative eigenvalues. *IEEE Transactions on Geoscience and Remote Sensing*, *49*, 3452–3459.

Verhegghen, A., Eva, H., Ceccherini, G., Achard, F., Gond, V., Gourlet-Fleury, S., & Cerutti, P. O. (2016). The potential of Sentinel satellites for burnt area mapping and monitoring in the Congo Basin forests. *Remote Sensing*, *8*, 986.

Vermote, E., Justice, C., Claverie, M., & Franch, B. (2016). Preliminary analysis of the performance of the Landsat 8/OLI land surface reflectance product. *Remote Sensing of Environment*, *185*, 46–56.

Waske, B., & Braun, M. (2009). Classifier ensembles for land cover mapping using multitemporal SAR imagery. *ISPRS Journal of Photogrammetry and Remote Sensing*, *64*, 450–457.

Watanabe, M., Koyama, C. N., Hayashi, M., Nagatani, I., & Shimada, M. (2018). Early-Stage Deforestation Detection in the Tropics With L-band SAR. *IEEE Journal of Selected Topics in Applied Earth Observations and Remote Sensing*, *11*, 2127–2133.

Van der Werf, G. R., Randerson, J. T., Giglio, L., Collatz, G., Mu, M., Kasibhatla, P. S., Morton, D. C., DeFries, R., Jin, Y. v., & van Leeuwen, T. T. (2010). Global fire emissions and the contribution of deforestation, savanna, forest, agricultural, and peat fires (1997–2009). *Atmospheric Chemistry and Physics*, *10*, 11707–11735.

Yamaguchi, Y., Moriyama, T., Ishido, M., & Yamada, H. (2005). Four-component scattering model for polarimetric SAR image decomposition. *IEEE Transactions on Geoscience and Remote Sensing*, *43*, 1699–1706.

Chapter 3

Optimum Sentinel-1 pixel spacing for burned area mapping

This chapter evaluates the relationship between mapping accuracy and computing time when detecting burned areas from Sentinel-1 C-band backscatter coefficient images processed at different pixel spacings (i.e., 20, 30, 40 and 50 m). The analysis was carried out in six study areas distributed worldwide. The algorithm described in Chapter 2, based on Sentinel-1 C-band post- to pre-fire backscatter coefficient differences and the Reed-Xiaoli anomaly detector, was used to detect and map the burned areas.

Marginal differences in accuracy were observed when varying the spatial spacing with slightly more accurate products being obtained at higher spacing as speckle was reduced. However, the computing time was considerably higher when processing at the lowest spacing (20 m). The results suggest that detecting burned areas at 30 to 50 m pixel spacing from C-band backscatter provides significant advantages over large areas (i.e., continental to global scales) while also improving the detection accuracy.

3.1   Introduction

Fire disturbance is considered an essential climatic variable since it has a leading part in the climatic system by altering the concentration of greenhouse gases and aerosols in the atmosphere (Van Der Werf et al., 2017).

Current estimations place global burned area from 4 to 4.5 million km^2 per year (Giglio et al., 2018; Lizundia-Loiola et al., 2020), although it exists a considerable uncertainty (Chuvieco et al., 2019). Two leading sources are behind such uncertainty, (i) the predominant use of passive remote sensing sensors which are of limited use in areas with persistent cloud cover, and (ii) the coarse spatial resolution (i.e., ≥ 250 m) of the sensors used to derive the global burned areas, which prevents the detection of small burned patches that may account for a significant portion of the burned area (Roteta et al., 2019).

The use of the synthetic aperture radar (SAR) provides a remarkable opportunity to reduce the mentioned uncertainty by allowing acquisitions independently from clouds and solar illumination conditions. The launch of ESA's Sentinel-1 satellites has increased the interest in SAR datasets for burned area detection due to its relatively high revisit periods (down to three days when ascending and descending passes are used). In addition, the Sentinel-1 mission provides dual-polarised information (vertical–vertical, VV; and vertical–horizontal, VH polarisations), increased incidence angles and a free data access policy. These improvements have allowed the development of burned area mapping algorithms based on Sentinel-1 C-band backscatter coefficient time-series (Lohberger et al., 2018; Belenguer-Plomer et al., 2019). The latter algorithm (Belenguer-Plomer et al., 2019), used to produce regional scale burned area maps over the Amazon basin in the framework of the ESA's Fire_cci project (FireCCIS1SA10) was used in this research.

The nominal resolution of Sentinel-1 SAR sensor is 20 m. However, reducing the spatial resolution of SAR datasets is often needed to improve image radiometry (i.e., reduce speckle). Therefore, the trade-off between increased pixel spacing and mapping accuracy needed to be evaluated. The objectives of this study were to (i) evaluate burned area detection accuracy at decreasing levels of radar speckle, (ii) evaluate the efficiency (i.e., computing time) of the classification process and its relationship with the product accuracy, and (iii) evaluate the ability to detect small fires, and thus reducing the uncertainty of global burned area estimation.

3.2   Study areas and datasets

Six study areas frequently affected by fires and distributed worldwide were considered in this work (Figure 3.1). The study areas corresponded to 100×100 km tiles according to the Military Grid Reference System (MGRS).

Ground Range Detected (GRD) C-band dual-polarised SAR images (VV and VH) acquired by the satellites Sentinel-1 A/B in interferometric wide (IW) swath mode were utilised to detect and map the burned area. Land cover information and thermal anomalies (i.e., hotspots) provided ancillary information during detection, as explained in Methods (see section 3.3). Land cover information was extracted from the most recent global prod-
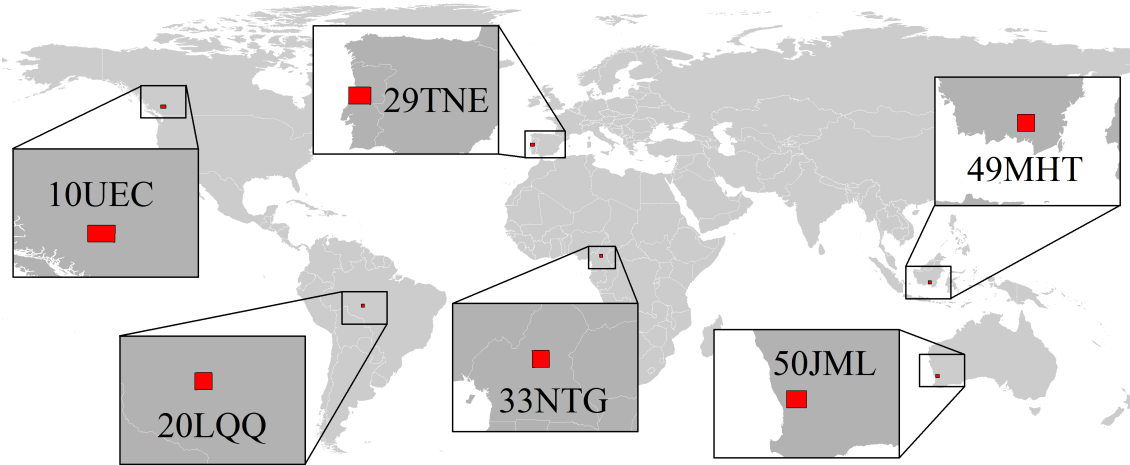
Figure 3.1: Location of the study areas.

uct generated in the framework of the ESA's Land_Cover_cci project. Hotspots recorded by the Visible Infrared Imaging Radiometer Suite (VIIRS) at 375 m and the Moderate Resolution Imaging Spectroradiometer (MODIS) at 1 km of spatial resolution, respectively, were downloaded from NASA's Fire Information for Resource Management System (FIRMS).

Landsat-8 images were used to generate the reference burned area perimeters needed to validate the mapping accuracy (Fernandez-Carrillo et al., 2018). The reference maps were derived in each study area for the periods shown in Table 3.1.

Table 3.1: Periods for which the reference fire perimeters were generated.

MGRS area	Reference period
10UEC	20170705 - 20170822
20LQQ	20160704 - 20160922
29TNE	20171005 - 20171106
33NTG	20161230 - 20170115
49MHT	20170307 - 20170510
50JML	20170307 - 20170510

3.3 Methods

3.3.1 Sentinel-1 data processing

The fully automatic processing chain S1Tiling, based on Orfeo ToolBox libraries (Inglada & Christophe, 2009) developed at National Centre for Space Studies (CNES) and the Centre d'Etudes Spatiales de la BIOsphère (CESBIO) was used to process the Sentinel-1 images. The processing chain was organised into three main tasks such as (i) data-preparation, where the images were calibrated to gamma nought using the information provided in the GRD metadata, (ii) geocoding, where the images were orthorectified, and

(iii) multi-temporal filtering, where the speckle was filtered considering multi-temporal values of each pixel (Quegan et al., 2000). The processing was carried out at 20 m, the native Sentinel-1 ground spatial resolution. For the proposed analysis, the 20 m images were aggregated to 30, 40 and 50 m.

3.3.2 Burned area detection algorithm

The detection of burned area using Sentinel-1 images was carried out employing an advanced algorithm based on Sentinel-1 C-band backscatter coefficient (Belenguer-Plomer et al., 2019). The algorithm used the Reed-Xiaoli detector (RXD) (Reed & Yu, 1990) over temporal ratios of backscatter coefficient to detect anomalous changes in each land cover class and detection period as defined by consecutive Sentinel-1 acquisitions. Depending on the study site and Sentinel-1 observation scenario, the revisit period was 6 or 12 days. Temporally and spatially coincident anomalous changes, as detected by RXD, and hotspots were used to derive burned and unburned regions of interest (ROIs). A random forests classification model was subsequently applied over areas not assigned as burned/unburned ROIs using the coincident anomalous changes and hotspots. Such areas arose as dense cloud cover may have obscured thermal radiation from the Earth surface (lack of hotspots) or due to insufficient radiative power of small fires which often are not recorded by the space-borne thermal sensors. The random forests models, trained (for each land cover class) using samples drawn from burned/unburned ROIs, were used to detect the burned area without hotspots information.

3.3.3 Validation metrics

The detected burned area was validated using confusion matrices computed through cross-tabulation of the Sentinel-1 detected burned area, and the Landsat-8 based reference fire perimeters (Table 3.2). Three accuracy metrics were computed for the burned area class, the omission error (Equation 3.1), the commission error (Equation 3.2) and the Dice coefficient (Equation 3.3) (Padilla et al., 2015). Besides, the computing time when detecting the burned area at each pixel spacing considered (i.e., 20, 30, 40 and 50 m) was stored to assess the trade-off between mapping accuracy and computing needs.

Table 3.2: Confusion matrix example.

| Detection | Refererence data | | |
	Burned	Unburned	Row total
Burned	P_{11}	P_{12}	P_{1+}
Unburned	P_{21}	P_{22}	P_{2+}
Col. total	P_{+1}	P_{+2}	N

$$\text{OE} = P_{21}/P_{+1} \tag{3.1}$$

$$\text{CE} = P_{12}/P_{1+} \tag{3.2}$$

$$\text{DC} = 2P_{11}/(P_{1+} + P_{+1}) \tag{3.3}$$

3.4 Results

3.4.1 Accuracy and computing time pixel spacing effects

Mapping accuracy (DC) and errors (OE and CE) were largely similar when detecting burned area using Sentinel-1 images regardless of the pixel spacing used (i.e., 20 30, 40 and 50 m) (Figure 3.2). According to the ANOVA analysis, no statistically significant differences (p-value > 0.05) were observed between the DC, OE and CE at the four pixel spacing analysed. However, for pixel spacings above 20 m, the CE decreased, and the OE increased marginally. Since the burned area detection algorithm is land cover dependent (Belenguer-Plomer et al., 2019), the ANOVA analysis was also carried out by land cover classes (Table 3.3). As for the overall values, the ANOVA showed no significant difference in accuracy by land cover classes (p-value > 0.05). It should be noticed that the coarser resolution of the global land cover product used (300 m) may have obscured the effects of the Sentinel-1 resolution over different landscapes.

Statistically significant differences were observed when analysing the computing time needed to detect the burned area at each pixel spacing and detection period as defined by the interval between consecutive Sentinel-1 acquisitions (Figure 3.2). At 20 m spacing, the average time needed for detection was 121 minutes, a 265%, 491% and 795% of increasing when compared to 30, 40 and 50 m, respectively.
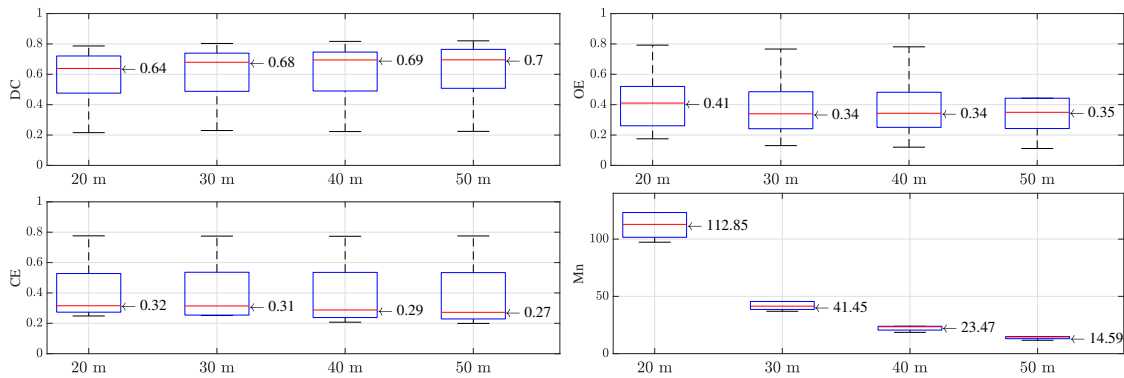

Figure 3.2: Dice coefficient, omission and commission errors and minuted needed to carry out the burned area mapping per detection period by Sentinel-1 sizes of pixel spacing.

Table 3.3: Dice coefficient, omission and commission errors by land cover class and pixel spacing (± confidence interval, 95%).

LC	m	DC	OE	CE
Crops	20	0.441±0.23	0.507±0.3	0.576±0.22
	30	0.381±0.27	0.548±0.36	0.581±0.21
	40	0.452±0.25	0.478±0.43	0.521±0.22
	50	0.473±0.28	0.499±0.39	0.478±0.24
Grasslands	20	0.396±0.17	0.679±0.12	0.441±0.36
	30	0.424±0.2	0.657±0.13	0.418±0.36
	40	0.417±0.2	0.677±0.13	0.392±0.35
	50	0.439±0.22	0.663±0.15	0.352±0.38
Shrubs	20	0.537±0.19	0.501±0.13	0.402±0.25
	30	0.567±0.21	0.458±0.15	0.388±0.26
	40	0.57±0.23	0.463±0.19	0.381±0.27
	50	0.576±0.23	0.455±0.19	0.37±0.28
Forests	20	0.638±0.16	0.32±0.16	0.379±0.2
	30	0.661±0.17	0.267±0.15	0.382±0.2
	40	0.674±0.17	0.277±0.16	0.357±0.19
	50	0.684±0.16	0.273±0.15	0.344±0.19

3.4.2   Pixel spacing effects over small burned patches

To respond to current burned area mapping necessities, the error analysis was also carried out over small burned patches (< 120 ha), where coarser spatial resolution sensors, such as MODIS, are more prone to have omission errors (Roteta et al., 2019; Belenguer-Plomer et al., 2019). The analysis showed little variation in accuracy and errors (ANOVA p-value > 0.05) among the four spatial resolutions tested (Table 3.4), with burned area mapping accuracy being low.

Table 3.4: Dice coefficient, omission and commission errors in small burned areas (< 120 ha) by Sentinel-1 sizes of pixel spacing (± confidence interval, 95%).

m	DC	OE	CE
20	0.187±0.16	0.635±0.2	0.852±0.17
30	0.19±0.16	0.612±0.2	0.856±0.16
40	0.192±0.16	0.637±0.2	0.849±0.17
50	0.19±0.16	0.647±0.2	0.848±0.18

3.5   Discussion

According to our results, the sole variable which needs to be considered when choosing the spacing of the final burned area product, and therefore the spatial resolution to process

the Sentinel-1 images, is the computing time. Computing requirements, coupled with the null improvement in mapping accuracy, suggest avoiding the nominal resolution of Sentinel-1 when mapping burned areas over a range of environments. Moreover, marginal improvements in the mapping accuracy were observed at higher pixel spacings. A low pixel spacing was linked to high CE due to speckle effects, while a coarser spacing implied a noise smoothing of the spatial data, reducing the CE and increasing the OE as some information was lost. The results presented here may have been limited by the resolution of the Landsat-8 images (30 m) used to derive the reference fire perimeters. The smallest burned areas detected at the nominal spatial resolution of Sentinel-1 (20 m) may offer a more accurate record than the reference fire perimeters derived from the coarser Landsat imagery. Such effects have not been considered in this study. Assuming such limitations, it seems that the best strategy when monitoring burned areas using Sentinel-1 is taking into account the time computing requirements when considering pixel spacings equal and lower than 50 m. Computing time is considerably higher at detailed spatial resolutions and apparently without providing more accurate maps even for the small fires.

3.6 Conclusions

This work has analysed and quantified the relationship between burned area mapping accuracy and the processing time at 20, 30, 40 and 50 m of pixel spacing. The study was carried out over six areas distributed worldwide. The results showed statistically non-significant differences of burned area accuracy detected at different spatial resolutions independently of the land cover type and the size of the burned patch. The most relevant effect when working at different spatial resolutions was the increasing computing time needed to detect and map the burned areas.

Acknowledgements

3.7 References

Belenguer-Plomer, M. A., Tanase, M. A., Fernandez-Carrillo, A., & Chuvieco, E. (2019). Burned area detection and mapping using Sentinel-1 backscatter coefficient and thermal anomalies. *Remote Sensing of Environment*, *233*, 111345.

Chuvieco, E., Mouillot, F., van der Werf, G. R., San Miguel, J., Tanasse, M., Koutsias, N., García, M., Yebra, M., Padilla, M., Gitas, I. et al. (2019). Historical background and current developments for mapping burned area from satellite Earth observation. *Remote Sensing of Environment*, *225*, 45–64.

Fernandez-Carrillo, A., Belenguer-Plomer, M., Chuvieco, E., & Tanase, M. (2018). Effects of sample size on burned areas accuracy estimates in the Amazon Basin. In *Earth*

Resources and Environmental Remote Sensing/GIS Applications IX (p. 107901S). International Society for Optics and Photonics volume 10790.

Giglio, L., Boschetti, L., Roy, D. P., Humber, M. L., & Justice, C. O. (2018). The Collection 6 MODIS burned area mapping algorithm and product. *Remote sensing of environment*, *217*, 72–85.

Inglada, J., & Christophe, E. (2009). The Orfeo Toolbox remote sensing image processing software. In *Geoscience and Remote Sensing Symposium, 2009 IEEE International, IGARSS 2009* (pp. IV–733). IEEE volume 4.

Lizundia-Loiola, J., Otón, G., Ramo, R., & Chuvieco, E. (2020). A spatio-temporal active-fire clustering approach for global burned area mapping at 250 m from MODIS data. *Remote Sensing of Environment*, *236*, 111493.

Lohberger, S., Stängel, M., Atwood, E. C., & Siegert, F. (2018). Spatial evaluation of Indonesia's 2015 fire-affected area and estimated carbon emissions using Sentinel-1. *Global change biology*, *24*, 644–654.

Padilla, M., Stehman, S. V., Ramo, R., Corti, D., Hantson, S., Oliva, P., Alonso-Canas, I., Bradley, A. V., Tansey, K., Mota, B. et al. (2015). Comparing the accuracies of remote sensing global burned area products using stratified random sampling and estimation. *Remote Sensing of Environment*, *160*, 114–121.

Quegan, S., Le Toan, T., Yu, J. J., Ribbes, F., & Floury, N. (2000). Multitemporal ERS SAR analysis applied to forest mapping. *IEEE Transactions on Geoscience and Remote Sensing*, *38*, 741–753.

Reed, I. S., & Yu, X. (1990). Adaptive multiple-band CFAR detection of an optical pattern with unknown spectral distribution. *Acoustics, Speech and Signal Processing, IEEE Transactions on*, *38*, 1760–1770.

Roteta, E., Bastarrika, A., Padilla, M., Storm, T., & Chuvieco, E. (2019). Development of a Sentinel-2 burned area algorithm: Generation of a small fire database for sub-Saharan Africa. *Remote Sensing of Environment*, *222*, 1–17.

Van Der Werf, G. R., Randerson, J. T., Giglio, L., Van Leeuwen, T. T., Chen, Y., Rogers, B. M., Mu, M., Van Marle, M. J., Morton, D. C., Collatz, G. J. et al. (2017). Global fire emissions estimates during 1997-2016. *Earth System Science Data*, *9*, 697–720.

Chapter 4

Backscatter coefficient temporal decorrelation in burned areas

Burned area algorithms from radar images are often based on temporal differences between pre- and post-fire backscatter values. However, such differences may occur long past the fire event, an effect known as temporal decorrelation. Improvements in radar-based burned areas monitoring depend on a better understanding of the temporal decorrelation effects as well as its sources. This chapter analyses the temporal decorrelation of the Sentinel-1 C-band backscatter coefficient over burned areas in Mediterranean ecosystems. Several environmental variables influencing radar scattering were analysed, including fire severity, post-fire vegetation recovery, vegetation water content, soil moisture, and local slope and aspect. The ensemble learning method random forests was employed to estimate the importance of these variables for the temporal decorrelation process by land cover classes.

The temporal decorrelation was observed for 32% of the burned pixels. Fire severity, vegetation water content, and soil moisture were the main drivers behind temporal decorrelation processes and are of the utmost importance for areas detected as burned immediately after the fire event. When burned areas were detected long after fire (decorrelated areas), due to reduced backscatter coefficient variations between pre- to post-fire acquisitions, the water content (soil and vegetation) was the main driver behind the backscatter coefficient changes. Therefore, for efficient synthetic aperture radar (SAR)-based monitoring of burned areas, the detection and mapping algorithms need to account for the interaction between fire impact and soil and vegetation water content.

4.1   Introduction

Fire has a key role in the global climatic balance modifying the greenhouse gases (GHGs) emission fluxes and the presence of aerosols in the atmosphere (Van Der Werf et al., 2017; Andreae & Merlet, 2001; Bowman et al., 2009). The Global Climate Observing System (GCOS) considers fire disturbance as an essential climatic variable (ECV) due to the close relationship between fire regime and climate. According to Bojinski et al. (2014), an ECV is a physical, chemical, biological, or a group of linked variables that have a major influence on the climate system and are key to predicting climate evolution. In 2010, the European Space Agency (ESA) started the Climate Change Initiative (CCI), a program focused on deriving remote sensing-based information on different ECVs to improve climate modelling efforts (Plummer et al., 2017; Hollmann et al., 2013). Given its importance for climate modelling (Mouillot et al., 2014; Poulter et al., 2015), fire disturbance was included in the CCI program (Fire CCI) since the beginning. The aim was to produce a long-term consistent time series of global burned area maps (Chuvieco et al., 2016). The most recent global burned area products estimate that around 4 million km^2 are burned every year (Chuvieco et al., 2018; Giglio et al., 2018). However, there is still a remarkable uncertainty about the worldwide burned area extent (Chuvieco et al., 2019), since the currently available global products are limited by (i) the use of passive remoted sensing datasets, which is associated with limitations in areas of persistent cloud cover (i.e., inter-equatorial latitudes), and (ii) relatively coarse spatial resolutions (250 m), which makes the detection of small fires difficult (Stroppiana et al., 2015; Randerson et al., 2012). A recent comparison between burned area products from Sentinel-2 and Moderate Resolution Imaging Spectrometer (MODIS) for Africa indicated that the latter missed almost half of the total burned area, mostly due to small fires omission (<100 ha) (Roteta et al., 2019).

Synthetic aperture radar (SAR) data have been increasingly used for land cover mapping, given their independence from cloud cover and solar illumination conditions (French et al., 1999; Bourgeau-Chavez et al., 2002). Burned area mapping algorithms have been developed from diverse SAR images, such as those acquired by the European Remote Sensing (ERS) satellites (ERS-1 and ERS-2) (Bourgeau-Chavez et al., 1997; Kasischke et al., 1994; Siegert & Hoffmann, 2000; Siegert & Ruecker, 2000; Ruecker & Siegert, 2000; Gimeno et al., 2004, 2002), RADARSAT (Gimeno & San-Miguel-Ayanz, 2004; French et al., 1999), and the Advanced Land Observation Satellite (ALOS) Phased Array type L-band Synthetic Aperture Radar (PALSAR) (Polychronaki et al., 2013). These SAR-based approaches were, however, limited by (i) the low temporal resolution of the satellites, (ii) the reduced number of polarisations available, (iii) the steep viewing geometries, which were less suitable for vegetation monitoring, and (iv) data access restrictions. With the launch of ESA's Sentinel-1 satellites these shortcomings were largely eliminated due to the significant improvement of the revisit period (i.e., theoretical revisit period of three days for ascending and descending passes combined), availability of dual-polarisation datasets (vertical–vertical, VV, and vertical–horizontal, VH polarisations), shallower incidence angle, and an open data access policy. Such advancements have generated interest in developing regional (Engelbrecht et al., 2017; Lohberger et al., 2018) to global (Belenguer-Plomer et al., 2019b) burned area mapping algorithms and products (i.e., FireCCIS1SA10 for the Amazon basin) based on Sentinel-1 SAR data. Most algorithms use the amount of signal returned to the sensor (backscatter coefficient) without considering the phase information (interferometry) as SAR data processing becomes more

complex and the accuracy of the burned area product is not improved when compared to algorithms based on backscatter coefficient alone (Tanase et al., 2018).

Burned area mapping approaches often use temporal differences between pre- and post-fire datasets (Belenguer-Plomer et al., 2019b; Lohberger et al., 2018; Engelbrecht et al., 2017; Verhegghen et al., 2016; Belenguer-Plomer et al., 2018a). Generally, over vegetated areas, the post-fire backscatter coefficient decreases when compared to unburned areas due to the reduction of the scattering elements (i.e., leaves and branches) through combustion (Van Zyl, 1993; Antikidis et al., 1998). However, opposite trends may be observed, particularly when rainfall occurs after a fire event, since the removal of vegetation allows for increased soil surface scattering particularly for the co-polarised waves (Imperatore et al., 2017; Gimeno & San-Miguel-Ayanz, 2004; Ruecker & Siegert, 2000). Furthermore, changes of the backscatter coefficient in areas affected by fire may take place long past the fire event (up to several months), an effect known as temporal decorrelation (Belenguer-Plomer et al., 2018b, 2019b). One should notice that temporal decorrelation was observed not only over fire-disturbed areas and C-band data. Similar effects were observed for L-band data over areas affected by logging (Watanabe et al., 2018). Therefore, a better understanding of the temporal decorrelation effects and its sources is needed to improve SAR-based burned area mapping algorithms. Thus, the specific objective of this study was to evaluate the influence of different environmental variables that may obscure fire combustion effect on the backscatter coefficient immediately after a fire.

4.2   Study area and datasets

The study was carried out in Portugal over fire-affected areas located in tile 29TNE of the Military Grid Reference System (MGRS). The area was affected by large fires in 2017 (Figure 4.1).

Besides the large areas affected by fires, tile 29TNE was also selected due to (i) Sentinel-1 A/B acquisitions from ascending and descending passes were available at the nominal temporal frequency of six days (Potin et al., 2018), (ii) ancillary data on environmental variables at a detailed spatial resolution were available from the Copernicus Land Monitoring Service program, and (iii) cloud cover was low (annual mean cloud cover of 27.2% as computed from MODIS images) when compared to the mean cloud cover over all Europe (Wilson & Jetz, 2016), which allowed using optical sensors indices as a proxy for a range of environmental variables that informed the analysis.

The SAR dataset was formed by temporal series of dual-polarised (VV and VH polarisations) C-band backscatter coefficient acquired by the Sentinel-1 A/B sensors. The ground range detected (GRD) product acquired using the interferometric wide (IW) swath mode was downloaded from online repositories. As ancillary datasets, optical images acquired by Sentinel-2 MultiSpectral Instrument (MSI) were retrieved. The Sentinel-2 images were used to derive proxy spectral indices for a range of environmental variables (e.g., vegetation water content, fire impact) that may affect C-band scattering processes. Sentinel-1 and -2 images were retrieved from Copernicus Open Access Hub. In addition, information on land cover and surface soil moisture (SSM) were extracted from operational products available through the Copernicus Land Monitoring Service. The Corine Land Cover (CLC) 2018 Version 20b2 at 100 m pixel spacing was used to obtain informa-
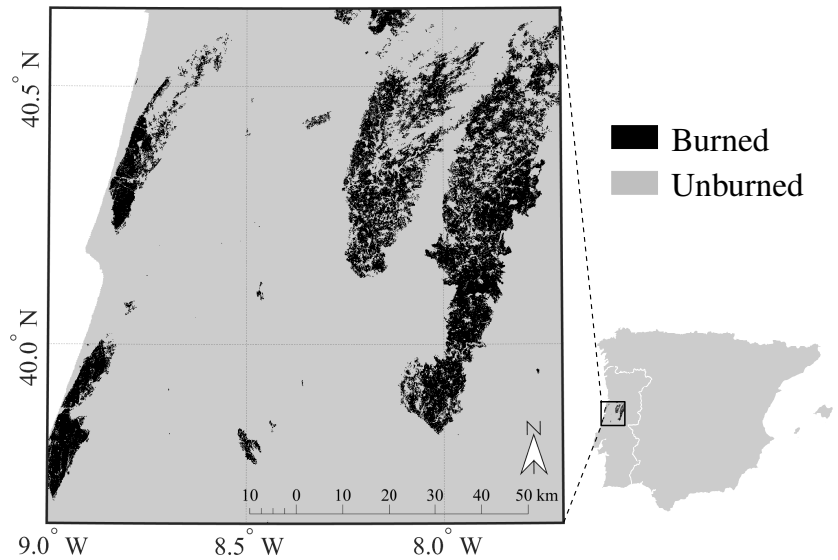
Figure 4.1: Location of the study area and fire scars.

tion on land cover types. The Copernicus Global SSM product, derived from Sentinel-1 data, was used to obtain information on soil moisture in the top few centimetres at 1 km spacing (Bauer-Marschallinger et al., 2018). Lastly, topographic information was derived using the global digital elevation model (DEM) available from the Shuttle Radar Topography Mission (SRTM) at 30 m pixel spacing.

Reference fire perimeters were obtained from atmospherically corrected Landsat-8 optical images retrieved from the United States Geological Survey repository (USGS). The fire perimeters were used to differentiate between burned and unburned pixels during the analysis. Landsat-8 images were used to maintain independence from the environmental variables estimated from Sentinel-2 (Tanase et al., 2018).

4.3   Methods

4.3.1   Earth observation data

The Orfeo ToolBox (OTB), an image processing software developed by the National Centre for Space Studies (CNES) (Inglada & Christophe, 2009), was used to pre-process the Sentinel-1 GRD images. The pre-processing step includes SAR data clipping according to the specified MGRS tiles and radiometric normalisation to gamma nought (γ^0) through the gamma nought lookup table provided with the product metadata. The calibrated images were orthorectified to ground geometry using the topographic information derived from the SRTM. Subsequently, the orthorectified images acquired from the same orbital path, but provided within different slices, were mosaicked. Finally, a multi-temporal filtering was carried out using images from the same orbital path (Quegan et al., 2000). The GRD data were processed to 20 m (Sentinel-1 nominal spatial resolution) and aggregated in post-processing to 40 m spacing, deemed more suitable for burned area detection and mapping from the Sentinel-1 C-band backscatter coefficient due to the reduced speckle (Tanase & Belenguer-Plomer, 2018). The equivalent number of looks for the temporally

filtered, spatially aggregated images was on average 75.

Bottom of atmosphere (BOA) surface reflectance images were derived using the sen-2cor (v.2.4.0) atmospheric correction algorithm from Level-1C (L1C) Sentinel-2 MSI images. Besides atmospheric corrections, sen2cor also allowed the ability to carry out topographic corrections based on the SRTM DEM. The resolution selected during the execution of sen2cor was 20 m, with the processed images being resampled (using a bi-cubic interpolation) to 40 m to match the spatial resolution of the processed Sentinel-1 SAR images. The soil moisture product was also resampled to 40 m using the same resampling method.

4.3.2 Ancillary data

Variables that may affect the C-band scattering process from vegetated areas were evaluated to ascertain their relationship with the observed temporal decorrelation. Fire severity, vegetation growth, and vegetation water content were studied through proxies (i.e., vegetation indices) estimated from Sentinel-2 optical images. Soil surface moisture was retrieved from the Copernicus Global Land Service while the SRTM digital elevation model was used to derive the topography-related variables (i.e., local incidence angle and slope orientation).

4.3.2.1 Fire severity

Fire severity is the degree of organic matter loss due to fire combustion and is strongly related to fire intensity (Keeley, 2009). The SAR backscatter coefficient from burned areas is conditioned by fire severity given the sensitivity to the amount of vegetation scattering elements (Tanase et al., 2010b, 2014). To estimate fire impact on vegetation, the relativized burn ratio (RBR) proposed by Parks et al. (2014) (Equation 4.1) was computed. RBR was shown to accurately represent fire severity levels (Marino et al., 2016; Quintano et al., 2018; Babu et al., 2018) and has a closer relationship with the composite burn index (Key & Benson, 2004), in situ measurement of fire impacts on vegetation when compared to other spectral indices. The RBR was derived using the normalized burn ratio (NBR) (García & Caselles, 1991) (Equation 4.2) and its temporal difference between the pre- and post-fire images, the dNBR (Equation 4.3).

$$\text{RBR} = \text{dNBR} / (\text{NBR}_{pre} + 1.001) \tag{4.1}$$
$$\text{NBR} = (\text{NIR} - \text{SWIR}_2) / (\text{NIR} + \text{SWIR}_2) \tag{4.2}$$
$$\text{dNBR} = \text{NBR}_{pre-fire} - \text{NBR}_{post-fire} \tag{4.3}$$

where NIR and SWIR$_2$ were derived from surface reflectivity of Sentinel-2 Bands 8A and 12, respectively.

4.3.2.2 Water content

The water content of vegetation and soil may alter dielectric proprieties and hence microwaves scattering (Steele-Dunne et al., 2012; Dubois et al., 1995). In this study, both vegetation and soil water content were included as variables that may induce temporal

decorrelation. The normalised difference water index (NDWI, Equation 4.4) was shown to be related to the liquid water molecules in canopies (Gao, 1996) and was therefore used as a proxy to evaluate general vegetation wetness. The Copernicus Global Surface Soil Moisture product, generated at 1 km pixel spacing from Sentinel-1 data, was used as a source of soil water content information (Bauer-Marschallinger et al., 2018).

$$\text{NDWI} = (\text{NIR} - \text{SWIR}_1) / (\text{NIR} + \text{SWIR}_1) \qquad (4.4)$$

where SWIR_1 is the surface reflectivity of Sentinel-2 band 11.

4.3.2.3 Vegetation growth

The normalized difference vegetation index (NDVI, Equation 4.5) (Rouse Jr et al., 1974; Tucker, 1979) is the most extensively used remote sensing index for vegetation monitoring (Xue & Su, 2017). This index offers information about general vegetation greenness, which depends on chlorophyll content and is related to canopy structure (Gamon et al., 1995). NDVI was used as a proxy to evaluate short-term post-fire vegetation recovery since the saturation of the index in Mediterranean ecosystems appears between 5–10 years after the fire event, depending on the vegetation type (Meng et al., 2015; Tanase et al., 2011).

$$\text{NDVI} = (\text{NIR} - \text{RED}) / (\text{NIR} + \text{RED}) \qquad (4.5)$$

where RED is the surface reflectivity of Sentinel-2 band 4.

4.3.2.4 Topography

Topography has a considerable influence on the C-band backscatter coefficient from burned areas through both terrain slope and its orientation with respect to the sensor looking geometry (Belenguer-Plomer et al., 2019b,a). The local incidence angle (LIA) has been frequently used to analyse topography effects on the backscatter coefficient (Tanase et al., 2009, 2010a; Kalogirou et al., 2014; Gimeno & San-Miguel-Ayanz, 2004; Kurum, 2015). However, the wide swath (250 km) of the Sentinel-1 satellites (IW mode) results in an incidence angle variation of approximately 17° from near (29°) to far (46°) range. Thus, the resulting LAI values, which are conditioned by the local slope and the satellite incidence angle, may not necessarily represent the same topographic conditions from near to far range. Therefore, in this study, the local slope and the orientation angle were used to evaluate the effect of topography. Both slope and orientation (aspect) were measured in degrees and derived from the SAR looking geometry and SRTM DEM. The slope values were between 0° to 90°; meanwhile, the aspect values were between -180° and 180°. Negative values indicate slopes oriented away from the sensor, while positive values indicate slopes oriented toward the sensor.

4.3.2.5 Land cover

Information on land cover type was obtained from the Corine Land Cover (CLC) 2018 classification (Kosztra et al., 2017). To reduce the number of land cover classes, the CLC 2018 classification was reduced to: (i) not burnable, which included artificial surfaces, water bodies, wetlands, sands, bare rocks, previous burned areas, and permanent snow

and ice surfaces; (ii) crops, which included all agricultural CLC classes; (iii) herbaceous, which included the natural grasslands, sparsely vegetated areas, moors, and heathlands; (iv) shrubs, which included sclerophyllous vegetation and transitional woodland-shrub; and (v) forests, which included broad-leaved, coniferous and mixed forest CLC classes. The re-classified CLC map was resized to 40 m, through nearest-neighbour interpolation, to match the pixel spacing of the SAR images.

4.3.3   Reference fire perimeters

The reference burned perimeters were obtained following a well-established framework (Padilla et al., 2014, 2015, 2017; Fernandez-Carrillo et al., 2018). Landsat-8 BOA reflectance images were classified in burned, unburned, and no data (i.e., clouds, cloud shadows) using a random forests classifier trained with manually selected polygons. The polygons were digitised over a false colour composite (RGB: SWIR, NIR, R) that allowed for a clear differentiation between burned and unburned patches. Polygon selection followed an iterative process (selection/training/classification), which was repeated until the classification was deemed accurate according to a visual inspection. Finally, the reference perimeters were visually revised again to correct possible misclassifications (Belenguer-Plomer et al., 2019b). A nearest-neighbour interpolation was utilised to resize the reference burned area perimeters to 40 m.

4.3.4   Estimating temporal decorrelation

In this study, only VH data were used to estimate the temporal decorrelation since the cross-polarised waves are more responsive to volumetric scattering from vegetation over Mediterranean ecosystems and less affected by changes in soil surface properties (e.g., soil moisture, surface roughness) when compared to the co-polarised (VV polarisation) channel (Freeman & Durden, 1998; Yamaguchi et al., 2005; Van Zyl et al., 2011; Belenguer-Plomer et al., 2018b). The different sensitivity between co- and cross-polarised waves when deriving burned area maps were previously noted by Belenguer-Plomer et al. (2019b).

To separate burned pixels affected by temporal decorrelation, a potential burned area detection framework was developed to determine if the temporal (pre- and post-fire) and contextual (burned and unburned) variations of VH backscatter were significant to label a pixel as burned. The potential detection framework was based on the analysis of the statistical properties of the VH backscatter coefficient (dB) within and outside the reference fire perimeters at different dates before and after the fire event date (Figure 4.2). The detection framework was established to ascertain the post-fire date at which a pixel may be labelled as burned using the SAR time series. The backscatter analysis was carried out for all burned pixels (determined from Landsat imagery) as well as unburned pixels located within 500 m of the fire scars. The data was first stratified by land cover class, local incidence angle (Tanase et al., 2010a) and slope orientation with respect to the sensor looking geometry (i.e., forward and backwards-looking slopes, respectively). A pixel was labelled as burned when (i) post-fire VH backscatter was greater than the maximum or lower than the minimum backscatter values recorded for the month before the fire date (t_0), and (ii) the difference between the backscatter coefficient of the pixel and the mean of the unburned reference pixels (within the corresponding land cover class) was greater than the maximum recorded during the month preceding the fire. When pre- to post-

fire backscatter variations were small immediately after fire event (i.e., first post-fire SAR image, t_{+1}) but sufficiently high to label a pixel as burnt sometime after the fire and t_{+1}, the pixel was considered temporally decorrelated. The lack of temporal decorrelation is exemplified in Figure 4.2a, as the pixel may be labelled as burned immediately after the fire (t_{+1}). On the contrary, the presence of temporal decorrelation is shown in Figure 4.2b, since the pixel may be labelled as burned (according to the two criteria above) some time after the fire date and t_{+1}, in t_{+i}, being $i > 1$.
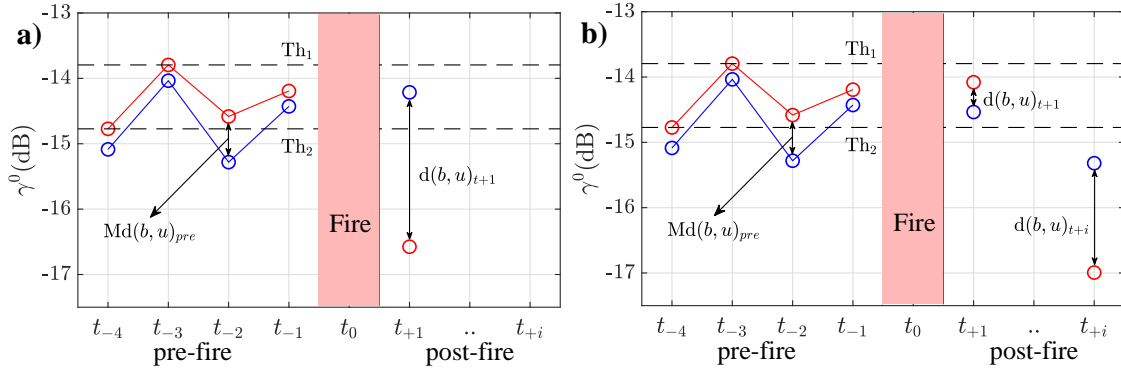

Figure 4.2: Graphical representation of potential burned area detection at pixel level for (**a**) absence of temporal decorrelation and (**b**) presence of temporal decorrelation. Th_1 and Th_2 are the maximum and the minimum backscatter coefficient, respectively, recorded within one month before the fire time (t_0) of a given burned pixel (b), $Md(b, u)_{pre}$ is the maximum difference of backscatter coefficient between b and the mean of the unburned reference pixels (u) one month before t_0, and $d(b, u)_{t+1}$ and $d(b, u)_{t+i}$ represent the difference of backscatter coefficient between b and u for different post-fire images.

4.3.5 Variables analysis

The importance of the variables which affect the C-band backscattering process in burned areas (see subsection 4.3.2) and thus on the perceived temporal decorrelation was analysed by using an ensemble learning algorithm, the random forests (Breiman, 2001). Random forests is frequently used in classification problems and consists in a group of decision trees $\{h(\mathbf{x}\prime, \Theta_z), z = 1, ...\}$, where $\mathbf{x}\prime$ is the input vector of a pixel (x), and Θ_z are a sampled vectors independently bootstrapped with replacement in each decision tree (z). A unique class for x is provided from each tree, with class most often voted being finally assigned to x (Breiman, 2001). During the classification process, random forests compute importance measures for each independent variable (Rodriguez-Galiano et al., 2012; Breiman, 2001). One may use the random forest importance, whose physical meaning is based on the degree with which each variable influences the classification process (Archer & Kimes, 2008), as information to assess the variable significance over a specific study area. Indeed, in recent years an increasing number of studies used random forests to such ends (Belgiu & Drăguţ, 2016; Belenguer-Plomer et al., 2019a; Nguyen et al., 2018; Hislop et al., 2019; Zhang et al., 2019).

Here, the importance of the selected environmental variables was estimated by building random forest models. Such models were customised through the number of trees and training samples used. The number of trees is a key part of the random forests adjustment

as it is known that the use of more trees generates a convergence of the generalisation error and reduce over-fitting (Breiman, 2001; Pal, 2005; Rodriguez-Galiano et al., 2012). However, the use of more trees requires more computational resources. A preliminary empirical analysis concluded that 200 trees provided the best balance between speed and accuracy as statistically significant differences (*t*-test, 95% confidence interval) between variable importance scores obtained from models of 100 and 200 trees, respectively, were not observed (*p*-value of 0.91). The number of variables taken into account for trees growing in each split was computed as the square root of the total number of variables since this reduces the correlation of trees (Rodriguez-Galiano et al., 2012; Gislason et al., 2006). Finally, for inter-comparability purposes, the variable importance values were converted to percentages (Equation 4.6) to evaluate differences between land cover classes as in previous studies (Belenguer-Plomer et al., 2019a).

$$\%VI_{ik} = \frac{VI_{ik} \times 100}{\sum_{i=1}^{n} VI_k} \tag{4.6}$$

where VI is the variable importance of a given variable i and a land cover class k, and n is the total number of variables considered in k.

4.4   Results

4.4.1   Temporal decorrelated pixels over burned areas

Over the entire study area, the frequency of pixels not affected by the temporal decorrelation (not-decorrelated pixels) was higher when compared to pixels mapped as burned at some point after the fire (Figure 4.3). Also, it was evident that pixels affected by temporal decorrelation were concentrated over specific areas.

Not-decorrelated pixels represented the majority (68%) of all burned pixels over all land cover classes, with decorrelated pixels representing the remaining 32% of the burned area. Over all land cover classes, most of the decorrelated pixels (86.88%) were detected within the first post-fire month (Table 4.1). Similar trends were observed for each land cover class. An ANOVA analysis showed no significant difference (*p*-value > 0.05) between the percentage of decorrelated pixels over different detection periods in each land cover class.

4.4.2   Decorrelation analysis

For the first post-fire SAR acquisition, the backscatter coefficient ($\gamma^0_{post-fire} - \gamma^0_{pre-fire}$) for not-decorrelated burned pixels decreased for all land cover classes (Figure 4.4, class Nd_A). Conversely, for pixels affected by temporal decorrelation, the backscatter coefficient was largely stable for the first post-fire SAR acquisition (Figure 4.4, class De_A). For temporally decorrelated burned pixels, the backscatter variations were considerable (Figure 4.4, class De_B), when considering later SAR acquisitions ($\gamma^0_{dec-date} - \gamma^0_{pre-fire}$, where dec-date was the post-fire SAR acquisition when burned area detection criteria were met, see subsection 4.3.4). However, the backscatter coefficient showed variable trends (i.e., decrease and increase) when compared to the pre-fire backscatter values.
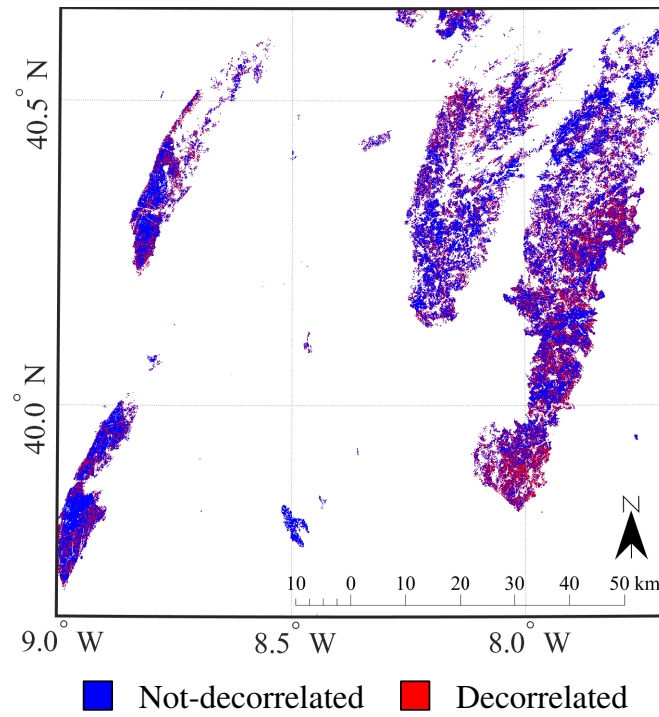
Figure 4.3: Not-decorrelated and decorrelated burned pixels.

Table 4.1: Burned area distribution (km^2) as a function of temporal decorrelation (TD) by land cover classes. PD stands for potential detection month, after post-fire date.

TD	Crops	Herbaceous	Shrubs	Forests	All classes
ND	68.26	68.71	380.9	466.77	984.64
PD 1st	37.30	21.76	148.36	187.03	394.45
PD 2nd	6.06	3.01	15.07	17.86	42
PD 3rd	1.34	0.65	2.64	3.15	7.78
PD 4th	0.88	0.44	1.8	1.82	4.94
PD 5th	0.38	0.57	1.63	1.01	3.59
PD 6th	0.13	0.27	0.56	0.29	1.25
Total	114.35	95.41	550.96	677.93	1438.65

Figure 4.4: Temporal backscatter coefficient variations ($\Delta\gamma^0$ dB) for vertical–horizontal (VH) polarisation for not-decorrelated (Nd) and decorrelated pixels (De). Boxplots show post-fire minus pre-fire values (A) as well as detection date (dec-date) minus pre-fire (B) values as a function of land cover class.

4.4.3 Variable importance on post-fire backscatter coefficient

Fire severity (RBR) was evidenced as the most important variable when separating (i.e., classifying) decorrelated from not-decorrelated pixels over all land cover classes except for the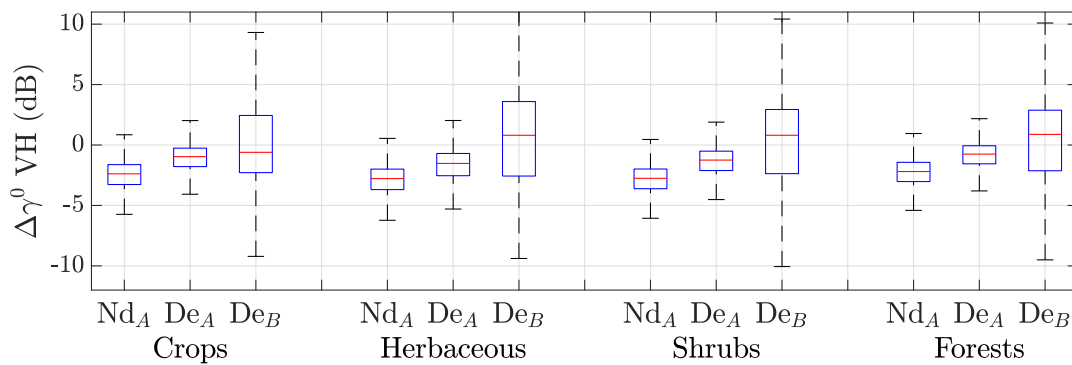 Herbaceous class (Figure 4.5). Over Crops and Forests classes, the fire severity importance was considerably higher (around 30%) when compared to the remaining variables. For the Shrubs class, fire severity was the most important although it was closely followed by slope and variations in the vegetation water content between post- and pre-fire images as estimated through the dNDWI. Variable importance by land cover classes was related to the mean topographic slope (Table 4.2). Aspect and slope showed high importance over Herbaceous and Shrubs classes which covered higher topographic slopes when compared to the Crops and Forests classes (Table 4.2). The reduced importance of aspect and slope on the decorrelation process for the Crops class was explained by its location on low lying terrain when compared to the remaining land cover classes (Figure 4.6).
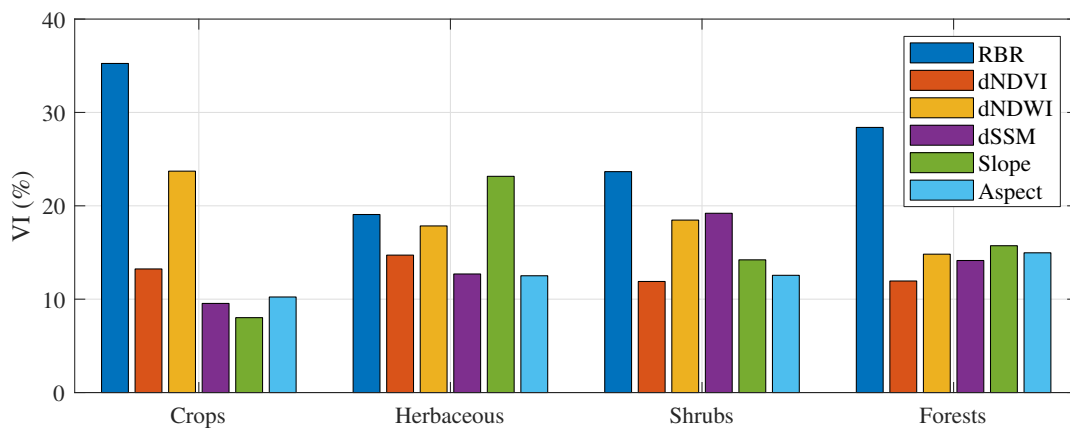
Figure 4.5: Relativized variable importance (VI) over temporal decorrelation process of burned areas by land cover classes. The temporal differences of the normalized difference vegetation index (NDVI), normalized difference water index (NDWI), and soil moisture (SSM) were computed as post-fire minus pre-fire (d).

Table 4.2: Mean topographic slope (°) and confidence interval (95%) as derived from the Shuttle Radar Topography Mission (SRTM) by land cover classes.

Crops	Herbaceous	Shrubs	Forests
6.3±1.06	15.92±1.01	11.51±1.09	9±1.02

Histograms for post- to pre-fire backscatter coefficient change by land cover class and variable (Figure 4.7) show that increased fire severity translates in a high frequency of not-decorrelated pixels, except in the Herbaceous class, where no significant differences were found. The frequency of decorrelated and not-decorrelated pixels was marginally affected by changes in vegetation growth (i.e., dNDVI) and vegetation water content (i.e., dNDWI), with largely similar frequencies observed along the post-to pre-fire variables change gradient. The influence of slope was analysed as a function of aspect (positive-slope oriented towards the sensor and negative-slopes oriented away from the sensor)

Figure 4.6: VH polarisation backscatter coefficient (γ^0 dB) by aspect (°) and land cover classes at post-fire date.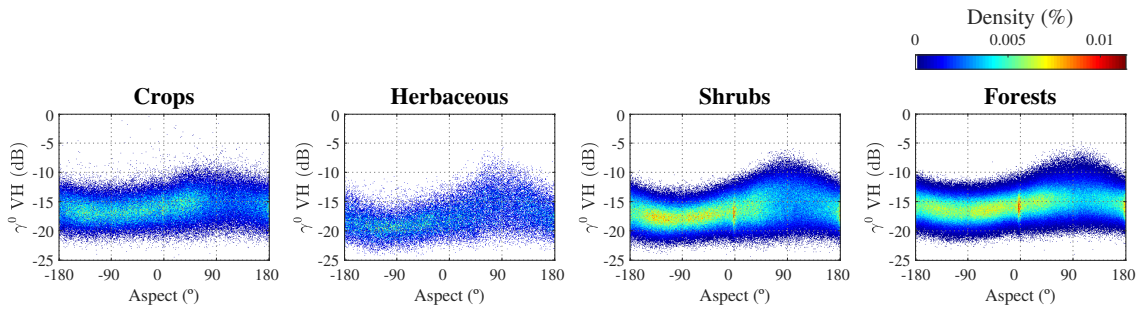 Positive and negative aspect angles correspond to slopes oriented towards and away from the sensor, respectively. Data density is shown as a percentage.

since both variables affect the distance between canopy top and ground surface (Castel et al., 2001). Lower distances are observed for steep slopes oriented towards the sensor when compared to flat areas and slopes oriented away from the sensor (Figure 4.8). Over flat areas (slope below 5°) the proportion of decorrelated and not-decorrelated pixels was similar over all land cover classes. However, over sloped areas (slopes $> 5°$), decorrelated and not-decorrelated pixels proportions differed. For decorrelated burned pixels, post-fire soil moisture was higher when compared to not-decorrelated areas, especially when only pixels from patch size greater or equal than 1 km^2 were considered (the spatial resolution of the soil moisture product used is 1 km).

4.4.4   Variables analysis over decorrelated pixels

As temporally decorrelated pixels are not detected immediately after the fire, it implies that some of the variables affecting the scattering process suffered variations between the post-fire date and the detection date (dec-date). The importance of each variable, except for slope and aspectwhich are not affected by temporal variations, for burned pixels detection, was computed through random forests after differentiating between decorrelated pixels where the backscatter coefficient decreased (Figure 4.9a) and pixels where the backscatter coefficient increased (Figure 4.9b) with respect to the pre-fire values.

When the backscatter coefficient decreases at some point after the fire, the most important variables for burned area detection were temporal changes in soil moisture followed by vegetation growth (dSSM$'$ and dNDVI$'$, respectively, in Figure 4.9a) over all land cover classes except Herbaceous for which all variables were equally important. Fire severity (RBR) importance was higher when the backscatter coefficient decreased at dec-date when compared to areas where the backscatter coefficient increased (Figure 4.9). Conversely, when the backscatter coefficient increased, the most important variable for burned area detection was, by a large margin, the soil moisture (dSSM$'$ in Figure 4.9b), although for the Herbaceous class the importance of the time differences of the soil moisture was lower when compared to the remaining land cover classes.

A backscatter coefficient reduction or increment at the dec-date, when compared to pre-fire values, for decorrelated burned pixels was mainly related to a reduction or respectively increment in soil moisture (Figure 4.10a). The importance of the dNDVI$'$, particularly over Forests, when the backscatter coefficient decreased was explained by a reduction
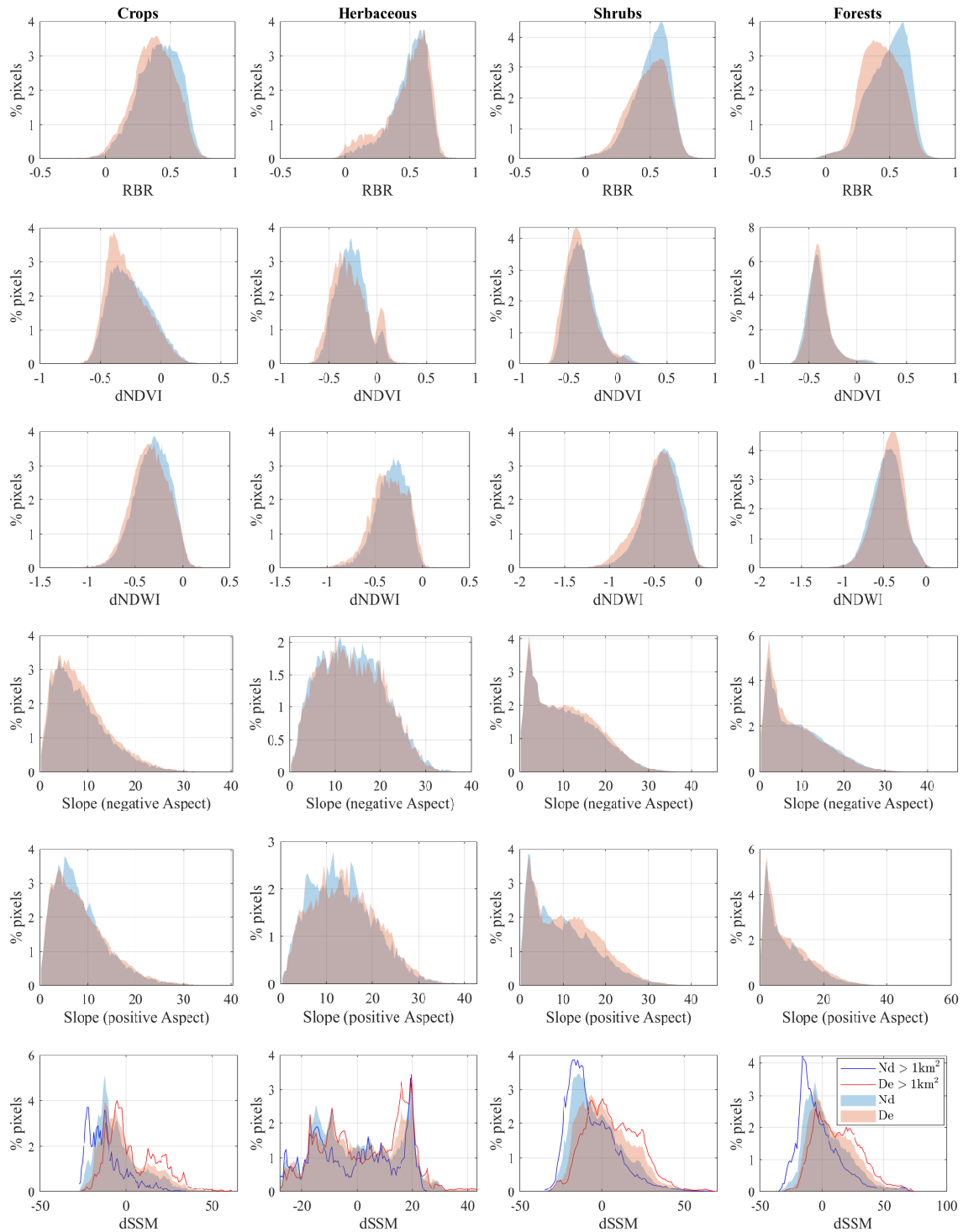
Figure 4.7: Relativized frequency (% of pixels) for decorrelated (De) and not-decorrelated (Nd) pixels by land cover classes (C—crops, H—herbaceous, S—shrubs, and F—forests) for each variable of interest. The temporal differences (d) were computed as post-fire minus pre-fire values. Blue and red lines represent not-decorrelated and decorrelated pixels, respectively, from patches greater or equal than 1 km^2.
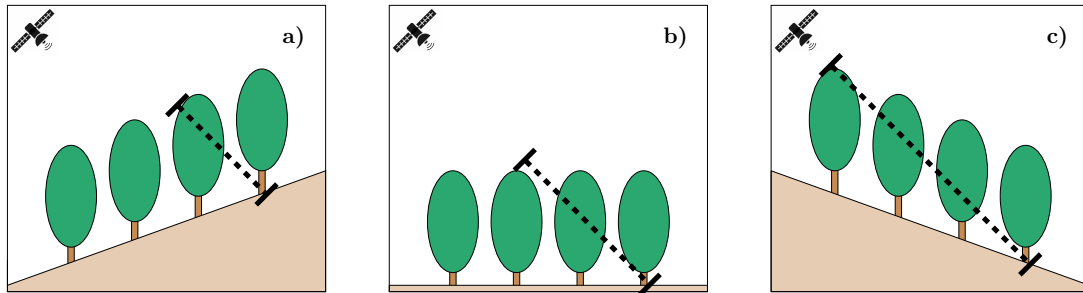
Figure 4.8: Illustration for the distance travelled by radar microwaves through the forest canopy for (**a**) slopes oriented towards the sensor, (**b**) flat areas, and (**c**) slopes oriented away from the sensor.
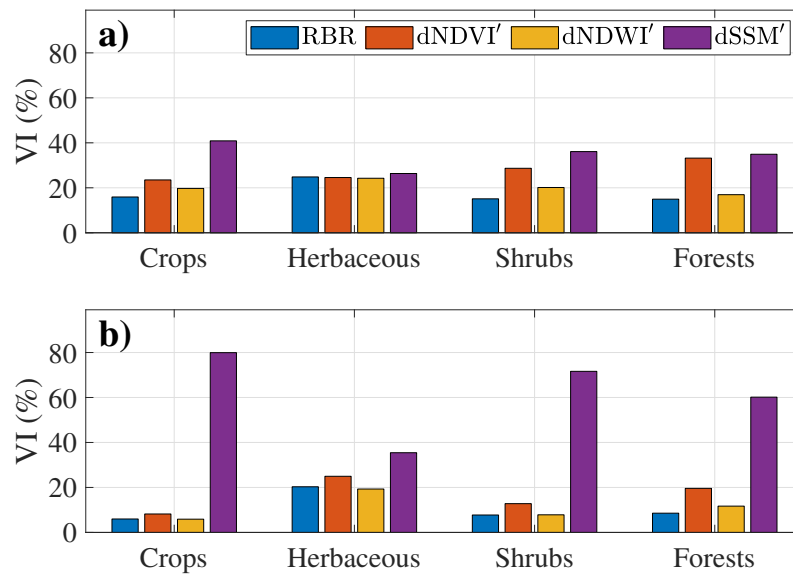
Figure 4.9: Relativized importance of the variables (VI) which changed between dec-date and post-fire and made possible meeting the burned area potential detection criteria after post-fire. Decorrelated burned pixels where the backscatter coefficient decreased (**a**) and increased (**b**) between dec-date and pre-fire were analyzed separately. Land cover classes were considered. The temporal differences of the variables (d...$'$) were computed as dec-date minus post-fire.

in vegetation greenness (Figure 4.10b,c). Decorrelated areas with backscatter decreasing between pre-fire and dec-date were affected by slightly higher fire severity when compared to areas where the backscatter increased between the two dates, particularly over the Forests class (Figure 4.10d).
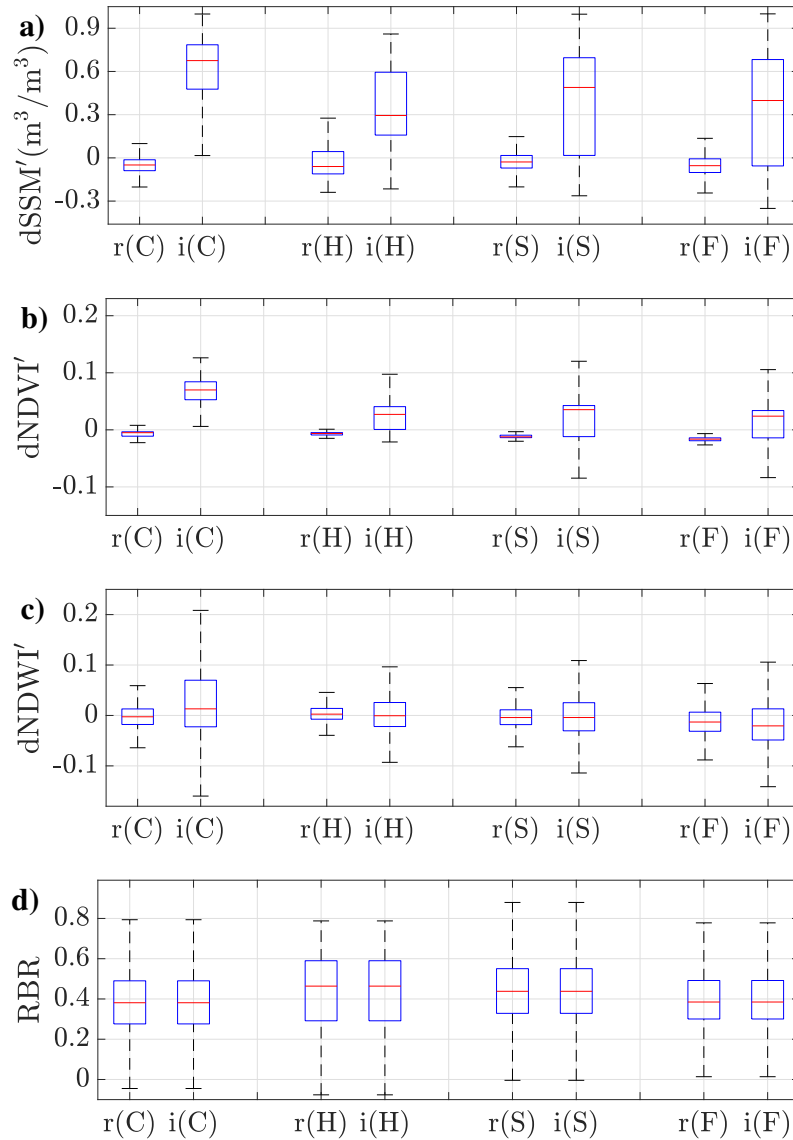
Figure 4.10: Temporal differences of soil moisture (SSM) (**a**), NDVI (**b**), and NDWI (**c**) between the dec-date and the post-fire date (d...$'$), and relativized burn ratio (RBR) (**d**) computed between pre- and post-fire date. The analysis was carried out by land cover classes (C—crops, H—herbaceous, S—shrubs, and F—forests) for temporally decorrelated burned pixels that showed backscatter coefficient reduction (r) and increments (i) at dec-date when compared to the pre-fire datasets.

4.5   Discussions

The existence of spatial patterns for decorrelated and not-decorrelated burned pixels suggested relationships between the temporal decorrelation and the environmental variables, removing the possibility that SAR speckle or detection uncertainty may induce this process randomly. Further, the radiometric uncertainty of the Sentinel-1 sensor, 0.36–0.38 dB (Schwerdt et al., 2017), did not influence the results as most (99.7%) not-decorrelated pixels showed post- to pre-fire temporal differences above this radiometric uncertainty.

Over most land cover classes, the utmost important factor controlling the temporal decorrelation process was fire severity for which higher values were observed over not-decorrelated areas when compared to the decorrelated ones. Such a trend was explained by the higher loss of scattering elements in areas affected by high fire severity (Tanase et al., 2010b, 2014), which translates into a greater backscatter change with respect to unburned vegetation and increased the potential for detecting the affected area immediately after the fire (no temporal decorrelation). As expected, over densely vegetated areas (Forests), fire severity was the most important factor affecting the temporal decorrelation process, which aligns with previous findings related to the sensitivity of the C-band backscatter coefficient to fire impacts in the Mediterranean forests (Tanase et al., 2010b). For the Herbaceous class, fire severity was the second most important factor affecting temporal decorrelation after terrain orientation with respect to the sensor looking geometry (i.e., aspect). This may be related to the mean topographic slope of the Herbaceous class, which was higher when compared to remaining land cover classes. Besides, the divergent results of the Herbaceous may be partly explained by the reduced C-band sensitivity to fire effects over burned herbaceous or grassland areas (Menges et al., 2004) as radar waves interact more with the soil surface. For this class, aspect had higher importance when compared to slope as the low vegetation height, and the lack of woody stems result in low C-band scattering, which is further reduced after the dry season (Menges et al., 2004). Thus, in areas covered by Herbaceous vegetation, the C-band microwaves mostly interact directly with the ground, with scattering being highly conditioned by orientation with respect to the SAR sensor (i.e., aspect).

Water content variations had considerable importance for the decorrelation process over most land cover classes. Higher post-fire soil moisture was observed for decorrelated burned pixels when compared to not-decorrelated ones. This resulted in a higher dielectric constant, and consequently, a higher backscatter coefficient, which may mask out scattering decreases due to the combustion of the vegetated scattering elements since soil influence on the scattering process increases as vegetation is removed through combustion (Tanase et al., 2010a). However, the perceived importance of soil moisture on the temporal decorrelation process was reduced when compared to temporal variations of vegetation water content (dNDWI) since (i) the random forests models were constructed considering all burned pixels, regardless of burned patch size. Thus, approximately half of the pixels used for training the random forests models (44.15% of decorrelated and 62.5% of not-decorrelated classes) were extracted from patches below 1 km^2, the spacing of the soil moisture product. This may have affected the soil moisture estimation accuracy since when only pixels from patches above 1 km^2 were analysed, a clearer effect of soil moisture over the decorrelation process was observed, (ii) for 40% of the decorrelated pixels and 38% of the not-decorrelated ones the pre- to post-fire temporal variations in

soil moisture were lower than 0.088 m^3/m^3, the error of the soil moisture product (Bauer-Marschallinger et al., 2018), and (iii) the dNDWI was derived from atmospherically corrected Sentinel-2 data at the same pixel spacing as the radar images (40 m), which thus having less uncertainty when compared to the SAR based soil moisture product (Sola et al., 2018). Sentinel-1 based soil moisture estimation may be affected by the groundwater content, intercepted rain, and SAR radiometric uncertainty (Benninga et al., 2019). These reasons may explain the difference in the observed importance of the decorrelation process between dNDWI and dSSM. However, this importance contrasts with the low differences of dNDWI between decorrelated and not-decorrelated pixels. It should be noted that random forests models allow for non-linearities and interactions between all variables considered (Grömping, 2009). Thus, it was evidenced that temporal decorrelation over burned areas is a complex process with several variables having a concurrent influence.

Decorrelated pixels tended to have a higher concentration over steep slopes oriented towards the sensor, especially for Herbaceous and Shrubs classes. Conversely, not-decorrelated pixels had a higher presence over shallower slopes and both positive and negative aspects. This result supports previous findings suggesting increased C-band sensitivity to fire over sloped terrain oriented towards the radar sensor (Tanase et al., 2010a; Belenguer-Plomer et al., 2019b). According to the soil moisture product, over sloped areas ($>10°$) soil moisture increased on average for the post-fire images in both Shrubs and Herbaceous classes. As explained above, soil moisture increment may have masked backscatter coefficient changes due to vegetation removal and consequently influenced the decorrelation process. Furthermore, the vegetation effect on the backscatter coefficient over steep slopes oriented towards the sensor (i.e., where the presence of decorrelated pixels was high) is reduced while the ground effects increased since the distance between canopy top and the ground surface is lower when compared to flat areas and slopes oriented away from the sensor (Castel et al., 2001). Such topographic effects are reduced over Forests due to denser canopy, which reduces ground interaction of C-band microwaves and over Crops due to its predominant location over flat areas. The larger scattering elements found in Forest and Shrubs vegetation coupled with the reduced slope allowed for increased C-band scattering from vegetation. Conversely, scattering from ground was reduced, which in turn reduced the importance of the aspectin Forest and Shrubs classes. The root mean square error of the STRM product over Portugal was estimated as 4 to 6 meters depending on land cover and terrain slope (Goncalves & Fernandes, 2005). However, SRTM errors may not have affected the results of this study as most elevation errors were found over (i) abrupt slopes, covered by unburnable land cover classes, and (ii) forested areas, mainly located over flat areas and smooth slopes, with low topography related effects on radar scattering.

Over the not-decorrelated burned pixels the backscatter coefficient decreased after the fire in all land cover classes due to the reduction of vegetation scattering elements through fire-combustion, an effect particularly important for the cross-polarised waves (Freeman & Durden, 1998; Yamaguchi et al., 2005; Van Zyl et al., 2011). However, over the decorrelated burned pixels both reductions and increments of the backscatter coefficient were observed, which indicates that at dec-date, a much wider range of environmental changes generated the backscatter coefficient variations needed to detect the burned area.

Backscatter coefficient reduction at dec-date, when compared to previous records, was mainly attributed to reduced soil moisture since burned areas have reduced albedo as well as increased sun exposure as a result of biomass loss. These effects may generate

a higher temperature regime after the fire event, which may increase soil moisture loss (Certini, 2005) and result in reduced dielectric constant and consequently reduced radar scattering from the ground. Also, the vegetation combustion, which is related to the fire severity, results in a reduced number of scattering elements, which enhances the importance of soil surface scattering (and thus soil moisture) when compared to unburned areas (Tanase et al., 2010a; Kurum, 2015). Alternatively, decreasing water content and vegetation greenness after the fire may occur when trees are damaged by fire but not completely burned. Such trees maintain some scattering elements (e.g., leaves) immediately after the fire, thus sustaining higher levels of radar scattering. However, as a consequence of fire damage, such trees may not recover and die shortly after the fire, which results in reduced backscatter coefficient as dry vegetation has a lower dielectric constant when compared to healthy vegetation (Tanase et al., 2015).

On the other hand, the backscatter coefficient increment at dec-date was mainly related to increased soil moisture. Post-fire vegetation recovery (dNDVI$'$) and canopy water content variations (dNDWI$'$) resulted in an increased backscatter coefficient at dec-date over burned areas. However, dNDVI$'$ and dNDWI$'$ values *per se* have a low influence when distinguishing burned from unburned pixels since unburned areas showed similar or greater changes. Hence, the increase of the NDVI and NDWI values at dec-date when compared to post-fire date was most likely related to vegetation phenology which was an underlying change that incremented the backscatter coefficient over both burned and unburned areas. Short-term post-fire vegetation recovery in the Mediterranean basin is dominated by (i) regeneration of fire-damaged stems, stumps, and roots (depending on the species), (ii) seeding from serotinous and semi-serotinous cones, and (iii) growth of understory species (Bartels et al., 2016). Since this study considered data acquired less than one year after the fire event, the NDVI increment due to such recovery processes has little influence on the backscatter coefficient increment, as few months are insufficient to substantially change scattering processes in slow-growing Mediterranean vegetation. Therefore, it seems most of backscatter increases at dec-date were related to increased soil and vegetation water content.

4.6   Conclusions

This study analysed C-band temporal decorrelation processes over burned areas in a Mediterranean environment. The main factors influencing post-fire radar scattering were analysed as a function of four land cover classes: Crops, Herbaceous, Shrubs, and Forests. Over the studied area, a third of the burned pixels were affected by temporal decorrelation. For most of these pixels (86.9%) the detection was possible during the first month after the fire, although not on the first post-fire SAR acquisition. Fire severity and water availability (in soil or vegetation) were the most important factors affecting the temporal decorrelation over all land cover classes except Herbaceous. The differences observed for the Herbaceous class were most likely related to the reduced sensitivity of C-band to monitor such vegetation types as well as the location in areas of higher topographic slopes.

Generally, the backscatter coefficient decreased in burned areas not affected by temporal decorrelation. The decrease was attributed to the reduction of vegetation scattering elements (i.e., leaves and branches) through fire combustion. Over burned areas affected

by temporal decorrelation, the backscatter coefficient showed diverging trends, e.g., an increase or decrease. Decreasing backscatter coefficient some time after the fire was attributed to (i) reduced soil moisture, and (ii) delayed vegetation death, which reduced post-fire scattering. For decorrelated pixels where the backscatter coefficient increased after the fire, the main factor affecting burned area detection was rainfall and the subsequent increase in soil moisture. In such areas, the backscatter coefficient increased more when compared to unburned areas as reduced vegetation cover increased the proportion of scattering from the wet soil surface.

The main limiting factor of the analysis was the reduced spatial resolution of the Copernicus soil moisture product (1 km) and its availability (Europe alone). Future work shall focus on analysing the decorrelation process in more ecosystems to confirm these findings once ancillary products of sufficient spatial resolution become available worldwide.

Acknowledgements

4.7 References

Andreae, M. O., & Merlet, P. (2001). Emission of trace gases and aerosols from biomass burning. *Global Biogeochemical Cycles*, *15*, 955–966.

Antikidis, E., Arino, O., Arnaud, A., & Laur, H. (1998). ERS SAR Coherence & ATSR Hot Spots: a Synergy for Mapping Deforested Areas. The Special Case of the 1997 Fire Event in Indonesia. *European Space Agency-Publications-ESA SP*, *441*, 355–360.

Archer, K. J., & Kimes, R. V. (2008). Empirical characterization of random forest variable importance measures. *Computational Statistics & Data Analysis*, *52*, 2249–2260.

Babu, K., Roy, A., & Aggarwal, R. (2018). Mapping of Forest Fire Burned Severity Using the Sentinel Datasets. *ISPRS-International Archives of the Photogrammetry, Remote Sensing and Spatial Information Sciences*, *425*, 469–474.

Bartels, S. F., Chen, H. Y., Wulder, M. A., & White, J. C. (2016). Trends in post-disturbance recovery rates of Canada's forests following wildfire and harvest. *Forest Ecology and Management*, *361*, 194–207.

Bauer-Marschallinger, B., Freeman, V., Cao, S., Paulik, C., Schaufler, S., Stachl, T., Modanesi, S., Massari, C., Ciabatta, L., Brocca, L. et al. (2018). Toward global soil moisture monitoring with Sentinel-1: Harnessing assets and overcoming obstacles. *IEEE Transactions on Geoscience and Remote Sensing*, *57*, 520–539.

Belenguer-Plomer, M. A., Chuvieco, E., & Tanase, M. A. (2019a). Evaluation of backscatter coefficient temporal indices for burned area mapping. In *Active and Passive*

Microwave Remote Sensing for Environmental Monitoring III (p. 111540D). International Society for Optics and Photonics volume 11154.

Belenguer-Plomer, M. A., Tanase, M. A., Fernandez-Carrillo, A., & Chuvieco, E. (2018a). Insights into burned areas detection from Sentinel-1 data and locally adaptive algorithms. In *Active and Passive Microwave Remote Sensing for Environmental Monitoring II* (p. 107880G). International Society for Optics and Photonics volume 10788.

Belenguer-Plomer, M. A., Tanase, M. A., Fernandez-Carrillo, A., & Chuvieco, E. (2018b). Temporal backscattering coefficient decorrelation in burned areas. In *Active and Passive Microwave Remote Sensing for Environmental Monitoring II* (p. 107880T). International Society for Optics and Photonics volume 10788.

Belenguer-Plomer, M. A., Tanase, M. A., Fernandez-Carrillo, A., & Chuvieco, E. (2019b). Burned area detection and mapping using Sentinel-1 backscatter coefficient and thermal anomalies. *Remote Sensing of Environment*, *233*, 111345.

Belgiu, M., & Drăguţ, L. (2016). Random forest in remote sensing: A review of applications and future directions. *ISPRS Journal of Photogrammetry and Remote Sensing*, *114*, 24–31.

Benninga, H.-J. F., van der Velde, R., & Su, Z. (2019). Impacts of Radiometric Uncertainty and Weather-Related Surface Conditions on Soil Moisture Retrievals with Sentinel-1. *Remote sensing*, *11*, 2025.

Bojinski, S., Verstraete, M., Peterson, T. C., Richter, C., Simmons, A., & Zemp, M. (2014). The concept of essential climate variables in support of climate research, applications, and policy. *Bulletin of the American Meteorological Society*, *95*, 1431–1443.

Bourgeau-Chavez, L., Harrell, P., Kasischke, E., & French, N. (1997). The detection and mapping of Alaskan wildfires using a spaceborne imaging radar system. *International Journal of Remote Sensing*, *18*, 355–373.

Bourgeau-Chavez, L., Kasischke, E., Brunzell, S., Mudd, J., & Tukman, M. (2002). Mapping fire scars in global boreal forests using imaging radar data. *International Journal of Remote Sensing*, *23*, 4211–4234.

Bowman, D. M., Balch, J. K., Artaxo, P., Bond, W. J., Carlson, J. M., Cochrane, M. A., D'Antonio, C. M., DeFries, R. S., Doyle, J. C., Harrison, S. P. et al. (2009). Fire in the Earth system. *Science*, *324*, 481–484.

Breiman, L. (2001). Random forests. *Machine learning*, *45*, 5–32.

Castel, T., Beaudoin, A., Stach, N., Stussi, N., Le Toan, T., & Durand, P. (2001). Sensitivity of space-borne SAR data to forest parameters over sloping terrain. Theory and experiment. *International journal of remote sensing*, *22*, 2351–2376.

Certini, G. (2005). Effects of fire on properties of forest soils: a review. *Oecologia*, *143*, 1–10.

Chuvieco, E., Lizundia-Loiola, J., Pettinari, M. L., Ramo, R., Padilla, M., Mouillot, F., Laurent, P., Storm, T., Heil, A., & Plummer, S. (2018). Generation and analysis of a new global burned area product based on MODIS 250m reflectance bands and thermal anomalies. *Earth Syst. Sci. Data Discuss*, *512*, 1–24.

Chuvieco, E., Mouillot, F., van der Werf, G. R., San Miguel, J., Tanasse, M., Koutsias, N., García, M., Yebra, M., Padilla, M., Gitas, I. et al. (2019). Historical background and current developments for mapping burned area from satellite Earth observation. *Remote Sensing of Environment*, *225*, 45–64.

Chuvieco, E., Yue, C., Heil, A., Mouillot, F., Alonso-Canas, I., Padilla, M., Pereira, J. M., Oom, D., & Tansey, K. (2016). A new global burned area product for climate assessment of fire impacts. *Global Ecology and Biogeography*, *25*, 619–629.

Dubois, P. C., Van Zyl, J., & Engman, T. (1995). Measuring soil moisture with imaging radars. *IEEE Transactions on Geoscience and Remote Sensing*, *33*, 915–926.

Engelbrecht, J., Theron, A., Vhengani, L., & Kemp, J. (2017). A simple normalized difference approach to burnt area mapping using multi-polarisation C-Band SAR. *Remote Sensing*, *9*, 764.

Fernandez-Carrillo, A., Belenguer-Plomer, M., Chuvieco, E., & Tanase, M. (2018). Effects of sample size on burned areas accuracy estimates in the Amazon Basin. In *Earth Resources and Environmental Remote Sensing/GIS Applications IX* (p. 107901S). International Society for Optics and Photonics volume 10790.

Freeman, A., & Durden, S. L. (1998). A three-component scattering model for polarimetric SAR data. *IEEE Transactions on Geoscience and Remote Sensing*, *36*, 963–973.

French, N. H., Bourgeau-Chavez, L. L., Wang, Y., & Kasischke, E. S. (1999). Initial observations of Radarsat imagery at fire-disturbed sites in interior Alaska. *Remote Sensing of Environment*, *68*, 89–94.

Gamon, J. A., Field, C. B., Goulden, M. L., Griffin, K. L., Hartley, A. E., Joel, G., Penuelas, J., & Valentini, R. (1995). Relationships between ndvi, canopy structure, and photosynthesis in three californian vegetation types. *Ecological Applications*, *5*, 28–41.

Gao, B.-C. (1996). NDWI—A normalized difference water index for remote sensing of vegetation liquid water from space. *Remote sensing of environment*, *58*, 257–266.

García, M. L., & Caselles, V. (1991). Mapping burns and natural reforestation using Thematic Mapper data. *Geocarto International*, *6*, 31–37.

Giglio, L., Boschetti, L., Roy, D. P., Humber, M. L., & Justice, C. O. (2018). The Collection 6 MODIS burned area mapping algorithm and product. *Remote sensing of environment*, *217*, 72–85.

Gimeno, M., San-Miguel, J., Barbosa, P., & Schmuck, G. (2002). Using ERS-SAR images for burnt area mapping in Mediterranean landscapes. *Forest Fire Research & Wildland Fire Safety. (Viegas T ed). Millpress, Rotterdam*, *90*.

Gimeno, M., & San-Miguel-Ayanz, J. (2004). Evaluation of RADARSAT-1 data for identification of burnt areas in Southern Europe. *Remote Sensing of Environment*, *92*, 370–375.

Gimeno, M., San-Miguel-Ayanz, J., & Schmuck, G. (2004). Identification of burnt areas in Mediterranean forest environments from ERS-2 SAR time series. *International Journal of Remote Sensing*, *25*, 4873–4888.

Gislason, P. O., Benediktsson, J. A., & Sveinsson, J. R. (2006). Random forests for land cover classification. *Pattern Recognition Letters*, *27*, 294–300.

Goncalves, J., & Fernandes, J. (2005). Assessment of SRTM-3 DEM in Portugal with topographic map data. In *Proceedings of the EARSeL Workshop 3D-Remote Sensing* (pp. 10–11). Citeseer.

Grömping, U. (2009). Variable importance assessment in regression: linear regression versus random forest. *The American Statistician*, *63*, 308–319.

Hislop, S., Jones, S., Soto-Berelov, M., Skidmore, A., Haywood, A., & Nguyen, T. H. (2019). A fusion approach to forest disturbance mapping using time series ensemble techniques. *Remote sensing of environment*, *221*, 188–197.

Hollmann, R., Merchant, C. J., Saunders, R., Downy, C., Buchwitz, M., Cazenave, A., Chuvieco, E., Defourny, P., de Leeuw, G., Forsberg, R. et al. (2013). The ESA climate change initiative: Satellite data records for essential climate variables. *Bulletin of the American Meteorological Society*, *94*, 1541–1552.

Imperatore, P., Azar, R., Calo, F., Stroppiana, D., Brivio, P. A., Lanari, R., & Pepe, A. (2017). Effect of the Vegetation Fire on Backscattering: An Investigation Based on Sentinel-1 Observations. *IEEE Journal of Selected Topics in Applied Earth Observations and Remote Sensing*, *10*, 4478–4492.

Inglada, J., & Christophe, E. (2009). The Orfeo Toolbox remote sensing image processing software. In *Geoscience and Remote Sensing Symposium, 2009 IEEE International, IGARSS 2009* (pp. IV–733). IEEE volume 4.

Kalogirou, V., Ferrazzoli, P., Della Vecchia, A., & Foumelis, M. (2014). On the SAR backscatter of burned forests: A model-based study in C-band, over burned pine canopies. *IEEE Transactions on Geoscience and Remote Sensing*, *52*, 6205–6215.

Kasischke, E. S., Bourgeau-Chavez, L. L., & French, N. H. (1994). Observations of variations in ERS-1 SAR image intensity associated with forest fires in Alaska. *IEEE Transactions on Geoscience and Remote Sensing*, *32*, 206–210.

Keeley, J. E. (2009). Fire intensity, fire severity and burn severity: a brief review and suggested usage. *International Journal of Wildland Fire*, *18*, 116–126.

Key, C., & Benson, N. (2004). Ground measure of severity, the Composite Burn Index; and Remote sensing of severity, the Normalized Burn Ratio. In G. T. R. RMRS-GTR-164 (Ed.), *FIREMON: Fire Effects Monitoring and Inventory System* chapter Landscape assessment (LA): Sampling and analysis methods. (pp. 1–51). Ogden: USDA Forest Service, Rocky Mountain Research Station.

Kosztra, B., Büttner, G., Hazeu, G., & Arnold, S. (2017). Updated CLC illustrated nomenclature guidelines. *Final Report by European Environmental Agency*, .

Kurum, M. (2015). C-band SAR backscatter evaluation of 2008 Gallipoli forest fire. *IEEE Geoscience and Remote Sensing Letters*, *12*, 1091–1095.

Lohberger, S., Stängel, M., Atwood, E. C., & Siegert, F. (2018). Spatial evaluation of Indonesia's 2015 fire-affected area and estimated carbon emissions using Sentinel-1. *Global change biology*, *24*, 644–654.

Marino, E., Guillén-Climent, M., Ranz Vega, P., & Tomé, J. (2016). Fire severity mapping in Garajonay National Park: comparison between spectral indices. *Flamma: Madrid, Spain*, *7*, 22–28.

Meng, R., Dennison, P. E., Huang, C., Moritz, M. A., & D'Antonio, C. (2015). Effects of fire severity and post-fire climate on short-term vegetation recovery of mixed-conifer and red fir forests in the Sierra Nevada Mountains of California. *Remote Sensing of Environment*, *171*, 311–325.

Menges, C., Bartolo, R., Bell, D., & Hill, G. E. (2004). The effect of savanna fires on SAR backscatter in northern Australia. *International Journal of Remote Sensing*, *25*, 4857–4871.

Mouillot, F., Schultz, M. G., Yue, C., Cadule, P., Tansey, K., Ciais, P., & Chuvieco, E. (2014). Ten years of global burned area products from spaceborne remote sensing—A review: Analysis of user needs and recommendations for future developments. *International Journal of Applied Earth Observation and Geoinformation*, *26*, 64–79.

Nguyen, T. H., Jones, S. D., Soto-Berelov, M., Haywood, A., & Hislop, S. (2018). A spatial and temporal analysis of forest dynamics using Landsat time-series. *Remote sensing of environment*, *217*, 461–475.

Padilla, M., Olofsson, P., Stehman, S. V., Tansey, K., & Chuvieco, E. (2017). Stratification and sample allocation for reference burned area data. *Remote Sensing of Environment*, *203*, 240–255.

Padilla, M., Stehman, S. V., & Chuvieco, E. (2014). Validation of the 2008 MODIS-MCD45 global burned area product using stratified random sampling. *Remote Sensing of Environment*, *144*, 187–196.

Padilla, M., Stehman, S. V., Ramo, R., Corti, D., Hantson, S., Oliva, P., Alonso-Canas, I., Bradley, A. V., Tansey, K., Mota, B. et al. (2015). Comparing the accuracies of remote sensing global burned area products using stratified random sampling and estimation. *Remote Sensing of Environment*, *160*, 114–121.

Pal, M. (2005). Random forest classifier for remote sensing classification. *International Journal of Remote Sensing*, *26*, 217–222.

Parks, S., Dillon, G., & Miller, C. (2014). A new metric for quantifying burn severity: the Relativized Burn Ratio. *Remote Sensing*, *6*, 1827–1844.

Plummer, S., Lecomte, P., & Doherty, M. (2017). The ESA Climate Change Initiative (CCI): A European contribution to the generation of the Global Climate Observing System. *Remote Sensing of Environment*, *203*, 2–8.

Polychronaki, A., Gitas, I. Z., Veraverbeke, S., & Debien, A. (2013). Evaluation of ALOS PALSAR imagery for burned area mapping in Greece using object-based classification. *Remote Sensing*, *5*, 5680–5701.

Potin, P., Rosich, B., Miranda, N., Grimont, P., Shurmer, I., Connell, A. O., Krassenburg, M., & Gratadour, J.-B. (2018). Sentinel-1 Constellation Mission Operations Status. In *IGARSS 2018-2018 IEEE International Geoscience and Remote Sensing Symposium* (pp. 1547–1550). IEEE.

Poulter, B., Cadule, P., Cheiney, A., Ciais, P., Hodson, E., Peylin, P., Plummer, S., Spessa, A., Saatchi, S., Yue, C. et al. (2015). Sensitivity of global terrestrial carbon cycle dynamics to variability in satellite-observed burned area. *Global Biogeochemical Cycles*, *29*, 207–222.

Quegan, S., Le Toan, T., Yu, J. J., Ribbes, F., & Floury, N. (2000). Multitemporal ERS SAR analysis applied to forest mapping. *IEEE Transactions on Geoscience and Remote Sensing*, *38*, 741–753.

Quintano, C., Fernández-Manso, A., & Fernández-Manso, O. (2018). Combination of Landsat and Sentinel-2 MSI data for initial assessing of burn severity. *International journal of applied earth observation and geoinformation*, *64*, 221–225.

Randerson, J., Chen, Y., Werf, G., Rogers, B., & Morton, D. (2012). Global burned area and biomass burning emissions from small fires. *Journal of Geophysical Research: Biogeosciences*, *117*.

Rodriguez-Galiano, V. F., Ghimire, B., Rogan, J., Chica-Olmo, M., & Rigol-Sanchez, J. P. (2012). An assessment of the effectiveness of a random forest classifier for land-cover classification. *ISPRS Journal of Photogrammetry and Remote Sensing*, *67*, 93–104.

Roteta, E., Bastarrika, A., Padilla, M., Storm, T., & Chuvieco, E. (2019). Development of a Sentinel-2 burned area algorithm: Generation of a small fire database for sub-Saharan Africa. *Remote Sensing of Environment*, *222*, 1–17.

Rouse Jr, J., Haas, R., Schell, J., & Deering, D. (1974). Monitoring vegetation systems in the Great Plains with ERTS. In *NASA. Goddard Space Flight Center 3d ERTS-1 Symp* (pp. 309–317). NASA volume 1.

Ruecker, G., & Siegert, F. (2000). Burn scar mapping and fire damage assessment using ERS-2 SAR images in East Kalimantan, Indonesia. *International Archives of Photogrammetry and Remote Sensing*, *33*, 1286–1293.

Schwerdt, M., Schmidt, K., Tous Ramon, N., Klenk, P., Yague-Martinez, N., Prats-Iraola, P., Zink, M., & Geudtner, D. (2017). Independent system calibration of sentinel-1B. *Remote Sensing*, *9*, 511.

Siegert, F., & Hoffmann, A. A. (2000). The 1998 forest fires in East Kalimantan (Indonesia): A quantitative evaluation using high resolution, multitemporal ERS-2 SAR images and NOAA-AVHRR hotspot data. *Remote Sensing of Environment*, *72*, 64–77.

Siegert, F., & Ruecker, G. (2000). Use of multitemporal ERS-2 SAR images for identification of burned scars in south-east Asian tropical rainforest. *International Journal of Remote Sensing*, *21*, 831–837.

Sola, I., García-Martín, A., Sandonís-Pozo, L., Álvarez-Mozos, J., Pérez-Cabello, F., González-Audícana, M., & Llovería, R. M. (2018). Assessment of atmospheric correction methods for Sentinel-2 images in Mediterranean landscapes. *International journal of applied earth observation and geoinformation*, *73*, 63–76.

Steele-Dunne, S. C., Friesen, J., & van de Giesen, N. (2012). Using diurnal variation in backscatter to detect vegetation water stress. *IEEE Transactions on Geoscience and Remote Sensing*, *50*, 2618–2629.

Stroppiana, D., Azar, R., Calò, F., Pepe, A., Imperatore, P., Boschetti, M., Silva, J., Brivio, P. A., & Lanari, R. (2015). Integration of optical and SAR data for burned area mapping in Mediterranean Regions. *Remote Sensing*, *7*, 1320–1345.

Tanase, M., de la Riva, J., Santoro, M., Pérez-Cabello, F., & Kasischke, E. (2011). Sensitivity of SAR data to post-fire forest regrowth in Mediterranean and boreal forests. *Remote Sensing of Environment*, *115*, 2075–2085.

Tanase, M., Santoro, M., de la Riva, J., & Pérez-Cabello, F. (2009). Backscatter properties of multitemporal TerraSAR-X data and the effects of influencing factors on burn severity evaluation, in a Mediterranean pine forest. In *Geoscience and Remote Sensing Symposium, 2009 IEEE International, IGARSS 2009* (pp. III–593). IEEE volume 3.

Tanase, M. A., & Belenguer-Plomer, M. A. (2018). 03. D3 Intermediate validation results: SAR pre-processing and burned area detection, version 1.0. In *ESA CCI ECV Fire Disturbance*. ESA Climate Change Initiative–Fire_cci.

Tanase, M. A., Belenguer-Plomer, M. A., Fernandez-Carrillo, A., Roteta, E., Bastarrika, A., Wheeler, J., Tansey, K., Wiedemann, W., & Navratil, P. (2018). O3.D5 Radar – Algorithm intercomparison document, version 1.1. In *ESA CCI ECV Fire Disturbance*. ESA Climate Change Initiative–Fire_cci.

Tanase, M. A., Ismail, I., Lowell, K., Karyanto, O., & Santoro, M. (2015). Detecting and quantifying forest change: the potential of existing C-and X-Band radar datasets. *PloS one*, *10*, e0131079.

Tanase, M. A., Perez-Cabello, F., de La Riva, J., & Santoro, M. (2010a). TerraSAR-X data for burn severity evaluation in Mediterranean forests on sloped terrain. *IEEE Transactions on Geoscience and Remote Sensing*, *48*, 917–929.

Tanase, M. A., Santoro, M., Aponte, C., & de la Riva, J. (2014). Polarimetric properties of burned forest areas at C-and L-band. *IEEE Journal of Selected Topics in Applied Earth Observations and Remote Sensing*, *7*, 267–276.

Tanase, M. A., Santoro, M., de La Riva, J., Fernando, P., Le Toan, T. et al. (2010b). Sensitivity of X-, C-, and L-band SAR backscatter to burn severity in Mediterranean pine forests. *IEEE Transactions on Geoscience and Remote Sensing*, *48*, 3663–3675.

Tucker, C. J. (1979). Red and photographic infrared linear combinations for monitoring vegetation. *Remote sensing of Environment*, *8*, 127–150.

Van Der Werf, G. R., Randerson, J. T., Giglio, L., Van Leeuwen, T. T., Chen, Y., Rogers, B. M., Mu, M., Van Marle, M. J., Morton, D. C., Collatz, G. J. et al. (2017). Global fire emissions estimates during 1997-2016. *Earth System Science Data*, *9*, 697–720.

Van Zyl, J. J. (1993). The effect of topography on radar scattering from vegetated areas. *IEEE Transactions on Geoscience and Remote Sensing*, *31*, 153–160.

Van Zyl, J. J., Arii, M., & Kim, Y. (2011). Model-based decomposition of polarimetric SAR covariance matrices constrained for nonnegative eigenvalues. *IEEE Transactions on Geoscience and Remote Sensing*, *49*, 3452–3459.

Verhegghen, A., Eva, H., Ceccherini, G., Achard, F., Gond, V., Gourlet-Fleury, S., & Cerutti, P. O. (2016). The potential of Sentinel satellites for burnt area mapping and monitoring in the Congo Basin forests. *Remote Sensing*, *8*, 986.

Watanabe, M., Koyama, C. N., Hayashi, M., Nagatani, I., & Shimada, M. (2018). Early-Stage Deforestation Detection in the Tropics With L-band SAR. *IEEE Journal of Selected Topics in Applied Earth Observations and Remote Sensing*, *11*, 2127–2133.

Wilson, A. M., & Jetz, W. (2016). Remotely Sensed High-Resolution Global Cloud Dynamics for Predicting Ecosystem and Biodiversity Distributions. *PLOS Biology*, *14*, 1–20. URL: `https://doi.org/10.1371/journal.pbio.1002415`. doi:doi: 10.1371/journal.pbio.1002415.

Xue, J., & Su, B. (2017). Significant remote sensing vegetation indices: a review of developments and applications. *Journal of Sensors*, *2017*.

Yamaguchi, Y., Moriyama, T., Ishido, M., & Yamada, H. (2005). Four-component scattering model for polarimetric SAR image decomposition. *IEEE Transactions on Geoscience and Remote Sensing*, *43*, 1699–1706.

Zhang, Y., Sui, B., Shen, H., & Ouyang, L. (2019). Mapping stocks of soil total nitrogen using remote sensing data: A comparison of random forest models with different predictors. *Computers and Electronics in Agriculture*, *160*, 23–30.

Chapter 5

Intercomparison of Sentinel-1 and Sentinel-2 burned area mapping based algorithms

T his chapter provides a comparative analysis of two Sentinel-1 and one Sentinel-2 burned area (BA) detection and mapping algorithms over 10 test sites (100×100 km) in tropical and sub-tropical Africa. The algorithms relied on diverse burned area (BA) mapping strategies regarding the data used (i.e., surface reflectance, backscatter coefficient, interferometric coherence) and the detection method. Algorithm performance was compared by evaluating the agreement between the detected BA with reference fire perimeters independently derived from medium resolution optical imagery (i.e., Landsat 8, Sentinel-2). The commission (CE) and omission errors (OE), as well as the Dice coefficient (DC) for burned pixels, were compared.

The mean OE and CE were 0.33 and 0.31 for the optical-based Sentinel-2 time-series algorithm and increased to 0.66 and 0.36, respectively, for the radar backscatter coefficient-based algorithm. For the coherence based radar algorithm, OE and CE reached 0.72 and 0.57, respectively. When considering all tiles, the optical-based algorithm provided a significant increase in agreement over the Synthetic Aperture Radar (SAR) based algorithms that might have been boosted by the use of optical datasets when generating the reference fire perimeters. However, in regions with persistent cloud cover, the radar sensors may provide a complementary data source for wall-to-wall BA detection and mapping.

5.1   Introduction

Fire has a key ecological role in large part of the Earth's surface since it affects global bio-chemical cycles, carbon sequestration, soil properties, water supply, and biodiversity. Due to its contribution to the global climate system, fire disturbance is considered an Essential Climatic Variable (ECV) (Bojinski et al., 2014) with global burned area (BA) products being routinely derived from coarse resolution sensors (>250 m) such as the Medium Resolution Imaging Spectrometer (MERIS), the Moderate Resolution Imaging Spectrora-diometer (MODIS), or SPOT Vegetation (Tansey et al., 2004; Plummer et al., 2006; Roy et al., 2008; Tansey et al., 2008; Giglio et al., 2009; Alonso-Canas & Chuvieco, 2015; Chuvieco et al., 2016, 2018; Giglio et al., 2018). A comparison analysis done with reference data from 2008 found that NASA's MCD64A1 was the most accurate global BA product of the existing global BA products (Padilla et al., 2015) with commission (CE) and omission errors (OE) reaching 0.42 and 0.68, respectively. More recent analyses, carried out with reference data from 2003 to 2014 (Chuvieco et al., 2018) and 2014 to 2015 (Boschetti et al., 2019), found average commission errors of 0.35 and 0.40, respectively, while omission errors reached 0.62 and 0.73, respectively. With these values, global BA products are far from achieving the accuracy requirements needed for climate modelling, i.e., omission and commission errors below 0.20, (Mouillot et al., 2014), in part due to the low spatial resolution, which results in small fires being overlooked (Randerson et al., 2012). In fact, the likelihood of detecting small burns (i.e., <100 ha) in coarse resolution products is low due to the frequent omission errors (Giglio et al., 2009; Padilla et al., 2015; Randerson et al., 2012).

A recent study suggested that contribution of small fires may be significant as BA products based on MODIS imagery (500 m) estimated 80% less burned area than those based on Sentinel-2 (20 m) in sub-Saharan Africa when compared to products based on medium resolution imagery (Roteta et al., 2019). Small fires have a large impact on emissions in most ecosystems (Van Der Werf et al., 2017). Apart from small fire size, BA uncertainties were also related to satellite instrument calibration and viewing geometry, the temporal sampling related to the persistence of the burn signal, and the detection algorithm design (Brennan et al., 2019). In addition, for atmospheric modelling, ancillary information becomes important, including the detection date, type of burned land (generally relying on external land cover products with their own uncertainties), and combustion completeness and fraction burned area, i.e., critical parameters for atmospheric emission estimations (Chuvieco et al., 2019). To overcome some of these limitations (e.g., small fire size, burned fraction), medium resolution optical sensors have been used for BA detection and mapping with early algorithms being mostly based on Landsat imagery (Stroppiana et al., 2012; Goodwin & Collett, 2014; Stroppiana et al., 2015; Hawbaker et al., 2017; Long et al., 2019). However, detection from Landsat imagery is challenging because of the low temporal resolution of this data (16 days), particularly over areas with persistent cloud cover and short post-fire signal persistence (e.g., savannah fires).

The launches of Sentinel-1 (radar) and Sentinel-2 (optical) sensors have incentivised the development of novel BA detection and mapping algorithms as the availability of relatively dense time-series (3–5 days when different sensors or Synthetic Aperture Radar (SAR) viewing geometries are combined) may significantly reduce omission errors for regions where small fires account for a large proportion of total BA or where the earth

surface is obscured by persistent cloud cover. However, most such algorithms have been developed and tested for rather small areas (Lasaponara & Tucci, 2019; Engelbrecht et al., 2017) or few fire events (Verhegghen et al., 2016; Mathieu et al., 2018; Roy et al., 2019; Stavrakoudis et al., 2019; Filipponi, 2019) except for the global BA prototype product with Landsat data for a single year (Long et al., 2019), and the wall-to-wall mapping of Sub-Saharan Africa performed with Sentinel-2 images for 2016 (Roteta et al., 2019).

Locally developed algorithms are difficult to transfer to other regions as changes in surface reflectance or backscatter coefficient are dependent on a range of factors, including vegetation type and structure, fire regimes, and climatic variables. To improve the characterisation of small fires over large areas, the European Space Agency (ESA) Climate Change Initiative (CCI) programme developed BA algorithms and products from medium resolution sensors for the generation of a small fire database (SFD) at regional to continental scales. The CCI programme aims to obtain information on different ECVs using remote sensing data to help improving climate modelling (Hollmann et al., 2013; Plummer et al., 2017). The SFD was initially focused on sub-Saharan Africa, the most burned continent worldwide (Chuvieco et al., 2018; Giglio et al., 2013), and was largely based on optical sensors (O) and time series (ts) analysis (Ots) (Roteta et al., 2019). Over areas with persistent cloud cover (daily mean cloud cover above 50%), the SFD was complemented by burned perimeters detected from time series of Sentinel-1 C-band radar (R) interferometric coherence (RtsC).

The SFD was complemented by regional BA products in tropical South-East Asia (1.5 million km^2) and South America (7 million km^2). To cope with the persistent cloud cover in these regions, the BA detection and mapping algorithms were based on synthetic aperture radar (SAR) backscatter coefficient acquired by the Sentinel-1 C-band sensor (Lohberger et al., 2018; Belenguer-Plomer et al., 2019). The BA product for tropical South America was based on temporal radar series of the backscatter (B) coefficient (RtsB) while the product for South-East Asia used a multi-temporal approach based on radar backscatter analysis at the beginning and the end of the fire season. The different components of the SFD are available for download from the Fire CCI website (https://www.esa-fire-cci.org).

While the algorithms were individually validated (Roteta et al., 2019; Belenguer-Plomer et al., 2019; Fernandez-Carrillo et al., 2018), such validation was carried out for different areas and time periods. Since the algorithms used to generate the SFD components were based on different input datasets (e.g., optical, SAR) and detection strategies, the objective of this study was to intercompare the algorithms, assessing them over the same areas and with the same reference datasets. However, as the algorithm developed for South-East Asia (Lohberger et al., 2018) was designed specifically for fires in low laying (<15° slope) peat swamp forests, its evaluation outside such conditions was not feasible. Therefore, this study only compared the three time-series algorithms (Ots, RtsB, and RtsC) designed to work over a variety of fire regimes and vegetation types.

5.2   Materials and Methods

5.2.1   Reference datasets

Ten Military Reference Grid System (MGRS) tiles (100×100 km) were used to analyse burned area agreement with reference fire perimeters derived from optical images within the 2015 and 2016 fire seasons (Figure 5.1 and Table 5.1). The tiles were selected along an east-west transect in areas with high fire activity and daily mean cloud cover below 75% to allow for the deployment of the optical-based algorithm (Figure 5.1). Four tiles were dominated (>75% cover) by forests. In the remaining tiles, the land cover was a mix of cropping areas, savannas, grasslands, shrublands, and forests (Table 5.1). The reference datasets were formed by (i) fire perimeters derived from Landsat 8 imagery (four tiles), and (ii) fire perimeters derived from Sentinel-2 imagery (six tiles). Tiles with reference fire perimeters derived from Landsat imagery were selected to assess the effect of temporal discrepancy between BA detection and validation dates.

The Landsat based reference fire perimeters were generated from consecutive image pairs. The time length between consecutive observations was limited (e.g., ideally one satellite cycle) to avoid confusion due to fire-unrelated land cover changes or misinterpretation of the fire signal over areas with rapid vegetation growth. However, in areas with frequent cloud cover, the interval was increased (e.g., up to 32 days) to allow the formation of additional sampling pairs. The use of a larger interval was reasonable as vegetation usually needs longer time to recuperate after fire. Indeed, the global median persistence time of fire scars visible on an optical dataset was estimated as 29 days (Melchiorre & Boschetti, 2018). For efficiency, the surface reflectance of each individual image pair was reformatted into a raster file containing six bands, the shortwave infrared ($SWIR_2$), near infrared (NIR), and RED bands of each image forming the pair. An independent interpreter digitised training polygons for burned and unburned areas and clouds. The polygons were subsequently used to train a Random Forest classifier (Breiman, 2001; Pedregosa et al., 2011), taking as input variables the pre- and post-reflectance and the multitemporal differenced Normalised Burn Ratio (dNBR) index (Key & Benson, 2004). The burned area classification was based on an iterative process of visual inspection, delineation of additional training polygons, and classification. When classification errors were spotted, the classification was improved by digitising missed areas or removing incorrectly labelled areas. Within post-processing, fire perimeters below 0.1 ha were removed.

The Sentinel-2 based reference fire perimeters were selected from an available pool of validation tiles and provided for more diverse land cover types. In each validation tile, two Sentinel-2 cloud-free images with a temporal difference as short as possible were selected in a period where fires were visually observed. The minimum temporal difference was the revisit period of 10 days, which was extended in some cases up to 1 or 2 months (30 or 60 days) due to high cloud coverage or low image availability, particularly in February 2016. The Sentinel-2 L1C products were processed to surface reflectance (Main-Knorn et al., 2017). Reference burned perimeters were generated from the pre- and post-fire reflectance images using the Burned Area Mapping Software (BAMS) (Bastarrika et al., 2014). BAMS also uses training polygons to classify burned areas. The classification results were subsequently analysed by a trained operator. The training polygons were modified until acceptable classification results were obtained. Polygons not correspond-

ing to burned areas were removed manually, with most being caused by cloud shadows and crop harvest.
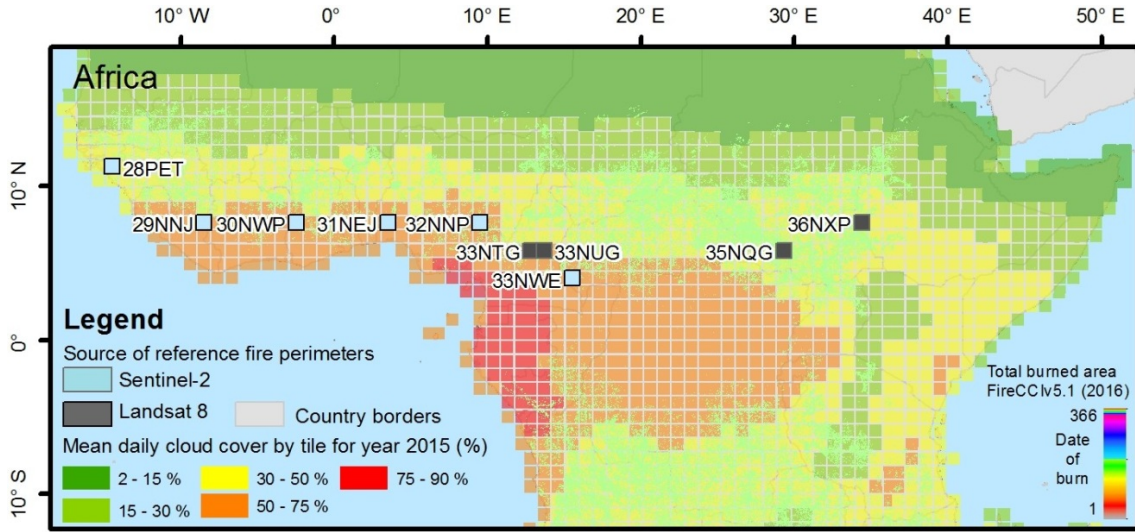

Figure 5.1: Tiles used for inter-comparison together with the mean daily cloud cover (2015) and the total burned (2016), according to the FireCCI5.1 global product. The source of the optical imagery used to generate the reference fire perimeters for each of the analysed tiles is also shown.

5.2.2   SFD algorithms description in brief

5.2.2.1   Optical time series

The optical-based detection algorithm (Ots) uses time-series of atmospherically corrected Sentinel-2 Multi Spectral Instrument (MSI) reflectance measurements from the L2A product (Roteta et al., 2019). The algorithm detects the burned areas using spectral changes in three bands, near-infrared (NIR) and short and long-short shortwave infrared bands (SWIR$_1$, SWIR$_2$) at the original spatial resolution of 20m. These bands are used to calculate two spectral indices the Mid-Infrared Burned Index (MIRBI) and the Normalised Burned Ratio 2 (NBR2) as in Equation 5.1 and Equation 5.2. The algorithm compares two consecutive Sentinel-2 images using the multitemporal difference and the post-fire values of the MIRBI, NBR2 spectral indices, and the NIR reflectance. The algorithm applies fixed thresholds to obtain an Initial Burned/Not Burned area which is cross-checked against the existence of MODIS active fire hotspots. When hotspots exist, the Initial Burned/Not Burned is confirmed (IBC). IBC areas are used to select burned seeds, which are subsequently used to derive a burned membership function, where the minimum and maximum values are extracted from the unburned background and burned areas. The algorithm is locally adapted as IBC existence is tested, and subsequent membership functions are derived for each MGRS tile and Sentinel-2 image pair analysed. As the membership functions are derived at tile level, the algorithm assumes a certain spectral homogeneity for different burned land cover classes. The algorithm uses consecutive Sentinel-2 acquisitions to derive BA maps at 20 m spacing. Unobserved areas (affected by clouds and cloud shadows) are gap-filled by using up to four pre-fire images to reduce omission errors. In areas where Sentinel-2A data were recorded at the nominal frequency and in the absence

Table 5.1: Military Grid Reference System (MGRS) tiles used for inter-comparison. The main land cover type (from CCI Land Cover product, 2015) and the total burned area. The sensor used to generate the reference fire perimeters was labelled [S] for Sentinel-2 and [L] for Landsat-8.

MGRS tile	Main LC (%)			Fire period	BA (km^2)	No. of patches	
	C	G&S	F			Small	Large
28PET[S]	18	14	54	11/01/2016–11/03/2016	1205.6	2717	525
29NNJ[S]	57	24	18	02/01/2016–02/03/2016	1139.4	9736	278
30NWP[S]	58	13	28	27/12/2015–16/01/2016	543.0	2469	182
31NEJ[S]	61	26	10	18/12/2015–07/01/2016	909.4	24957	544
32NNP[S]	50	32	16	22/12/2015–10/02/2016	3609.1	37868	1144
33NTG[L]	0	10	89	15/01/2016–16/02/2016	456.0	4104	274
33NUG[L]	0	28	72	22/10/2016–25/12/2016	271.4	4255	193
33NWE[S]	2	10	87	02/01/2016–22/01/2016	859.5	7212	674
35NQG[L]	0	0	99	01/11/2016–19/12/2016	3529.1	4538	658
36NXP[L]	5	53	42	09/09/2016–12/11/2016	11.6	41	12
All	25.1	21	51.5	————————————	12534.1	97897	4484

LC - land cover (C-crops, G-grassland, S-shrub, F-forest); BA - burned area; Small <25 ha and Large ≥25 ha.

of heavy cloud cover (>95% cloud-free), the BA maps temporal frequency is ten days. A detailed description of the algorithm is found in Roteta et al. (2019).

$$MIRBI = 10 \times SWIR_2 - 9.8 \times SWIR_1 + 2 \tag{5.1}$$
$$NBR2 = (SWIR_1 - SWIR_2) / (SWIR_1 + SWIR_2) \tag{5.2}$$

where $SWIR_2$ and $SWIR_1$ are, respectively, short wave infrared long reflectance and short wave infrared short reflectance.

5.2.2.2   SAR coherence time series

To complement the optical-based burned area in regions affected by persistent cloud cover, a BA detection and mapping algorithm was developed based on time-series of Sentinel-1 interferometric coherence (RtsC). The algorithm needs four consecutive Sentinel-1 acquisitions (12 days apart) to identify the burned areas over the period of interest. For each period of interest, the algorithm generates three interferometric products corresponding to pre-, fire, and post-fire epochs. The post-fire epoch is used to cross-check that burns have indeed taken place. The burned area detection and mapping algorithm uses pre-trained machine learning algorithms such as Random Forests (RF). The training is based on manually selected polygons over four land cover classes (no data, burned, unburned, and water). The training polygons were selected and digitised for each biome in independent tiles distributed over Sub-Saharan Africa using pre- and post-fire Sentinel-2 observations of burn events. Biome specific pre-trained models are used to map burned area at 30 m spacing every 12 days.

5.2.2.3 SAR backscatter coefficient time series

An algorithm based on temporal time-series of Sentinel-1 backscatter coefficient (RtsB) was also developed to identify anomalous changes in the radar signal and associate them with biomass burning (Belenguer-Plomer et al., 2019). The algorithm considers multi-temporal changes of incoherent SAR-based metrics (e.g., backscatter intensities) together with ancillary information on land cover and active fires (hotspots). The Reed-Xiaoli detector (Reed & Yu, 1990) is used to distinguish areas affected by anomalous changes (AC) with respect to a reference state provided by Sentinel-1 dataset acquired before the period of interest. When hotspots coincide in space and time with ACs, these areas are labelled as burned. The remaining ACs are labelled as burned/unburned using machine learning (i.e., RF). The RFs are trained locally (within 100×100 tiles) by main land cover types (e.g., crops, forests). RF training samples are obtained from ACs overlapping hotspots after applying a series of filtering mechanisms to ensure high burned/unburned probabilities of the selected samples. As for the Ots algorithm, the RtsB algorithm is self-calibrating over each MGRS tile and detection period. The algorithm uses consecutive Sentinel-1 acquisitions to derive BA maps at 40 m spacing. The temporal resolution may vary between six days to one month depending on Sentinel-1 actual acquisition frequency. A detailed description of the algorithm is found in Belenguer-Plomer et al. (2019) while its further validation was detailed in Fernandez-Carrillo et al. (2018).

5.2.3 Burned area detection accuracy assessment

The three algorithms were deployed to detect, and map burned area over the time periods with available reference fire perimeters. As inference processes (models) are affected by errors, there is an element of uncertainty regarding the results produced using remote sensing data. Therefore, the quality of remote sensing data and the derived products need to be characterised quantitatively to facilitate critical information on product reliability to end-users. The accuracy of the results is usually characterised through cross-tabulation against reference datasets by accounting for the spatio-temporal coincidences and disagreements. The approach is widely used in BA mapping projects (Giglio et al., 2009; Padilla et al., 2015; Boschetti et al., 2004, 2009; Roy & Boschetti, 2009; Boschetti et al., 2016; Chuvieco et al., 2008; Padilla et al., 2014, 2017). However, one should also bear in mind that cross-tabulation based on ancillary reference datasets derived from remote sensing data acquired by other sensors, largely indicates the agreement between different BA products as the accuracy of the reference dataset is often not known.

For each tile, the agreement between the reference and the detected burned areas was computed through cross-tabulation (Congalton et al., 1991; Latifovic & Olthof, 2004). The result of the cross-tabulation can be represented by the error matrix (Table 5.2), which express the amount of agreement between a product and a reference classification. From the confusion matrix, omission errors (OE, Equation 5.3), commission (CE, Equation 5.4) and the Dice coefficient (DC, Equation 5.5) were computed. DC summarises both commission and omission errors showing the global accuracy for the target category (Padilla et al., 2014).

The detected BA products were matched to the reference BA perimeters dates as closely as possible. However, due to the different satellite orbital cycles, the detection

and validation periods often differed except for the Ots algorithm when deployed over tiles where reference burn perimeters were derived from Sentinel-2 images (i.e., the same sensor was used when generating both reference fire perimeter and the BA product). The validation metrics were computed over each tile, over all tiles, and by main land cover classes (e.g., crops, grasslands, shrubs, and forests). The CCI Land Cover product v2.0.7 for the year 2015 (Kirches et al., 2014) was used to segment the area by main land cover types. Cloud affected areas, no data areas, and Sentinel-1 and -2 pre-processing errors were masked out and were not used when computing the accuracy metrics. The pixel-wise spatial agreement between the optical (Ots) and radar (RtsB) based algorithms was also computed. The RtsB algorithm was used as it showed higher accuracies when compared to the RtsC algorithm.

Table 5.2: Sampled error matrix on a sampling unit. e_{ij} express the agreements (diagonal cells) or disagreements (off diagonal) between the BA product (map) and the reference data.

Product	Refererence		
	Burned	Unburned	Total
Burned	e_{11}	e_{12}	e_{1+}
Unburned	e_{21}	e_{22}	e_{2+}
Total	e_{+1}	e_{+2}	N

$$\text{OE} = e_{21}/e_{+1} \tag{5.3}$$
$$\text{CE} = e_{12}/e_{1+} \tag{5.4}$$
$$\text{DC} = 2e_{11}/(e_{1+} + e_{+1}) \tag{5.5}$$

5.3 Results

Although reference validation periods were common, the detection periods varied slightly depending on the algorithm input data (e.g., Sentinel-1, Sentinel-2), thus limiting a like for like comparison. However, general trends could be distinguished (Table 5.3). The Ots Sentinel-2 algorithm provided superior agreement with the reference fire perimeters when compared to the Sentinel-1 algorithms for all tiles except 33NUG, 33NQG, and 36NXP. Considering all tiles, the Ots algorithm showed OE and CE around 0.3 while for the radar backscatter coefficient-based algorithm (RtsB), the OE and CE were 0.66 and 0.36, respectively. For the coherence-based algorithm (RtsC), slightly higher OE (0.67) and CE (0.55) errors were observed. Over all tiles, the largest difference between the three algorithms was observed for the omission errors, which were twice as much for the radar-based algorithms (0.66 vs 0.33). One should notice that much higher accuracies were obtained for the Ots algorithm over tiles where the validation data were generated from Sentinel-2 images (Table 5.3) when compared to tiles where the validation data was generated from Landsat-8 images. For the later tiles, the Ots algorithm showed OE and CE estimates in the same range as those observed for the RtsB algorithm.

Table 5.3: Agreement between reference and detected BA by algorithm and tile. L- validation data from Landsat-8 images; S-validation data from Sentinel-2 images. All tiles shows values computed for a confusion matrix formed by all pixels from the 10 tiles analysed.

Algorithm	MGRS tile	BA detected (rounded) with respect to reference (in parenthesis) by LC (km^2)					Accuracy metrics (tile level)		
		Total	C	G	S	F	DC	OE	CE
Ots	28PET^S	795 (1206)	43 (64)	3 (4)	53 (84)	679 (1029)	0.76	0.37	0.03
	29NNJ^S	1753 (1139)	923 (696)	65 (13)	266 (234)	487 (194)	0.77	0.09	0.33
	30NWP^S	575 (543)	133 (116)	0 (0)	80 (87)	360 (340)	0.89	0.16	0.04
	31NEJ^S	867 (909)	427 (454)	5 (5)	268 (280)	165 (168)	0.85	0.17	0.12
	32NNP^S	3430 (3609)	1351 (1434)	25 (27)	1281 (1347)	763 (791)	0.89	0.14	0.09
	33NTG^L	442 (456)	0 (0)	0 (0)	74 (83)	366 (372)	0.53	0.5	0.43
	33NUG^L	19 (271)	0 (2)	0 (0)	3 (66)	16 (202)	0.04	0.98	0.51
	33NWE^S	834 (860)	19 (22)	12 (13)	122 (130)	681 (694)	0.86	0.22	0.03
	35NQG^L	3901 (3529)	0 (0)	0 (0)	17 (13)	3880 (3514)	0.37	0.61	0.64
	36NXP^L	216 (12)	4 (1)	0 (0)	92 (10)	118 (0)	0.12	0.57	0.93
	All tiles	12831 (12534)	2901 (2789)	109 (63)	2256 (2335)	7516 (7304)	0.68	0.33	0.31
RtsB	28PET^S	426 (1206)	16 (64)	1 (4)	17 (84)	379 (1029)	0.44	0.71	0.16
	29NNJ^S	935 (1139)	574 (696)	0 (13)	195 (234)	156 (194)	0.72	0.35	0.19
	30NWP^S	1707 (543)	723 (116)	0 (0)	204 (87)	780 (340)	0.49	0.5	0.52
	31NEJ^S	262 (909)	123 (454)	1 (5)	82 (280)	57 (168)	0.16	0.89	0.63
	32NNP^S	1090 (3609)	408 (1434)	8 (27)	412 (1347)	251 (791)	0.31	0.8	0.32
	33NTG^L	343 (456)	0 (0)	0 (0)	63 (83)	279 (372)	0.46	0.61	0.43
	33NUG^L	335 (271)	3 (2)	0 (0)	75 (66)	257 (202)	0.53	0.52	0.41
	33NWE^S	726 (860)	13 (22)	8 (13)	104 (130)	602 (694)	0.61	0.47	0.28
	35NQG^L	2235 (3529)	1 (0)	0 (0)	8 (13)	2225 (3514)	0.46	0.63	0.41

Table 5.3 – continued from previous page

Algorithm	MGRS tile	BA detected (rounded) with respect to reference (in parenthesis) by LC (km^2)					Accuracy metrics (tile level)		
		Total	C	G	S	F	DC	OE	CE
	36NXP^L	101 (12)	3 (1)	0 (0)	56 (10)	42 (0)	0.39	0.18	0.74
	All tiles	8161 (12534)	1864 (2789)	29 (63)	1215 (2335)	5026 (7304)	0.45	0.66	0.36
RtsC	28PET^S	310 (1206)	12 (64)	1 (4)	34 (84)	242 (1029)	0.2	0.87	0.47
	29NNJ^S	143 (1139)	78 (696)	3 (13)	29 (234)	32 (194)	0.15	0.91	0.26
	30NWP^S	344 (543)	27 (116)	0 (0)	37 (87)	279 (340)	0.33	0.76	0.48
	31NEJ^S	244 (909)	127 (454)	1 (5)	74 (280)	41 (168)	0.04	0.98	0.91
	32NNP^S	3933 (3609)	2230 (1434)	31 (27)	1202 (1347)	466 (791)	0.41	0.58	0.61
	33NTG^L	537 (456)	0 (0)	0 (0)	99 (83)	437 (372)	0.19	0.72	0.85
	33NUG^L	19 (271)	0 (2)	0 (0)	5 (66)	14 (202)	0.08	0.96	0.19
	33NWE^S	172 (860)	3 (22)	2 (13)	24 (130)	144 (694)	0.11	0.93	0.54
	35NQG^L	2321 (3529)	0 (0)	0 (0)	12 (13)	2308 (3514)	0.72	0.14	0.38
	36NXP^L	17 (12)	0 (1)	1 (0)	9 (10)	7 (0)	0.12	0.93	0.62
	All tiles	8040 (12534)	2477 (2789)	38 (63)	1524 (2335)	3969 (7304)	0.38	0.67	0.55

By land cover type, the Ots algorithm showed small (<0.20) OE and CE over cropping areas, and shrublands, which increased for savanna (0.17–0.50) and forest (0.42–0.44) vegetation. For the RtsB algorithm, the errors were largely similar over most classes with OE around 0.70 and CE between 0.30 and 0.40 (Table 5.4). For the coherence-based algorithm (RtsC), the OE and CE varied within higher intervals 0.60 to 0.80 and 0.45 to 0.70, respectively. The smallest difference between the optical and the SAR BA mapping accuracy was observed for the forest class (DC 0.57 vs 0.46) and the RtsB algorithm.

The pixel-wise spatial agreement for the total burned area detected by the optical-based Ots and the radar-based RtsB algorithm ranged between 7% and 65% (Table 5.5) except for tile 33NUG where the Ots algorithm performed poorly (Table 5.3). For un-burned areas, the spatial agreement between the two algorithms was above 91% (Table 5.5) except for tile 35NQG where both algorithms had large (>60%) omission errors (Table 5.3 and Figure 5.2). Commission errors usually occurred over different areas for the two algorithms as the spatial agreement was below 1% for six tiles. For tiles 35NQG and 36NXP, CE agreement was much higher (around 20%), which may be related with the low mean daily cloud cover (<30%) or different landscapes in eastern Africa. For the omission er-

Table 5.4: Agreement between reference and detected burned areas by land cover type using a common confusion matrix formed by all pixels from the 10 tiles analysed.

Algorithm	Ots			RtsB			RtsC		
Land cover	DC	OE	CE	DC	OE	CE	DC	OE	CE
Crops	0.85	0.15	0.16	0.43	0.69	0.30	0.29	0.72	0.69
Grasslands	0.62	0.17	0.50	0.39	0.72	0.36	0.29	0.77	0.61
Shrubs	0.84	0.19	0.13	0.41	0.71	0.33	0.34	0.72	0.56
Forests	0.57	0.44	0.42	0.46	0.63	0.38	0.45	0.61	0.46

rors, the agreement between the algorithms reached over 30% in four tiles and over 10% in nine tiles (Table 5.5). Over tiles dominated by low vegetation and high small fires activity (31NEJ, 32NNP), the agreement between the two algorithms was low (<10%) due to the high omission errors observed for the Sentinel-1 algorithm (Figure 5.2). The maximum agreement of the detected burned area (nearly 65%) was observed over tile 29NNJ (Table 5.5 and Figure 5.2). Notice that for unburned areas, the percentage spatial agreement in Table 5.5 was computed using the unburned reference area as the reference. For burned areas, OE and CE, the spatial agreement was computed using as reference the burned area. BA detection accuracy (i.e., DC), as well as the size of the detected burned area, was positively related to the number of large size fire patches (Figure 5.3).

Table 5.5: Spatial agreement (%) between detections from Sentinel-1 (RtsB) and Sentinel-2 (Ots) based algorithms (NB–not burned, BA–burned area, CE–commission errors, OE–omission errors).

MGRS tile	NB S-1 & S-2	BA Sl-1 & S-2	CE S-1 & S-2	OE S-1 & S-2
28PET	98.6	23.3	0.2	30.9
29NNJ	91.4	64.7	2.2	3.6
30NWP	95.7	37.3	0.9	12.4
31NEJ	98.0	6.7	0.4	16.3
32NNP	93.7	7.1	0.7	12.9
33NTG	96.7	21.5	5.7	32.9
33NUG	98.0	1.0	0.3	53.7
33NWE	96.0	41.8	0.4	10.6
35NQG	66.6	18.4	18.6	41.8
36NXP	98.1	36.0	23.1	10.7

The classification rate (classified vs not classified) was also analysed. Not classified pixels corresponded to areas of clouds/shadows in optical images (Ots) or pre-processing errors (e.g., difficulties in deriving coherence estimates) in the radar-based algorithms. The average classification rates for the Ots, RtsB, and RtsC algorithms were 83%, 100%, and 85%, respectively.
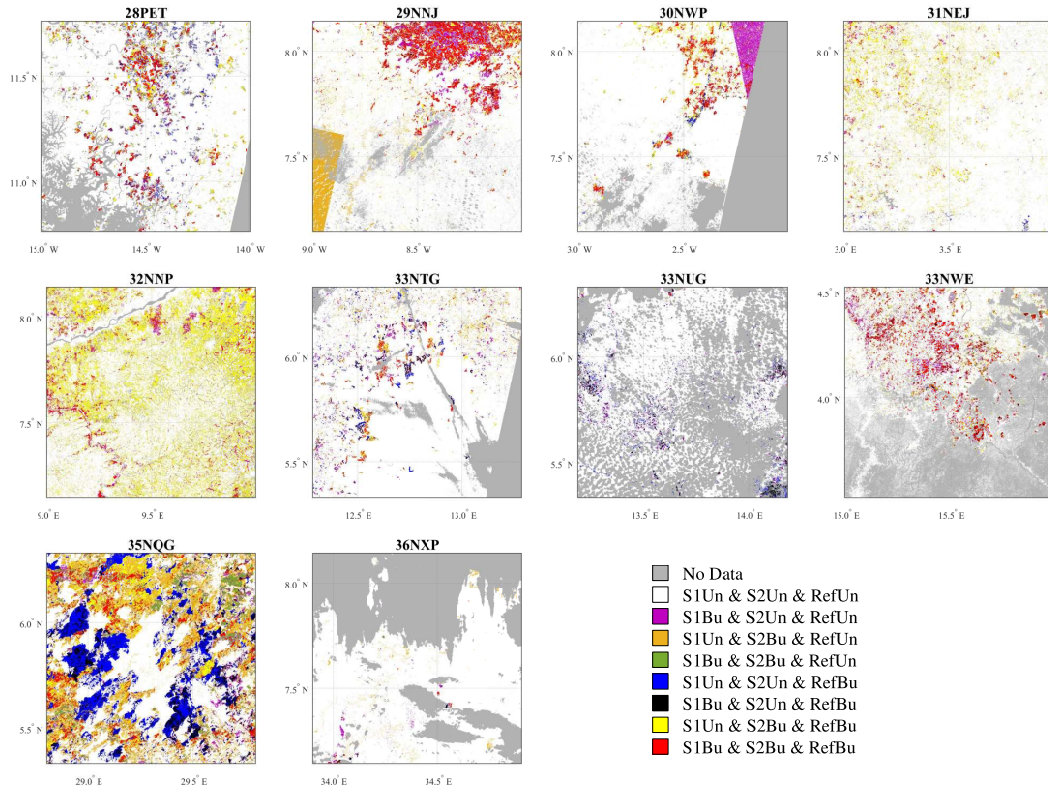
Figure 5.2: Pixel-wise agreement between reference and burned areas detected by the Sentinel-2 (i.e., Ots) and Sentinel-1 (i.e., RtsB) algorithms.
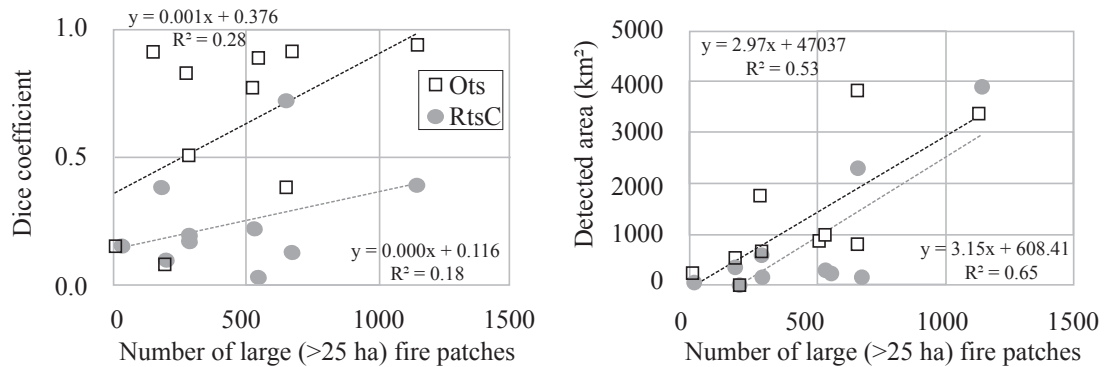

Figure 5.3: The relationship between detection accuracy (left) and detected area (right) for the optical-based (Ots) and interferometric coherence based (RtsC) algorithms for the 10 tiles analysed.

5.4 Discussion

The algorithms compared here were developed using diverse input datasets (optical, radar backscatter, and interferometric coherence) and change detection strategies. Considering all tiles, the use of an optical-based algorithm (Ots) increased the accuracy of burned area detection by about 23% when compared to the most accurate radar-based (RtsB) algorithm (DC 0.68 vs 0.45). When compared to reference fire perimeters derived from independent sensors (i.e., Landsat-8), the RtsB algorithm provided more accurate detection for three of the four tiles analysed (33NUG 35NQG, 36NXP). However, the particularly high errors observed over the 33NUG tile for the Ots algorithm seemed to be related to the few cloud-free observations of the Sentinel-2 sensor. Over tiles where Sentinel-2 images were used to derive the validation perimeters, the BA detection accuracy improved noticeably (OE 0.19 and CE 0.11, average values) for the Ots algorithm (also based on Sentinel-2 images) when compared to tiles where reference perimeters were derived from Landsat images. The increased agreement with the reference data was attributed to (i) exact matching of validation and detection periods thus avoiding errors due to missing or extra days, (ii) the same spatial resolution (20 m) at which validation and detection were carried out and thus lower errors along fire borders, (iii) the use of the same spectral information (Sentinel-2 bands), and (iv) similarities between the BAMS algorithm (used for validation perimeters) and the Ots algorithm as both use a two-step mapping strategy. However, accuracy metrics for the Ots algorithm over Sub-Saharan Africa were higher (DC 0.77, OE 0.27, CE 0.19) when using a fully statistical validation approach (Roteta et al., 2019), which included unmatched validation periods (from Landsat-7 and -8) and temporally long sample units. This suggests that the tiles selected for algorithms inter-comparison may not represent average burn conditions over all of Africa and that temporally short sample units may underestimate BA detection accuracy. Such an assumption is also supported by the higher accuracy observed for the RtsC coherence algorithm, (DC 0.48, OE 0.53, CE 0.57) when assessed over a significantly larger area in the same region (Sub-Saharan Africa) (Padilla et al., 2018). Over the studied tiles, the time series coherence-based algorithm (RtsC) showed larger errors when compared to the time-series backscatter-based algorithm (RtsB) over all areas as well as lower detection rates (85% vs 100%). This suggests that the coherent scattering properties of the vegetation before and after the fire event may not be changing sufficiently in the post-fire image to indicate a fire event may have been present. It was also noticed that the interferometric coherence was very dynamic in Sub-Saharan Africa, possibly as a result of fire-unrelated vegetation structure and moisture changes as a result of the on-going dry season that coincides with the fire season.

Of the three algorithms, only the RtsB algorithm was previously validated over other study areas including 44 sites (20×30 km each) in the Amazon basin (Fernandez-Carrillo et al., 2018) and 18 MGRS tiles globally distributed (Belenguer-Plomer et al., 2019). In the Amazon basin, the RtsB algorithm provided more accurate (DC 0.63 vs 0.45) overall results (Fernandez-Carrillo et al., 2018). The increased accuracy may be related to the different fire regime for the Amazon grasslands (few repeat burns, large fire patches), the large number of sites dominated by forests (25 out of 44), and the use of temporally long sampling units over the Amazon sites (Padilla et al., 2017). When compared to globally distributed MGRS tiles, the accuracy observed in Africa for the RtsB algorithm was generally lower except for the Australian grasslands and shrublands (Belenguer-Plomer et al., 2019). Such spatial differences suggest that the radar-based algorithm may need further

refinement to better adapt to the local conditions (fire regime, vegetation type, environmental factors).

The optical-based Ots algorithm showed a higher variation of the DC by land cover type with values ranging from 0.57 to 0.85. In particular, OE and CE for forests were more than double when compared to other land covers. Such large errors were attributed to the poor performance of the Ots algorithm over the heavily burned 35NQG tile (dominated by forest cover). The large OE (0.61) and CE (0.64) errors in tile 35NQG seemed unrelated to the daily mean cloud cover (15%–30%) or the number of small fire patches as for tile 33NWE (also dominated by forest cover) the OE and CE were much lower (0.22 and 0.03) despite increased mean daily cloud cover (50%–75%), and a similar number of small fire patches. Instead, higher errors in tiles dominated by forest vegetation (33NTG, 35NUG, 35NQG) seemed to be related to mismatches between detection and validation periods due to the use of Landsat imagery when generating the reference fire perimeters. Indeed, for forest dominated tiles (28PET, 33NWE) where reference fire perimeters were generated from Sentinel-2 imagery (i.e., exact matching of detection and validation dates), the observed OE and CE where much lower.

The accuracy of the radar-based algorithms was more stable with DC differences below 0.07 and 0.16 for the RtsB and RtsC, respectively. The Ots and RtsB algorithms showed a consistent pattern in regard to the location of commission errors. Such errors largely occurred over different areas (spatial agreement <6% for most tiles), suggesting potential synergies with a combined radar-optical detection method. The spatial agreement of the burned area detected by the Ots and RtsB algorithms did not depend on the total burned area but was negatively correlated with the number of large fire patches particularly when tile 33NUG was discarded from the analysis (Pearson's r = 0.55). Notice that the Ots algorithm showed poor results (DC = 0.04) over tile 33NUG as explained above. Correlation of DC values with the number of large fire patches reached 0.52, −0.30 and 0.43 for Ots, RtsB, and RtsC respectively suggesting more accurate results with an increasing number of large fire patches for the Ots and RtsC algorithms and the opposite for the RtsB algorithm although the relationship for the latter was weak. In addition, strong correlations (>0.7) were observed between the total burned area detected by the Ots and RtsC algorithms and the number of large fire patches.

The validation of medium resolution (10–30 m) BA products is a known issue due to the difficulty in obtaining reference datasets from high spatial resolution optical sensors (e.g., WorldView, GeoEye, Planet) over large areas and temporal spans. This study was limited by the lack of reference fire perimeters from such high spatial resolution sensors. However, the rather small difference between the spatial resolution at which the burned area was detected 20–40 m and the imagery used to derive the reference fire perimeters (20–30 m) should not impede obtaining at least some preliminary conclusions as shown in this study.

5.5 Conclusions

The analysis suggested that optical-based algorithms may provide for a significant increase in accuracy over SAR based algorithms, particularly over regions where persistent cloud cover is not an issue as detection rates may otherwise drop considerably. However,

BA detection from SAR time series is in its infancy when compared to the decades-long research based on optical sensors. Therefore, more mature SAR-based BA detection algorithms may provide accuracy metrics like those obtained from high-resolution optical data (e.g., Sentinel-2) by taking advantage of combined backscatter-coherence information. Further work is needed to better understand the relationship between interferometric SAR coherence from C-band and the process of vegetation burning in terms of the influence of scatters and their post-fire stability. Furthermore, locally adaptive SAR-based algorithms that use information from different polarisations depending on the land cover type, topography, and post-fire backscatter change direction (increase vs decrease) may improve burned area detection particularly over grass and shrub-dominated areas. Nevertheless, the added complexity of SAR data interpretation and the massive amount of data generated by interferometric SAR processing may only be justified over areas of persistent cloud cover where optical-based algorithms struggle.

Future work should also assess the consequences of the high BA, OE, and CE for greenhouse gases emissions, mitigation actions, restoration work, non-carbon ecosystem services, etc., as such analysis was beyond the scope of this study.

Acknowledgements

5.6   References

Alonso-Canas, I., & Chuvieco, E. (2015).   Global burned area mapping from ENVISAT-MERIS and MODIS active fire data. *Remote Sensing of Environment*, *163*, 140–152.

Bastarrika, A., Alvarado, M., Artano, K., Martinez, M. P., Mesanza, A., Torre, L., Ramo, R., & Chuvieco, E. (2014). BAMS: A tool for supervised burned area mapping using Landsat data. *Remote Sensing*, *6*, 12360–12380.

Belenguer-Plomer, M. A., Tanase, M. A., Fernandez-Carrillo, A., & Chuvieco, E. (2019). Burned area detection and mapping using Sentinel-1 backscatter coefficient and thermal anomalies. *Remote Sensing of Environment*, *233*, 111345.

Bojinski, S., Verstraete, M., Peterson, T. C., Richter, C., Simmons, A., & Zemp, M. (2014). The concept of essential climate variables in support of climate research, applications, and policy. *Bulletin of the American Meteorological Society*, *95*, 1431–1443.

Boschetti, L., Flasse, S. P., & Brivio, P. A. (2004). Analysis of the conflict between omission and commission in low spatial resolution dichotomic thematic products: The Pareto Boundary. *Remote Sensing of Environment*, *91*, 280–292.

Boschetti, L., Roy, D., & Justice, C. (2009). International Global Burned Area Satellite Product Validation Protocol Part I–production and standardization of validation reference data. *Unpublished data*, .

Boschetti, L., Roy, D. P., Giglio, L., Huang, H., Zubkova, M., & Humber, M. L. (2019). Global validation of the collection 6 MODIS burned area product. *Remote Sensing of Environment*, *235*, 111490.

Boschetti, L., Stehman, S. V., & Roy, D. P. (2016). A stratified random sampling design in space and time for regional to global scale burned area product validation. *Remote sensing of environment*, *186*, 465–478.

Breiman, L. (2001). Random forests. *Machine learning*, *45*, 5–32.

Brennan, J., Gómez-Dans, J. L., Disney, M., & Lewis, P. (2019). Theoretical uncertainties for global satellite-derived burned area estimates. *Biogeosciences*, *16*, 3147–3164.

Chuvieco, E., Lizundia-Loiola, J., Pettinari, M. L., Ramo, R., Padilla, M., Mouillot, F., Laurent, P., Storm, T., Heil, A., & Plummer, S. (2018). Generation and analysis of a new global burned area product based on MODIS 250m reflectance bands and thermal anomalies. *Earth Syst. Sci. Data Discuss*, *512*, 1–24.

Chuvieco, E., Mouillot, F., van der Werf, G. R., San Miguel, J., Tanasse, M., Koutsias, N., García, M., Yebra, M., Padilla, M., Gitas, I. et al. (2019). Historical background and current developments for mapping burned area from satellite Earth observation. *Remote Sensing of Environment*, *225*, 45–64.

Chuvieco, E., Opazo, S., Sione, W., Valle, H. d., Anaya, J., Bella, C. D., Cruz, I., Manzo, L., López, G., Mari, N. et al. (2008). Global burned-land estimation in Latin America using MODIS composite data. *Ecological Applications*, *18*, 64–79.

Chuvieco, E., Yue, C., Heil, A., Mouillot, F., Alonso-Canas, I., Padilla, M., Pereira, J. M., Oom, D., & Tansey, K. (2016). A new global burned area product for climate assessment of fire impacts. *Global Ecology and Biogeography*, *25*, 619–629.

Congalton, R. G. et al. (1991). A review of assessing the accuracy of classifications of remotely sensed data. *Remote sensing of environment*, *37*, 35–46.

Engelbrecht, J., Theron, A., Vhengani, L., & Kemp, J. (2017). A simple normalized difference approach to burnt area mapping using multi-polarisation C-Band SAR. *Remote Sensing*, *9*, 764.

Fernandez-Carrillo, A., Belenguer-Plomer, M., Chuvieco, E., & Tanase, M. (2018). Effects of sample size on burned areas accuracy estimates in the Amazon Basin. In *Earth Resources and Environmental Remote Sensing/GIS Applications IX* (p. 107901S). International Society for Optics and Photonics volume 10790.

Filipponi, F. (2019). Exploitation of Sentinel-2 Time Series to Map Burned Areas at the National Level: A Case Study on the 2017 Italy Wildfires. *Remote Sensing*, *11*, 622.

Giglio, L., Boschetti, L., Roy, D. P., Humber, M. L., & Justice, C. O. (2018). The Collection 6 MODIS burned area mapping algorithm and product. *Remote sensing of environment*, *217*, 72–85.

Giglio, L., Loboda, T., Roy, D. P., Quayle, B., & Justice, C. O. (2009). An active-fire based burned area mapping algorithm for the MODIS sensor. *Remote Sensing of Environment*, *113*, 408–420.

Giglio, L., Randerson, J. T., & van der Werf, G. R. (2013). Analysis of daily, monthly, and annual burned area using the fourth-generation global fire emissions database (GFED4). *Journal of Geophysical Research: Biogeosciences*, *118*, 317–328.

Goodwin, N. R., & Collett, L. J. (2014). Development of an automated method for mapping fire history captured in Landsat TM and ETM+ time series across Queensland, Australia. *Remote Sensing of Environment*, *148*, 206–221.

Hawbaker, T. J., Vanderhoof, M. K., Beal, Y.-J., Takacs, J. D., Schmidt, G. L., Falgout, J. T., Williams, B., Fairaux, N. M., Caldwell, M. K., Picotte, J. J. et al. (2017). Mapping burned areas using dense time-series of Landsat data. *Remote Sensing of Environment*, *198*, 504–522.

Hollmann, R., Merchant, C. J., Saunders, R., Downy, C., Buchwitz, M., Cazenave, A., Chuvieco, E., Defourny, P., de Leeuw, G., Forsberg, R. et al. (2013). The ESA climate change initiative: Satellite data records for essential climate variables. *Bulletin of the American Meteorological Society*, *94*, 1541–1552.

Key, C., & Benson, N. (2004). Ground measure of severity, the Composite Burn Index; and Remote sensing of severity, the Normalized Burn Ratio. In G. T. R. RMRS-GTR-164 (Ed.), *FIREMON: Fire Effects Monitoring and Inventory System* chapter Landscape assessment (LA): Sampling and analysis methods. (pp. 1–51). Ogden: USDA Forest Service, Rocky Mountain Research Station.

Kirches, G., Brockmann, C., Boettcher, M., Peters, M., Bontemps, S., Lamarche, C., Schlerf, M., Santoro, M., & Defourny, P. (2014). Land cover cci-product user guide-version 2. In *ESA Public Document CCI-LC-PUG*. ESA Climate Change Initiative–Land Cover_cci.

Lasaponara, R., & Tucci, B. (2019). Identification of burned areas and severity using SAR sentinel-1. *IEEE Geoscience and Remote Sensing Letters*, *16*, 917–921.

Latifovic, R., & Olthof, I. (2004). Accuracy assessment using sub-pixel fractional error matrices of global land cover products derived from satellite data. *Remote sensing of Environment*, *90*, 153–165.

Lohberger, S., Stängel, M., Atwood, E. C., & Siegert, F. (2018). Spatial evaluation of Indonesia's 2015 fire-affected area and estimated carbon emissions using Sentinel-1. *Global change biology*, *24*, 644–654.

Long, T., Zhang, Z., He, G., Jiao, W., Tang, C., Wu, B., Zhang, X., Wang, G., & Yin, R. (2019). 30 m Resolution Global Annual Burned Area Mapping Based on Landsat Images and Google Earth Engine. *Remote Sensing*, *11*, 489.

Main-Knorn, M., Pflug, B., Louis, J., Debaecker, V., Müller-Wilm, U., & Gascon, F. (2017). Sen2Cor for sentinel-2. In *Image and Signal Processing for Remote Sensing XXIII* (p. 1042704). International Society for Optics and Photonics volume 10427.

Mathieu, R., Main, R., Roy, D., Naidoo, L., & Yang, H. (2018). Detection of burned areas in Southern African Savannahs using time series of C-band sentinel-1 data. In *IGARSS 2018-2018 IEEE International Geoscience and Remote Sensing Symposium* (pp. 5337–5339). IEEE.

Melchiorre, A., & Boschetti, L. (2018). Global analysis of burned area persistence time with MODIS data. *Remote Sensing*, *10*, 750.

Mouillot, F., Schultz, M. G., Yue, C., Cadule, P., Tansey, K., Ciais, P., & Chuvieco, E. (2014). Ten years of global burned area products from spaceborne remote sensing—A review: Analysis of user needs and recommendations for future developments. *International Journal of Applied Earth Observation and Geoinformation*, *26*, 64–79.

Padilla, M., Olofsson, P., Stehman, S. V., Tansey, K., & Chuvieco, E. (2017). Stratification and sample allocation for reference burned area data. *Remote Sensing of Environment*, *203*, 240–255.

Padilla, M., Stehman, S. V., & Chuvieco, E. (2014). Validation of the 2008 MODIS-MCD45 global burned area product using stratified random sampling. *Remote Sensing of Environment*, *144*, 187–196.

Padilla, M., Stehman, S. V., Ramo, R., Corti, D., Hantson, S., Oliva, P., Alonso-Canas, I., Bradley, A. V., Tansey, K., Mota, B. et al. (2015). Comparing the accuracies of remote sensing global burned area products using stratified random sampling and estimation. *Remote Sensing of Environment*, *160*, 114–121.

Padilla, M., Wheeler, J., & Tansey, K. (2018). D4. 1.1 Product Validation Report (PVR). In *ESA CCI ECV Fire Disturbance*. ESA Climate Change Initiative–Fire_cci.

Pedregosa, F., Varoquaux, G., Gramfort, A., Michel, V., Thirion, B., Grisel, O., Blondel, M., Prettenhofer, P., Weiss, R., Dubourg, V. et al. (2011). Scikit-learn: Machine learning in Python. *the Journal of machine Learning research*, *12*, 2825–2830.

Plummer, S., Arino, O., Simon, M., & Steffen, W. (2006). Establishing a earth observation product service for the terrestrial carbon community: The GLOBCARBON initiative. *Mitigation and Adaptation Strategies for Global Change*, *11*, 97–111.

Plummer, S., Lecomte, P., & Doherty, M. (2017). The ESA Climate Change Initiative (CCI): A European contribution to the generation of the Global Climate Observing System. *Remote Sensing of Environment*, *203*, 2–8.

Randerson, J., Chen, Y., Werf, G., Rogers, B., & Morton, D. (2012). Global burned area and biomass burning emissions from small fires. *Journal of Geophysical Research: Biogeosciences*, *117*.

Reed, I. S., & Yu, X. (1990). Adaptive multiple-band CFAR detection of an optical pattern with unknown spectral distribution. *Acoustics, Speech and Signal Processing, IEEE Transactions on*, *38*, 1760–1770.

Roteta, E., Bastarrika, A., Padilla, M., Storm, T., & Chuvieco, E. (2019). Development of a Sentinel-2 burned area algorithm: Generation of a small fire database for sub-Saharan Africa. *Remote Sensing of Environment*, *222*, 1–17.

Roy, D. P., & Boschetti, L. (2009). Southern Africa validation of the MODIS, L3JRC, and GlobCarbon burned-area products. *IEEE transactions on Geoscience and Remote Sensing*, *47*, 1032–1044.

Roy, D. P., Boschetti, L., Justice, C. O., & Ju, J. (2008). The collection 5 MODIS burned area product—Global evaluation by comparison with the MODIS active fire product. *Remote Sensing of Environment*, *112*, 3690–3707.

Roy, D. P., Huang, H., Boschetti, L., Giglio, L., Yan, L., Zhang, H. H., & Li, Z. (2019). Landsat-8 and Sentinel-2 burned area mapping-A combined sensor multi-temporal change detection approach. *Remote Sensing of Environment*, *231*, 111254.

Stavrakoudis, D., Katagis, T., Minakou, C., & Gitas, I. Z. (2019). Towards a fully automatic processing chain for operationally mapping burned areas countrywide exploiting Sentinel-2 imagery. In *Seventh International Conference on Remote Sensing and Geoinformation of the Environment (RSCy2019)* (p. 1117405). International Society for Optics and Photonics volume 11174.

Stroppiana, D., Azar, R., Calò, F., Pepe, A., Imperatore, P., Boschetti, M., Silva, J., Brivio, P. A., & Lanari, R. (2015). Integration of optical and SAR data for burned area mapping in Mediterranean Regions. *Remote Sensing*, *7*, 1320–1345.

Stroppiana, D., Bordogna, G., Carrara, P., Boschetti, M., Boschetti, L., & Brivio, P. (2012). A method for extracting burned areas from Landsat TM/ETM+ images by soft aggregation of multiple Spectral Indices and a region growing algorithm. *ISPRS Journal of Photogrammetry and Remote Sensing*, *69*, 88–102.

Tansey, K., Grégoire, J.-M., Defourny, P., Leigh, R., Pekel, J.-F., van Bogaert, E., & Bartholomé, E. (2008). A new, global, multi-annual (2000–2007) burnt area product at 1 km resolution. *Geophysical Research Letters*, *35*.

Tansey, K., Grégoire, J.-M., Stroppiana, D., Sousa, A., Silva, J., Pereira, J., Boschetti, L., Maggi, M., Brivio, P. A., Fraser, R. et al. (2004). Vegetation burning in the year 2000: Global burned area estimates from SPOT VEGETATION data. *Journal of Geophysical Research: Atmospheres*, *109*.

Van Der Werf, G. R., Randerson, J. T., Giglio, L., Van Leeuwen, T. T., Chen, Y., Rogers, B. M., Mu, M., Van Marle, M. J., Morton, D. C., Collatz, G. J. et al. (2017). Global fire emissions estimates during 1997-2016. *Earth System Science Data*, *9*, 697–720.

Verhegghen, A., Eva, H., Ceccherini, G., Achard, F., Gond, V., Gourlet-Fleury, S., & Cerutti, P. O. (2016). The potential of Sentinel satellites for burnt area mapping and monitoring in the Congo Basin forests. *Remote Sensing*, *8*, 986.

Chapter 6

CNN-based burned area mapping using radar and optical data

In this chapter, we present an in-depth analysis of the use of convolutional neural networks (CNN), a deep learning method widely applied in remote sensing-based studies in recent years, for burned area (BA) mapping from combined radar and optical datasets acquired by Sentinel-1 and respectively Sentinel-2 sensors. Five areas, distributed worldwide, are used to establish the optimum (i) CNN dimensionality for feature extraction (i.e., 1D or 2D), (ii) data normalization (i.e., z-score or [0, 1] interval), and (iii) number of hidden layers. Five independent areas are used to validate the optimum CNN model.

The optimum CNN dimension and data normalisation parameters were conditioned by the observed land cover class and the type of sensor (optical or radar) while increasing the network complexity (i.e., number of hidden layers) affected the computing time without improving the BA mapping accuracy. The use of optimum CNN settings when considering combining SAR and optical data allowed for (i) mapping the burned areas with similar or slightly better accuracy to those achieved in previous approaches carried based on Sentinel-1 (Dice coefficient 0.57) and Sentinel-2 (DC 0.7) sensors, respectively, and (ii) wall-to-wall mapping by eliminating information gaps due to cloud cover when using optical-based algorithms.

6.1   Introduction

Fire is one of the natural disturbance processes that apart from generating significant social and economic consequences (Chuvieco et al., 2010), most modifies the terrestrial ecosystems by reducing biodiversity, changing water supply and liberating vegetated-sequestered carbon (Hansen et al., 2013; Aponte et al., 2016; Pausas & Paula, 2012; Lavorel et al., 2007). At global scale, emissions of aerosols and greenhouse gases (GHGs) from fires may modify the Earth's biochemical cycles and the radiative energy balance (Van Der Werf et al., 2017; Bowman et al., 2009; Jin & Roy, 2005). Fire-induced carbon emissions have been estimated to be 2.2 PgC per year over the period 1997-2016 (Van Der Werf et al., 2017), which translates to 20-30% of global emissions from burning fossils fuels, triggering the current global warming (Kloster et al., 2012; Flannigan et al., 2009). Besides, it is observed a direct relationship between the rising of Earth's temperature and the frequency of fires (Hoffmann et al., 2002; Knorr et al., 2016). Hence, given the global warming current context, such a relationship may reinforce the fire role progressively on climate change (Flannigan et al., 2006; Langenfelds et al., 2002). However, fires may also result in opposite effects by enabling global cooling processes as a result of increased aerosols in the atmosphere, which induce negative radiative forcing (Ward et al., 2012). Such opposite effects suggest a limited understanding of fire effects on global climate (Krawchuk et al., 2009; Liu et al., 2019).

Due to its undeniable climatic and environmental importance, fire is considered by the Global Climate Observing System (GCOS) as an Essential Climatic Variable (ECV). An ECV is a physical, biological, chemical, or a group of connected variables capable of altering the climate system (Bojinski et al., 2014). The European Space Agency (ESA), through the Climate Change Initiative (CCI) programme, is generating remote sensing-based ECVs to improve climate modelling (Plummer et al., 2017; Hollmann et al., 2013). Fire has been included in the CCI programme since 2010 (Fire_cci project). Improving current BA products by developing new algorithms based on state-of-the-art Earth observation datasets as well as generating a long-term time series of global BA have been the main goals of the Fire_cci project (Chuvieco et al., 2018). One driving factor behind the project was the need for more accurate BA products that reduce current uncertainties when studying the fire-induced climate impacts (Mouillot et al., 2014; Poulter et al., 2015). In particular, emissions from small size fires were of particular concern (Van Der Werf et al., 2017).

Many BA global products have been released over the past decade, predominantly based on optical imagery acquired by the Moderate Resolution Imaging Spectroradiometer (MODIS), such as the MCD45 (Roy et al., 2008), MCD64 (Giglio et al., 2009, 2018), Fire_cci v5.0 (Chuvieco et al., 2018) and Fire_cci v5.1 (Lizundia-Loiola et al., 2020). However, such products have limitations as small-sized fires are difficult to detect due to the coarse pixel spacing (>250 m). Such limitations generate uncertainty about the extent of the global burned area (Chuvieco et al., 2019). In order to reduce BA mapping uncertainty, imagery acquired by medium spatial resolution optical sensors such as Landsat-8 and Sentinel-2 are increasingly used to map BA at regional and global scales. Indeed, a recent study over sub-Sahara Africa based on Sentinel-2 images for 2016 quantified an increase of 80% over existing global BA products (MCD64A1 product Version 6) for the same region and year (Roteta et al., 2019). In addition to problems observed to detect

small fire patches, global BA products are also affected by cloud cover, which difficulties detection of burn pixels, particularly in Tropical regions where fire signal lasts short. In particular, the continuous cloud cover at inter-tropical and boreal latitudes prevents BA mapping from optical sensors. In order to circumvent such limitations, active sensors (e.g., synthetic aperture radar – SAR) have been used as an alternative to optical imagery for mapping BA (Bourgeau-Chavez et al., 2002; French et al., 1999). The launch of ESA's Sentinel-1 A and B in October 2014 and December 2015, respectively, have greatly improved the availability of SAR images, by operationally acquiring (i) dual-polarisation C-band imagery (i.e., vertical–vertical, VV, and vertical–horizontal, VH polarisations), while (ii) providing precise orbital information, (iii) allowing for viewing geometries more suitable for vegetation monitoring through increased incidence angle, and (iv) improving spatial and temporal resolution, as revisit period of Sentinel-1 mission is three days when combining ascending and descending passes from Sentinel- A and B. Such advances, coupled to a free data access policy, have allowed for the development of SAR-based BA mapping algorithms (Belenguer-Plomer et al., 2019c). Indeed, a first large scale BA product based on Sentinel-1 datasets was released recently for the Amazon basin for the year 2017 (https://www.esa-fire-cci.org/, last accessed March 15th, 2020).

Availability of near-concurrent active (Sentinel-1) and passive (Sentinel-2) datasets allows taking advantage of similar spatial and temporal resolutions of radar and optical information. Nevertheless, few studies have considered combining such sensors when mapping BA. In addition, there is little consensus regarding the benefits of such data combination. Some studies noted that active-passive data might reduce limitations associated with each data-source (Verhegghen et al., 2016). On the contrary, other studies suggest limited to nil benefits (Brown et al., 2018). The potential of radar-optical based approaches depends on several limiting factors depending on the sensor type. Optical sensors are severely restricted by cloud cover or strong variations in solar illumination (Bourgeau-Chavez et al., 2002; French et al., 1999). SAR data limitations are related to sensitivity to fire unrelated changes such as soil moisture variations and steep topography (Belenguer-Plomer et al., 2019a, 2018). Besides, BA detection and mapping accuracy from both types of sensors are affected by the land cover class (Tanase et al., 2020). Previous studies investigating the SAR-optical (SAR-O) combination potential for BA mapping have been carried out over relatively small study areas or single biomes, which reduces results validity of global BA detection and mapping algorithms (Verhegghen et al., 2016; Brown et al., 2018; Stroppiana et al., 2015). Furthermore, the strengths and weaknesses of combining active and passive datasets within a single BA classification algorithm as opposed to by sensor BA detection and subsequent results combination have only been superficially analysed.

In recent years, deep learning methods have been widely applied in many remote sensing-based studies (Zhu et al., 2017). Among deep learning methods, the convolutional neural networks (CNN) are extensively used for classifying satellite images (Ma et al., 2019) with few studies addressing BA detection and mapping (Ban et al., 2020; Pinto et al., 2020). The limited literature on CNN applied to BA mapping, and the need for a more profound understanding of its strengths and limitations over the previous classification approaches, particularly the impact of different configurations on BA detection accuracy, and the relevance of land cover and fire severity impacts on detection performance. This chapter analyses the potential of CNN for BA mapping when SAR and optical data are combined, considering a wide range of burning conditions. Data from Sentinel-1,

Sentinel-2 and the combination of the two satellite sensors have been used to test different CNN configurations for classifying burned pixels. The analysis was carried out over different ecosystems and biomes with significant fire activity. The specific objectives of the study were to (i) determine the optimum CNN parameters (i.e., image dimensionality for feature extraction, data normalisation, and the number of hidden layers) for each input dataset (i.e., radar, optical and SAR-O) and land cover class, and (ii) to find the optimal active-passive approach for BA mapping. This optimal configuration was validated over independent study areas located in fire-prone biomes worldwide.

6.2   Study areas and datasets

Ten Military Grid Reference System (MGRS) tiles distributed over biomes frequently affected by fires were used as study areas. Five tiles were used to find the optimum mapping configuration through CNN parameters and sensor combination (i.e., training tiles) whereas the remaining five were reserved for validating results with independent sites, as well as to check the algorithm generalisation capability (i.e., test tiles) (Figure 6.1).
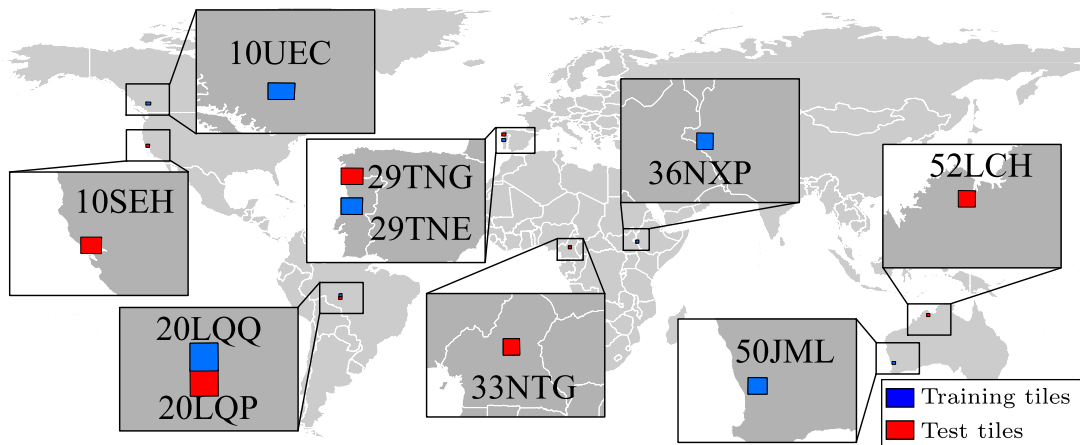

Figure 6.1: Location of the Military Grid Reference System tiles used for training and test.

Ground range detected (GRD) C-band backscatter coefficient temporal series acquired by the Sentinel-1 A and B satellites using the interferometric wide (IW) swath mode were the source of radar information. Images acquired by the MultiSpectral Instrument (MSI) aboard the Sentinel-2 A and B satellites were the source of optical information. As ancillary data, the enhanced Shuttle Radar Topography Mission (STRM) DEM at 30 m pixel spacing was used when pre-processing the SAR and optical datasets (see subsection 6.3.1). Sentinel-1 and Sentinel-2 data were downloaded from Copernicus Open Access Hub. Additional ancillary datasets including land cover information as well as thermal anomalies (i.e., hotspots) of active fires were used within the BA mapping algorithm. The land cover information was extracted from the ESA's landcover CCI product for the year 2015 Land_Cover_cci, which uses the Land Cover Classification System (LCC) (Di Gregorio, 2005). In order to simplify the BA mapping procedure, the LCC legend was simplified to six landscapes (i.e., shrublands, grasslands, forests, crops, non-burnable and others, which includes transitional woodland-shrub as well as sclerophyllous vegetation) as in our previous research study (Belenguer-Plomer et al., 2019c). Hotspots from

VIIRS (Visible Infrared Imaging Radiometer Suite) (Schroeder et al., 2014) and MODIS (Giglio et al., 2016) sensors at 375 m and 1 km of spatial resolution, respectively, were downloaded from NASA's Fire Information for Resource Management System (FIRMS).

Reference fire perimeters were used to validate the BA products. The reference perimeters were derived from independent sensors (i.e., Landsat imagery) to avoid auto-correlation (Tanase et al., 2020). Landsat-8 BOA (Bottom Of Atmosphere) reflectance images with cloud cover below 70% were downloaded from the United States Geological Survey repository (USGS) for each tile. The extraction of the reference fire perimeters is explained in detail in section subsection 6.3.4.

6.3 Methods

6.3.1 Sentinel-1 pre-processing

Sentinel-1 GRD images were processed using the Orfeo ToolBox (OTB), an open-source software developed by the Centre National D'Etudes Spatiales (CNES), France (Inglada & Christophe, 2009). The processing chain has been utilised in previous studies (Belenguer-Plomer et al., 2019c,b; Ottinger et al., 2017; Bouvet et al., 2018) and when generating the FireCCIS1SA10 product, the first large scale BA product from Sentinel-1 data for the Amazon basin. Sentinel-1 data processing may be divided into three steps: data-preparation, geocoding, and multi-temporal filtering (Figure 6.2). Sentinel-1 data was calibrated radiometrically to gamma nought (γ^0) via a lookup table obtained from the product metadata. The calibrated imagery was orthorectified using topographical information from the SRTM DEM. Since ESA often provides Sentinel-1 images of the same relative orbit within distinct slices, images from the same orbit were mosaicked and then spatially trimmed to the coordinates of the MGRS tile. Lastly, the processed images of each orbit were filtered using a multi-temporal filter (Quegan et al., 2000). All images were processed to the Sentinel-1 nominal resolution (20 m) and subsequently aggregated to 40 m to reduce speckle (Tanase & Belenguer-Plomer, 2018).

BA mapping is an iterative process with the fire-detection period being defined by the temporal gap between two consecutive acquisitions. For each fire-detection period (t_0), determined by two Sentinel-1 consecutive acquisition dates (t_{-1} and t_{+1}), the two most recent images acquired before t_0 (i.e., pre-fire) and all images acquired up to 180 days after t_0 (post-fire) were used as input for the CNN BA mapping algorithm. Information from both polarisations (VV and VH), as well as their ratio (VH/VV), was extracted and used for each SAR image. The 180 days post-fire interval accounted for fire-induced temporal variation of the backscattering process that may occur at some point after a fire event due to temporal decorrelation (Belenguer-Plomer et al., 2019b).

6.3.2 Sentinel-2 pre-processing

The ESA's atmospheric correction algorithm sen2cor (v.2.4.0) was used to derive bottom of atmosphere (BOA) Sentinel-2 images and correct for topographic effects on surface reflectance. The bi-cubic interpolation was subsequently used to resample the 20 m Sentinel-2 images to the pre-processed Sentinel-1 output resolution of 40 m. Tempo-
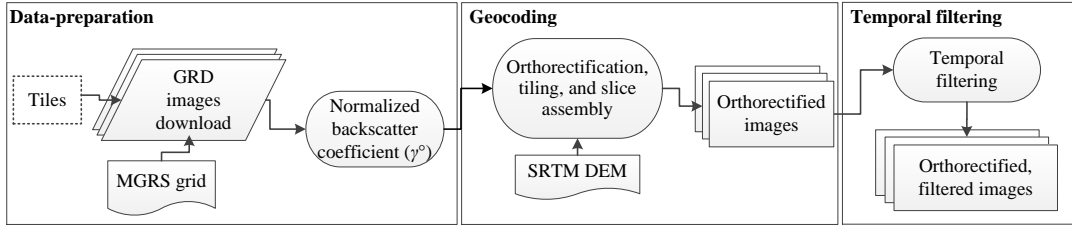
Figure 6.2: Data chain pre-processing of SAR images with Orfeo ToolBox (Belenguer-Plomer et al., 2019c).

ral composites were generated to reduce the number of cloud-affected pixels using both Sentinel-2 A and B images for the selected bands (i.e., B02, B03, B04, B05, B06, B07, B8a, B11 and B12). Given a fire-detection period (t_0), as determined by two consecutive acquisition dates of Sentinel-2 A and B (t_{-1} and t_{+1}), the sen2cor-based Scene Classification (SCL) was considered when generating the temporal composites for t_{-1} and t_{+1}. Pixels affected by clouds or shadows were gap-filled using data from Sentinel-2 imagery acquired at the closest date before t_{-1} and past t_{+1}, up to 30 days (Melchiorre & Boschetti, 2018) (Figure 6.3).
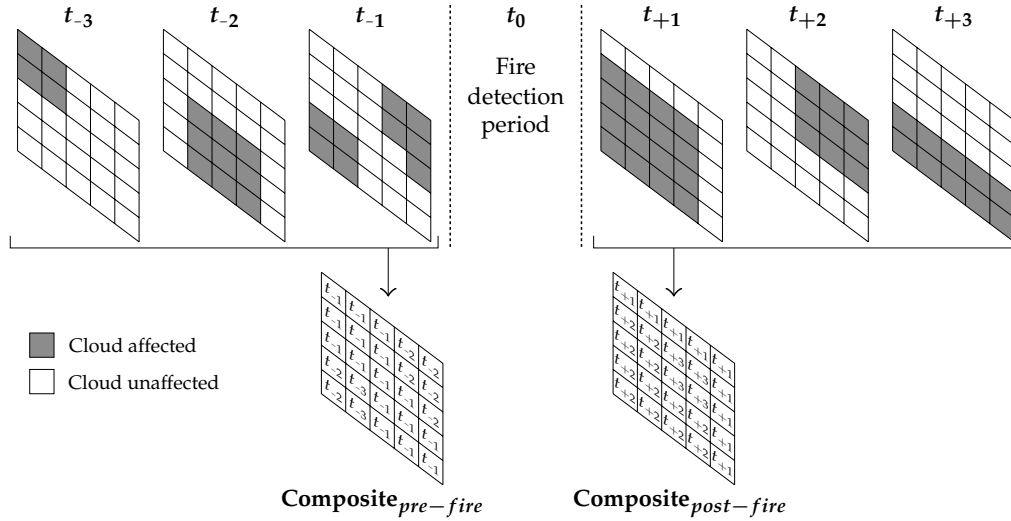

Figure 6.3: Graphical representation of temporal composite formation.

Along with the surface reflectance for each of the two temporal composites (pre- and post-fire), the following indices were computed and fed into the CNN: (i) the Normalized Burn Ratio (García & Caselles, 1991) (NBR, Equation 6.1); (ii) the Normalized Difference Water Index (Gao, 1996) (NDWI, Equation 6.3); (iii) the Normalized Difference Vegetation Index (Rouse Jr et al., 1974; Tucker, 1979) (NDVI, Equation 6.2); and (iv) the Mid InfraRed Burn Index (Trigg & Flasse, 2001) (MIRBI, Equation 6.4). These indices are frequently used for BA mapping from optical datasets (Roteta et al., 2019; Loboda et al.,

2007; Fraser et al., 2000).

$$NBR = (NIR - SWIR_2) / (NIR + SWIR_2) \tag{6.1}$$
$$NDVI = (NIR - Red) / (NIR + Red) \tag{6.2}$$
$$NDWI = (NIR - SWIR_1) / (NIR + SWIR_1) \tag{6.3}$$
$$MIRBI = 10 \times SWIR_2 - 9.8 \times SWIR_1 + 2 \tag{6.4}$$

where Red, NIR, SWIR1 and SWIR2 are the surface reflectances of bands 4 (650-680 nm), 8a (785-899 nm), 11 (1565-1655 nm) and 12 (2100-2280 nm), respectively, of MSI aboard Sentinel-2 satellites.

6.3.3 SAR-optical data integration

As Sentinel-1 and Sentinel-2 acquisition dates may not coincide when capturing images over the same geographical area, the acquisition dates of Sentinel-1 defined each fire-detection period (t_0), when jointly using SAR and optical data, due to their complete spatial coverage (e.g., no missing pixels due to cloud cover). Sentinel-2 images are then matched to the Sentinel-1 dates for each detection period as follows: (i) for the pre-fire date, the closest Sentinel-2 image acquired before (if no coincident image is available) is selected as t_{-1} date; and (ii) for the post-fire date, the closest image acquired after (if no coincident image is available coincident) is selected as t_{+1} date. Once the Sentinel-2 interval is matched with the Sentinel-1detection interval, cloud-related gaps are filled through the temporal composite process (see subsection 6.3.2). Subsequently, the Sentinel-1 radar-derived images (i.e., VV, VH and VH/VV ratio) acquired on t_{-1} and t_{+1} as well as the Sentinel-2 temporal composites (i.e., spectral bands and spectral-indices) were stacked and fed into the classification algorithm. Similar to Sentinel-1 and Sentinel-2 fusion approaches have been previously used for vegetation monitoring (Sharma et al., 2018; Tavares et al., 2019), also employing CNN (Scarpa et al., 2018).

6.3.4 Reference burned perimeters and validation

The reference fire perimeters were extracted from Landsat-8 surface reflectance. The extraction was based on the validation framework previously established for BA products (Padilla et al., 2014, 2015, 2017; Fernandez-Carrillo et al., 2018). A random forests classifier was trained using burned and unburned samples as well as no data (i.e., clouds). Sample selection was carried out via manual digitisation of polygons over a false colour composite (RGB: SWIR$_2$, NIR, R) which provided an experienced user with a clear visual distinction between burned and unburned pixels. Input data for the random forests classifier were (i) the band 5 (NIR; 0.85-0.88 ʈm) and band 7 (SWIR$_2$; 2.11-2.29 ʈm) of post-fire date, (ii) the NBR of post-fire (Equation 6.1), and (iii) the temporal difference between pre- and post-fire of NBR values (dNBR) from Landsat-8 images. Model-training and scene classification was carried out iteratively until the reference fire perimeters were considered accurate through visual inspection.

Confusion matrices were used to validate the CNN-based BA maps (Table 6.1). The Dice coefficient (Equation 6.7) and the omission (Equation 6.5) and commission errors (Equation 6.6), which are widely used metrics when validating BA products, were com-

puted from the matrix to assess the quality of the maps (Padilla et al., 2015).

Table 6.1: Confusion matrix example.

Detection	Refererence data		
	Burned	Unburned	Row total
Burned	P_{11}	P_{12}	P_{1+}
Unburned	P_{21}	P_{22}	P_{2+}
Col. total	P_{+1}	P_{+2}	N

$$\text{OE} = P_{21}/P_{+1} \tag{6.5}$$

$$\text{CE} = P_{12}/P_{1+} \tag{6.6}$$

$$\text{DC} = 2P_{11}/\left(P_{1+} + P_{+1}\right) \tag{6.7}$$

6.3.5   Burned area mapping experimental setup

The burned area mapping algorithm identifies changes in C-band backscatter and surface reflectance associated with burning events. BA mapping was carried out using (i) Sentinel-1 derived incoherent SAR-based metrics (see subsection 6.3.1), (ii) Sentinel-2 surface optical reflectance (see subsection 6.3.2), and (iii) combining SAR and optical selected datasets (see subsection 6.3.3). Thus, up to three BA maps derived from different input datasets were generated for each detection period. Hotspots and land cover information were used for algorithm training purposes (see subsubsection 6.3.5.2).

6.3.5.1   Convolutional Neural Networks (CNN) background

Deep learning methods are increasingly applied to remote sensing problems (Zhu et al., 2017) with CNN being widely used in land cover classification, the retrieval of bio-geophysical variables (Ma et al., 2019) or BA detection and classification (Ban et al., 2020; Pinto et al., 2020). CNNs are structured by stages of convolution, non-linearity and pooling, followed by at least one fully connected layer (LeCun et al., 2015; Zhu et al., 2017). Each convolutional layer carries out a spatial-spectral feature extraction (Zhong et al., 2019), generating a set of filtered data where patterns such as edges are emphasised (Strigl et al., 2010). From the convoluted filtered data, each neuron takes a vector and applies an activation function of a weighted linear summation (Equation 6.8) (Maggiori et al., 2016).

$$a = f\left(\mathbf{w}\mathbf{x} + b\right) \tag{6.8}$$

where a is the neuron output, $\mathbf{w}$ is the weight given to the vector $\mathbf{x}$, b is the bias value, and f is the activation function which introduces non-linearity into the network and permits learning complex features from data (Agostinelli et al., 2014; Saha et al., 2019). The most common activation function in remote sensing applications is the rectified linear unit (ReLU) (Nair & Hinton, 2010), which activates values greater than or equal to zero,

while it converts the remaining to zero (Equation 6.9).

$$f(x) = \begin{cases} x, \ x \geq 0 \\ 0, \ x < 0 \end{cases} \tag{6.9}$$

A loss function is used to quantify the errors when classifying a training vector data, comparing the CNN-based prediction with the label of such vector (Maggiori et al., 2016). The weights and biases of each neuron are adjusted using the backpropagation criterion during the network training, carrying out multiple iterations forward and backwards to minimise the errors via gradient descent (Anantrasirichai et al., 2019; Schmidhuber, 2015). The activated data is sub-sampled to reduce the tensor size, which increases the receptor field to the next convolutional layer of the network (Kellenberger et al., 2018; Strigl et al., 2010). The last layer of the network oversees the classification instead of the feature extraction. Thus, a fully connected neural network layer is used. Usually, such a fully connected network is followed by a softmax layer, which models the input data to the probability of belonging to each considered class (Hu et al., 2015; Anantrasirichai et al., 2019; Zhang et al., 2018).

6.3.5.2 Selection of training data

CNN is a supervised learning method, and thus it needs sample data (i.e., burned and unburned pixels) for training purposes. In this study, the extraction of the training dataset took advantage of hotspots and land cover information. The use of hotspots, well established for BA mapping (Belenguer-Plomer et al., 2019c; Roteta et al., 2019), is essential, particularly when using the radar-derived metrics to differentiate changes due to fires (Huang & Siegert, 2006). On the other hand, processing pixels according to their land cover class allows for improved characterisation of patterns which results in more accurate separation of burned and unburned areas when considering both, SAR and optical datasets (Belenguer-Plomer et al., 2018; Tanase et al., 2020). Therefore, CNNs training and the subsequent mapping process were carried out class-by-class, with the number of CNN models built depending on the land cover classes present in each study area. For a land cover class k, training pixels of the burned category were selected within a spatial buffer determined as the double of the thermal sensor spatial resolution (Langner et al., 2007; Sitanggang et al., 2013). The unburned training pixels were those outside the hotspot buffer areas as well as from not burnable (e.g., water) land cover classes according to CCI land cover map reference.

6.3.5.3 Assessment of optimum CNN configuration for BA mapping

The architecture of the CNNs was based on AlexNet (Krizhevsky et al., 2012), and integrate hidden convolutional layers, the ReLU activation function, max-pooling, fully-connected layers, dropout and softmax classification. According to Bashiri & Geranmayeh (2011), the parameters that define a CNN model such as the number of layers, neurons and filters need to be adjusted for each dataset. Thus, to determine the optimal network for BA detection and mapping up to eight combinations by each input dataset were analysed (Table 6.2).

Four architectures were analysed after combining two CNN-groups that differed in

terms of (i) the number of hidden layers and filters, and (ii) the image domain (i.e., spatial or spectral) where the convolutional feature extraction was executed. The first group included two CNN models with a different number of hidden layers and filters. The first model used two hidden layers with 32 and 64 filters, respectively, whereas the second model had a third additional hidden layer where 128 filters were applied. Hereafter the models with two and three hidden layers are referred to as the simple (S) and the complex (C), respectively. The second group involved two convolution-based filters for feature extraction. Given any pixel located at row i and column j of the input image $\mathbf{X}$, the first filter implied a pixel-wise convolution over the spectral domain (1D). It was considered three-pixels size kernel to extract features from the spectral information of the previously stacked optical images and radar channels (see subsection 6.3.1 to subsection 6.3.3). The second filter considered a 3×3 kernel around the centre pixel (spatial domain, 2D) to extract the features used for BA detection (Kussul et al., 2017; Xu et al., 2017; Zhang et al., 2019) (Figure 6.4).
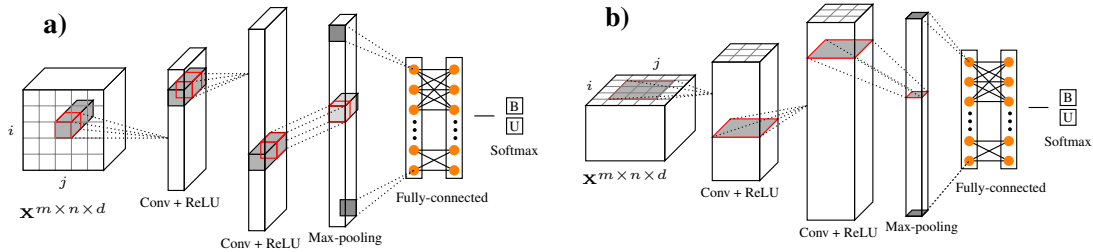

Figure 6.4: Feature extraction carried out in a convolution (Conv) though (a) the spectral-domain (1D) and (b) the spatial-domain (2D) of the input image. Relevant parts of CNN such as ReLU, max-pooling, fully-connected network and softmax layers are also shown.

Two normalization methods were tested separately with each image band being normalized (i) in the interval [0, 1] (Benedetti et al., 2018b), and (ii) applying the z-score normalization (Zhong et al., 2017) (Equation 6.10).

$$z\text{-}score\left(x\right) = \frac{x - \mu\left(b\right)}{\sigma\left(b\right)} \tag{6.10}$$

where x is a given pixel of a band b of the image, and μ and σ are the mean and standard deviation, respectively. In Table 6.2, there are the eight configurations considered whose performance when mapping BA is going to be assessed in this study for each dataset (i.e., SAR, optical and SAR-O combination).

6.4 Results

6.4.1 Optimum CNN configuration

Depending on the MGRS tile, the optimum CNN configuration varied (Figure 6.5). When Sentinel-1 (S-1) data was fed into the CNN, accuracy metrics dispersion (i.e., between tiles) at any CNN configuration was larger when compared to feeding Sentinel-2 (S-2)

Table 6.2: The eight configurations assessed for each input dataset (S – simple, C – complex)

CNN model	Convolution dimension	Data normalization
S	1D	z-score
S	1D	[0, 1]
S	2D	z-score
S	2D	[0, 1]
C	1D	z-score
C	1D	[0, 1]
C	2D	z-score
C	2D	[0, 1]

data or both Sentinel-1 and Sentinel-2 data (S-1+S-2). For the radar-fed CNN inter-tiles accuracy dispersion was reduced when the convolution and feature extraction was carried out through the spatial domain of the image (2D) by decreasing omission errors (36NXP, 20LQQ and 50JML) despite a slight increase in commission errors for some tiles (10UEC and 29TNE). Similar results were achieved when feeding only Sentinel-2 data. When feeding both types of data (i.e., S-1+S-2) into the CNN, the convolution dimension (i.e., 1D, 2D) did not influence the accuracy. In addition, the time required when training 2D models were lower compared to 1D, particularly when considering complex (C) networks and regardless of data normalisation type. The use of more complex (C) CNN models, as opposed in using the simplest ones (S), did not result in increased accuracy regardless of the type of data fed into the network. Similarly, time computing differences as a result of a different data normalisation method (z-score vs [0, 1]) were marginal for any of the input data. However, marginal accuracy increments of mapping accuracy were observed when using the z-score normalisation for the Sentinel-1 fed CNN, particularly in tile 50JML (i.e., Australian grasslands), where OE was reduced significantly (for 2D CNN). Conversely, when feeding Sentinel-2 or Sentinel-1 and Sentinel-2 data, the [0, 1] normalisation provided slightly more accurate BA detection and mapping.

By land cover classes, the lowest BA mapping accuracy was observed over Grasslands, particularly when using Sentinel-1 data due to high OE (Figure 6.6). However, combining 2D convolution with z-score normalisation resulted in improved DC (by 59%) from 1D convolution-based approaches with z-score (DC 0.35±0.24 vs 0.22±0.2, mean ± the standard deviation). The same configuration (2D and z-score) also improved the accuracy over Crops, especially when compared to 1D with [0, 1] data normalisation (DC 0.37±0.14 vs 0.30±0.25), although to a lesser extent, while over Forests the improvement was marginal. Accuracy metrics were stable for Shrubs over all configurations tested, although the 2D and z-score configuration provided less overall dispersion among the analysed tiles. In Others class, the highest mapping accuracy based on Sentinel-1 data was achieved using the convolution in the spectral domain (1D).

Although Sentinel-2 fed CNN achieved better accuracy when compared to Sentinel-1 fed CNN, such improvements were conditioned by land cover classes and configurations. When using optical data, the spectral-based feature extraction (1D) was the most accurate except for Crops where the spatial-based (2D) improved the results. Marginal differences in BA accuracy were found between the two data normalisation types with the z-score normalisation providing higher DC values over all land cover classes except for Forests.
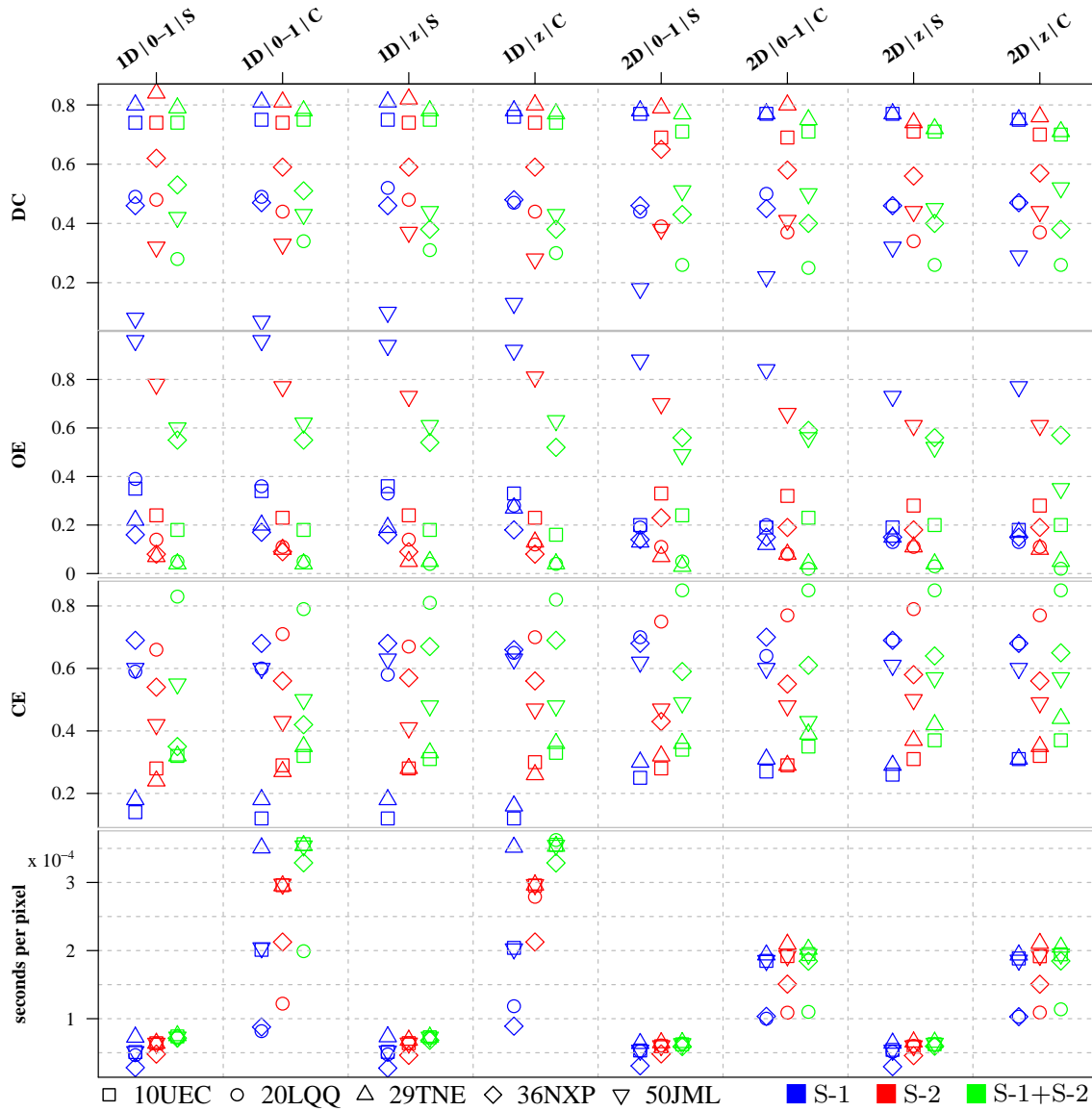
Figure 6.5: Dice coefficient (DC), commission and omission errors (CE and OE) and seconds needed when training the models by training tiles considering different CNN configuration and input data (Sentinel-1 - S-1, Sentinel-2 - S-2 and both datasets - S-1+S-2).
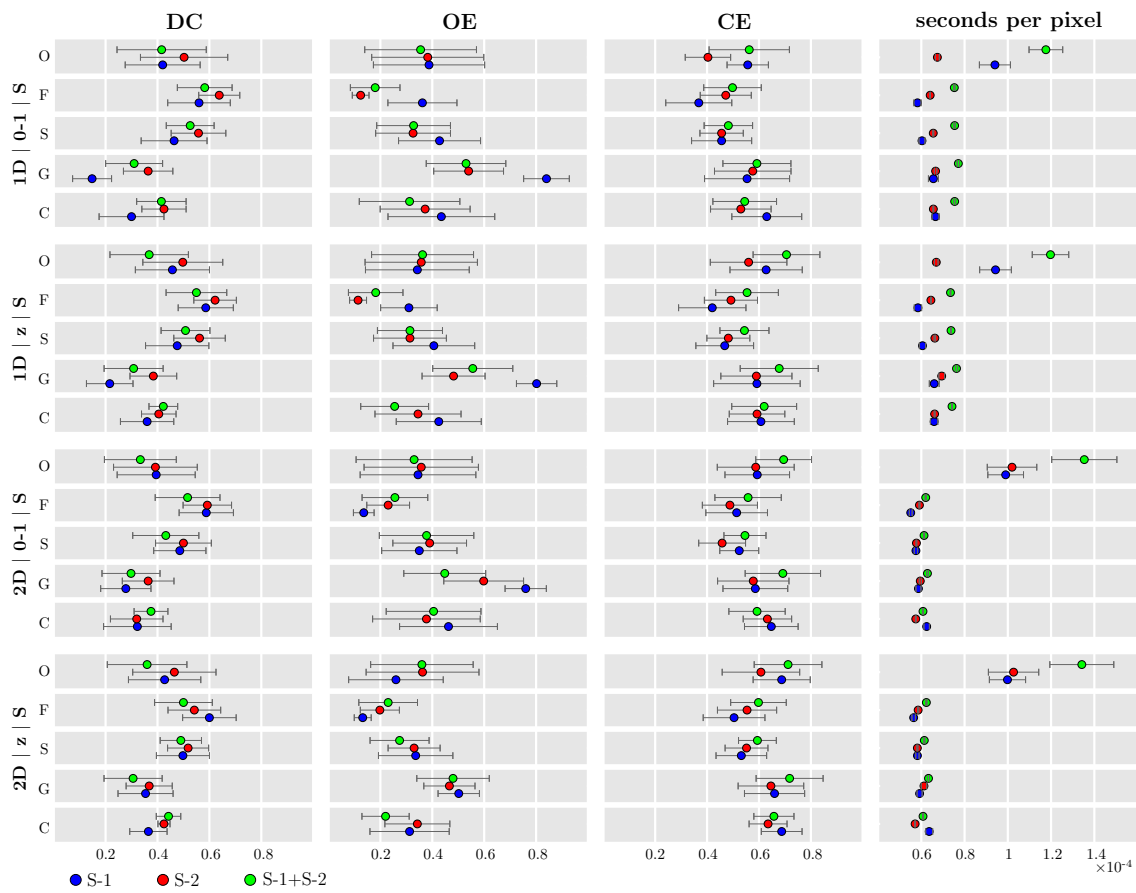
Figure 6.6: Mean and standard error of Dice coefficient (DC), commission and omission errors (CE and OE) and seconds per pixel needed when training the models by land cover classes (O-others, F-forests, S-shrubs, G-grasslands and C-crops) of training tiles considering different CNN configuration and input data (Sentinel-1 - S-1, Sentinel-2 - S-2 and both datasets - S-1+S-2).

When both, Sentinel-1 and Sentinel-2 data were fed to the CNN, the BA classification did not improve (except for Crops) when compared to only using Sentinel-2 data despite requiring more computation time in all configurations tested. Over cropping areas, SAR or optical data alone provided a low mapping accuracy (highest DCs achieved 0.37±0.14 and 0.42±0.05, respectively). However, the SAR-O combination improved the accuracy (DC 0.44±0.09) by reducing the OE. Such an improvement was maximum for the 2D convolution and z-score normalisation. For the remaining land cover classes, the SAR and optical combination did not improve the results when cloud cover was not an issue. Notice that, despite Sentinel-2 temporal compositing, gaps remained over areas frequently affected by clouds. As for the CNN optimum configuration, 1D convolution and [0, 1] normalisation improved the mapping accuracy (as for the Sentinel-1 based network). The highest mapping accuracy was observed over Forests regardless of data normalisation method, convolution dimension and input remote sensing data (i.e., S-1, S-2, S-1+S-2). The optimum CNN configuration for each land cover class is presented in Table 6.3 as a function of the input remote sensing data.

Table 6.3: Optimum CNN configuration and Dice coefficient mean (± standard deviation) by land cover classes (O-others, F-forests, S-shrubs, G-grasslands and C-crops) of the training tiles and input data (Sentinel-1 - S-1, Sentinel-2 - S-2 and both datasets - S-1+S-2).

LC	S-1	DC (S-1)	S-2	DC (S-2)	S-1+S-2	DC (S-1+S-2)
O	1D | z	0.46±0.31	1D | z	0.50±0.31	1D | [0, 1]	0.42±0.38
F	2D | z	0.60±0.23	1D | [0, 1]	0.64±0.21	1D | [0, 1]	0.58±0.24
S	2D | z	0.50±0.23	1D | z	0.56±0.22	1D | [0, 1]	0.53±0.20
G	2D | z	0.35±0.24	1D | z	0.38±0.20	all	0.31±0.23
C	2D | z	0.37±0.15	2D | z	0.43±0.19	2D | z	0.44±0.11

The last layer of the CNN utilised, the softmax layer, predicted the probability of each pixel to belong to burned and unburned classes. All previous analyses assigned a pixel as burned when the softmax probability was equal or above 50%. However, such a fixed threshold may have not always provided the optimum results, depending on the input datasets and land cover class (Figure 6.7). The effect of using a variable threshold probability was studied to improve BA mapping accuracy and balance CE and OE. Such variation depended on land cover class and the input data fed to the CNN (Table 6.4). Over Grasslands, Crops and Shrubs, the classes with the highest OE (Figure 6.6), improved accuracies were observed when the softmax burned threshold probability was reduced (40 to 50%), depending on the input dataset. Conversely, for Forests class, a more restrictive threshold improved BA mapping accuracy. The optimum threshold differed with the input data, from 65% when using Sentinel-2 data alone to 75% when using Sentinel-1 or integrating SAR and optical data. BA accuracy improved marginally for Others class when varying the threshold until a probability of 80% for Sentinel-1 and 70% for Sentinel-2. However, when integrating SAR and optical, the improvement was considerable for the 55-75% interval with the highest accuracy being achieved for a softmax of 70%. Such improvement allowed that maps based on SAR-O integration achieved higher accuracy when compared to maps derived from individual Sentinel-1 or Sentinel-2 datasets. Past the optimum threshold, mapping accuracy reduces considerably, particularly when using Sentinel-2 data. This effect was observed for all land cover classes except Grasslands,
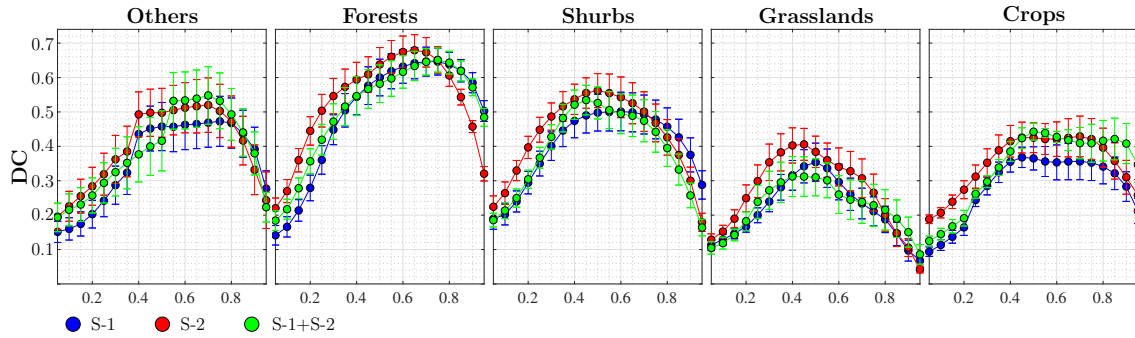
where the opposite was true.

Figure 6.7: Variation of mapping accuracy measured through the mean and standard error of Dice coefficient (DC) as a function of changes in softmax probability by land cover classes of training tiles and input data (Sentinel-1 - S-1, Sentinel-2 - S-2 and both datasets - S-1+S-2).

Table 6.4: Most suitable burned thresholds (Bt) of softmax classification probability layer when mapping burned area (BA) and the mean Dice coefficient (± standard deviation) by land cover classes (O-others, F-forests, S-shrubs, G-grasslands and C-crops) of training tiles and input data (Sentinel-1 - S-1, Sentinel-2 - S-2 and both datasets - S-1+S-2).

LC	Bt (S-1)	DC (S-1)	Bt (S-2)	DC (S-2)	Bt (S-1+S-2)	DC (S-1+S-2)
O	0.75	0.47±0.32	0.70	0.52±0.35	0.70	0.55±0.36
F	0.75	0.65±0.17	0.65	0.68±0.20	0.75	0.65±0.15
S	0.55	0.50±0.24	0.50	0.56±0.22	0.45	0.53±0.19
G	0.50	0.35±0.24	0.45	0.41±0.20	0.40	0.31±0.25
C	0.45	0.37±0.13	0.50	0.43±0.19	0.50	0.44±0.11

6.4.2 SAR-optical mapping strategy

Three different BA mapping strategies from combined SAR and optical datasets were analysed: (i) stacking radar, and optical metrics (e.g., backscatter coefficient, surface reflectance and indices) and feeding them to the CNN (Figure 6.8, a); (ii) using BA detected from the optical data and filling the gaps (e.g., due to cloud cover) with pixels mapped from radar data (Figure 6.8, b); and (iii) joining the BA detected independently from radar and optical datasets (Figure 6.8, c). For Forests class, the three mapping strategies provided similar results (i.e., DC values). However, joining individual Sentinel-1 and Sentinel-2 maps may provide an advantage by reducing missed burned areas due to those clouds or shadows, not possible when using optical temporal composites alone. For Shrubs, the observed DC values were similar for all mapping strategies with radar-filled optical-based BA maps showing slightly higher DC values when compared to the remaining two strategies. Over Grasslands, the radar-filled optical-based BA maps provided the most accurate results. Over the two remaining land cover classes (i.e., Others and Crops), the use of radar-optical stacks into the CNN allowed improving the accuracy when compared to using radar or optical data separately and combining the results. In particular, over class Others, the radar-optical stacks allowed reducing the CE by 20%.
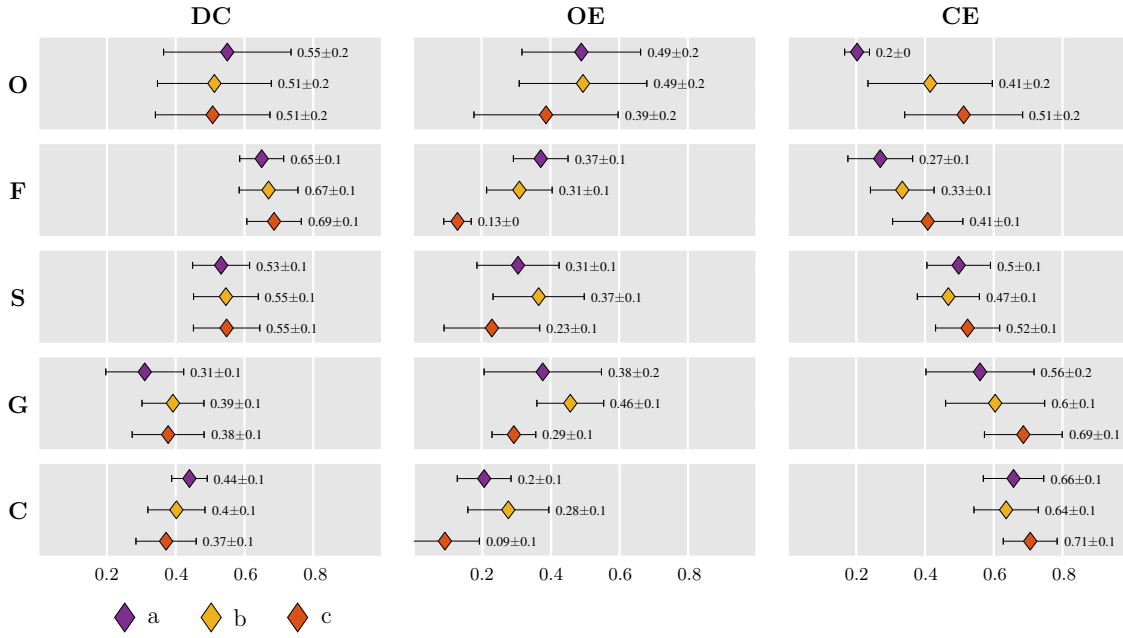
Figure 6.8: Mean and standard error of Dice coefficient (DC) and commission and omission errors (CE and OE) by land cover classes (O-others, F-forests, S-shrubs, G-grasslands and C-crops) of training tiles when combining Sentinel-1 and Sentinel-2 data applying three different approaches: (a) data stacking of SAR and optical images to feed the CNN; (b) filling Sentinel-2 based maps pixels with information-gaps using those derived from Sentinel-1; and (c) joining all burned pixels detected using both SAR and optical images separately.

6.4.3   Burned area mapping validation

The optimum CNN configuration and mapping strategy, according to the observed trends over the training tiles, were assessed over the test tiles (Table 6.5) with the mapping accuracy varying depending on the input data (i.e., S-1, S-2 and S-1+S-2). Higher mapping errors (DC<0.6) were observed over grasslands dominated tiles in Africa and Australia (33NTG and 52LCH, respectively), regardless of the input data. Over the remaining tiles, DC values were above 0.7. Over two tiles (20LQP and 33NTG), the radar-based maps were more accurate when compared to the optical-based (DC of 0.81 vs 0.71 and 0.50 vs 0.47, respectively) with the opposite being valid for the remaining three tiles. However, the use of Sentinel-1 data (i.e., cloud cover independent) allowed for wall-to-wall mapping. In tile 52LCH the optical-based maps did not provide information for 17.6% (Figure 6.9).

By land cover type, the highest accuracy was observed over forested areas when mapping BA through the SAR-O combination (DC 0.72) as opposed to only using SAR (DC 0.63) or optical (DC 0.66) information (Figure 6.10). The most relevant improvement when combining Sentinel-1 and Sentinel-2 was found over the Others class, where the synergy of both sensors reduced OE and CE considerably when compared to the single sensor approaches. The lowest accuracy was achieved over Crops class, mainly due to high CE (near 0.8) observed for both sensor types. In addition, for the radar-based maps, BA accuracy over cropping areas was also negatively influenced by high OE, which did not occur when using optical datasets. The combination of Sentinel-1 and Sentinel-2 data generally improved or maintained the accuracy achieved from SAR or optical only mapping except for tile 20LQP, where the SAR-based maps were the most accurate. Improvements

Table 6.5: Error metrics for burned area (BA) maps based on Sentinel-1 (S-1), Sentinel-2 (S-2) and the optimum combination of both datasets (S-1+S-2) for each test tile.

MGRS	R. period	Sat	Detection period	DC	OE	CE	%N
10SEH	04/10/2017 05/11/2017	S-2	07/10/2017–01/11/2017	0.70	0.12	0.41	2.26
		S-1+S-2	28/09/2017–03/11/2017	0.70	0.10	0.43	0.00
		S-1	28/09/2017–03/11/2017	0.46	0.69	0.13	0.00
20LQP	20/07/2016 22/09/2016	S-2	17/07/2016–25/09/2016	0.71	0.20	0.37	0.00
		S-1+S-2	03/07/2016–25/09/2016	0.73	0.04	0.41	0.00
		S-1	03/07/2016–25/09/2016	0.81	0.08	0.27	0.00
29TNG	05/10/2017 06/11/2017	S-2	05/10/2017–09/11/2017	0.75	0.27	0.22	0.06
		S-1+S-2	28/09/2017–09/11/2017	0.77	0.23	0.22	0.00
		S-1	28/09/2017–09/11/2017	0.64	0.44	0.25	0.00
33NTG	15/01/2016 16/02/2016	S-1	15/01/2016–20/02/2016	0.50	0.53	0.47	0.00
		S-2	18/01/2016–/17/02/2016	0.47	0.65	0.31	0.39
		S-1+S-2	15/01/2016–20/02/2016	0.56	0.47	0.42	0.00
52LCH	05/04/2017 21/04/2017	S-2	19/03/2017–08/04/2017	0.55	0.59	0.15	17.6
		S-1+S-2	26/03/2017–19/04/2017	0.56	0.55	0.24	0.00
		S-1	26/03/2017–19/04/2017	0.36	0.75	0.34	0.00

C - continent for each tile (Af-Africa, Au-Australia, Eu-Europe, NA-North America and SA-South America); R. period - period for which it was derived the reference burn perimeters using Landsat-8; Sat - input dataset considered; Detection period - first and last Sentinel-1 or Sentinel-2 images of the temporal series; DC - Dice coefficient; OE - omission error; CE - commission error; and %N - the percentage of no data pixels over all the MGRS tile.
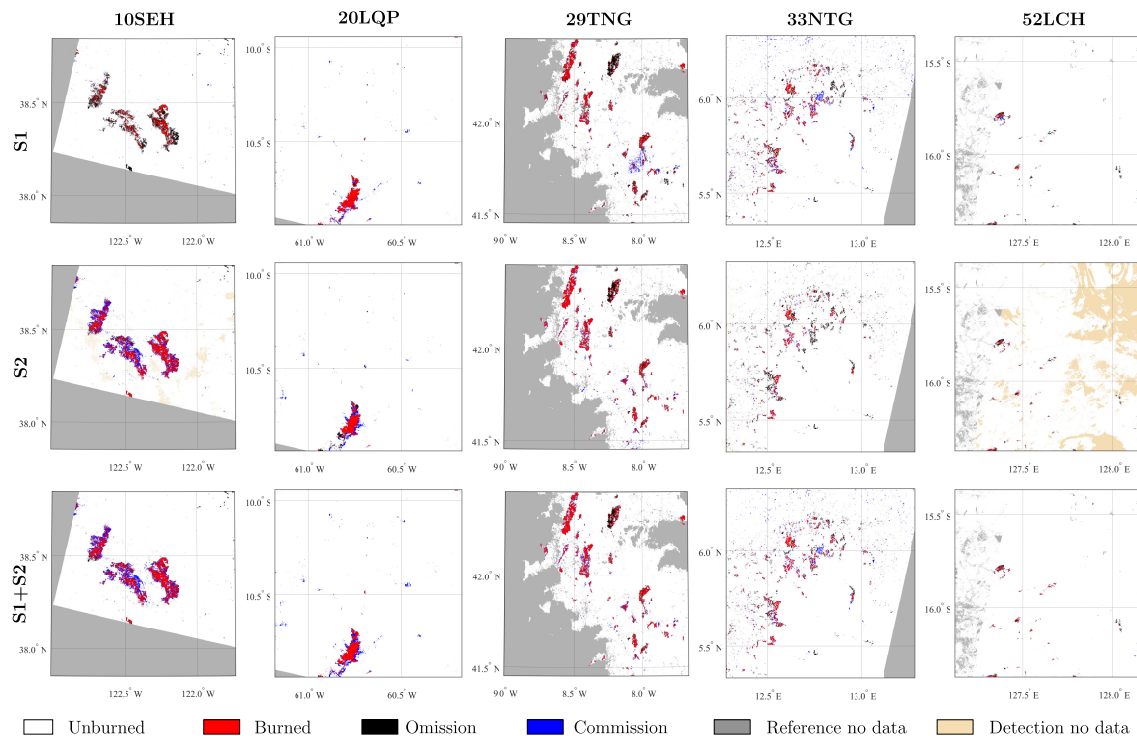
Figure 6.9: Burned area (BA) maps based on Sentinel-1 (S-1), Sentinel-2 (S-2) and the optimum combination of both datasets (S-1+S-2) for test tiles. Errors of omission and commission, as well as no data pixels due to reference or input datasets, are also shown.

when combining the two sensor types were related to a considerable reduction in OE which coupled with a marginal increase in CE. The average OE reduction and CE increase over the five test tiles was 0.22±0.22 and 0.05±0.17 when compared to radar-based maps and 0.09±0.08 and 0.05±0.05 when compared to optical-based maps. Apart from accuracy improvements, SAR-O data integration reduced gaps due to cloud cover to nil, a significant advantage of combining active and passive sensors. Although computationally intensive, a combined SAR-O approach took advantage of the optical sensor improving BA mapping accuracy and of the radar atmospheric independence, providing consistently wall-to-wall products.
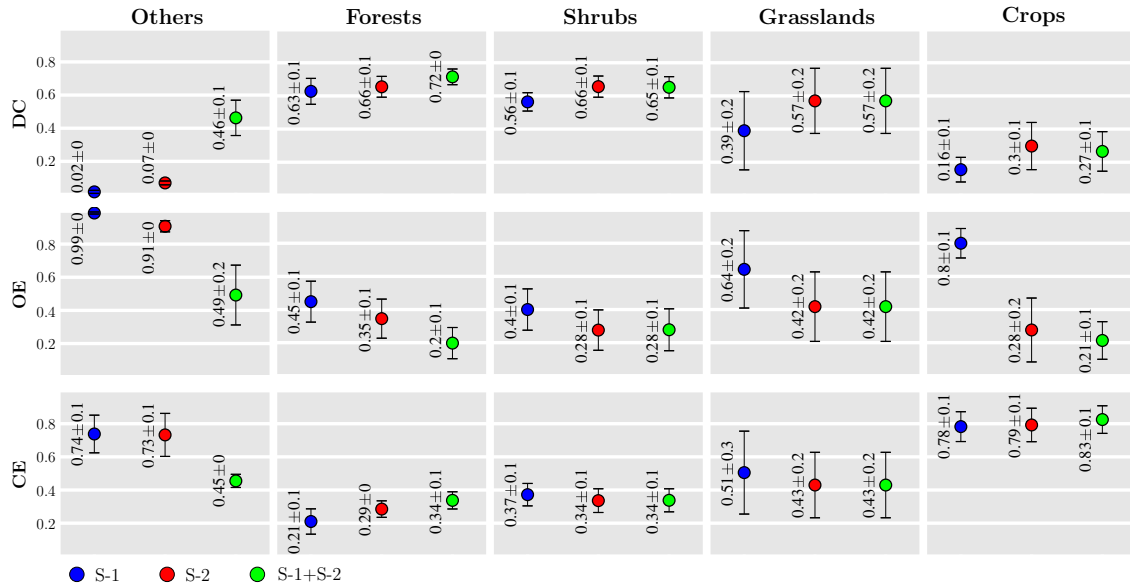

Figure 6.10: Mean and standard error of Dice coefficient (DC), commission and omission errors (CE and OE) by land cover classes of test tiles as a function of the input datasets used (Sentinel-1 - S-1, Sentinel-2 - S-2 and the optimum combination of both datasets - S-1+S-2).

6.5 Discussion

6.5.1 Optimum CNN parameters

In terms of data normalisation, our results show that the optimum was based on the z-score regardless of the input data (radar or optical) except for forested lands mapped from Sentinel-2 imagery, which aligns with findings from previous research (Zhong et al., 2017). Conversely, for combined SAR-O approaches the [0, 1] normalisation was better suited to BA mapping applications as also observed in previous studies that combined imagery from different sensors (Benedetti et al., 2018a). The [0, 1] normalisation provided more accurate BA detections when stacking SAR and optical datasets except for Grasslands (no difference with z-score normalisation) and Crops. The insensitivity to the normalisation method used may be related to the low accuracies observed for BA mapping over Grasslands as previously shown by other authors (Menges et al., 2004). For Crops, the intrinsic class vegetation differences given by the variability of different agricultural fields as well as the vegetation season may explain the need for a different normalisation

type.

The optimum feature extraction was achieved via the spectral domain (1D) when optical or the SAR-O combination was used. Conversely, the spatial domain (2D) provided more accurate results when using SAR data alone. Such a difference may be due to optical reflectance allows for improved BA detection when compared to the radar backscatter coefficient (Belenguer-Plomer et al., 2019c). Hence, considering the spectral reflectance (i.e., of wavelengths highly sensitive to fire effects (i.e., 1D) results in accurate classification of burned areas. When optical information is absent (i.e., only the backscatter coefficient is available), considering the surrounding pixels improves differentiation between burned and unburned pixels explaining the improved performance of the spatial feature extraction (2D).

The optimum Softmax threshold, when classifying burned and unburned pixels, differed as a function of land cover classes. The most considerable improvement, when chaining the threshold from 50% probability, was observed for class Others which was mapped more accurately when considering SAR-O using a 60% probability. The optimum thresholds also varied as a function of the input dataset (SAR, optical or SAR-O combination) over each land cover class. For Crops, Grasslands and Shrubs the optimum thresholds were less restrictive (i.e., close to 50%) while for Forests and Others the optimum thresholds were more restrictive (i.e., around 70%). Except for Shrubs, a higher threshold (for burned area) seemed appropriate for the land cover classes mapped with higher accuracy (i.e., Forests and Others). The higher mapping accuracy may be related to the biomass level of each land cover class as it influences the level of pre- to post-fire changes for both, the backscatter coefficient and optical reflectance. In addition, the Fire Radiative Power (FRP) is dependent on fuels availability (i.e., biomass) which implies that in land cover classes with a reduced amount of biomass the capability to detect hotspots from thermal sensors is lower when compared to biomass rich land cover classes (Wooster et al., 2005). CNN models are land cover dependent and trained using information derived from hotspots. A reduced number of hotspots for a specific land cover class (due to low FRP, related to low biomass levels), resulted in poorer training and thus increased uncertainty when compared to land cover classes with increased fuel availability (and thus hotspots) explaining of different optimum thresholds for each land cover class.

Lastly, in terms of computing time, mapping the BA over vegetation with considerable intrinsic heterogeneity (i.e., Others class) increased the computing time. However, the most significant time increment was found when using additional hidden layers which did not translate in improvements of the mapping accuracy. Although including more hidden layers does not deteriorate the mapping accuracy, the considerable increase of computing time may hinder algorithm deployment from continental to global scales, the final objective of this research (Chuvieco et al., 2019).

6.5.2 SAR and optical data integration for BA mapping

The input dataset (SAR, optical, joint use) providing the highest accuracy differed with the land cover class. For Others and Crops classes, the joint use of active and passive data provided the most accurate results. As these land cover classes are more heterogeneous, the mapping process takes advantage of the differentiated sensitivity of the two types of

sensors through the CNN training thus allowing for a more precise separation between burned and unburned areas overall. Notice that over the test tiles, the joint use of both sensor types did not improve results for the Crops class suggesting that research is needed ascertain the optimum combination of active and passive datasets. A possible explanation is a reduced variability among the types of crops within the test tiles. Such reduced variability was suggested by the reduced VH backscatter coefficient variability (i.e., standard deviation), related to the vegetation volumetric scattering process (Freeman & Durden, 1998), over the Crops in the test tiles when compared to the training tiles (0.10 vs 0.15). Increased homogeneity over the agricultural fields, induced by different crop types and/or growing season, may reduce the need for SAR-derived information for monitoring purposes (Van Tricht et al., 2018). Nevertheless, comparing SAR-O and optical-based results over the test tiles suggest only marginal DC differences over cropping areas and demonstrate the reliability of the CNN-based predictions even when some of the input data are redundant.

For Forests and Shrubs classes, the combination of BA mapping products from individual SAR and optical data sources allowed for more accurate detections although such improvements were marginal (especially for Shrubs) when compared to the remaining data-integration strategies. The improvement resulted from a considerable OE reduction when joining the independently generated maps. In particular, OE was reduced for pixels located at the border of fire patches which are more susceptible to be misclassified due to residual pixel co-registration errors between maps and validation datasets (Mandanici & Bitelli, 2016). Hence, combining maps obtained from sensors with different viewing geometries (i.e., SAR and optical) reduced the effect of geolocation errors without meaningfully increasing the CE. Lastly, over Grasslands, the use of Sentinel-2 data for BA mapping and Sentinel-1 for gap filling (due to cloud cover) provided the most accurate results. Such findings align with previous research which suggested reduced utility of C-band backscatter coefficient when monitoring fire effects in fire-affected grasslands (Menges et al., 2004).

6.5.3 Algorithm independent validation

The joint use of Sentinel-1 and Sentinel-2 data improved slightly (or maintained) the BA accuracy achieved using a sole input data (i.e., SAR or optical) in most test tiles while providing wall-to-wall mapping capabilities (all pixels were mapped), a feature particularly crucial in tile 52LCH were cloud gaps amounted for 17.6% of the area. Further, the joint use of active and passive datasets allowed combining the strengths of SAR (i.e., a cloud cover independence) and optical data (i.e., better sensitivity to fire-induced changes in vegetation) as also suggested in previous studies (Verhegghen et al., 2016). As an exception, for tile 20LQP, the highest accuracy was obtained using the SAR data (DC 0.81). The OE increased by 0.2 when using Sentinel-2 data as an input and by 0.04 when jointly using the active and passive datasets. However, for the latter, the CE significantly increased when joining all burned pixel detected separately from SAR and optical datasets due to the large commission errors of the Sentinel-2 based maps. The discrepant results in tile 20LQP were explained by fire location, as 83% of the fire patches burned forested areas and did not reflect the general trends as discussed in subsection 6.5.4. Overall, using SAR and optical data for BA mapping requires more computing power or increased processing time. However, such effort may be worth as end-users are provided with the most accurate

BA products without information gaps, particularly beneficial at inter-tropical and boreal latitudes.

By land cover classes, the higher mapping accuracies were observed for Forests, Shrubs and Grasslands classes with DC values of 0.72, 0.65 and 0.57, respectively. Lower DC values (0.46) were observed for the class Others. A rather low mapping accuracy was observed for Crops (DC 0.27) regardless of the input datasets. However, one should notice that most accuracy metrics analysed here were based on reference fire perimeters over short periods (i.e., one month or less) which may significantly affect accuracy assessment. According to previous research, evaluating BA maps over short periods tends to underestimate mapping accuracy regardless of the input datasets (Padilla et al., 2018). Such effects were also found when assessing Sentinel-2 based BA maps with DC values increasing from 0.34 to 0.77 from short to long temporal periods (Roteta et al., 2019).

In this study, most of the evaluated periods were short. However, two clearly defined groups of tiles were observed when analysing the BA mapping accuracy from Sentinel-2 data. For the first group, formed by tiles 10SEH, 20LQP and 29TNG, the fire activity was concentrated around dates timely covered by both the reference (as set by Landsat 8 acquisition dates) and the detection period (set by the Sentinel-2 acquisition dates). Over these tiles, the DC values were similar (DC >0.7) and in line with those observed in previous studies (Roteta et al., 2019). For the second group, tiles 33NTG and 52LCH, many fires were active during dates not simultaneously covered by Landsat-8 and Sentinel-2 acquisitions. In fact, 8.8% (33NTG) and 39.4% (52LCH) hotspots were recorded within the interval covered by the Lansat-8 imagery but outside the interval covered by the Sentinel-2 imagery. Such a mismatching resulted in increased OE (0.65 and 0.59, respectively) and thus lower accuracy as the average DC was 0.21 lower when compared to the remaining tiles (DC 0.51 vs 0.72).

The accuracy observed for the Sentinel-1 based BA maps was similar to that observed in previous studies based on the same sensor (Belenguer-Plomer et al., 2019c). For the test tiles, the CNN-based maps achieved an average DC of 0.55±0.17 compared an average DC of 0.57±0.18 observed for a Reed-Xiaoli detector proposed by Belenguer-Plomer et al. (2019c). Although only marginal differences, in terms of accuracy, were found between the two approaches, the CNN-based algorithm was considerable faster (Belenguer-Plomer et al., 2019c). The reduced number of studies taking advantage of a combined active/passive sensor approach for BA mapping precluded meaningful comparisons as such studies were carried out over homogeneous areas with little variations in vegetation types and fire regimes (Verhegghen et al., 2016; Brown et al., 2018; Stroppiana et al., 2015).

6.5.4 Main sources of error

Commission and omission burned area mapping errors depended, to a large degree, on the input data source. SAR and optical datasets were affected differently by factors including variations in soil moisture, slope orientation and post-fire vegetation response (Kurum, 2015; Belenguer-Plomer et al., 2019a). For tile 10SEH (North America), the main limiting factor when using SAR data was the steep topography since fire patches were located on steeper (13.46°±7.7) when compared to the remaining test tiles (7.15°±6). The steeper topography may reduce the backscatter suitability when monitoring fires which translate in

increased OE (0.69) (Belenguer-Plomer et al., 2019c). Conversely, considerable CE (0.41) was observed for the optical-based maps as during the automatic training low-fire severity pixels (i.e., reduced pre- to post-fire variations) were considered due to their proximity to hotspots. However, the reference data only included visible burned pixels as it was based on manually supervised classification. The mean dNBR, a reliable indicator of fire severity (Key & Benson, 2004), in pixels affected by CE was 0.15±0.16, a value considerably higher when compared to that of unburned pixels (0.01±0.7) and, at the same time, far from the values observed for the burned pixels (0.46±0.26), suggesting that reference perimeters include partially burned pixels as the observed CE should have been lower.

Fire severity was also the main limiting factor in tiles 33NTG (Africa) and 52LCH (Australia). According to the MIRBI spectral index (Equation 6.4), found as the most suitable index when assessing fire severity over grasslands (Lu et al., 2016), low fire severity was observed for pixels affected by OE (1.67±0.38 and 1.62±0.21, respectively). In contrast, moderate severities were observed for accurately detected burned pixels (1.8±0.32 and 1.76±0.12, respectively). Although marginal differences were found when comparing accuracies from SAR-O and optical-based maps (DC 0.56 vs 0.55), when evaluating the accuracy of latter, pixels covered by clouds (17.6%) were not included despite some of them being affected by fires. When assessing the SAR-O map in tile 52LCH, ignoring the influence of optical-affected cloud pixels, the accuracy improved up to 12.5% (DC 0.63). Furthermore, as indicated in subsection 6.5.3, mismatched reference and detection periods may have increased the observed errors (particularly OE) in tiles 33NTG and 52LCH.

Hotspots availability may have also affected the observed mapping accuracy. For example, in tile 29TNG (Portugal), most areas affected by omission errors were located within a unique fire scar with only one hotspot detected by the thermal MODIS and VIIRS sensors. Reduced number of hotspots hindered CNN training for both, SAR and optical datasets. However, the absence of hotspots was an exception as within the remaining fire patches (same tile) or the remaining tiles such limitations were not observed.

Finally, the high CE observed in tile 20LQP (South America), particularly for the optical-based map (0.37), was related to similar post-fire increment in SWIR reflectance over both burned (+0.046) and unburned (+0.05) areas. The SWIR increment over unburned areas may be related to drying unburned vegetation during the post-fire period (Gao, 1996). Most pixels (77%) affected by CE were concentrated along the largest fire perimeter, a fire that accounted for 93.3% of all burned pixels in this tile. According to the MODIS-based hotpots product (Giglio et al., 2016), FRP values up to 339.9 MW were observed for this fire, a 15th fold increase when compared to value registered over the remaining fire-patches (20.3 MW), which suggests that heat radiating from the very intense fire-affected vegetation on the neighbouring areas. As CNN training is based on larger areas around hotspots, unburned fire-dried pixels were mixed within the training samples resulting in an incorrect learning process. Such errors may be easily rectified by relating the sampling areas around hotspots with the FRP, i.e., training pixels from intense fires are sampled within a lower radius.

6.6 Conclusions

This study provides insights for the optimum configuration of CNN fed by Sentinel-1 and/or Sentinel-2 datasets for BA mapping by land cover classes. The analysis was carried out over 10 study areas (1M ha each) distributed within fire-prone biomes. CNN models with two hidden layers allowed reducing the computing time with virtually no loss in maintaining mapping accuracy (when compared to deeper networks) regardless of the input data set (Sentinel-1, Sentinel-2, both) or the observed land cover class. Three factors were relevant when defining an optimum CNN configuration: (i) the dimension where the convolution-based feature extraction was executed (1D or 2D); (ii) the data normalisation method applied (z-score or interval [0, 1]); and (iii) the optimum threshold of the soft-max output layer. The land cover class was also relevant when defining the most accurate SAR-O data integration strategy.

The optimum CNN parameters were used to map BA over the five independent test areas, finding similar accuracies to those achieved over the training tiles. Error analysis over the test tiles suggested a strong relationship between mapping accuracy and the land cover classes, as expected. The highest and lowest accuracies were found over Forests and Grasslands, respectively. When individual sensors were fed into the CNN (i.e., Sentinel-1, Sentinel-2), the observed mapping accuracies were similar to those found in previous studies. However, the proposed CNN approach was considerably more versatile when compared to the existing BA mapping algorithms. Besides, this study also provided insights into the optimum SAR-O data integration, which allows (i) improving BA mapping accuracy when compared to using a single sensor type, and (ii) wall-to-wall mapping since cloud-related gaps of optical datasets were eliminated. Despite these strengths, CNN-based BA mapping accuracy was limited by different sources of errors including steep topography, low FRP, absence of hotspots, and presence of fire unrelated land changes. Further research should focus on confirming our results over additional areas and further reducing mapping uncertainty by incorporating additional data streams into the CNN, including high temporal but low spatial resolution imagery.

Acknowledgements

6.7 References

Agostinelli, F., Hoffman, M., Sadowski, P., & Baldi, P. (2014). Learning activation functions to improve deep neural networks. *arXiv preprint arXiv:1412.6830*, .

Anantrasirichai, N., Biggs, J., Albino, F., & Bull, D. (2019). A deep learning approach to detecting volcano deformation from satellite imagery using synthetic datasets. *Remote Sensing of Environment*, *230*, 111179.

Aponte, C., de Groot, W. J., & Wotton, B. M. (2016). Forest fires and climate change: causes, consequences and management options. *International Journal of Wildland Fire*, *25*, i–ii.

Ban, Y., Zhang, P., Nascetti, A., Bevington, A. R., & Wulder, M. A. (2020). Near Real-Time Wildfire Progression Monitoring with Sentinel-1 SAR Time Series and Deep Learning. *Scientific Reports*, *10*, 1–15.

Bashiri, M., & Geranmayeh, A. F. (2011). Tuning the parameters of an artificial neural network using central composite design and genetic algorithm. *Scientia Iranica*, *18*, 1600–1608.

Belenguer-Plomer, M. A., Chuvieco, E., & Tanase, M. A. (2019a). Evaluation of backscatter coefficient temporal indices for burned area mapping. In *Active and Passive Microwave Remote Sensing for Environmental Monitoring III* (p. 111540D). International Society for Optics and Photonics volume 11154.

Belenguer-Plomer, M. A., Chuvieco, E., & Tanase, M. A. (2019b). Temporal Decorrelation of C-Band Backscatter Coefficient in Mediterranean Burned Areas. *Remote Sensing*, *11*, 2661.

Belenguer-Plomer, M. A., Tanase, M. A., Fernandez-Carrillo, A., & Chuvieco, E. (2018). Insights into burned areas detection from Sentinel-1 data and locally adaptive algorithms. In *Active and Passive Microwave Remote Sensing for Environmental Monitoring II* (p. 107880G). International Society for Optics and Photonics volume 10788.

Belenguer-Plomer, M. A., Tanase, M. A., Fernandez-Carrillo, A., & Chuvieco, E. (2019c). Burned area detection and mapping using Sentinel-1 backscatter coefficient and thermal anomalies. *Remote Sensing of Environment*, *233*, 111345.

Benedetti, A., Picchiani, M., & Del Frate, F. (2018a). Sentinel-1 and sentinel-2 data fusion for urban change detection. In *IGARSS 2018-2018 IEEE International Geoscience and Remote Sensing Symposium* (pp. 1962–1965). IEEE.

Benedetti, P., Ienco, D., Gaetano, R., Ose, K., Pensa, R. G., & Dupuy, S. (2018b). M^3 Fusion: A Deep Learning Architecture for Multiscale Multimodal Multitemporal Satellite Data Fusion. *IEEE Journal of Selected Topics in Applied Earth Observations and Remote Sensing*, *11*, 4939–4949.

Bojinski, S., Verstraete, M., Peterson, T. C., Richter, C., Simmons, A., & Zemp, M. (2014). The concept of essential climate variables in support of climate research, applications, and policy. *Bulletin of the American Meteorological Society*, *95*, 1431–1443.

Bourgeau-Chavez, L., Kasischke, E., Brunzell, S., Mudd, J., & Tukman, M. (2002). Mapping fire scars in global boreal forests using imaging radar data. *International Journal of Remote Sensing*, *23*, 4211–4234.

Bouvet, A., Mermoz, S., Ballère, M., Koleck, T., & Le Toan, T. (2018). Use of the SAR shadowing effect for deforestation detection with Sentinel-1 time series. *Remote Sensing*, *10*, 1250.

Bowman, D. M., Balch, J. K., Artaxo, P., Bond, W. J., Carlson, J. M., Cochrane, M. A., D'Antonio, C. M., DeFries, R. S., Doyle, J. C., Harrison, S. P. et al. (2009). Fire in the Earth system. *Science*, *324*, 481–484.

Brown, A. R., Petropoulos, G. P., & Ferentinos, K. P. (2018). Appraisal of the Sentinel-1 & 2 use in a large-scale wildfire assessment: A case study from Portugal's fires of 2017. *Applied geography*, *100*, 78–89.

Chuvieco, E., Aguado, I., Yebra, M., Nieto, H., Salas, J., Martín, M. P., Vilar, L., Martínez, J., Martín, S., Ibarra, P. et al. (2010). Development of a framework for fire risk assessment using remote sensing and geographic information system technologies. *Ecological Modelling*, *221*, 46–58.

Chuvieco, E., Lizundia-Loiola, J., Pettinari, M. L., Ramo, R., Padilla, M., Mouillot, F., Laurent, P., Storm, T., Heil, A., & Plummer, S. (2018). Generation and analysis of a new global burned area product based on MODIS 250m reflectance bands and thermal anomalies. *Earth Syst. Sci. Data Discuss*, *512*, 1–24.

Chuvieco, E., Mouillot, F., van der Werf, G. R., San Miguel, J., Tanasse, M., Koutsias, N., García, M., Yebra, M., Padilla, M., Gitas, I. et al. (2019). Historical background and current developments for mapping burned area from satellite Earth observation. *Remote Sensing of Environment*, *225*, 45–64.

Di Gregorio, A. (2005). *Land Cover Classification System: Classification Concepts and User manual*. United Nations Food and Agriculture Organization.

Fernandez-Carrillo, A., Belenguer-Plomer, M., Chuvieco, E., & Tanase, M. (2018). Effects of sample size on burned areas accuracy estimates in the Amazon Basin. In *Earth Resources and Environmental Remote Sensing/GIS Applications IX* (p. 107901S). International Society for Optics and Photonics volume 10790.

Flannigan, M. D., Amiro, B. D., Logan, K. A., Stocks, B., & Wotton, B. (2006). Forest fires and climate change in the 21 st century. *Mitigation and Adaptation Strategies for Global Change*, *11*, 847–859.

Flannigan, M. D., Krawchuk, M. A., de Groot, W. J., Wotton, B. M., & Gowman, L. M. (2009). Implications of changing climate for global wildland fire. *International Journal of Wildland Fire*, *18*, 483–507.

Fraser, R., Li, Z., & Cihlar, J. (2000). Hotspot and NDVI differencing synergy (HANDS): A new technique for burned area mapping over boreal forest. *Remote Sensing of Environment*, *74*, 362–376.

Freeman, A., & Durden, S. L. (1998). A three-component scattering model for polarimetric SAR data. *IEEE Transactions on Geoscience and Remote Sensing*, *36*, 963–973.

French, N. H., Bourgeau-Chavez, L. L., Wang, Y., & Kasischke, E. S. (1999). Initial observations of Radarsat imagery at fire-disturbed sites in interior Alaska. *Remote Sensing of Environment*, *68*, 89–94.

Gao, B.-C. (1996). NDWI—A normalized difference water index for remote sensing of vegetation liquid water from space. *Remote sensing of environment*, *58*, 257–266.

García, M. L., & Caselles, V. (1991). Mapping burns and natural reforestation using Thematic Mapper data. *Geocarto International*, *6*, 31–37.

Giglio, L., Boschetti, L., Roy, D. P., Humber, M. L., & Justice, C. O. (2018). The Collection 6 MODIS burned area mapping algorithm and product. *Remote sensing of environment*, *217*, 72–85.

Giglio, L., Loboda, T., Roy, D. P., Quayle, B., & Justice, C. O. (2009). An active-fire based burned area mapping algorithm for the MODIS sensor. *Remote Sensing of Environment*, *113*, 408–420.

Giglio, L., Schroeder, W., & Justice, C. O. (2016). The collection 6 MODIS active fire detection algorithm and fire products. *Remote Sensing of Environment*, *178*, 31–41.

Hansen, M. C., Potapov, P. V., Moore, R., Hancher, M., Turubanova, S., Tyukavina, A., Thau, D., Stehman, S., Goetz, S., Loveland, T. et al. (2013). High-resolution global maps of 21st-century forest cover change. *Science*, *342*, 850–853.

Hoffmann, W. A., Schroeder, W., & Jackson, R. B. (2002). Positive feedbacks of fire, climate, and vegetation and the conversion of tropical savanna. *Geophysical Research Letters*, *29*, 9–1.

Hollmann, R., Merchant, C. J., Saunders, R., Downy, C., Buchwitz, M., Cazenave, A., Chuvieco, E., Defourny, P., de Leeuw, G., Forsberg, R. et al. (2013). The ESA climate change initiative: Satellite data records for essential climate variables. *Bulletin of the American Meteorological Society*, *94*, 1541–1552.

Hu, F., Xia, G.-S., Hu, J., & Zhang, L. (2015). Transferring deep convolutional neural networks for the scene classification of high-resolution remote sensing imagery. *Remote Sensing*, *7*, 14680–14707.

Huang, S., & Siegert, F. (2006). Backscatter change on fire scars in Siberian boreal forests in ENVISAT ASAR wide-swath images. *IEEE Geoscience and Remote Sensing Letters*, *3*, 154–158.

Inglada, J., & Christophe, E. (2009). The Orfeo Toolbox remote sensing image processing software. In *Geoscience and Remote Sensing Symposium, 2009 IEEE International, IGARSS 2009* (pp. IV–733). IEEE volume 4.

Jin, Y., & Roy, D. P. (2005). Fire-induced albedo change and its radiative forcing at the surface in northern Australia. *Geophysical Research Letters*, *32*.

Kellenberger, B., Marcos, D., & Tuia, D. (2018). Detecting mammals in UAV images: Best practices to address a substantially imbalanced dataset with deep learning. *Remote sensing of environment*, *216*, 139–153.

Key, C., & Benson, N. (2004). Ground measure of severity, the Composite Burn Index; and Remote sensing of severity, the Normalized Burn Ratio. In G. T. R. RMRS-GTR-164 (Ed.), *FIREMON: Fire Effects Monitoring and Inventory System* chapter Landscape assessment (LA): Sampling and analysis methods. (pp. 1–51). Ogden: USDA Forest Service, Rocky Mountain Research Station.

Kloster, S., Mahowald, N., Randerson, J., & Lawrence, P. (2012). The impacts of climate, land use, and demography on fires during the 21st century simulated by CLM-CN. *Biogeosciences*, *9*, 509–525.

Knorr, W., Jiang, L., & Arneth, A. (2016). Climate, CO 2 and human population impacts on global wildfire emissions. *Biogeosciences*, *13*, 267–282.

Krawchuk, M. A., Moritz, M. A., Parisien, M.-A., Van Dorn, J., & Hayhoe, K. (2009). Global pyrogeography: the current and future distribution of wildfire. *PloS one*, *4*, e5102.

Krizhevsky, A., Sutskever, I., & Hinton, G. E. (2012). Imagenet classification with deep convolutional neural networks. In *Advances in neural information processing systems* (pp. 1097–1105).

Kurum, M. (2015). C-band SAR backscatter evaluation of 2008 Gallipoli forest fire. *IEEE Geoscience and Remote Sensing Letters*, *12*, 1091–1095.

Kussul, N., Lavreniuk, M., Skakun, S., & Shelestov, A. (2017). Deep learning classification of land cover and crop types using remote sensing data. *IEEE Geoscience and Remote Sensing Letters*, *14*, 778–782.

Langenfelds, R., Francey, R., Pak, B., Steele, L., Lloyd, J., Trudinger, C., & Allison, C. (2002). Interannual growth rate variations of atmospheric CO2 and its δ13C, H2, CH4, and CO between 1992 and 1999 linked to biomass burning. *Global Biogeochemical Cycles*, *16*, 21–1.

Langner, A., Miettinen, J., & Siegert, F. (2007). Land cover change 2002–2005 in Borneo and the role of fire derived from MODIS imagery. *Global Change Biology*, *13*, 2329–2340.

Lavorel, S., Flannigan, M. D., Lambin, E. F., & Scholes, M. C. (2007). Vulnerability of land systems to fire: Interactions among humans, climate, the atmosphere, and ecosystems. *Mitigation and Adaptation Strategies for Global Change*, *12*, 33–53.

LeCun, Y., Bengio, Y., & Hinton, G. (2015). Deep learning. *nature*, *521*, 436.

Liu, Z., Ballantyne, A. P., & Cooper, L. A. (2019). Biophysical feedback of global forest fires on surface temperature. *Nature communications*, *10*, 1–9.

Lizundia-Loiola, J., Otón, G., Ramo, R., & Chuvieco, E. (2020). A spatio-temporal active-fire clustering approach for global burned area mapping at 250 m from MODIS data. *Remote Sensing of Environment*, *236*, 111493.

Loboda, T., O'neal, K., & Csiszar, I. (2007). Regionally adaptable dNBR-based algorithm for burned area mapping from MODIS data. *Remote Sensing of Environment*, *109*, 429–442.

Lu, B., He, Y., & Tong, A. (2016). Evaluation of spectral indices for estimating burn severity in semiarid grasslands. *International journal of wildland fire*, *25*, 147–157.

Ma, L., Liu, Y., Zhang, X., Ye, Y., Yin, G., & Johnson, B. A. (2019). Deep learning in remote sensing applications: A meta-analysis and review. *ISPRS journal of photogrammetry and remote sensing*, *152*, 166–177.

Maggiori, E., Tarabalka, Y., Charpiat, G., & Alliez, P. (2016). Convolutional neural networks for large-scale remote-sensing image classification. *IEEE Transactions on Geoscience and Remote Sensing*, *55*, 645–657.

Mandanici, E., & Bitelli, G. (2016). Preliminary comparison of sentinel-2 and landsat 8 imagery for a combined use. *Remote Sensing*, *8*, 1014.

Melchiorre, A., & Boschetti, L. (2018). Global analysis of burned area persistence time with MODIS data. *Remote Sensing*, *10*, 750.

Menges, C., Bartolo, R., Bell, D., & Hill, G. E. (2004). The effect of savanna fires on SAR backscatter in northern Australia. *International Journal of Remote Sensing*, *25*, 4857–4871.

Mouillot, F., Schultz, M. G., Yue, C., Cadule, P., Tansey, K., Ciais, P., & Chuvieco, E. (2014). Ten years of global burned area products from spaceborne remote sensing—A review: Analysis of user needs and recommendations for future developments. *International Journal of Applied Earth Observation and Geoinformation*, *26*, 64–79.

Nair, V., & Hinton, G. E. (2010). Rectified linear units improve restricted boltzmann machines. In *Proceedings of the 27th international conference on machine learning (ICML-10)* (pp. 807–814).

Ottinger, M., Clauss, K., & Kuenzer, C. (2017). Large-scale Assessment of coastal aquaculture ponds with sentinel-1 time series data. *Remote Sensing*, *9*, 440.

Padilla, M., Olofsson, P., Stehman, S. V., Tansey, K., & Chuvieco, E. (2017). Stratification and sample allocation for reference burned area data. *Remote Sensing of Environment*, *203*, 240–255.

Padilla, M., Stehman, S. V., & Chuvieco, E. (2014). Validation of the 2008 MODIS-MCD45 global burned area product using stratified random sampling. *Remote Sensing of Environment*, *144*, 187–196.

Padilla, M., Stehman, S. V., Ramo, R., Corti, D., Hantson, S., Oliva, P., Alonso-Canas, I., Bradley, A. V., Tansey, K., Mota, B. et al. (2015). Comparing the accuracies of remote sensing global burned area products using stratified random sampling and estimation. *Remote Sensing of Environment*, *160*, 114–121.

Padilla, M., Wheeler, J., & Tansey, K. (2018). D4. 1.1 Product Validation Report (PVR). In *ESA CCI ECV Fire Disturbance*. ESA Climate Change Initiative–Fire_cci.

Pausas, J. G., & Paula, S. (2012). Fuel shapes the fire–climate relationship: evidence from Mediterranean ecosystems. *Global Ecology and Biogeography*, *21*, 1074–1082.

Pinto, M. M., Libonati, R., Trigo, R. M., Trigo, I. F., & DaCamara, C. C. (2020). A deep learning approach for mapping and dating burned areas using temporal sequences of satellite images. *ISPRS Journal of Photogrammetry and Remote Sensing*, *160*, 260–274.

Plummer, S., Lecomte, P., & Doherty, M. (2017). The ESA Climate Change Initiative (CCI): A European contribution to the generation of the Global Climate Observing System. *Remote Sensing of Environment*, *203*, 2–8.

Poulter, B., Cadule, P., Cheiney, A., Ciais, P., Hodson, E., Peylin, P., Plummer, S., Spessa, A., Saatchi, S., Yue, C. et al. (2015). Sensitivity of global terrestrial carbon cycle dynamics to variability in satellite-observed burned area. *Global Biogeochemical Cycles*, *29*, 207–222.

Quegan, S., Le Toan, T., Yu, J. J., Ribbes, F., & Floury, N. (2000). Multitemporal ERS SAR analysis applied to forest mapping. *IEEE Transactions on Geoscience and Remote Sensing*, *38*, 741–753.

Roteta, E., Bastarrika, A., Padilla, M., Storm, T., & Chuvieco, E. (2019). Development of a Sentinel-2 burned area algorithm: Generation of a small fire database for sub-Saharan Africa. *Remote Sensing of Environment*, *222*, 1–17.

Rouse Jr, J., Haas, R., Schell, J., & Deering, D. (1974). Monitoring vegetation systems in the Great Plains with ERTS. In *NASA. Goddard Space Flight Center 3d ERTS-1 Symp* (pp. 309–317). NASA volume 1.

Roy, D. P., Boschetti, L., Justice, C. O., & Ju, J. (2008). The collection 5 MODIS burned area product—Global evaluation by comparison with the MODIS active fire product. *Remote Sensing of Environment*, *112*, 3690–3707.

Saha, S., Bovolo, F., & Bruzzone, L. (2019). Unsupervised Deep Change Vector Analysis for Multiple-Change Detection in VHR Images. *IEEE Transactions on Geoscience and Remote Sensing*, *57*, 3677–3693.

Scarpa, G., Gargiulo, M., Mazza, A., & Gaetano, R. (2018). A CNN-based fusion method for feature extraction from sentinel data. *Remote Sensing*, *10*, 236.

Schmidhuber, J. (2015). Deep learning in neural networks: An overview. *Neural networks*, *61*, 85–117.

Schroeder, W., Oliva, P., Giglio, L., & Csiszar, I. A. (2014). The New VIIRS 375 m active fire detection data product: Algorithm description and initial assessment. *Remote Sensing of Environment*, *143*, 85–96.

Sharma, R., Hara, K., & Tateishi, R. (2018). Developing Forest Cover Composites through a Combination of Landsat-8 Optical and Sentinel-1 SAR Data for the Visualization and Extraction of Forested Areas. *Journal of Imaging*, *4*, 105.

Sitanggang, I., Yaakob, R., Mustapha, N., & Ainuddin, A. (2013). Predictive models for hotspots occurrence using decision tree algorithms and logistic regression. *Journal of applied sciences*, *13*, 252–261.

Strigl, D., Kofler, K., & Podlipnig, S. (2010). Performance and scalability of GPU-based convolutional neural networks. In *2010 18th Euromicro Conference on Parallel, Distributed and Network-based Processing* (pp. 317–324). IEEE.

Stroppiana, D., Azar, R., Calò, F., Pepe, A., Imperatore, P., Boschetti, M., Silva, J., Brivio, P. A., & Lanari, R. (2015). Integration of optical and SAR data for burned area mapping in Mediterranean Regions. *Remote Sensing*, *7*, 1320–1345.

Tanase, M. A., & Belenguer-Plomer, M. A. (2018). 03. D3 Intermediate validation results: SAR pre-processing and burned area detection, version 1.0. In *ESA CCI ECV Fire Disturbance*. ESA Climate Change Initiative–Fire_cci.

Tanase, M. A., Belenguer-Plomer, M. A., Roteta, E., Bastarrika, A., Wheeler, J., Fernández-Carrillo, Á., Tansey, K., Wiedemann, W., Navratil, P., Lohberger, S. et al. (2020). Burned Area Detection and Mapping: Intercomparison of Sentinel-1 and Sentinel-2 Based Algorithms over Tropical Africa. *Remote Sensing*, *12*, 334.

Tavares, P. A., Beltrão, N. E. S., Guimarães, U. S., & Teodoro, A. C. (2019). Integration of sentinel-1 and sentinel-2 for classification and LULC mapping in the urban area of Belém, eastern Brazilian Amazon. *Sensors*, *19*, 1140.

Trigg, S., & Flasse, S. (2001). An evaluation of different bi-spectral spaces for discriminating burned shrub-savannah. *International Journal of Remote Sensing*, *22*, 2641–2647.

Tucker, C. J. (1979). Red and photographic infrared linear combinations for monitoring vegetation. *Remote sensing of Environment*, *8*, 127–150.

Van Der Werf, G. R., Randerson, J. T., Giglio, L., Van Leeuwen, T. T., Chen, Y., Rogers, B. M., Mu, M., Van Marle, M. J., Morton, D. C., Collatz, G. J. et al. (2017). Global fire emissions estimates during 1997-2016. *Earth System Science Data*, *9*, 697–720.

Van Tricht, K., Gobin, A., Gilliams, S., & Piccard, I. (2018). Synergistic use of radar Sentinel-1 and optical Sentinel-2 imagery for crop mapping: A case study for Belgium. *Remote Sensing*, *10*, 1642.

Verhegghen, A., Eva, H., Ceccherini, G., Achard, F., Gond, V., Gourlet-Fleury, S., & Cerutti, P. O. (2016). The potential of Sentinel satellites for burnt area mapping and monitoring in the Congo Basin forests. *Remote Sensing*, *8*, 986.

Ward, D., Kloster, S., Mahowald, N., Rogers, B., Randerson, J., & Hess, P. (2012). The changing radiative forcing of fires: global model estimates for past, present and future. *Atmospheric Chemistry and Physics*, *12*, 10857–10886.

Wooster, M. J., Roberts, G., Perry, G., & Kaufman, Y. (2005). Retrieval of biomass combustion rates and totals from fire radiative power observations: FRP derivation and calibration relationships between biomass consumption and fire radiative energy release. *Journal of Geophysical Research: Atmospheres*, *110*.

Xu, X., Li, W., Ran, Q., Du, Q., Gao, L., & Zhang, B. (2017). Multisource remote sensing data classification based on convolutional neural network. *IEEE Transactions on Geoscience and Remote Sensing*, *56*, 937–949.

Zhang, C., Pan, X., Li, H., Gardiner, A., Sargent, I., Hare, J., & Atkinson, P. M. (2018). A hybrid MLP-CNN classifier for very fine resolution remotely sensed image classification. *ISPRS Journal of Photogrammetry and Remote Sensing*, *140*, 133–144.

Zhang, C., Sargent, I., Pan, X., Li, H., Gardiner, A., Hare, J., & Atkinson, P. M. (2019). Joint Deep Learning for land cover and land use classification. *Remote sensing of environment*, *221*, 173–187.

Zhong, L., Hu, L., & Zhou, H. (2019). Deep learning based multi-temporal crop classification. *Remote sensing of environment*, *221*, 430–443.

Zhong, Y., Fei, F., Liu, Y., Zhao, B., Jiao, H., & Zhang, L. (2017). SatCNN: satellite image dataset classification using agile convolutional neural networks. *Remote Sensing Letters*, *8*, 136–145.

Zhu, X. X., Tuia, D., Mou, L., Xia, G.-S., Zhang, L., Xu, F., & Fraundorfer, F. (2017). Deep learning in remote sensing: A comprehensive review and list of resources. *IEEE Geoscience and Remote Sensing Magazine*, *5*, 8–36.

Chapter 7

Evaluation of backscatter coefficient temporal indices for burned area mapping

This chapter evaluates several temporal indices based on temporal backscatter coefficient to understand their suitability for burned area detection in future approaches. The analysis was carried out using the random forests machine learning classifier, which provides a rank for each independent variable used as input. Depending on land cover type, soil moisture, and topographic conditions, remarkable differences were observed between the temporal backscatter indices trends in areas affected by fires. Such trends conditioned burned area mapping accuracy.

7.1   Introduction

Fire is considered an essential climate variable (ECV) by the Global Climate Observing System (GCOS) since, at global scale, fire-related emission of aerosols and greenhouse gases (GHGs) into the atmosphere may alter the global biochemical cycles and consequently the climate (Andreae & Merlet, 2001; Bowman et al., 2009). Furthermore, at regional and local scales, fire has a key role in ecosystems resilience since it may induce soil fertility reduction, changes in water supply, soil erosion and biodiversity loss (Lavorel et al., 2007; Van der Werf et al., 2010; Pausas & Paula, 2012). Nowadays, remote sensing has become an essential source of fires-related information for climate modelling (Poulter et al., 2015; Mouillot et al., 2014). However, most of the current global burned area products are based on optical and thermal data, which are limited by meteorological conditions (i.e., cloud cover). To overcome such limitations, the use of synthetic aperture radar (SAR) data in fire monitoring is increasing since SAR sensors are independent of clouds, smog, and solar illumination (French et al., 1999; Bourgeau-Chavez et al., 2002).

Vegetation combustion due to fire may result in a reduction of the scattering elements able to reflect SAR microwaves, which may translate into reduced post-fire backscatter coefficient when compared to pre-fire records (Van Zyl, 1993; Antikidis et al., 1998). Nevertheless, the reduction of the scattering elements may also increase ground surface scattering as signal attenuation by vegetation is reduced (Tanase et al., 2010b). Thus, the increased influence of soil moisture and surface roughness may result in increased post-fire backscatter coefficients (Siegert & Hoffmann, 2000). Besides, land cover, radar polarisation, and observation geometry may also influence the backscatter coefficient (Belenguer-Plomer et al., 2019).

The launch of Sentinel-1 A and B C-band SAR sensors in 2014 and respectively in 2016 by the European Space Agency (ESA) allowed for the acquisition of satellite imagery every three days when both ascending and descending satellite trajectories are considered. The amount of SAR data from ESA's Sentinel-1 mission has boosted the interest in SAR based approaches for burned area detection and mapping (Belenguer-Plomer et al., 2019, 2018b,a; Engelbrecht et al., 2017; Lohberger et al., 2018; Verhegghen et al., 2016). Such studies extracted changes related to fire activity using C-band backscatter coefficient temporal indices. In the present study, a suitability analysis of such temporal indices derived from Sentinel-1 data was carried out. The analysis considered different biomes and land cover classes, soil moisture conditions, as well as the local topographic conditions. The objective of this study was, therefore, the detailed evaluation of weaknesses and strengths for different backscatter coefficient indices for burned area monitoring. The overarching aim was improving the exploitation of Sentinel-1 data for burned area detection and mapping.

7.2   Study areas

Five Military Grid Reference System (MGRS) tiles (100 × 100 km each) distributed worldwide were used in this work (Figure 7.1). Reference burned areas were extracted for each tile using Landsat-8 and Sentinel-2 images using the same methods as in our previous studies (Belenguer-Plomer et al., 2019; Fernandez-Carrillo et al., 2018). The period

for which the reference burned area was extracted together with the acquisition dates of the Sentinel-1 images used in each tile was provided in Table 7.1. It should be noted that the periods for reference burned area do not exactly match with the acquisition dates of Sentinel-1 due to differences between satellites orbital pass and periods of overcast skies that affected the optical imagery.
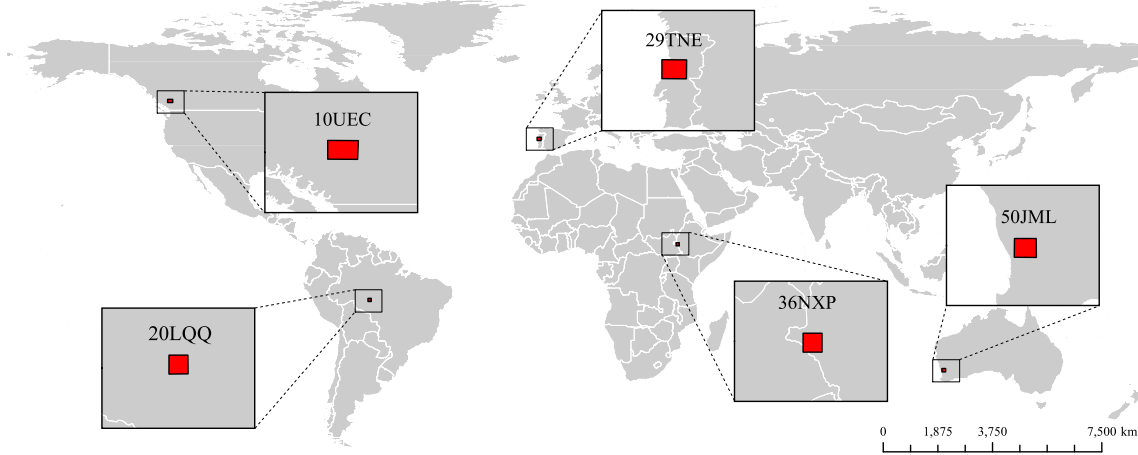

Figure 7.1: Location of the study areas.

Table 7.1: Periods of reference burned area and acquisition time of Sentinel-1 images used.

MGRS tile	Burned area period	Sentinel-1 period
10UEC	20170705 - 20170822	20170626 - 20170825
20LQQ	20160704 - 20160922	20160703 - 20160925
29TNE	20171005 - 20171106	20170929 - 20171110
36NXP	20161230 - 20170115	20161209 - 20170126
50JML	20170307 - 20170510	20170304 - 20170515

7.3 Methods

7.3.1 Datasets

7.3.1.1 SAR data and pre-processing

Ground Range Detected (GRD) dual-polarised (vertical-vertical VV, and vertical-horizontal VH polarisation) SAR images acquired by C-band Sentinel-1 A/B satellites in interferometric wide (IW) swath mode, were used in this study. Such images were processed employing the fully automatic processing chain S1Tiling. S1Tiling was developed by Thierry Koleck at National Centre for Space Studies (CNES) and Centre d'Etudes Spatiales de la BIOsphère (CESBIO) and is based on the open-source libraries available in the Orfeo ToolBox (OTB) (Inglada & Christophe, 2009). S1Tiling was used in our previous studies as it provides similar results when compared to well-established SAR processing

commercial packages (Belenguer-Plomer et al., 2019, 2018b; Tanase & Belenguer-Plomer, 2018). S1Tiling processing may be grouped in three steps: (i) pre-processing, where the images were calibrated to gamma nought; (ii) geocoding, where the orthorectification was carried out; and (iii) multi-temporal filtering (Quegan et al., 2000). The Sentinel-1 data were processed to 20 m, the nominal Sentinel-1 ground spatial resolution. For the analysis, the images were aggregated to 40 m since this pixel spacing was found as having the best trade-off between speckle reduction, computing requirements, and accuracy when detecting burned area (Tanase & Belenguer-Plomer, 2018).

7.3.1.2   Land cover

Information of land cover was needed to understand the importance of the temporal backscatter coefficient indices when detecting burned area since the main scattering process may vary with the land cover class. The most recent (i.e., 2015) global product of land cover types, from ESA's Land_Cover_cci project, was used. Since land cover data was produced at 300 m pixel spacing, it was resized using a nearest-neighbour interpolation to coincide with the processed SAR spacing (40 m). The land cover classes were simplified in Crops, Grasslands, Shrubs, Forests, and Others as per our previous work (Belenguer-Plomer et al., 2019).

7.3.1.3   Soil moisture

Soil moisture is an important factor affecting radar backscatter (Schoups et al., 1998). In this study information of soil moisture was obtained from the global Soil Moisture Active Passive (SMAP) Enhanced Level 3 Passive Soil Moisture Product, which is based on an L-Band Radiometer. The radar indices importance when detecting burned area was computed when a reduction, an increment or a no change in soil moisture between pre- and post-fire dates respectively were observed in the SMAP product. Any variation lower than 0.059 m^3/m^3, the error of the SMAP Enhanced Passive product when compared to *in situ* measurements (Chen et al., 2017), was assumed as a no change.

7.3.1.4   Topography

Topographic slope affects burned area detection from C-band Sentinel-1 data and needs to be accounted for (Belenguer-Plomer et al., 2019). In this study, the topographic conditions were studied through the local slope and the slope orientation (i.e., aspect) with respect to the SAR looking geometry. To assess the importance of the SAR temporal indices in different topographical conditions, the slope and orientation were derived using the Shuttle Radar Topography Mission (SRTM). Pixels were grouped in ten degrees classes of local slope after taking into account the orientation, i.e., slopes oriented away and towards the sensor. Notice that for local slopes below $10°$ the aspect information was not taken into account since these pixels correspond to nearly flat areas.

7.3.2   SAR temporal indices

Eight backscatter coefficient temporal radar indices (RI) were computed to evaluate their importance when detecting burned area (Equation 7.1-7.8). RI_1 and RI_2 indices were

used in previous approaches focused on fire severity estimation (Tanase et al., 2015); RI_3 and RI_4 were log-ratios used in SAR based change detection (Bovolo & Bruzzone, 2005); RI_5, RI_6, and RI_7 (with RI_1 and RI_2) were used in burned area detection using Sentinel-1 images (Belenguer-Plomer et al., 2019) and RI_8 was the log-ratio of the RI_7.

$$RI_1 = \gamma^0 VV_{t-1} / \gamma^0 VV_{t+1} \tag{7.1}$$

$$RI_2 = \gamma^0 VH_{t-1} / \gamma^0 VH_{t+1} \tag{7.2}$$

$$RI_3 = \log\left(\gamma^0 VV_{t-1} / \gamma^0 VV_{t+1}\right) \tag{7.3}$$

$$RI_4 = \log\left(\gamma^0 VH_{t-1} / \gamma^0 VH_{t+1}\right) \tag{7.4}$$

$$RI_5 = \gamma^0 VV_{t-1} - \gamma^0 VV_{t+1} \tag{7.5}$$

$$RI_6 = \gamma^0 VH_{t-1} - \gamma^0 VH_{t+1} \tag{7.6}$$

$$RI_7 = \left(\gamma^0 VH_{t-1} / \gamma^0 VV_{t-1}\right) / \left(\gamma^0 VH_{t+1} / \gamma^0 VV_{t+1}\right) \tag{7.7}$$

$$RI_8 = \log\left(\left(\gamma^0 VH_{t-1} / \gamma^0 VV_{t-1}\right) / \left(\gamma^0 VH_{t+1} / \gamma^0 VV_{t+1}\right)\right) \tag{7.8}$$

where γ^0 is the backscatter coefficient in linear scale of VV or VH polarisations, and $t-1$ and $t+1$ are pre-fire and respectively post-fire dates.

7.3.3 Importance prediction

RIs importance was analysed by using the random forests classifier (Breiman, 2001). The importance of each index was computed by the random forests during the classification between burned and unburned areas. The reference burned area obtained from the optical sensors were used to label both classes. Such an approach was used recently in an increasing number of studies to extract the importance of the independent variables used for the classification process (Belgiu & Drăguţ, 2016; Nguyen et al., 2018; Hislop et al., 2019; Zhang et al., 2019). Notice that for each group of land cover class, local slope and aspect, and soil moisture variation class (i.e., reduction, increment, no-change) an individual random forests model was constructed. The importance values recorded for each index were converted to percentages (Equation 7.9) to carry out an inter-comparison between different groups.

$$\text{pImp}_{RI_i} = \frac{\text{Imp}_{RI_i} \times 100}{\sum_{i=1}^{8} \text{Imp}_{RI_i}} \tag{7.9}$$

where pImp is the percentage importance of a given radar index (RI) i.

7.4 Results and discussions

7.4.1 Indices importance as a function of land cover class

The importance of RIs varied with the land cover class (Figure 7.2). Apart from the variable vegetation structure by land cover class, these differences might also be related to variations in the moisture content and topographic effects (see subsection 7.4.2 and subsection 7.4.3). The largest difference between RIs importance was observed for Grasslands, where RI_5 and RI_6 had the highest importance when distinguishing between burned and

unburned pixels. This is an important finding as low burned area mapping accuracies were observed over Grasslands when using RI_2 and RI_7 (Belenguer-Plomer et al., 2019).

Indices based on VV polarisation tended to have higher importance when compared to VH over Grasslands. This trend is unusual when comparing to previous studies where C-band cross-polarised data (HV or VH) was found to provide more accurate results due to its increased sensitivity to the volumetric scattering from vegetation (Tanase et al., 2010b; Imperatore et al., 2017; Belenguer-Plomer et al., 2019). Therefore, future algorithms pursuing burned area detection and mapping over large areas must consider different indices depending on the land cover type as opposed to using a standard set of indices regardless of vegetation type (Belenguer-Plomer et al., 2019). Such a rationale is supported by other studies (Belenguer-Plomer et al., 2018a) which suggest that VV polarisation may improve burned area detection when changes in soil and vegetation moisture conditions have occurred between the SAR observations (Bourgeau-Chavez et al., 2002). Since co-polarised backscatter is more responsive to changes in soil surface properties when compared to the cross-polarised backscatter (Freeman & Durden, 1998; Van Zyl et al., 2011) and biomass reduction by fire may increase the effect of ground in scattering processes (penetration of the microwave across burned vegetation increases) the co-polarised waves may provide the needed edge when detecting BA at least for some land cover types (Tanase et al., 2010b). The log-ratio indices (RI_3, RI_4, and RI_8) had similar or lower importance than simple ratios, which have been used widely in fire monitoring using SAR data.
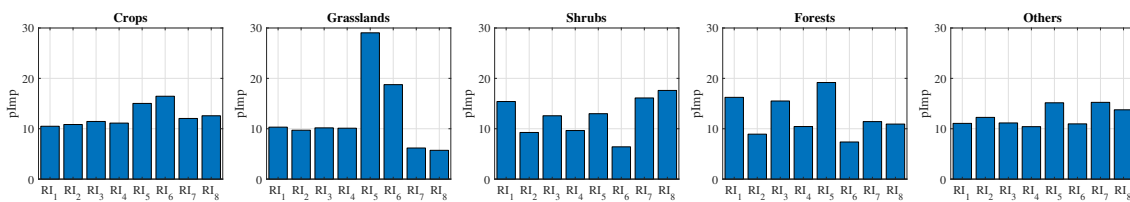

Figure 7.2: Radar indices importance when detecting burned area by land cover classes.

7.4.2   Indices importance as a function of changes in soil moisture

Differences in temporal backscatter coefficient indices importance when detecting burned area also depend on soil moisture variations between pre- and post-fire dates (Figure 7.3). The influence of soil moisture was analysed under three different scenarios: increment, reduction, and no-change of post-fire when compared to pre-fire levels. When soil moisture increased, the VV polarisation tended to have higher importance for BA detection. For Grasslands and Others land cover classes this trend was only observed for RI_5 and RI_6. Conversely, for reduced post-fire soil moisture levels, the VH channel tended to have higher importance. Notice reduced post-fire soil moisture conditions were not observed in our study areas for Grasslands and Others land classes.

Such differences between VV and VH-based RIs importance as a function of soil moisture variations are in accordance with previous findings since the co-polarised waves (e.g., VV) are more responsive to changes in surface properties (i.e., soil moisture) when compared to the cross-polarised waves (Freeman & Durden, 1998; Yamaguchi et al., 2005; Van Zyl et al., 2011). For the specific case of burned area, increased soil moisture levels

after fire increase the VV channel variability, which explains its greater importance when monitoring burned areas.

It should be noted that the pixel spacing of the SMAP product (9 km) used to extract the soil moisture variations may affect the significance of this analysis. This may explain the increased importance of VV-based RIs when compared to VH-based ones observed for some cases under a no soil moisture change scenario.
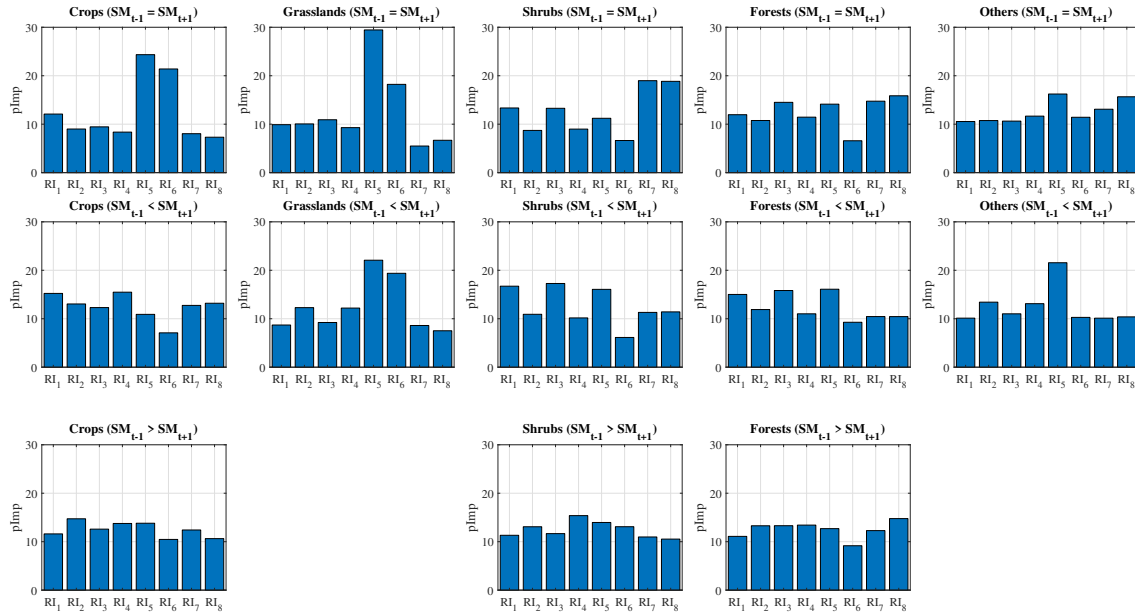

Figure 7.3: Radar indices importance when detecting burned area for three soil moisture variation (post- to pre-fire) scenarios: increment, reduction, no-change. The importance is analysed separately by land cover class. The upper row shows the no-change scenario. The middle row shows the increment in soil moisture for post-fire dates. The bottom row shows a reduction in soil moisture for post-fire dates.

7.4.3 Indices importance as a function of topography

The importance of each radar index by local slope and aspect (positive-towards the sensor and negative-away from the sensor) is shown in Figure 7.4 for each land cover class. Notice the increased number of slope categories for the Forests class. The importance of RI_5 and RI_6, considerable over Grasslands, was reduced when the local slope increased, with the smallest importance values being observed for slopes above $20°$. This trend was observed for both positive and negative aspects, particularly over Grasslands and Others land cover classes.

VH polarisation-based indices had the largest importance when local slope was significant ($>30°$) over negative aspects. This may be related to a reduced scattering from ground in shadowed areas (Tanase et al., 2010a), which results in a reduced ground backscatter when compared to the positive aspects.
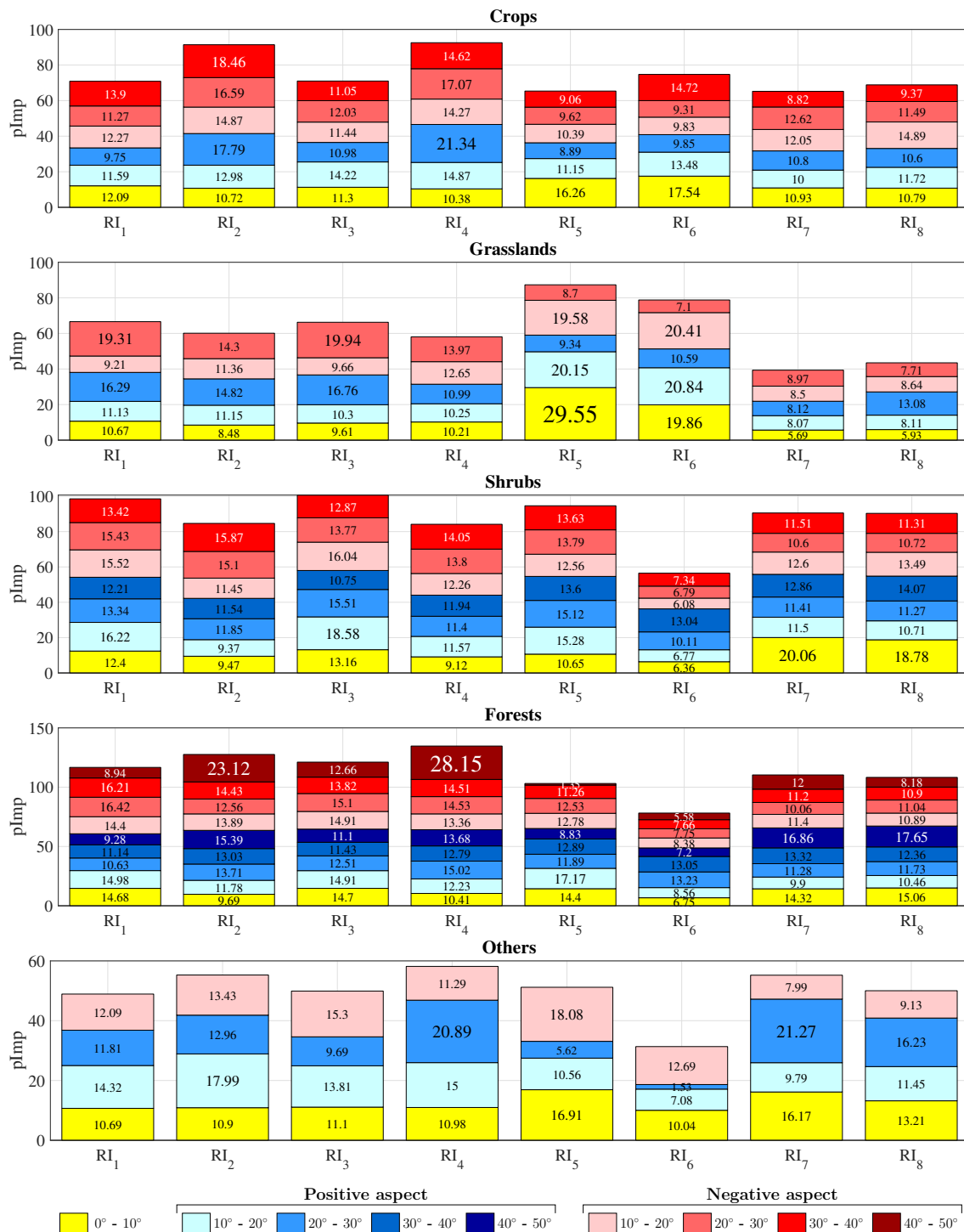
Figure 7.4: Radar indices importance when detecting burned area by land cover classes, local slope and aspect. Positive aspects denote slopes oriented towards the sensor. Negative aspects denote slopes oriented away from the sensor.

7.5 Conclusions

This work has quantified and analysed the importance of several Sentinel-1's backscatter coefficient (VV and VH polarisations) based temporal indices for burned area detection. The study was carried out over five areas (one million hectares each) distributed world-wide. The random forests classifier was used to predict indices importance during the classification process. The results showed differences in RIs importance depending on the land cover type. In particular, significant importances were observed over Grasslands for two indices, RI_5 and RI_6.

Soil moisture was a key element by improving the detection capability of different radar indices. Rainfall after fire events resulted in an increased importance of the VV-based indices, while reduced post-fire soil moisture resulted in an increased importance of the VH-based indices. Topography also affected indices significance. Over shadowed regions (negative aspect and slope $>30°$), the VH polarisation had higher importance when detecting the burned area as a consequence of a reduced backscattering process from ground.

Future burned area mapping research based on C-band Sentinel-1 backscatter coefficient shall consider the differentiated potential of VV and VH based indices depending on land cover, changes in soil moisture and topographic conditions to improve mapping accuracies.

Acknowledgements

7.6 References

Andreae, M. O., & Merlet, P. (2001). Emission of trace gases and aerosols from biomass burning. *Global Biogeochemical Cycles*, *15*, 955–966.

Antikidis, E., Arino, O., Arnaud, A., & Laur, H. (1998). ERS SAR Coherence & ATSR Hot Spots: a Synergy for Mapping Deforested Areas. The Special Case of the 1997 Fire Event in Indonesia. *European Space Agency-Publications-ESA SP*, *441*, 355–360.

Belenguer-Plomer, M. A., Tanase, M. A., Fernandez-Carrillo, A., & Chuvieco, E. (2018a). Insights into burned areas detection from Sentinel-1 data and locally adaptive algorithms. In *Active and Passive Microwave Remote Sensing for Environmental Monitoring II* (p. 107880G). International Society for Optics and Photonics volume 10788.

Belenguer-Plomer, M. A., Tanase, M. A., Fernandez-Carrillo, A., & Chuvieco, E. (2018b). Temporal backscattering coefficient decorrelation in burned areas. In *Active and Passive Microwave Remote Sensing for Environmental Monitoring II* (p. 107880T). International Society for Optics and Photonics volume 10788.

Belenguer-Plomer, M. A., Tanase, M. A., Fernandez-Carrillo, A., & Chuvieco, E. (2019). Burned area detection and mapping using Sentinel-1 backscatter coefficient and thermal anomalies. *Remote Sensing of Environment*, *233*, 111345.

Belgiu, M., & Drăguţ, L. (2016). Random forest in remote sensing: A review of applications and future directions. *ISPRS Journal of Photogrammetry and Remote Sensing*, *114*, 24–31.

Bourgeau-Chavez, L., Kasischke, E., Brunzell, S., Mudd, J., & Tukman, M. (2002). Mapping fire scars in global boreal forests using imaging radar data. *International Journal of Remote Sensing*, *23*, 4211–4234.

Bovolo, F., & Bruzzone, L. (2005). A detail-preserving scale-driven approach to change detection in multitemporal SAR images. *IEEE Transactions on Geoscience and Remote Sensing*, *43*, 2963–2972.

Bowman, D. M., Balch, J. K., Artaxo, P., Bond, W. J., Carlson, J. M., Cochrane, M. A., D'Antonio, C. M., DeFries, R. S., Doyle, J. C., Harrison, S. P. et al. (2009). Fire in the Earth system. *Science*, *324*, 481–484.

Breiman, L. (2001). Random forests. *Machine learning*, *45*, 5–32.

Chen, Q., Zeng, J., Cui, C., Li, Z., Chen, K.-S., Bai, X., & Xu, J. (2017). Soil moisture retrieval from smap: A validation and error analysis study using ground-based observations over the little washita watershed. *IEEE Transactions on Geoscience and Remote Sensing*, *56*, 1394–1408.

Engelbrecht, J., Theron, A., Vhengani, L., & Kemp, J. (2017). A simple normalized difference approach to burnt area mapping using multi-polarisation C-Band SAR. *Remote Sensing*, *9*, 764.

Fernandez-Carrillo, A., Belenguer-Plomer, M., Chuvieco, E., & Tanase, M. (2018). Effects of sample size on burned areas accuracy estimates in the Amazon Basin. In *Earth Resources and Environmental Remote Sensing/GIS Applications IX* (p. 107901S). International Society for Optics and Photonics volume 10790.

Freeman, A., & Durden, S. L. (1998). A three-component scattering model for polarimetric SAR data. *IEEE Transactions on Geoscience and Remote Sensing*, *36*, 963–973.

French, N. H., Bourgeau-Chavez, L. L., Wang, Y., & Kasischke, E. S. (1999). Initial observations of Radarsat imagery at fire-disturbed sites in interior Alaska. *Remote Sensing of Environment*, *68*, 89–94.

Hislop, S., Jones, S., Soto-Berelov, M., Skidmore, A., Haywood, A., & Nguyen, T. H. (2019). A fusion approach to forest disturbance mapping using time series ensemble techniques. *Remote sensing of environment*, *221*, 188–197.

Imperatore, P., Azar, R., Calo, F., Stroppiana, D., Brivio, P. A., Lanari, R., & Pepe, A. (2017). Effect of the Vegetation Fire on Backscattering: An Investigation Based on Sentinel-1 Observations. *IEEE Journal of Selected Topics in Applied Earth Observations and Remote Sensing*, *10*, 4478–4492.

Inglada, J., & Christophe, E. (2009). The Orfeo Toolbox remote sensing image processing software. In *Geoscience and Remote Sensing Symposium, 2009 IEEE International, IGARSS 2009* (pp. IV–733). IEEE volume 4.

Lavorel, S., Flannigan, M. D., Lambin, E. F., & Scholes, M. C. (2007). Vulnerability of land systems to fire: Interactions among humans, climate, the atmosphere, and ecosystems. *Mitigation and Adaptation Strategies for Global Change*, *12*, 33–53.

Lohberger, S., Stängel, M., Atwood, E. C., & Siegert, F. (2018). Spatial evaluation of Indonesia's 2015 fire-affected area and estimated carbon emissions using Sentinel-1. *Global change biology*, *24*, 644–654.

Mouillot, F., Schultz, M. G., Yue, C., Cadule, P., Tansey, K., Ciais, P., & Chuvieco, E. (2014). Ten years of global burned area products from spaceborne remote sensing—A review: Analysis of user needs and recommendations for future developments. *International Journal of Applied Earth Observation and Geoinformation*, *26*, 64–79.

Nguyen, T. H., Jones, S. D., Soto-Berelov, M., Haywood, A., & Hislop, S. (2018). A spatial and temporal analysis of forest dynamics using Landsat time-series. *Remote sensing of environment*, *217*, 461–475.

Pausas, J. G., & Paula, S. (2012). Fuel shapes the fire–climate relationship: evidence from Mediterranean ecosystems. *Global Ecology and Biogeography*, *21*, 1074–1082.

Poulter, B., Cadule, P., Cheiney, A., Ciais, P., Hodson, E., Peylin, P., Plummer, S., Spessa, A., Saatchi, S., Yue, C. et al. (2015). Sensitivity of global terrestrial carbon cycle dynamics to variability in satellite-observed burned area. *Global Biogeochemical Cycles*, *29*, 207–222.

Quegan, S., Le Toan, T., Yu, J. J., Ribbes, F., & Floury, N. (2000). Multitemporal ERS SAR analysis applied to forest mapping. *IEEE Transactions on Geoscience and Remote Sensing*, *38*, 741–753.

Schoups, G., Troch, P., & Verhoest, N. (1998). Soil moisture influences on the radar backscattering of sugar beet fields. *Remote sensing of environment*, *65*, 184–194.

Siegert, F., & Hoffmann, A. A. (2000). The 1998 forest fires in East Kalimantan (Indonesia): A quantitative evaluation using high resolution, multitemporal ERS-2 SAR images and NOAA-AVHRR hotspot data. *Remote Sensing of Environment*, *72*, 64–77.

Tanase, M., Kennedy, R., & Aponte, C. (2015). Radar Burn Ratio for fire severity estimation at canopy level: An example for temperate forests. *Remote Sensing of Environment*, *170*, 14–31.

Tanase, M. A., & Belenguer-Plomer, M. A. (2018). 03. D3 Intermediate validation results: SAR pre-processing and burned area detection, version 1.0. In *ESA CCI ECV Fire Disturbance*. ESA Climate Change Initiative–Fire_cci.

Tanase, M. A., Perez-Cabello, F., de La Riva, J., & Santoro, M. (2010a). TerraSAR-X data for burn severity evaluation in Mediterranean forests on sloped terrain. *IEEE Transactions on Geoscience and Remote Sensing*, *48*, 917–929.

Tanase, M. A., Santoro, M., de La Riva, J., Fernando, P., Le Toan, T. et al. (2010b). Sensitivity of X-, C-, and L-band SAR backscatter to burn severity in Mediterranean pine forests. *IEEE Transactions on Geoscience and Remote Sensing*, *48*, 3663–3675.

Van Zyl, J. J. (1993). The effect of topography on radar scattering from vegetated areas. *IEEE Transactions on Geoscience and Remote Sensing*, *31*, 153–160.

Van Zyl, J. J., Arii, M., & Kim, Y. (2011). Model-based decomposition of polarimetric SAR covariance matrices constrained for nonnegative eigenvalues. *IEEE Transactions on Geoscience and Remote Sensing*, *49*, 3452–3459.

Verhegghen, A., Eva, H., Ceccherini, G., Achard, F., Gond, V., Gourlet-Fleury, S., & Cerutti, P. O. (2016). The potential of Sentinel satellites for burnt area mapping and monitoring in the Congo Basin forests. *Remote Sensing*, *8*, 986.

Van der Werf, G. R., Randerson, J. T., Giglio, L., Collatz, G., Mu, M., Kasibhatla, P. S., Morton, D. C., DeFries, R., Jin, Y. v., & van Leeuwen, T. T. (2010). Global fire emissions and the contribution of deforestation, savanna, forest, agricultural, and peat fires (1997–2009). *Atmospheric Chemistry and Physics*, *10*, 11707–11735.

Yamaguchi, Y., Moriyama, T., Ishido, M., & Yamada, H. (2005). Four-component scattering model for polarimetric SAR image decomposition. *IEEE Transactions on Geoscience and Remote Sensing*, *43*, 1699–1706.

Zhang, Y., Sui, B., Shen, H., & Ouyang, L. (2019). Mapping stocks of soil total nitrogen using remote sensing data: A comparison of random forest models with different predictors. *Computers and Electronics in Agriculture*, *160*, 23–30.

Chapter 8

Conclusions

In this last chapter, the conclusions derived from all research activities carried out within the doctoral thesis are resumed. The main findings, as well as the observed limitations, are described together with potential lines for future research that may help improving global mapping of burned areas from radar datasets and the combination of radar and optical datasets.

This doctoral thesis addressed burned area mapping from medium spatial resolution radar time series as well as joint radar-optical datasets over fire-prone biomes. As burned area mapping algorithms from radar time series are currently less mature, when compared to optical-based algorithms, most efforts have focused on improving the radar-based mapping methods. The research has taken advantage of the Sentinel-1 mission open data policy as well as its global availability at high spatial and temporal resolution.

The developed radar-based algorithms relied on the C-band backscatter coefficient due to the much-reduced computing demands when compared to using the interferometric coherence. The Sentinel-1 data was aggregated to 40 m since such a spacing allow reducing computing time considerably with marginal accuracy differences being observed when compared to using the nominal Sentinel-1 spatial resolution (i.e., 20 m). A significant achievement of the developed radar-based mapping algorithms was their potential to work without *a priori* information (except for ancillary thermal-based hotspots and land cover maps) and pre-determined thresholds. The algorithm independence *a priori* data and its self-adapting to local conditions ability allow mapping burned areas in any ecosystem from regional to global scales. Such capabilities are determinant as previous radar-based approaches were limited to regional or local scales.

When analysing the results from the first mapping algorithm developed based on detecting anomalous changes of the backscatter coefficient through the Reed-Xiaoli detector, the mapping accuracy was positively related with the presence of thermal anomalies derived from Earth observation products (i.e., hotspots). Despite such dependency, the radar-based mapping accuracy was higher when compared to that of available products such as MCD64A1, the most widely used global burned area product. In particular, the increased accuracy of the radar-based algorithm was related to the reduction of omission errors. Such improvement suggests that Sentinel-1 data may become a determinant information-source over areas with persistent cloud cover were optical-based algorithm more limited. Such improvements may allow for reducing burned area mapping uncertainty by estimating the near-real extension at global levels when compared to current products based on coarser spatial resolution optical sensors.

Apart from hotspots dependency, radar-based mapping was limited over areas with pronounced topography with slopes oriented away from the sensor being affected by omission errors. However, such omission errors were reduced by combining images from ascending and descending Sentinel-1 satellite passes. Omission errors were also related to low fire severity levels, i.e., reduced biomass consumption and consequently low pre- to post-fire backscatter coefficient variations. Commission errors were linked to fire-unrelated changes which modify the scattering process such as variation in soil moisture. Likewise, the land cover also influenced the mapping errors. In particular, higher accuracies were found over Forests, while lower mapping accuracies were observed over Grasslands. Such differences were explained by the lower sensitivity of C-band data when monitoring some vegetation types.

An additional limiting factor for the radar-based algorithm was the temporal decorrelation, linked to variations in soil moisture or fire severity. Temporal decorrelation may

limit the accuracy of burned area mapping as more extended radar temporal series are needed to account for the decorrelation between fire events and backscatter changes. Nevertheless, for most burned pixels affected by temporal decorrelation, burned area detection and mapping was possible during the first month after the fire, as opposed to detection on the first post-fire acquisition. Over burned areas affected by temporal decorrelation, the backscatter coefficient increased or decreased when compared to pre- and post-fire values. Reduced soil moisture and delayed vegetation death were the main influencing factors behind backscatter coefficient decrease. Conversely, increased post-fire soil moisture was behind post-fire backscatter coefficient increases. Notice that these findings were validated over Mediterranean ecosystems where more detailed (1 km spacing) soil moisture products were available. However, temporal decorrelation was observed in many ecosystems. Thus, further research is needed to confirm such findings over larger areas and different biomes.

On the other hand, deep learning methods, and concretely CNN, were also used to for burned area mapping from radar as well as joint radar-optical datasets. Despite its recent spawn in remote sensing-based applications, to date, few studies have addressed fire events monitoring. In this thesis, a detailed analysis was carried out to ascertain the optimum CNN configuration for burned area mapping. The results suggested that two hidden layers provided the best trade-off between accuracy and computing time while the optimum image-dimension for feature extraction, data normalisation, and softmax thresholding, depended on the input data (radar, optical, radar-optical) and land cover class. The CNN-based burned area mapping accuracy was similar, regardless of the input datasets (i.e., radar or optical), with that observed in previous studies that used Sentinel-1 or Sentinel-2 imagery. However, CNNs-based mapping was considerably more versatile and required less developing-time when compared to ad-hoc algorithms developed over relatively small areas. Such a versatility, as well as the radar-optical data integration, allowed exploiting Sentinel-1 and Sentinel-2 synergies by improving slightly the highest mapping accuracy achieved when considering single sensors (i.e., radar or optical), and also providing wall-to-wall mapping as gaps from clouds, a characteristic of optical-based products, were eliminated.

The estimation of real mapping accuracy may have been obscured by the absence of high quality burned area perimeters. Mapping algorithms developed in this thesis were validated using independent datasets, mainly Landsat-8; however, the medium spatial resolution of such imagery and the mismatch between detection and reference periods may artificially increase the observed mapping errors. Ground truthing large areas affected by fire with field campaigns distributed worldwide is non-viable due to high cost. However, the availability of data acquired by high-resolution optical sensors such as the Planet constellation may allow obtaining improved datasets for validation in the future. Future research shall also focus on reducing the limitations highlighted in this thesis. Such efforts are essential particularly for the radar-based mapping as such datasets are an essential and complementary (to optical) source of information.

Radar indices analysis revealed that soil moisture is an essential factor that needs to be considered if higher accuracy mapping products are needed from Sentinel-1 backscatter coefficient. Soil moisture may change the importance of VV and VH polarisations when distinguishing between burned and unburned areas. In particular, the VV polarisation enhances burned area discrimination after rainfall events as well as at later dates

when soil humidity decreases. As mentioned above, water content was also found as a key driver affecting backscatter coefficient temporal decorrelation. Hence, future algorithms based on Sentinel-1 datasets shall take into account reliable information on soil moisture as ancillary global products become available at higher spatial resolutions when compared to current global products (e.g., SMAP at 9 km).

Likewise, the dual-polarised (i.e., VV and VH) C-band frequency, despite being an asset when compared to previous spaceborne SAR sensors, may have limited the potential of mapping burned areas using radar imagery. Full-polarised datasets (i.e., VV, VH, HH and HV) acquired by future SAR missions such as NISAR which will provide datasets at S- and L-band (launch in 2021) as well as P-band Biomass mission (launch in 2022), may provide additional information potentially improving current burned area mapping algorithms. Thus, the findings of this doctoral thesis provide a useful research starting point into global application of medium spatial resolution sensors for operational burned area mapping.